All-polymer microfluidic systems for droplet based sample analysis

Bringing droplet technologies to life: Bridging the gap between academia and industry

Poulsen, Carl Esben

Publication date:
2016

Document Version
Publisher's PDF, also known as Version of record

All-polymer microfluidic systems for droplet based sample analysis

Bringing droplet technologies to life:
Bridging the gap between academia and industry

Carl Esben Poulsen
PhD Thesis April 2016

DTU Nanotech
Department of Micro- and Nanotechnology

Technical University of Denmark
Deparment of Micro- and Nanotechnology

All-polymer microfluidic systems for droplet based sample analysis

Bringing droplet technologies to life: Bridging the gap between academia and industry

PhD thesis

Carl Esben Poulsen

Department of Micro- and Nanotechnology
TECHNICAL UNIVERSITY OF DENMARK
Kgs. Lyngby 2016

PhD thesis, April 2016

All-polymer microfluidic systems for droplet based sample analysis

Bringing droplet technologies to life: Bridging the gap between academia and industry

Carl Esben Poulsen

Department of Micro- and Nanotechnology
BioLabChip Group
Anders Wolff
Technical University of Denmark
Kgs. Lyngby 2016

All-polymer microfluidic systems for droplet based sample analysis
Bringing droplet technologies to life: Bridging the gap between academia and industry
Carl Esben Poulsen

Supervisor: Anders Wolff, Department of Micro- and Nanotechnology
Co-supervisor: Martin Dufva, Department of Micro- and Nanotechnology
Examiner: Name, Department

PhD thesis, April 2016
Department of Micro- and Nanotechnology
BioLabChip Group
Anders Wolff
Technical University of Denmark
Kgs. Lyngby
Telephone +45 45 25 57 00

Cover: Fluorescence image of droplets loaded with pre-amplified negative control LAMP reaction mix (false colours). For more on this particular experiment, see Figure 9.5 on page 149

Typeset in LaTeX
Document compiled: April 21, 2016

All-polymer microfluidic systems for droplet based sample analysis
Bringing droplet technologies to life: Bridging the gap between academia and industry
Carl Esben Poulsen
Department of Micro- and Nanotechnology
Technical University of Denmark

Abstract

In this PhD project, I pursued to develop an all-polymer injection moulded microfluidic platform with integrated droplet based single cell interrogation. To allow for a proper "one device - one experiment" methodology and to ensure a high relevancy to non-academic settings, the systems presented here were fabricated exclusive using commercially relevant fabrication methods such as injection moulding and ultrasonic welding. Further, to reduce the complexity of the final system, I have worked towards an all-in-one device which includes sample loading, priming (removal of air), droplet formation, droplet packing, imaging and amplification (heating).

The project has been broken into sub-projects, in which several devices of simpler application have been developed. Most of these employ gravity for concentrating and packing droplets, which has been made possible by the use of large area chambers bonded by ultrasonic welding.

In the sub-projects of this PhD, improvements have been made to multiple aspects of fabricating and conducting droplet (or multiphase) microfluidics:

- Design phase: Numerical prediction of the capillary burst pressure of a multiphase system.
- Fabrication: Two new types of energy directors for ultrasonic welding of microfluidic systems have been presented:
  1. Tongue-and-groove energy directors.
  2. Laser ablated micropillar energy directors.
- Fabrication: Annealing of polymer devices for use with hydrocarbon based multiphase systems.
- Experimental design and data analysis: Optimised estimators for single-hit limiting-dilution assays.

A range of concurrent activities have also been undertaken:

- TransForm-technologies, a to-be spin-out of this PhD project has been initiated, and 725,000 DKK has been raised and spent on maturation of the mould microstructuring technology, incorporating and testing the technology in a commercial setting, and formulating a business plan.
- Three patent applications have been submitted to the European Patent Office.

Keywords: Droplet, microfluidics, digital PCR, injection moulding, ultrasonic welding.

All-polymer microfluidic systems for droplet based sample analysis
Bringing droplet technologies to life: Bridging the gap between academia and industry
Carl Esben Poulsen
Department of Micro- and Nanotechnology
Technical University of Denmark

Dansk resumé

Dette PhD-projekt omhandler udviklingen af et mikrofluid plastikdevice med integreret dråbebaseret celleanalyse. For at realisere devicet som et éngangsredskab, og kun udføre ét eksperiment per device, har jeg hovedsageligt benyttet fabrikationsmetoder, der er relevante i en industriel produktion. Disse metoder inkluderer sprøjtestøbning og ultralydssvejsning. Projektet er blevet realiseret som underprojekter, der har været centeret om hvert sit underproblem rettet imod at opnå et "alt-i-et" device med bl.a. følgende funktioner: påfyldning af prøvemateriale, mulighed for fjernelse af luftbobler, konvertering af prøve til dråber, pakning af dråber, varming af dråber, samt analyse af dråber (fluorescence-billede).

Hovedparten af de dråberelaterede underprojekter benytter tyngdekraften til at kontrollere dråberne. Dette blev muliggjort ved brugen af dråbekamre med store arealer, svejset vha. ultralydssvejsning.

Under udarbejdelsen af underprojekterne, har jeg og mine kollegaer identificeret og løst adskillige problemer relateret til fabrikation af mikrofluide systemer samt multifasesystemer (så som vanddråber i olie):

- Design fasen: Vi har demonstreret hvordan man numerisk kan forudsige "burst pressure" for en så-kaldt capillary microvalve.
- Fabrikation: Vi har udviklet to nye typer svejseledere til ultralydssvejsning af mikrofluide systemer:
  1. Tongue-and-groove svejseledere.
  2. Laser ablamerede mikrostrukturerede svejseledere.
- Fabrikation: Afhærdning af plastikdevices til brug med hydrokarbon-baserede multifasesystemer.
- Forsøgsdesign og dataanalyse: Optimerede estimatorer til "single-hit limiting-dilution assays".

Sideløbende er følgende blevet udarbejdet:

- TransForm-technologies, et kommende spin-out af dette PhD-projekt er blevet etableret, og 725.000 kr er blevet tildelt i forskningsstøtte. Disse midler er blevet benyttet til at modne teknologien, og afprøve den med kommercielle partnere. Der er ydermere blevet formuleret en business plan.
- Tre patenter er blevet indsendt til det Europæiske Patentkontor.

Nøgleord: Dråber, mikrofluide systemer, digital PCR, sprøjtestøbning, ultralydssvejsning.

Acknowledgements

This PhD project was made possible by the constant and faithful support of my beloved wife Maja. Your encouragement and advice are invaluable.

I would also like to thank the rest of my family for support and for understanding when work sometimes were highest priority.

The groups of BioLabChip (Associate Professor Anders Wolff, DTU Nanotech) and LAMINATE (Professor Dang Duong Bang, DTU Food) have been helpful, supportive and inventive. I thank you all.

Big thanks to my supervisor Associate Professor Anders Wolff, for being supportive in all my work and projects, and for always contributing to- and challenging my ideas and solutions.

Lastly, I would like to thank the The Oticon Foundation, The Augustinus Foundation and The Otto Mønsted Foundation for economic support during my external stay, and Copenhagen Spin-Outs and the DTU PoC Fund for financing my leave for working on TransForm-technologies.

Esben, April 2016

Table of content

Appendices

Foreword: Introduction to this thesis

The work presented in this PhD thesis has been conducted in the period of August 15th 2012 to April 21st 2016, including a total of 8.5 months of leave for working on the spin-out-project TransForm (Appendix A). All work have been conducted at the Technical University of Denmark except that of Paper 4 which was partly conducted at the laboratory of the deMello group, Institute of Chemical and Bioengineering, Department of Chemistry and Applied Biosciences, ETH Zürich, Zürich, Switzerland, in the months of August to October 2014.

The work of this PhD project is segmented into chapters introducing their corresponding papers which is then included immediately after. To avoid confusion with the page numbers of this thesis, the papers are reduced slightly in size, and a frame has been added. When browsing through this thesis, the border on the outer margin is useful for identifying the papers. Further, when references are made from the thesis to e.g. a figure in a paper, the destination page number is always that of the thesis. The page numbering of the papers are never used. The list of publications and joint author statements contains lists of my contributions. However, in chapters of papers of which I am second author (Chapters 4 and 5) I have elaborated on my contribution and details not included in the papers.

I am of the opinion that the origin of an illustration is irrelevant if it only serves to *sketch* the message I, the author of this thesis, am trying to send. Illustrations used to *prove* a point are very different, and the origin of the illustration must be treated with high source criticism. What I am getting at, is that when inserting illustrations for *sketching* purposes, I have used a wide range of sources, including Wikipedia.org, which to some may be provocative. I am responsible for the sketches I include in my thesis, and I find no point in drawing a sketch identical to one available on the internet.

If the reader should desire a graphical presentation of the outline of work (and this thesis), please refer to Figure 1.11 on page 20.

Welcome to my PhD thesis.

Esben, April 2016

List of publications

Journal papers

Paper 3:
Carl Esben Poulsen, Kasper Kistrup, Nis Andersen, Rafael Taboryski, Mikkel Hansen, and Anders Wolff. Laser ablated micropillar energy directors for ultrasonic welding of microfluidic systems. *Journal of Micromechanics and Microengineering*. Accepted: February 29$^{\text{th}}$ 2016.[1]

- Planning of experiments (together with K. Kistrup).
- Development of micropillar energy directors (together with K. Kistrup)
- Characterisation of chip system (together with K. Kistrup).
- Writing of manuscript (together with K. Kistrup).

Paper 4:
Carl Esben Poulsen, Robert C. R. Wootton, Anders Wolff, Andrew J. DeMello, and Katherine S. Elvira. A Microfluidic Platform for the Rapid Determination of Distribution Coefficients by Gravity-Assisted Droplet-Based Liquid–Liquid Extraction. *Analytical Chemistry*, 87(12):6265–6270, jun 2015[2]

- Contributed to the planning of experiments
- Contributed to the designing phase of the microfluidic device
- Fabricated/tested microfluidic device
- Developed analytical design rules for microfluidic device
- Designed COMSOL model and conducted nummerical modelling
- Conducted all experimental work
- Contributed to data analysis and writing of manuscript

Paper 1:
Kasper Kistrup*, **Carl Esben Poulsen***, Peter Friis Østergaard, Kenneth Brian Haugshøj, Rafael Taboryski, Anders Wolff, and Mikkel Fougt Hansen. Fabrication and modelling of injection moulded all-polymer capillary microvalves for passive microfluidic control. *Journal of Micromechanics and Microengineering*, 24(12):125007, dec 2014[3]

- * **Equally contributing authors**
- Planning of experiments (together with K. Kistrup).
- Design of COMSOL model
- Nummerical modelling
- Writing of manuscript (together with K. Kistrup).

Paper 2:
Kasper Kistrup, **Carl Esben Poulsen**, Mikkel Hansen, and Anders Wolff. Ultrasonic welding for fast bonding of self-aligned structures in lab-on-a-chip systems. *Lab Chip*, 15:1998–2001, 2015[4]

- Assisted with experiment planning (main work done by K. Kistrup).
- Assisted with design of microfluidic chip and milling of replication master for injection moulding (main work done by K. Kistrup).

- Assisted with bonding of chip by ultrasonic welding (main work done by K. Kistrup).
- Assisted with characterisation of chip system (main work done by K. Kistrup).
- Design/fabrication/experimentation with droplet chip.
- Writing of manuscript (together with K. Kistrup).

Paper 5:
Carl Esben Poulsen, Anders Wolff, and Henrik Flyvbjerg. Optimized protocols for droplet-based single-hit limiting-dilution assays. (To-be submitted)

- Conceived the idea for the studying the consequences of deviating of the established assumptions.
- Programmed and conducted the *Monte Carlo* simulations.
- Derived the maximum likelihood estimator and studied its properties numerically.
- Proposed and studied (numerically) the usefulness of $\hat{c}_{\mathrm{ml}}$ for experimental planning for quantification of unknown concentrations (real samples)
- Participated in analytical derivations
- Made first paper draft
- Produced all figures.

Patent applications

Patent application 1:
Carl Esben Poulsen, Kasper Kistrup, Nis Korsgaard Andersen, Flemming Larsen, Rafael Taboryski, and Anders Wolff. Replication Tool and Method of Providing a Replication Tool. Priority claim of regional application 05/12/2014.[5]

- Participation in development of patented method for tool fabrication.
- Participation in development of patented method for tool use.
- Participation in proof of concept.
- Participation in writing of the patent.
- Formulation of reports for patent attorney.

Patent application 2:
Carl Esben Poulsen, Kasper Kistrup, Nis Korsgaard Andersen, Rafael Taboryski, and Anders Wolff. Micropillar Energy directors for ultrasonic welding. Priority claim of regional application 05/12/2014.[6]

- Participation in development of patented method for tool fabrication.
- Participation in development of patented method for tool use.
- Participation in proof of concept.
- Participation in writing of the patent.
- Formulation of reports for patent attorney.

Patent application 3:
Carl Esben Poulsen, Kasper Kistrup, Nis Korsgaard Andersen, Rafael Taboryski, and Anders Wolff. Method of Producing an Item with Enhanced Wetting Properties by Fast Replication and Replication Tool Used in the Method. Priority claim of regional application 05/12/2014.[7]

- Participation in development of patented method for tool fabrication.
- Participation in development of patented method for tool use.
- Participation in proof of concept.
- Participation in writing of the patent.
- Formulation of reports for patent attorney.

Conferences

Carl Esben Poulsen, Kasper Kistrup, Nis Korsgaard Andersen, Rafael J Taboryski, Mikkel Fougt Hansen, and Anders Wolff. *TransForm: Injection moulded 3D superhydrophobic surfaces.* Technical University of Denmark, Kgs. Lyngby, 2014[8]

- Oral presentation.
- Contribution based on Patent applications 1 through 3.

Carl Esben Poulsen, Dang Duong Bang, Martin Dufva, and Anders Wolff. An injection moulded microfluidic chip for polymerase chain reaction (PCR) thermocycling and imaging of droplets to detect food-borne pathogens Campylobacter spp. *In 15th International Conference on Biomedical Engineering*, 2014[9]

- Poster.
- Preliminary data of Paper 2. The final data is described in Section 5.1 on page 64.

Kasper Kistrup, **Carl Esben Poulsen**, Nis Korsgaard Andersen, Rafael J Taboryski, Anders Wolff, and Mikkel Fougt Hansen. Ultrasonic welding for bonding of microfluidic chip systems. *In 20th International Conference on Commercializing Micro- and Nanotechnology*, Kraków, Poland, 2015[10]

- Poster based on Paper 3.

Other contributions

Tran Quang Hung, Yi Sun, **Carl Esben Poulsen**, Quyen Than Linh, Wai Hoe Chin, Bang Dang Duong, and Anders Wolff. Miniaturization of a micro-optics array for highly sensitive and parallel detection on injection moulded lab-on-a-chip. *Lab Chip*, 2015[11]
&
Tran Quang Hung, Yi Sun, **Carl Esben Poulsen**, Wai Hoe Chin, Anders Wolff, and Dang Duong Bang. Injection Moulded Micro-Optics Arrays for Quantification of Surface Bound Fluorescent Molecules in Air and Aqueous Media. *Proceedings Microtas* 2015, 2015[12]

- Constructed MATLAB model and contributed to nummerical modelling.
- Contributed to writing and correction of manuscript.

1

Introduction to microfluidics

Microfluidics is a relatively new science which combines physics (material science, optics, electronics etc.) with chemistry (reactions, surface modification), biology (cell growth, tissue engineering, drug testing) to down scale, simplify, speed up or enable a biological assay. Usually, the central unit in a microfluidic system is a single microfluidic chip, which integrates active and passive components for sample handling, preparation, incubation and analysis. In the optimal scenario, this chip incorporates the entirety of the assay and it's dependencies, and this "Lab-on-a-Chip" (LoC) functions more or less autonomously at the Point-of-Care (PoC), and we denote it a "micro-Total-Analysis-System" (μTAS)[13]. A good example on this is the pregnancy strip test, which is PoC (home use), cheap, simple (no training needed), fast, private and reliable. Similarly, devices for home blood glucose monitoring and insulin pens for administering insulin for treatment of diabetes have improved the lives of millions.

Currently, most true LoC systems are those available commercially, since these have all passed approvals and regulations. Further, many devices are allowed for use by non-laboratory-trained personal, by receiving the so-called "CLIA waiver"[14], which verifies that they (amongst others[15])

- Are fully-automated and self contained.
- Require no specialised training.
- Yield easily interpreted results.
- Are robust and yield repeatable results.

Turning to academia, a large amount of research in microfluidics often compromise the above mentioned LoC criteria. Deviating from these basic , but often commercially essential qualities, a multitude of examples of "chip-in-a-lab" microfluidic systems have been demonstrated[16]. The chip-in-a-lab systems are important prototypes in that they benchmark the prospective capabilities of the to-be-developed equivalent μTAS systems, but the fabrications methods, materials and simplicity is often hugely different[17]. The consequences of these differences in material and fabrication choices will be elaborated in Chapter 2.

Currently, 63% of the expanding global market of microfluidics is comprised by inkjet manufacturing. However, as seen in Table 1.1, the fields of high-throughput screening and compound profiling, diagnostic and point-of-care, and drug delivery were account-

Table 1.1: Global market forecast for microfluidic technologies ($ millions) and Compound Annual Growth Rate (CAGR). Table data is adapted from McWilliams *et al.* (2013)[18].

Microfluidic technology	**2011**	**2012**	**2017**	**CAGR 2012-2017**
Inkjet printing	3,182.7	3,373.1	4,574.5	6.3 %
High-throughtput screening and compound profiling	1,085.0	1,275.0	2,910.0	17.9 %
Diagnostic and point-of-care	415.0	533.3	1,868.5	28.5 %
Drug delivery	183.3	203.3	523.0	20.8 %
Chemical analysis and synthesis	120.0	132.0	280.0	16.2 %
Proteomics	33.0	36.0	55.3	9.0 %
Defence and public safety	0	0	15.0	–
Other	35.0	37.6	54.0	7.5 %
Total	5,054.0	5,590.3	10,280.3	13.0 %

ing for $ 1,683.3 million, and these technological fields have a high Compound Annual Growth Rate (CAGR) of $18 - 28\%$.

1.1 Why microfluidics?

There are several obvious and not so obvious reasons to why microfluidics was and still is expected to revolutionise biomedical research, the obvious includes; (1) Reduced sample material volume and reagent use: E.i. going from blood samples to finger pricks[19], or from needing to use large quantities of synthesised candidate drug to estimate its partition and distribution coefficient[2] or biological effect[20]. (2) Automation: Reduced labour cost and human error. (3) Small instrumental foot print: Allows for hand-held devices[21] and lower power consumption. (4) Parallelism: Multiple samples may be analysed in parallel[22,23] or in sequence[24].

The less obvious advantages (and disadvantages) are those which are governed by surface or viscous forces since these forces tend to dominate in microfluidics. As elaborated mathematically in Chapter 3, when the viscous forces dominate the inertial forces in a microfluidic system, the fluid follows a strict flow pattern through the system, regardless of direction and speed (up until viscosity becomes significant). This is termed laminar flow and is in contrast to turbulent flow, both of which are illustrated in Figure 1.1.

One application which relies on laminar flow is pinched flow fractionation[26]. Here, particles are sorted by size (e.g. droplet diameter[27]) by flow pinching the objects against a wall, follow by a expansion of the channel, which separates the flow lines and hence the particle trajectories. Similarly, deterministic lateral displacement exploit the principle behind pinched flow fractionation to perform sorting by size without

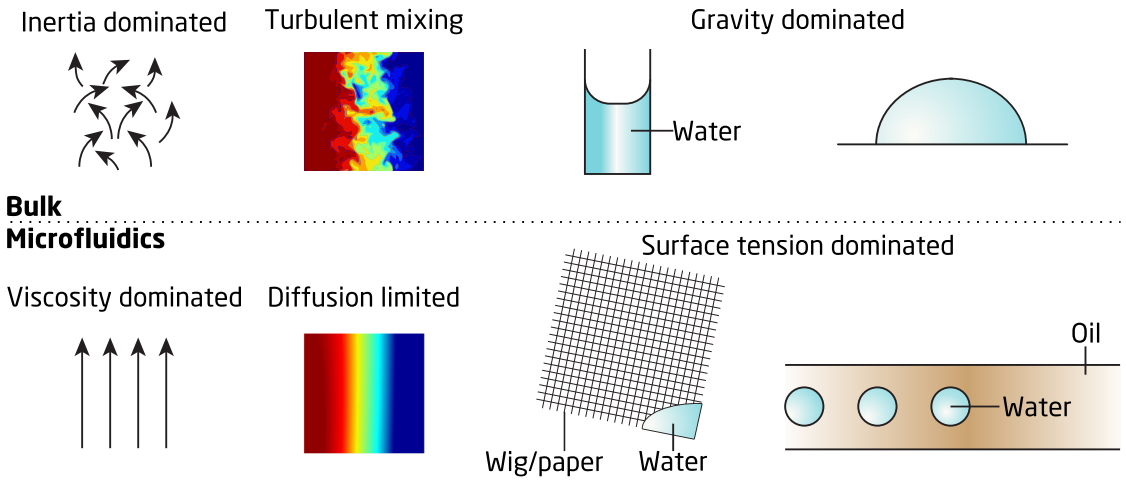

Figure 1.1: Comparison of physics of bulk- and microfluidics. The mathematics are elaborated later, but the generally, inertia and body forces such as gravity dominate in macroscopic systems, whereas microfluidics are dominated by surface forces and viscosity. Figure is adapted and modified from Sackmann *et al.* (2014)[25].

diluting the sample[28]. The working principles of these two techniques are presented and elaborated in Figure 1.2.

Another implication of laminar flow is that mixing is highly reduced since in microfluidics, it is almost solely a product of diffusion. Consequently, if two streams of fluid are required to mix in a microfluidic system in a fast[a] manner, geometries such as the staggered herringbone mixer[29] may be introduced to effectively "fold" the fluid stream like a swiss roll, reducing the required diffusion length by two per "roll". See Figure 1.3.

Conversely, the fact that mass transport of diluted species is limited by diffusion allows for measuring and separating different species according to their diffusion constant. This is embodied in the so called H-filter, presented in Figure 1.4. The method for achieving a concentration gradient in the H-filter has also been employed for studying chemotaxis[30], the migration of cells in response to a chemical gradient. Prior to microfluidics, this was done using a Boyden chamber or "Transwell assay" which does not allow for continuous observation[25].

[a] "Fast" referring to limited in time and space (e.g., length of channels). The required channel length to achieve mixing may be estimated by calculating the so called *Péclet* number which is ratio between the average times a characteristic length scale is covered by diffusion and convection: $Pè \equiv \frac{\text{diffusion time}}{\text{convection time}} = \frac{\text{rate of convection}}{\text{rate of diffusion}}$. In brief: High flow rates result in high *Péclet* numbers, which indicates that a longer residence time (and hence a longer channel) is required to achieve mixing by diffusion.

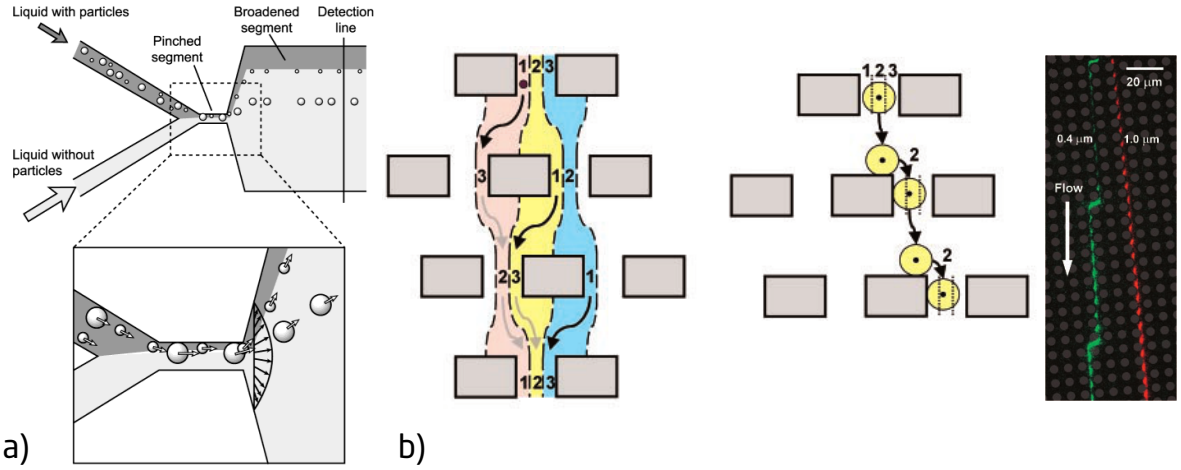

Figure 1.2: Applications of laminar flow for particle sorting. (a) Pinched flow fractionation: A flow containing particles is pinched by a stream without particles. This aligns the edges of the particles to the side wall of the microfluidic device. As the microfluidic channel expands, the flow lines separate, dictating the trajectories of the particles. Figure adapted and modified from Yamada *et al.* (2004)[26]. (b) Deterministic lateral displacement. (left) In this example, an array of pillars are engineered to cause a flow pattern separated into three different areas, designated by the three different colours: red, yellow and blue. A particle of diameter smaller than 1/3 of the pillar spacing (equal to the width of one coloured streams) entering the top of the image in the red stream (designated as position one) will move to the left to position 3 in the red stream as i travels downwards to the row of pillars below. As the particle stays in the red stream and moves another row down (to row 3), the particle is now in position 2, the middle position. As it continues downwards in the red stream it finally ends back in position 1, and it is back in its original horizontal position. Evidently, smaller particles stay in one "colour zone", and it is of no significance if the chip is entered in position 1, 2 or 3, the trajectory will effectively be vertical. On the contrary, particles of diameter bigger than the width of the individual zones (colours) will all ways occupy position 2 in junctions since 2/3 of the flow is flowing to the right at junctions, and will therefore always move to the right. (right) Fluorescence imaging of nano particles separating into populations according to sizes. Figure is adapted and modified from Huang *et al.* (2004)[28].

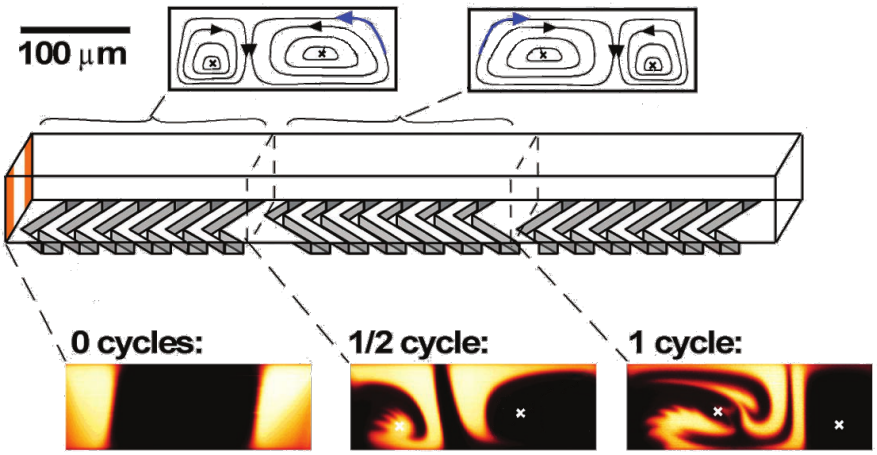

Figure 1.3: Staggered herringbone mixer. An unmixed stream comprised of three coflowing streams of fluorophore solution, buffer and fluorophore solution enters the device from the left, see inset "0 cycles". As the streams pass the herring bone geometries, the streams are folded multiple times, and and after 1 cycle, the diffusion length required for mixing is significantly lower than at the inlet. Figure adapted and modified fromStroock *et al.* (2002)[29].

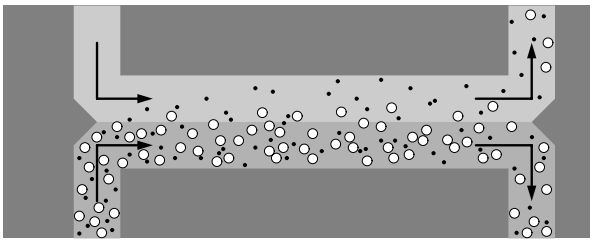

Figure 1.4: Demonstration of H-filter: A mixture of large (∘) particles with low diffusion constant, D, and small (·) particles with higher value of D enters the device in the bottom left inlet and merges with a stream of buffer from the top left inlet. As the coflowing streams propagate through the center channel, matter is exchanged by (and limited to) diffusion. Particles with higher diffusion coefficients have higher mobility and have a higher probability of migrating to the top half of the center stream in the time span available. Observing the compositions of the output streams, the upper right exit contains a majority of small particles compared to big particles, and the lower right exit has a reduced concentration of the small particles compared to the inlet concentration. Figure is adapted from Bruus (2008)[31].

The shape and propagation of interfaces in triple phase systems such as those illustrated in Figure 1.1 are dictated by several forces including surface tension and body forces. As discussed in mathematical detail in Section 3.2.2, the capillary pressure of a simple cylindrical capillary scales as $1/radius$, which may be exploited to passively drive porous microfluidic system such as paper microfluidics[32], see Figure 1.5.

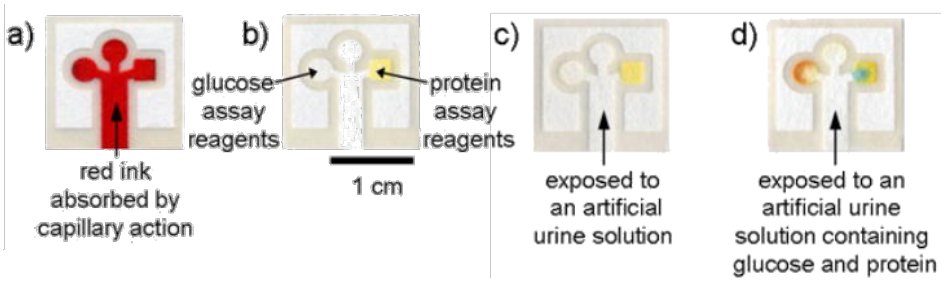

Figure 1.5: Paper patterned with photoresist for defining the paperfluidic geometry (this may also be done using wax[33]) and reagents for glucose- and protein assay embedded. (a) Paperfluidic geometric layout. b) Paperfluidic with preloaded assay reagents. (c) Assay read out from negative control. (d) Assay read out from positive control. Figure adapted and modified from Martinez *et al.* (2007)[32]

1.2 Droplet microfluidics

Droplet microfluidics is a branch of microfluidics which works with dispersed multiphase systems where one phase acts as a continuous carrier phase and the other as a dispersed sample phase. Since Thorsen *et al.* (2001)[34] demonstrated that inverse micelles (aqueous droplets) may be produced continuously and uniformly by using a so called droplet junction, droplet microfluidics have been a rapidly developing field of research. Consequently, the rate of publications per year of the topics microfluidic* and droplet* (* refering to optional characters) has been increasing linearly since 2001, and currently approximately 10% of publications with the topic microfluidic* also has the topic of droplet*. In Figure 1.6, the number of publications per year with the topics microfluidic* and the combinations of topics microfluidic* and droplet* is plotted for the past 25 years.

As with other branches of microfluidics, many applications and embodiments of droplet microfluidics are highly inspired by its bulk counter part which for droplet microfluidics is the micro titer plate. By dispersing an aqueous phase in a continuous oil phase, each droplet may be considered an isolated reaction vessel which may be manipulated and interrogated, and a large arsenal of tools, reagents (oils and surfactants[35]), methods and best-practice[36] have been established. A sample of documented droplet manipulation capabilities include droplet generation (passively[37] or actively[38]), sorting/guiding (by applying an electric field[39–41], also known as fluorescent activated droplet sorting, FADS), merging (using surface acoustic waves[42] or by applying an electric field[27,39]), splitting (by geometric branching[43] or by applying an electric field[39]), and trapping (geometrically[44–46]). Droplet interrogation is usually done by using fluorescence

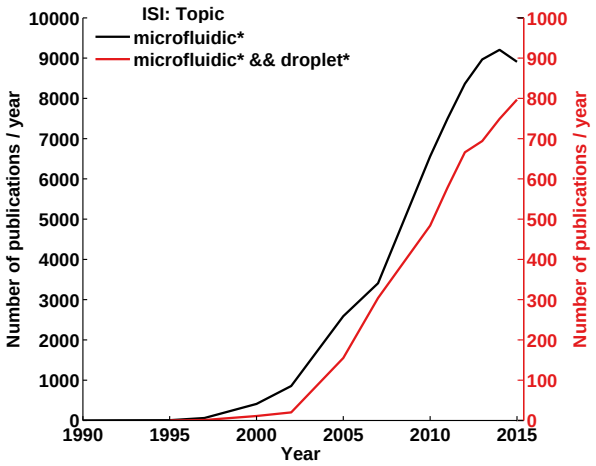

Figure 1.6: Rate of publication release with topics microfluidic* and the combinations of topics microfluidic* and droplet*. * Refers to optional characters. Data is obtained from webofknowledge.com February 8$^{\text{th}}$ 2016.

imaging[47–49] or a single point fluorescence read-out[39–41]. Two principles of droplet generation are illustrated in Figure 1.7.

Typical early applications of droplet microfluidics mirror well established micro titer plate based methods and offer the same "scaling benefits" as microfluidics. However, droplet microfluidics have more to offer, also compared to microfluidics: (1) Taylor dispersion is eliminated by the confinement and the rapid movement of fluid inside the droplets[43,50]. This allows for studying rapid protein crystalisation[51], studying chemical reactions (particularly useful for determining transition times in autocatalytic reactions[52]). Similarly, with no Taylor dispersion, delay lines may be applied to interrogate a continuous stream of droplets multiple times with no cross contamination[53]. (2) Wide volume working range of 10^{-6} to 10^{-15} L[54]. This is only possible because (3) the oil phase reduce sample evaporation. The high curvature of small droplets results in large Laplace pressures which would cause spontaneous evaporation in an atmospheric environment. As shown in Chapter 3.3, the Laplace pressure is also a highly contributing factor to the droplet stability. (4) Adsorption of dissolved/suspended species on the walls of the device/vesicle may be eliminated by appropriate choice of surfactant[35,55]. (5) Increased sensitivity when working with highly diluted samples. This is particularly important when analysing cells: the bulk cell concentration may e.g. be 10^5 cells/mL, but dividing the sample into e.g. 1 nL droplets results in many empty droplets and some including cells. The effective cell concentration in a droplet harvesting a single cell is then 1 cells/nL = 10^6 cfu/mL, a 10-fold increase in concentration[56]. (6) Similarly, by compartmentalising the sample, higher levels of discrimination between individual cells are achieved, enabling for detection of rare events which would otherwise be masked by background (wild type events)[57,58]. This is also important when amplifying large libraries, since compartmentalisation reduces the risk of cross-talk[59] or one reaction dominating the others exponentially, skewing the output with regards to the input[60]. (7) Though the total amount of sample material is unchanged, the compartmentalisation increases information density: As shown in Chapter 8, if sample

material is limited more information is obtained by separating it into smaller possible segments. (8) Segmentation may enable digitalisation as an alternative to analog sample analysis, simplifying read out, increasing precision and accuracy, and enabling a dynamic range of more than four magnitudes[47]. This is the principle of droplet digital PCR (ddPCR). Polymerase Chain Reaction (PCR) is explained in Box 1.1 on page 14. (9) The confinement and short diffusion lengths inside the droplets allow for the establishment of simple "protocells"[61] or for studying organelles[62]. (10) Cell-cell interactions may also be avoided (isolation)[63] or enhanced (pairing)[64].

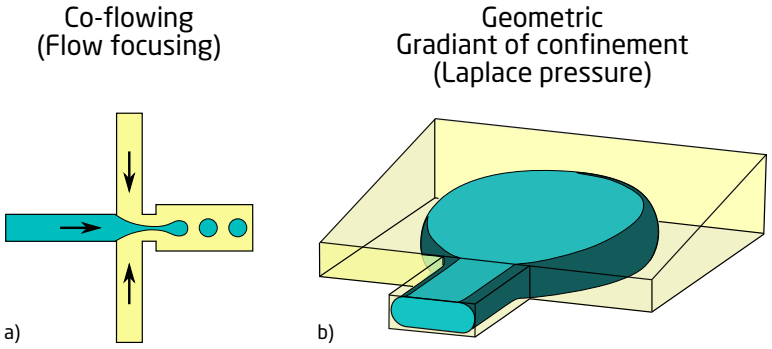

Figure 1.7: Examples of droplet forming strategies. This topic is further elaborated in Section 3.3 and Figure 3.6 on page 44. (a) Droplet formation by co-flowing streams of aqueous phase and oil. (b) Droplet formation by gradient of confinement. In this method, the Laplace pressure is used to drive the droplet formation. Figures are adapted and inspired by Christopher *et al.* (2007)[65] and Dangla *et al.* (2013)[66].

1.3 Limiting dilution assays

One method which has been revolutionised by being transferred first to a microfluidic platform, and later to a droplet platform is limiting dilution assays such as digital PCR. Limiting dilution assays work to quantify a target substance by dividing the sample into a multitude of reaction volumes. If the target substance concentration is sufficiently low, some of the reaction volumes will be unoccupied, while others will receive one or more targets[67]. As shown mathematically in Chapter 8, the variance of the estimate of the target concentration is $\sim 1/N$ where N is the number of reaction vesicles used in the assay. Further, by separating the sample into smaller (and more numerous) vesicles, the dynamic range of the assay is increased. Most digitised detection methods are adaptations of previous analogue methods, and the number one motivation to digitise is the fact that no internal control or references are needed. As shown in Chapter 8 and Paper 1, since the signal of the individual vesicles are interpreted binary, the information obtained from one digital experiment supplies enough information for estimating the target concentration.

1.3.1 Droplet limiting dilution assays

Limiting dilution assays have successfully been transferred to a droplet platform for quantification of DNA by PCR (droplet digital PCR)[4,47,58,68–79] (methylation specific[80]) or isothermal amplification methods[24,81–83], or quantification of RNA[84–87]. The small (pL) but numerous (millions[47]) vesicles allows for more information to be generated per sample, improving the precision and accuracy of the target concentration estimate[b]. Since the droplets may be stable enough to be pipetted, a multitude of strategies and protocols exist for conducting ddPCR, however, there normally are three general steps, as illustrated in Figure 1.8: Generation, amplification and interrogation. (1) Generation is typically conducted by co-flowing the two immiscible phases in a so called droplet junction. As described in Section 3.3, several droplet generation regimes exist for the same system (fluids and geometry) depending on the flow rates. Generally, however, segmentation arrise due to shear forces (Figure 1.7a) or differences in pressure (Figure 1.7b). In most studies, the droplet production is conducted passively and continuously (reviewed by Collins *et al.* (2015)[37]), but droplet break-off may also be actively induced by pneumatically altering the droplet junction geometry[88] or by employing electrostatic or magnetic forces (reviewed here by Chong *et al.* (2015)[38]). (2) Amplification (or storage[53]) may be done off-chip in tubes[58], in-line in tubing[24] or on-chip[47]. For ddPCR, the incubation step involves thermo-cycling the droplets to conduct the PCR reaction. For this reason, most ddPCR studies use off-chip incubation in PCR tubes, employing standard PCR machines for the thermo-cycling[58]. Flow-through ddPCR systems require specialised heating systems to be constructed, but are simple in that they operate in a steady state mode[24,74]. (3) Interrogation. This is mostly conducted optically, since breaking the emulsion may compromise the integrity of the assay, and may be accomplished in serial in a flow cytometric manner[24,27,57,58,70,78,79,86,89–92] or in parallel by imaging multiple droplets at once[4,47,73,76,85,93–96]. In the latter case, real time PCR in droplets have also been demonstrated by continuously monitoring the droplets as they amplify[93,96].

[b] Note that if the droplet volumes are assumed to be monodisperse but are polydisperse in the actual experiment, the estimate will be biased towards underestimation. In Chapter 8, it is demonstrated how to correct the estimator and eliminate bias.

Box 1.1: PCR and digital PCR

Polymerase Chain Reaction is a method for achieving exponential amplification of a target sequence of DNA. After its invention in 1980 by Kary Mullis, it has been modified into a large palette of tools for e.i. modifying the amplified sequence. PCR consists of three repeating steps:

1. Denaturation of double stranded DNA by heating to ~ 94 °C.
2. Annealing of primers specific for the sequences flanking both ends of the target sequence at $30 - 65$ °C. One primer attaches to each strand of single stranded DNA (the coding and complimentary strands), and the primers are designed so that their 3' points toward the sequence of interest.
3. Extension at $(65 - 75$ °C) of primers by a DNA polymerase enzyme, integrating nucleoside triphosphates (NTP)s corresponding to the template strand.

These steps are repeated for ~ 40 times, and since a product can never be longer than its template, the smallest product stretching from primer to primer will quickly dominate and grow exponentially. The product may be used for cloning or analysed by fluorescence staining (targeting only double stranded DNA).[97]

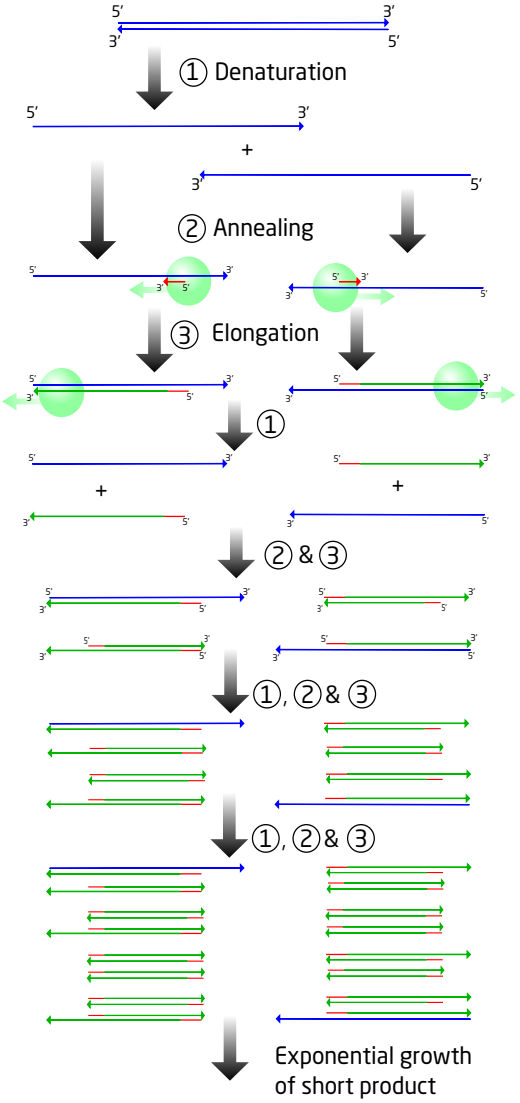

The figure is downloaded and modified from Wikimedia.org and is used under a creative commons license[98].

Digital PCR (dPCR). If two PCR reactions with two different target sequences (e.g. wildtype + mutant) compete for reagents, the exponential amplification of PCR may cause one sequence to completely dominate the result. By compartmentalising (digitising), this may be avoided, and the statistics may be applied for estimating the starting concentrations/ratios. These equations are described in Chapter 8.

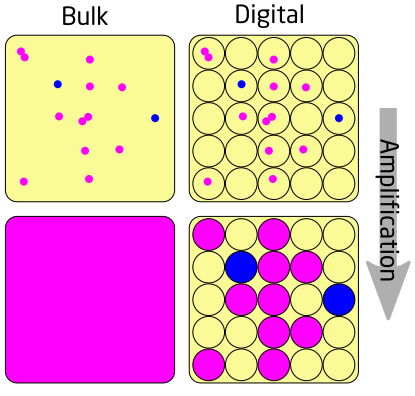

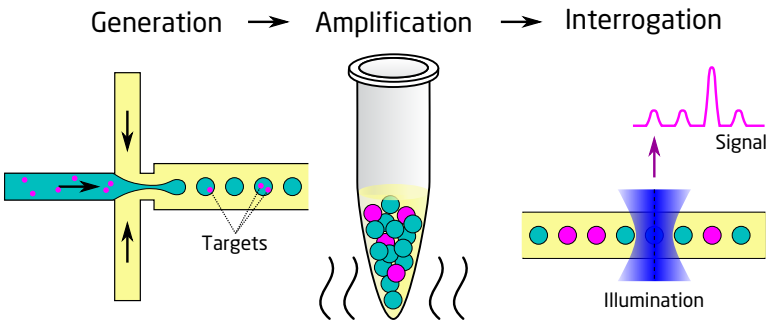

Figure 1.8: Typical work flow for conducting ddPCR: Generation (typically by flow focusing), amplification (typically by thermo-cycling), and interrogation. As mentioned in the main text, several strategies exist for generation, incubation and interrogation, depending on the application. The figure is inspired by Rosenfeld *et al.* (2014)[99]. The droplet junction is inspired by[65].

1.3.2 Commercial digital systems

The landmark work done by Thorsen *et al.* (2002)[100] presented a fully digitised microfluidic PDMS chip featuring 256 individually addressable and sealable chambers[100]. The methodology was further developed by Quake *et al.* which resulted in the Spin-Out Fluidigm. Gaining immediate popularity in the academia, Fluidigms systems have been applied to map species of soil bacteria[101], quantify fetal DNA from maternal blood (very high background signal)[102], study gene expression levels using RT-PCR[103] and measure copy number variation[77]. At the time of writing, the most used Fluidigm chip can process 12 samples which are each split into 765 wells, yielding a total of 9216 digital data points, however, a 48 sample chip (digital array chip 765 wells each) is also available. Other variants have also been launched, including a 9216 point devices with 96 inlets and 96 wells instead.

Similarly, Life Technologies (ThermoFisher Scientific) have launch the OpenArray® real-time PCR system. This system use microscope slide sized plates perforated by 3,072 through-holes which act as wells (64 in 48 arrays) due to an outer hydrophobic coating, and an inner hydrophilic coating. This principle is illustrated in Figure 1.9 together with the Fluidigm array chip.

The latest commercial digital PCR system launched, is the Constellation PCR system from Formulatrix. This system employs a proprietary injection moulded 96 well plate format harvesting 96 inlets each connected to 496 wells. After loading the samples by pipetting, the plate is sealed by using adhesive foil, whereafter it is transferred to the Constellation machine for priming. The liquid is driven into the wells by a flexible membrane which is actuated by a pneumatic piston. After loading, compartmentalisation is achieved by collapsing the bottom most layer of flexible tape covered with pressure sensitive adhesive using an automated roller system. The chip is then thermo-cycled on a conventional thermo-cycler, where after it is installed in the Imaging Station of the Constellation instrument. The process is presented in Figure 1.10.

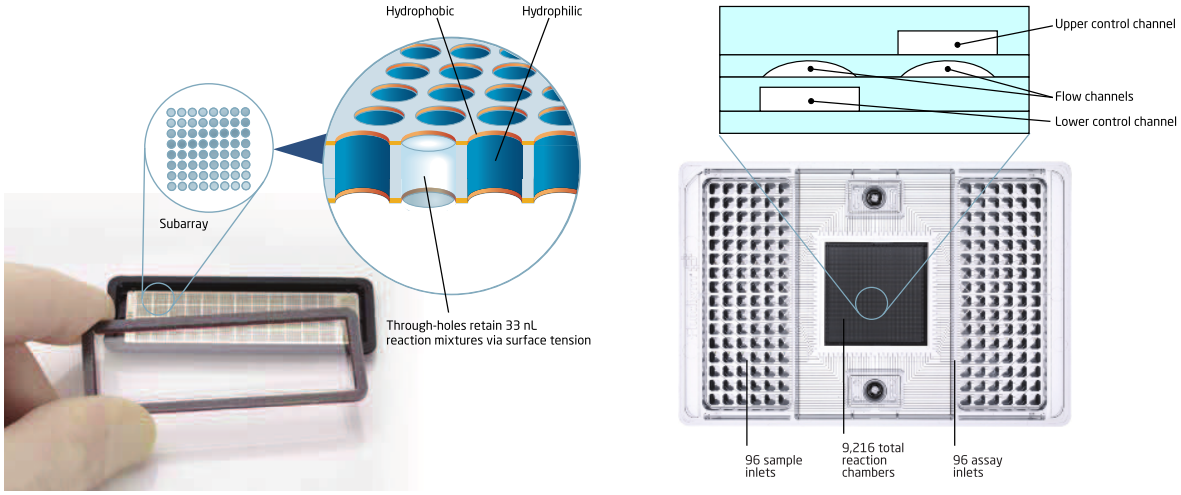

Figure 1.9: (left) OpenArray® real-time PCR system from Life Technologies. Segmentation is achieved by using capillary forces from an outer hydrophobic coating combined with internal hydrophilic coating. The figure is modified and adapted from Life Technologies (2016)[104]. (right) Biomark® HD chip from Fluidigm. Segmentation is achieved by applying pneumatic air pressure in control channels to cause local channel "collapse" of the flow channels. The figure is created from figures adapted from Melin and Quake (2007)[105] and Fluidigm (2016)[106].

As with the microfluidic limiting dilution assays, droplet based limiting dilution assays have also recently been transferred to commercially available platforms; Bio-Rad has launched the QX100 (later QX200) which works by converting a premixed ddPCR reaction mix into droplets by using a proprietary droplet generation chip and the QX200 Droplet Generator instrument. Next, the droplets are pipetted into a 96-well plate which is thermo-cycled on a conventional thermo-cycler. After thermo-cycling, the 96-well plate is sealed and transferred to a QX200 Droplet Reader instrument which auto samples one reaction at a time, analysing the fluorescence signal of each droplet in a flow cytometric manner[108]. This instrument has been applied to ddPCR on DNA[68–71] and RNA[109,110].

RainDance Technologies have also launched a droplet based digital PCR system, RainDrop®, which works with a work flow similar to the QX-models from Bio-Rad; up to 8 ddPCR reaction mixtures are pipetted to a proprietary Source Chip (droplet generator chip), which is then mounted in the Source instrument (droplet generation device), converting the samples into droplets and depositing them in a strip of 8 PCR tubes. The PCR tubes are thermo-cycled on a conventional thermo-cycler. After amplification, the tubes are mounted in the Sense instrument (droplet interrogation device) together with a proprietary Sense Chip (droplet interrogation chip), and the droplet of the 8 samples are analysed in a flow cytometric manner in 8 parallel streams of droplets flowing in series. A list of these five commercial digital PCR offerings is compiled in Table 1.2.

From Table 1.2, it is evident that for quantification purposes, information is cheaper with droplet based digital PCR versus microfluidic digital PCR since the partitions are

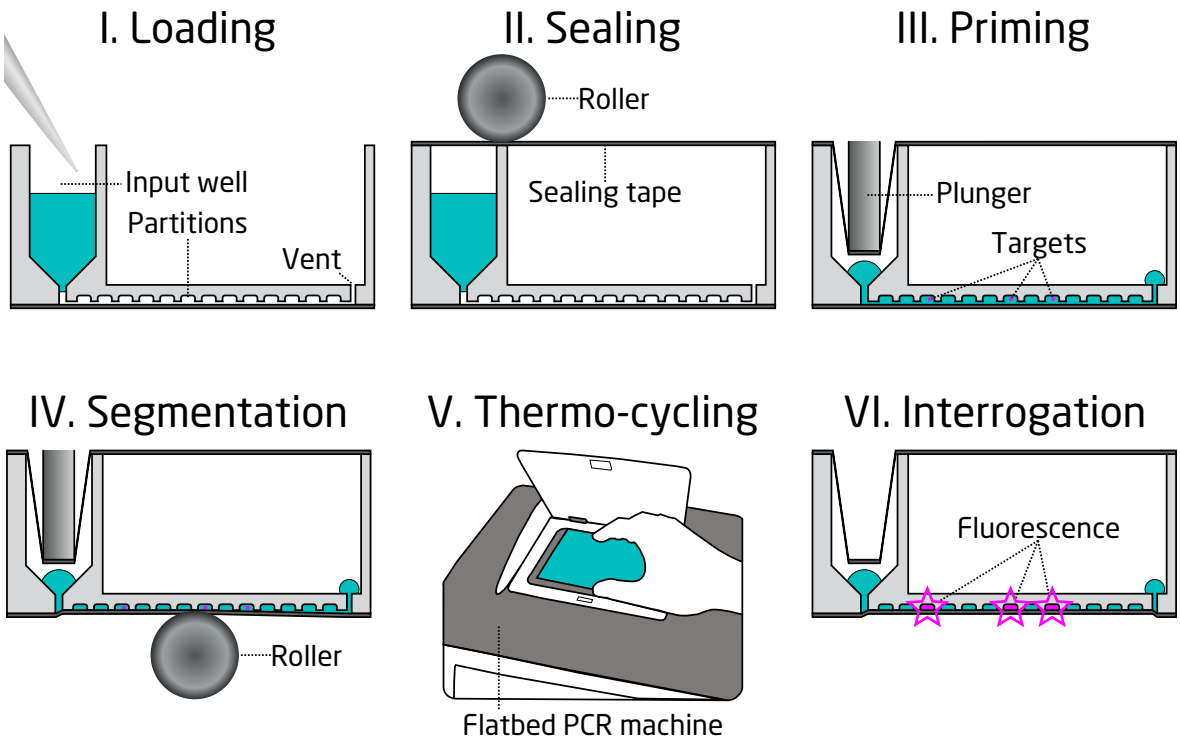

Figure 1.10: Methodology for performing digital PCR in a Formulatrix Constellation system. (I) Loading by pipetting. (II) Sealing using adhesive foil. (III) Priming into the chambers by pneumatic pressure from actuation of the sealing foil by the plunger of the Constellation machine. The targets are randomly distributed into the chambers of the well. (IV) Segmentation by collapsing the priming channel by rolling on the pressure adhesive bottom tape. (V) Thermo-cycling in conventional thermo-cycler. (VI) Interrogation by fluorescence imaging in the Constellation instrument. Figure is adapted and modified from Formulatrix (2016)[107].

cheaper, even when taking multiplexing into account. What droplet digital PCR lag though is the capability to conduct real-time PCR, which, assuming standard curves exist, yields rich information on the starting concentration of the reaction[c]. Producers of chip/well based solutions (Fluidigm, Life Technologies and Formulatrix) point out that the response curve of a PCR reaction is important for discriminating false positives, however, advocates of droplet based solutions explain that the higher number of partitions allows for calculating the false positive rate[111]. Further, since false positives are mainly expected to arise from primer dimers, it is common to use sequence specific probes such as TaqMan[4,47,57,58,70–72,75,76,79,85,92,93,96,109,110,116] for ddPCR. Further, for detecting rare events masked by as much as 1:200.000, a very high number of partitions are needed to obtain a realiable estimate[57,58], and only ddPCR is this scalable[111].

As may be evident from the differences in specifications of the different instruments, they each excel in different applications[111]. One important thing they all lack to some extent is flexibility; For the well based systems (Fluidigm, Life Technologies and Formulatrix), a single sample may be distributed in more wells for increased partitioning,

[c] Droplet real-time PCR has been demonstrated in a academic setting[93,96]

Table 1.2: Comparison of commercial digital PCR instruments.

Vendor	Instrument price	Consumable price	Partitions per sample	Price per partition	Time per partition	Samples per run	Additional features
Fluidigm Corporation	Biomark® HD: $\$200,000 - \$250,000$[111]	9180 well chip: \$400/chip[111]	9,180 to 756	\$−cent 4.4	1.18 s, 3 hours/chip [112].	Up to 12, 765 partitions each.	5x multiplex. Real time PCR capable.
Life Technologies	OpenArray RealTime PCR System: $\$140,000$[111]	OpenArray plates, 48 arrays, 64 wells per array: \$150 per plate[111]	3,072 to 64	\$−cent 4.9	1.17 s, 4 hours/chip.[a]	Up to 48, 64 partitions each.	2x multiplex. Real time PCR capable.
Formulatrix	Constellation Digital PCR: $\$50,000$[b]	47,616-well, (96-inlet) microplate: \$75 per plate[114]	47,616 to 496.	\$−cent 1.6	227 ms.[c]	Up to 12, 496 partitions each	2x multiplex.
Bio-Rad Laboratories	QX100 ddPCR System: $\$89,000$[111]	Droplet generator chip for 8 samples: \$8.77 per chip[115][d]	20,000	$\$6.6 \times 10^{-5}$	361 to 4.7 ms.	Up to 8[e].	2x multiplex.
RainDance Technologies	RainDrop Digital PCR system: $\$100,000$[111]	\$10 to 30 per sample[111]	Up to 10,000,000	$\$1 \times 10^{-6}$ to $\$3 \times 10^{-6}$	2.85 to 3.68 ms.	Up to 8[f].	2x multiplex.

[a] Assuming 4 chips are run in parallel on the machine[113].
[b] Constellation prices (machines and consumables) are Formulatrix estimates prior to release of the product[114].
[c] Not available. I have assumed 3 hours/chip, estimated from the Biomark® HD.
[d] Also needs 60 µl[68] to 70 µl[109,110] of droplet generator oil (\$3.8/ml)[115] per sample, and droplet reader oil (\$0.37/ml)[115].
[e] Up to 8 for droplet generation, and up to 96 for thermo-cycling and reading.
[f] Up to 8 for droplet generation, up to 96 for thermo-cycling, and up to 8 for read-out.

but the user is required to consume an entire kit (including a \$400 plate) regardless of the number of samples run or partitions needed. This is also true for the ddPCR kit of Bio-Rad and RainDance; though the number of droplets produced may be set from experiment to experiment, the amount of consumable is almost unchanged since the price of oils are insignificant compared to the plates. Common between the mentioned technologies is also that the partition sizes are fixed[d]. Moreover, the instruments offer no possibility for altering the detection filters (excitation and emission wavelengths), possibly because interrogation is done by using laser LEDs (Bio-Rad QX100[117]).

1.4 Project description

The purpose of this project was to (1) identify and solve limitations of the state-of-the-art droplet based quantification systems, (2) reduce the number of failure points, (3) widen the applicability range of on-chip droplet microfluidics, and (4) enable research in droplet technologies, specifically in ddPCR, by using and (5) developing commercially relevant fabrication technologies.

[d] Obviously, the well chips have fixed volumes, but the ddPCR systems do not allow for selecting different droplet volume either.

Box 1.1: Project description

As stated in the official DTU study plan of this thesis:
In this PhD-project we will develop an all-polymer injection moulded microfluidic platform with integrated droplet based single cell interrogation. The system will be fabricated using commercial relevant fabrication methods such as injection moulding and ultrasonic welding. Additionally, the system will be designed to be simple to use and require only standard laboratory equipment for operation.

Working towards this goal, I have addressed issues and challenges of in separate sub-projects and published the results independently from the supreme goal of the thesis[e]. The topics of the papers are all combinations of fabrication of microfluidics, and droplet microfluidics, but the path of exploration may be less obvious at first glance. I have therefore created Figure 1.11, which serves to show the motivations linking the papers, the topic[f], and the achievements and observations.

Before commencing on presenting papers and results of the thesis, I would like to introduce and discuss fabrication methods for microfluidics in the literature and of this thesis.

[e] e.i. a fabrication paper is general for microfluidics and should not be limited to the field of ddPCR.
[f] indicated by background arrows, fabrication and droplet microfluidics

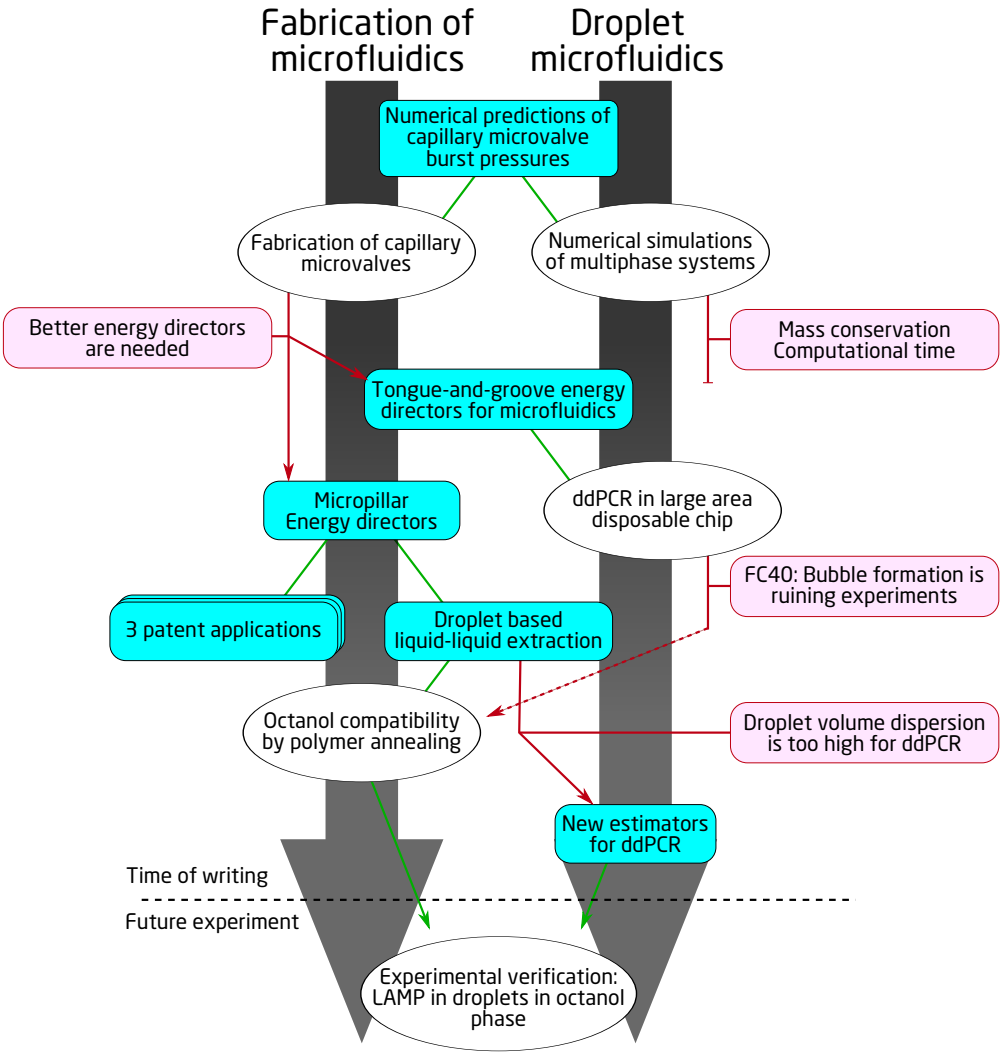

Figure 1.11: Thematic build up of this thesis and PhD project. (cyan) papers/chapters/subprojects. (circles) achievements (linked with green lines). (red boxes) Issue/challenge/motivation for next project (linked by red lines).

2

Fabrication of microfluidics

2.1 Materials and methods for microfluidics

The initial mind set and development methods applied in microfluidics originates from - and have many equivalents to the development of integrated electronic circuits and semi conductors; The photo lithographic methods applied for electronics offer an extremely high resolution, and millions of features may be packed into a single 1 cm^2 piece of silicon. For this reason, initial microfluidic research was based on silicon[118] and glass[119]. Tapping on the resources of MEMS fabrication (inkjet printing heads are MEMS based), these materials were expensive and complicated to work with, and was by far outmatched by the introduction of soft lithography which allowed large structures to be produced cheaply and rapidly in PDMS[120]. This fabrication method revolutionised the academic field of microfluidics in that it enables researchers to rapidly prototype flexible microfluidics[25,121–123].

2.1.1 PDMS and soft lithography

The popularity of PDMS for prototyping of microfluidic devices in academia by using soft lithography stems from it jack-of-all trades properties[25]: (1) PDMS is a soft material which flexes instead of breaking (contrary to glass and silicon). This allows for easier demoulding of high aspect ratio micro structures[124] and nano structures[125], while enabling advance components such valves and pumps[126] to be fabricated using only one material[a]. Further, the flexibility of the PDMS ensures "o-ring-like" seals to connectors[125]. Beyond fabrication, the flexibility of PDMS has also been applied to regulate cell functions by adjusting the elastomeric properties of the culture surface[127] and by applying mechanical stress to the cells[128]. (2) Prototyping in PDMS is rapid: a PDMS device may be designed and fabricated within a single day[129]. (3) PDMS may be readily bonded to itself[129–131], to glass[129,131], silicon, silicon oxide, quartz, silicon nitride, polyethylene, polystyrene, and glassy carbon[129]. (4) PDMS is readily surface modified to tailor its properties, such as hydrophilicity, hydrophobicity, surface proteins etc[132]. (5) PDMS is highly permeable to gasses[133], allowing for priming of dead-end

[a] This is the working principle of the Fluidigm Biomark® HD mentioned in Section 1.3.2

chambers[134]. (6) PDMS is 50 times cheaper than silicon as a base material[125], and the capital equipment required for commencing PDMS work is far cheaper and less contamination stringent than those used for MEMS[125]. Importantly, this enables more laboratories to engage in PDMS prototyping, creating a big community and knowledge base on the use of PDMS. A typical soft lithography fabrication scheme for creating a microfluidic device is shown in Figure 2.1.

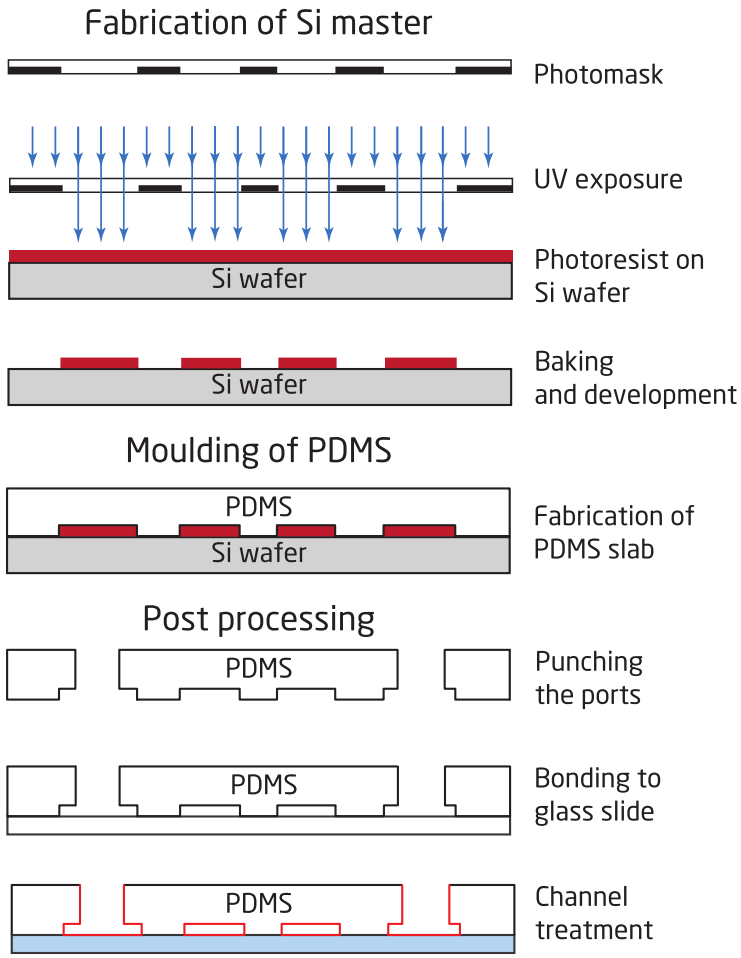

Figure 2.1: Microfluidic fabrication scheme by using soft lithography. The process may be separated into three categories: (1) Fabrication of silicon master, (2) moulding of PDMS slap and (3) post processing (backend). Curing of the PDMS is time consuming and limiting for the throughput of the silicon master. The figure is adapted from Mazutis *et al.* (2013)[135].

In addition to the advantages of soft lithography and PDMS (some of which were mentioned above), there are also challenges when working with PDMS: (1) The high flexibility and self adhesion may cause structures to collapse[124,136]. (2) Water may evaporate through the PDMS causing osmotic stress of cell systems and inducing bubble formation[137]. (3) PDMS is also highly permeable to small hydrophobic molecules, and compounds of the experiment (e.g. growth factors) may be absorbed[137,138]. Similarly, surface bound molecules may migrate into the bulk of the material[123], recovering the unaltered PDMS surface[139]. (4) Being a thermosetting elastomer, uncured monomers may be released from the device during experimentation, intoxicating

cells[137,140]. (5) Fabrication throughput is limited by thermosetting of the elastomer, and is not suited for commercialisation[b].

2.1.2 Thermoplastics

Contrary to academic microfluidic research, the abundance of PDMS usage in industry is by far outweighed by other materials such as thermoplastics[17]. In particular, polystyrene, polycarbonate and polypropylene have been the dominating materials in the commercial setting, but cyclic olefin copolymer (COC) have also recently gained increased popularity for cell growth and optical applications[137]. Thermoplastics have multiple pros and cons versus PDMS depending on the application[137], but the fundamental reason for this affinity for thermoplastics in industry is economical: thermoplastics are cheaper to buy, faster to process, and scale better with the number produced[18,141]. Figure 2.2 illustrates how the production price per part decreases with the number of parts produced[141]. This material and fabrication gap[c] between academic research and industrial implementation may pose a serious (if not catastrophic) challenge for technology transfer[17]. Therefore, the choices of materials and fabrication methods should be made with care - preferably from the beginning of the research and development. After all, in the studies claiming to deliver "on-site", "hand-held", "disposable" or "single use" devices, »*All relevant participants [...] need to emphasize that the final goal in microfluidics research is product development*«[142].

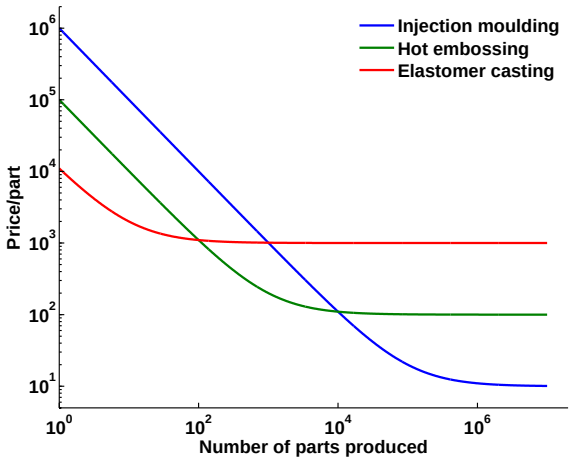

Figure 2.2: Price per part versus scaling up of production volume using different production methods for microfluidics. The figure is constructed by suggesting that the "initialisation price" of injection moulding is ×10 of hot embossing, which in turn is ×10 of elastomer casting, which is 10.000 currency. Similarly, the "production cost / piece" of elastomer casting is ×10 of hot embossing, which in turn is ×10 of injection moulding, which is 10 currency. Inspired by Becker *et al.* (2009)[141]. The figure is included for sake of argument, and numbers are approximate.

[b] Fluidigms Biomark® HD system is a special case in that the value proposition of the instrument allows for selling each chip for $400. See Table 1.2. I had the pleasure of asking S. R. Quake in person how commercial fabrication of microfluidics is realised. The answer: Lots of moulds!

[c] See *Mind the gap!* by Becker *et al.* (2010)[17]

2.1.2.1 Injection moulding

A multitude of methods and machinery exists for shaping and manipulating thermoplastics, including roll-to-roll fabrication of foils[143], injection moulding and hot embossing for producing 2.5D[d] polymer parts. As mentioned above, the popularity of injection moulding stems from its economic scaling properties with regards to part number (Figure 2.2), which to a great extent is due to the speed of fabrication. By rapidly injecting molten thermoplastic (hotter than its T_g, glass transition temperature) into a mould cavity of temperature set to below the T_g, features on the nano-scale may be reproduced with a chip cycle-time of less than a minute[144]. Further, a single mould may feature multiple cavities for parallelisation. Injection moulding is mostly fully automated, reducing labour cost and machine pause time. The process of injection moulding is outlined in Box 2.1. Note that some process steps occurs slightly parallelised, such as polymer loading for next shot while the previous injection cools in the mould.

Box 2.1: Injection moulding

Injection moulding process. (i) Polymer granules are loaded from the hopper into the barrel by the rotation of the screw. (ii) As the screw rotates and the barrel fills, the screw is pushed backwards in the barrel. (iii) By hydrolic actuation, the screw is advanced in the barrel, injecting the polymer (the *injection pressure* is often tightly controlled/monitored). After the machine senses that the cavity has been filled, it switches to the *holding pressure*. After a few seconds of holding, the pressure from the barrel is relieved, and the screw begins loading the polymer for the next injection. (iv) After a set *cooling time*, the mould is opened and the solidified polymer piece is ejected. As soon as the piece has been removed, the mould closes, and the process repeats from step ii.

The figure is downloaded and modified from Wikimedia.org and is used under a creative commons license[145].

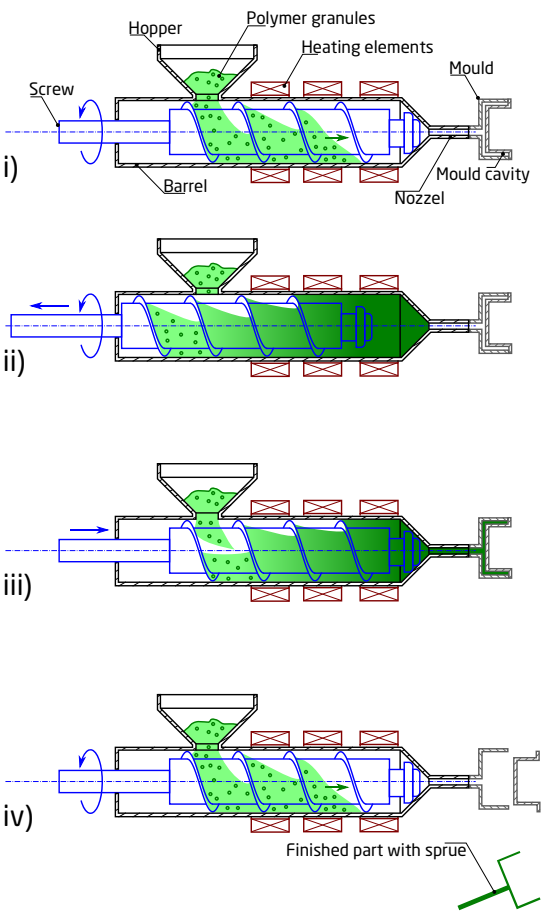

[d] 2.5D refers an object which has no internal cavities or overhanging structures. If the object cannot be moulded in 2.5D by orienting it appropriately with regards to the mould opening direction, movable pins may be added to the mould. This will however greatly increase the price of the mould.

2.1.2.2 Polymer fusion by ultrasonic welding

As is common with soft lithography and polymer injection moulding, the demoulded device must be sealed in order to gain channels (2.5D[d]) and function as a microfluidic device. The choice of part joining method is evidently material and application dependent, and a wast range of methods are applied in academia and in industry. Among those applied for joining of thermoplastics for microfluidics are solvent assisted bonding, ultrasonic welding, thermal bonding, laser welding, mechanical clamping and adhesives[146] (and the list goes on for plastic joining of larger parts[147]). Each of these methods has its pros and cons[146,147], and, without elaborating on the methodology of each of these methods[e], the major advantages of ultrasonic welding is (1) speed: Ultrasonic welding may be conducted in less than a second[147], and (2) no foreign materials are used (such as adhesives, ink for absorbing laser energy, or solvents). (3) Flexibility: The same machine configuration may be used to weld multiple devices. (4) Low contamination risk: The process is simple to incorporate in a sterile environment and little or no particulate is generated[f]. (5) The heating is localised at the energy directors, and biological material may be preloaded and enclosed without loosing activity.

Ultrasonic welding works by introducing ultrasonic vibrations (energy) of frequencies 15 kHz to 70 kHz to the parts to be fused (most machines are either 20 kHz or 40 kHz). These vibrations cause heating in the contact points between the two parts, which in turn melts the polymer locally[147]. Usually so-called energy directors, i.e. apex-shaped protrusions, are introduced at the point of contact to give additional control of were the melting occurs. Not all mould making strategies enable for the fabrication of the ED, so this requirement[g] must be considered a downside of ultrasonic welding. The process of ultrasonic welding is illustrated in Figure 2.3.

A typical ultrasonic welding machine consists of a few components critical to ultrasonic welding which may be introduced by describing the process of ultrasonic welding step by step. Several modes of welding exists, but the most common type is us using *near field welding* [h] and *welding delay*[i]. The components mentioned in the following are highlighted in Figure 2.4. Initially, the machine is held in loading position by a pneumatic cylinder. After loading the devices to be fused into the *fixture*, the pressure of the pneumatics is switched to *down pressure* and the ultrasonics of the machine begins to slowly approach the loaded pieces. As the bottom most surface of the *sonotrode* contacts the pieces, the machine senses the stop in motion and switches the pneumatic pressure to *weld pressure*. After a set *delay time*, the *generator* (not shown) powers the *piezoelectric transducer* with a high frequency alternating current. The *piezoelectric transducer* expands and retracts in responds to the current, and high frequency phononic (sound) waves are created, propagating downwards. To achieve a

[e] Tsao *et al.* (2008)[148] have published a review on thermoplastic bonding methods.

[f] More on this in Chapter 6 on page 83.

[g] Luo *et al.* (2010)[149] have demonstrated ultrasonic welding of microfluidic devices without energy directors by combining it with solvent assisted bonding.

[h] welding happens within 1/4 inch of the sonotrode, and the ultrasonic vibrations are therefore not dampened by propagating through the polymer piece[150].

[i] explained in the following.

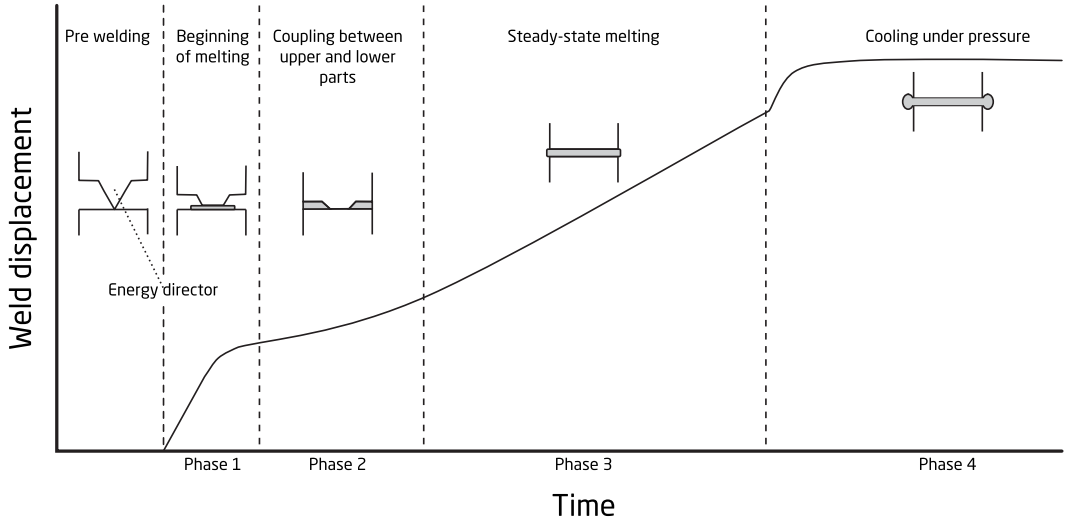

Figure 2.3: Ultrasonic welding process. The two pieces are forced together with the energy directors contacting. As the ultrasonic generator is engaged (phase 1), the contact area between the contacting polymer pieces is small, which results in rapid heating and displacement of the limited amount of contacting polymer. The rate of weld displacement is greatest in this phase but decreases as the more and more molten polymer contacts the two pieces. In phase 2, other parts of the two pieces begin to contact. Heating is slower than in phase 1 (due to large area being heated), but when melting accelerates, so does the welding, and a steady welding/melting begins (phase 3). After a set time (or energy) of melting, the ultrasonic generator is terminated, and (phase 4) the pieces are clamped together (often with increased force, giving rise to further weld displacement) and the polymer is allowed to cool. Since heating is local, the melt heat quickly dissipates in the surrounding polymer. Figure is adapted from Troughton (2009)[147].

planar wave and the desired amplitude (also adjusted on the generator voltage), these longitudinal waves first enter a booster and then the sonotrode. Finally, the ultrasonic energy is transferred to the top most polymer piece from the vibrating underside of the sonotrode. As the wave reaches the point of intersection at the energy directors, frictional heating causes the energy directors to melt, fusing the two pieces together (elaborated in Figure 2.3). After a desired amount of energy has been deposited in the system, the generator stops, and the welding pressure is kept for *holding time*, where after the ultrasonic systems is retracted and the fused piece may be removed.

Several types of energy director layouts exists depending on the application[147] and as will be presented in Paper 2 (Chapter 5 on page 63) and Paper 3 (Chapter 6 on page 83), we have contributed with energy directors geometries suited for bonding of microfluidics. As may be evident from Figure 2.3, welding phases 3 and 4 generates substantial amounts of additional molten polymer, which, if diverted into a micro channel may disrupt the function of the system[j]. For this reason, welding was primarily tuned to only melt the polymer of the energy directors (Phase 1+2, Figure 2.3), and as will presented, we introduced so-called flash-traps (Chapter 5) and smaller, and flatter

[j] Excess melted polymer is termed "flash".

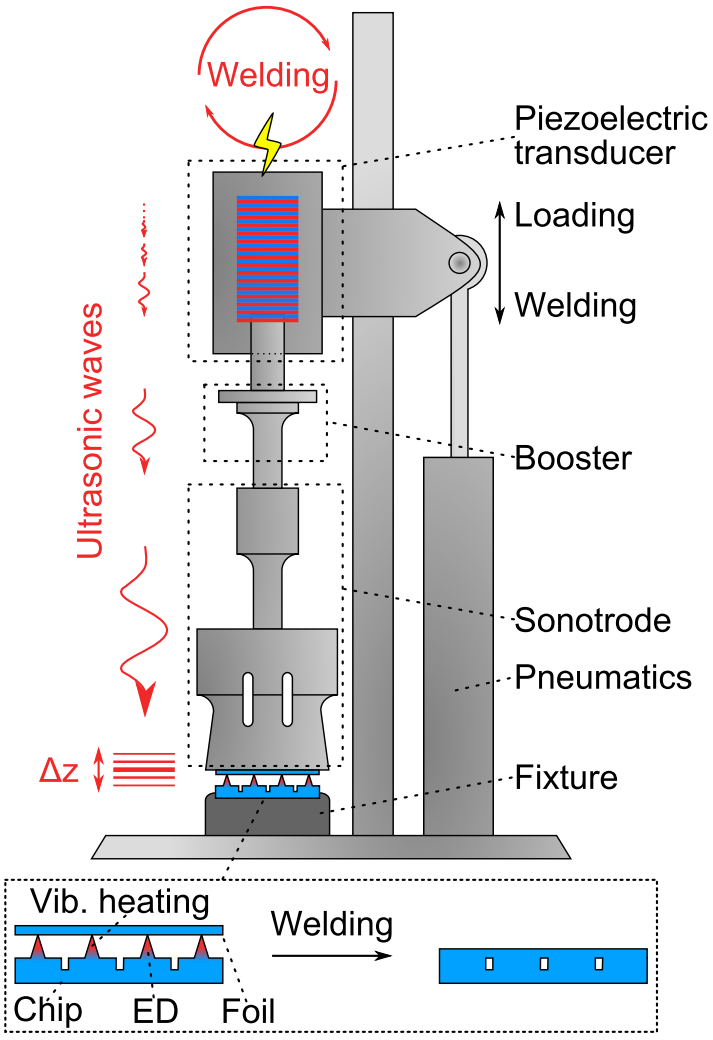

Figure 2.4: Schematic of the ultrasonic welding machine used in this PhD-project. Note that the generator is not shown. Adapted from Poulsen *et al.* (2016)[1].

energy directors (Chapter 6) for welding the microfluidic systems fabricated in this PhD-project.

2.2 Chip fabrication scheme of this PhD-project

In this PhD-project, the methods applied for chip fabrication was chosen to be as commercially relevant as possible. Not only did this allow for great volumes of devices to be produced (important for testing chip-to-chip variation in experiments[17]), but it also enabled a different material catalogue than the more common PDMS/glass/Si palette. The main scheme of fabrication included (1) design of master insert in Autodesk Inventor Professional 2012 (conversion to G-code in CimatronE 10), (2) fabrication of aluminum mould insert by micromilling (optional: energy directors may be added by laser ablation), (3) injection moulding and (4) back-end processing by surface coating

(optional: used for capillary microvalves), ultrasonic welding and annealing (optional: used for multiphase applications containing hydrocarbon oils). The chip development flow chart is illustrated in Figure 2.5. The individual process steps are elaborated below.

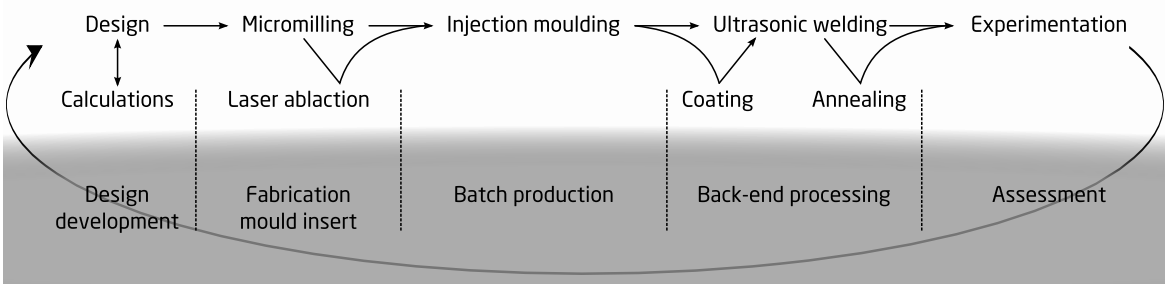

Figure 2.5: The chip development scheme employed in this PhD-project. The top most line process steps are common for all chips produced. Other process steps are optional.

2.2.1 Milling of injection moulding insert

Mould inserts for injection moulding were designed in Autodesk Inventor Professional 2012, converted to G-code in CimatronE 10 and fabricated in 2017 aluminium alloy by micro milling. For milled energy directors, the energy directors were defined using a 60° helical engraving tool (#7025, DIXI polytool) producing a $\sim$ 150 µm high apex shaped energy director in the final piece. To reduce roughness from the milling process, AUTOSOL CHROM GLANS metal polish cream was applied with a clean room fibre cloth.

2.2.2 Laser ablation of injection moulding insert

As applied in Paper 3 (Chapter 6 on page 83) and patent application 2 (Appendix C), micropillar energy directors were written using a FUEGO 1064 nm, 50 W pico second laser (Time Bandwidth, 3D-Micromac AG, Chemnitz, Germany) mounted in a microSTRUCT vario (3D-Micromac AG). The microstructures from micro phase explosions were introduced by scanning designated areas with parallel lines (10 µm spacing), repeated 20 times at 50% power and 1000 mm/s with the focus plane 1.3 mm above the surface. With a spot size of approximately 50 µm (when in focus, suppliers manual), multiple laser pulses/treatments hitting the same points on the surface. By tuning the treatment dose (altering the scanning speed, number of repetitions or power), the characteristics of the generated micro structures could be tailored. As disclosed in Patent application 1 (Appendix B) superhydrophobicity and superoliophilicity was achieved by replicating the microstructures in a hydrophobic material such as polypropylene (PP).

2.2.3 Injection moulding

The aluminium insert was installed in one of two injection moulds, deciding if the finished chip should have a twelve luer backside or just a simple flat disc. In Figure 2.6 the injection moulding insert and a 12-luer layout disc is illustrated with dimensions (to scale). To emphasise: The luer side was strictly binary: either all luers were present, or no luers was present. The injection moulding machine was a Victory 80/45 Tech injection moulder (Engel), and several polymer substrates were used, depending on the application:

COC Cyclic olefin copolymer. TOPAS grade 5013L-10 (TOPAS Advanced Polymers). Glass transition temperature (Tg) of 135 °C.

PP Polypropylene. HD120MO (Borealis) with a heat deflection temperature (0.45 MPa, N/mm^2) of 88 °C.

PS Polystyrene. 158 K (BASF SE, Germany). Heat deflection temperature (0.46 MPa) of 98.0 °C.

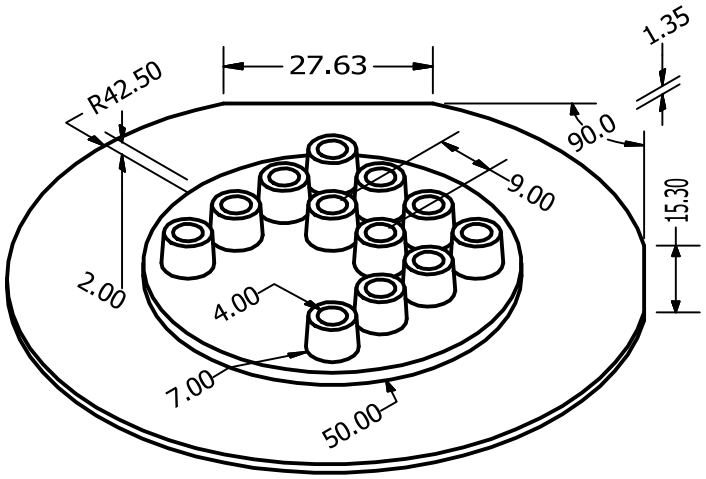

Figure 2.6: Drawing of luer chip and injection moulding insert applied in this project. Dimensions are in mm. Horizontal axis is to scale.

2.2.3.1 Troubleshooting

In this section, I disseminate some of the practical experiences I have gained whilst conducting the work and research of this PhD-project. Some points may be more obvious than others, and no systematic study have been made of these observations. They are not intended for journal publication.

- **Poor replication** observed as rounding of corners is often due to too low polymer injection speed, too low holding pressure, or too low mould temperature.
  - Adjust the injection speed and holding pressure before increasing the mould temperature. Increasing the mould temperature can have dire consequences for demoulding.

- **Demoulding not successful** (device is stuck on microstructures).
  - Decrease mould temperature if feature fidelity allows.
  - Increase cooling time or decrease the temperature of back side (luer) of mould to ensure a firm hold from the back mould and a stiffer chip.
  - Decrease mould opening speed for the first 5 mm. If mould opening is too rapid, the device may crack and be released from the back mould.
  - Milling: Add a slip angle to the microstructures by using $2-3°$ sloped tools for milling.
  - Milling: Increase the final device thickness and thereby strength. This is particularly useful for avoiding device damage from flexing during demoulding.
  - Design: Place structures of high friction closer to the ejector pins if possible. It is tempting to place all microstructures in the center region of the device, but this increases the risk of damaging the device during demoulding - particularly when injection moulding devices in elongated designs such as microscope slides.
  - If all of the above fails: Briefly flush the water cooling of the structured mould side prior to mould opening. If the insert is made of aluminium, the rapid drop in temperature and hence thermal expansion may cause the device and mould insert to "unclick". If using this trick and operating the injection moulder in fully automated mode, confirm that the mould reaches the correct temperature prior to polymer injection.
- **Deformed item**
  - Increase cooling time or decrease the mould temperature.
  - If injection speed is low, the polymer cools as it propagates throughout the mould. This results in uneven polymer temperatures and therefore uneven thermal contraction of the finished device.

2.2.4 Ultrasonic welding

Ultrasonic welding was conducted on a Telsonic-USP4700 ultrasonic welder (Telsonic) operating at 20 kHz. The booster/sonotrode combination utilised allowed for vibrational amplitudes to be in the range of 29.5 µm to 59 µm by running the generator at 50% (the minimum) to 100%, respectively. When sealing devices, bonding was always conducted between like materials; Either directly to another (flat) chip injection moulded in the same material, or to an extruded foil such as 152-500 µm thick COC sheet (TOPAS grade 5013S-04, TOPAS Advanced Polymers).

2.2.4.1 Troubleshooting

Similar to Section 2.2.3.1, this is a list of my most frequently used ”tips and tricks” for troubleshooting ultrasonic welding.

- **Estimating initial welding parameters:**.
  - The typical (final) energy for welding is 300 J per meter of energy director. To enable easy adjustment of the fixation, however, it is advisable to start with 200 J/m. This results in an incomplete welding with the with of the melting polymer indicating the flatness of the system.
  - Set the down pressure as low as the machine allows, typically 0.05 bar. The process becomes slightly more time consuming (a few seconds slower), but the risk of damaging or displacing the polymer pieces is reduced.
  - Welding pressure is typically 7.5 bar per meter of energy director but is also very dependent on materials and flatness (see below).
  - (For delay time triggered welding) Delay time should be set to a value ”sufficiently high” for allowing the pressure to stabilise - typically 2 seconds. Otherwise, increasing the welding pressure later will have no effect since its maximum is never reached.
  - (For force triggered welding) Trigger force is typically 3 kN per meter of energy director.
- **Non-uniform welding**.
  - If the welding is good in one side/end but not the other, the fixture may need balancing to accommodate obliquity of the system.
  - If welding along one energy director suddenly terminates, it may be due to too high welding pressure causing all energy to dissipate locally as soon as welding commences. Often, when using too high welding pressure, the unwelded energy directors are embedded in the facing polymer, but no melting has happened.
  - If no foaming is observed, increasing the energy.
  - If the fixation has been balanced, the welding pressure is not too high and the problem persists and is consistent (e.g. welding happens on the perimeter of the device but not in the center), increase amplitude as a last resort.
  - Check if the top of the energy directors form a single plane (is the chip flat?). Fix this by milling a new mould or redoing the injection moulding (see ”deformed item” in Section 2.2.3.1).
- **Skating** (example of this is presented in Figure 6.1 on page 84).
  - Ensure that the system is flat with regards to the sonotrode.
  - Increase welding pressure.
  - Improve clamping of parts: Make a custom, tight fit fixture for the device.
  - Increase friction between top part and the sonotrode: Apply a thin layer of flexible single-sided sticky-tape under the sonotrode to function as a padding layer. Soft, thick tape such as 75 µm PVC film Semiconductor Wafer Tape SWT 20P+ (Nitto) may be used for chip-to-chip welding. If thin foils are welded, the flexible tape may cause the foil to break at the energy directors, and thinner tape such as packaging tape should be tried instead.

- **Polymer foaming**.
  - If the welding is generally nice, too much energy is used.
  - If the foaming only happens on the corners of geometry (channels), and the energy used is not sufficient for welding the remaining EDs of the device, it may be necessary to mill a new mould with rounded features. If sharp features are absolutely necessary, one possibility is to round the energy directors inside corners. Alternatively, slightly reducing the height of the energy directors in the corners is also possible but more experimental.
- **flash** or **undesired polymer flow**.
  - Increase the offset distance of the energy directors from the channels.
  - Use lower and wider energy directors (such as the micropillar energy directors presented in Paper 3 on page 83).
- **Cracked foil**.
  - Too high welding pressure/down pressure.
  - If foil cracks over large chambers (for example those of Paper 2 (page 63) the foil may be cracking from resonating with the sonotrode. Reduce amplitude, change foil thickness, add support under the foil (such as pillars), or add a padding layer to the sonotrode (see above).
- **Cracked device** (in fixture).
  - Design the fixture so that it mainly clamps on bulk sections (such as the base disc of the luer chip, Figure 2.6). The chip dimensions wary with injection moulding settings due to thermal expansion.
  - Dampen vibrations in unsupported features[k].
  - If the device stress-cracks during long-term storage: reduce amplitude or anneal the devices after welding (see Paper 4 on page 97).
- **Welding beyond the energy directors**.
  - Check flatness of the system (see non-uniform welding above)
  - Consider defining channels by protruding walls as shown in Figure 6.2 on page 85 and Figure 5 of Paper 3 on page 90. This reduces the flatness stringency of the system and reduces complications from moulding defects.
  - Check the polymer pieces for excess polymer such as ears and sprue pieces. Remove with a knife.
- **Milled energy directors have poor finish**.
  - Ensure that the last milling step has a sufficiently low feed rate < 50 mm/min.
  - Apply the milling strategy illustrated in Figure 2.7.

[k] In the fixture I have made for the luer chip, if the luers are 'free-hanging", they will shoot clean off. Therefore I add a single rubber gasket supporting each luer for dampening.

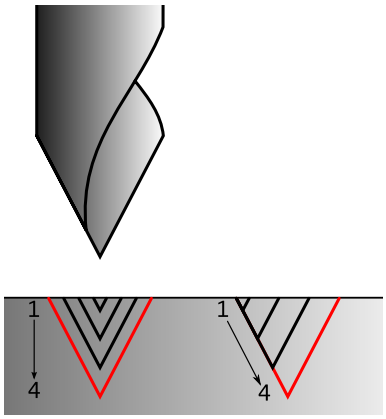

Figure 2.7: Comparison of milling strategies for milling energy directors. Numbers denote pass number. Final pass is highlighted in red. The right hand strategy has less load on the milling tip throughout the milling, and yields better finish than the vertical (left) strategy.

2.2.5 Annealing

To remove residual stress from injection moulding, the COC devices were oven-thermocycled from room temperature to 125 °C (10 °C below the T_g, glass transition temperature) over a period of 2 hours. Annealing was only used in hydrocarbon applications, and more information can be found in Section 7.1 on page 98.

This is page 34:
For typesetting reasons, it has intentionally been left completely blank.

3

Microfluidic theory

Having introduced some of the consequences and applications of scaling down to microfluidics in Section 1.1, I will in the following introduce and discuss some of the main governing equations of microfluidics. Subsequently, I will introduce concepts related to surface effects, such as surface tension, Laplace pressure and contact angles. Finally, I will describe the mechanics of droplet generation and stability in microfluidics.

3.1 Equations of motion

[a]As in classical mechanics, it is necessary to establish the equations of motion to properly describe and understand a microfluidic system. For a particle of mass m, influenced by external forces, Newton's second law reads

$$m\mathrm{d}_t\boldsymbol{v} = \sum_j \boldsymbol{F}_j.$$

Here, d_t is the total time derivative which is required to go from a Lagrangian description following an individual fluid particle in time $\boldsymbol{v}(\boldsymbol{r}(t), t)$ to and Eulerian velocity field observing specific point in space $\boldsymbol{v}(\boldsymbol{r}, t)$. It is defined as

$$\mathrm{d}_t F \equiv \frac{\mathrm{d}F}{\mathrm{d}t} = \partial_t F + (\boldsymbol{v}\cdot\boldsymbol{\nabla})F.$$

In microfluidics, it is most practical to work with force densities, and so Newton's second law expressed for an Eulerian velocity field, originating from the Lagrangian description of a fluid particle is

[a] Derivations and equations of this section are adapted from Bruus (2008)[151] when nothing else is stated.

$$\begin{aligned}\rho D_t \boldsymbol{v}(\boldsymbol{r},t) \equiv& \rho \mathrm{d}_t \boldsymbol{v}(\boldsymbol{r}(t),t) \\ =& \rho\left[\partial_t \boldsymbol{v}(\boldsymbol{r},t) + (\boldsymbol{v}\cdot\boldsymbol{\nabla})\boldsymbol{v}(\boldsymbol{r},t)\right] \\ =& \sum_j \boldsymbol{f}_j,\end{aligned}$$

where $\boldsymbol{f}_j$ is the body force densities consisting of the pressure, viscosity and other body-force densities (gravity, electric forces...).

The derivation of the terms describing these body-force densities have been demonstrated elsewhere[151], but in brief: By calculating the resulting force on an infinitesimal fluid particle from variations in the pressure integrated over its surface, the pressure term is found to be $-\boldsymbol{\nabla}p$. Additionally, the viscous term may be determined by integrating the frictional forces (tensors) between adjacent fluid particles moving with different velocities. This leads to the term $\eta\boldsymbol{\nabla}^2\boldsymbol{v}(\boldsymbol{r},t)$ + a term containing $\boldsymbol{\nabla}\cdot\boldsymbol{v}(\boldsymbol{r},t)$, however, by considering the mass flux into a region, applying mass conservation and Gauss law, and assuming incompressibility, it may be shown that the divergence of the velocity field is zero.

We now arrive at the famous Navier-Stokes equation:

$$\rho\left[\partial_t \boldsymbol{v}(\boldsymbol{r},t) + (\boldsymbol{v}\cdot\boldsymbol{\nabla})\boldsymbol{v}(\boldsymbol{r},t)\right] = -\boldsymbol{\nabla}p + \eta\boldsymbol{\nabla}^2\boldsymbol{v}(\boldsymbol{r},t) + \text{Other body-force densities} \quad (3.1)$$

The turbulence in fluid flow may be ascribed to this equation's non-linear term, $\rho(\boldsymbol{v}\cdot\boldsymbol{\nabla})\boldsymbol{v}$. Further, this term also makes the equation difficult or impossible to solve in most cases. In the following, we shall see when this is not the case.

We may choose to denote all physical variables in terms of dimensionless variables normalised to a common characteristic scale. For example, we may describe $\boldsymbol{r} = L_0\tilde{\boldsymbol{r}}$, $\boldsymbol{v} = V_0\tilde{\boldsymbol{v}}$, $p = P_0\tilde{p}$, $\boldsymbol{\nabla} = 1/L_0\tilde{\boldsymbol{\nabla}}$ and $\partial_t = 1/T_0\tilde{\partial}_t$. This yields

$$\begin{aligned}Re\left[\tilde{\partial}_t\tilde{\boldsymbol{v}} + (\tilde{\boldsymbol{v}}\cdot\tilde{\boldsymbol{\nabla}})\tilde{\boldsymbol{v}}\right] =& -\tilde{\boldsymbol{\nabla}}\tilde{p} + \tilde{\boldsymbol{\nabla}}^2\tilde{\boldsymbol{v}} \quad (3.2)\\ Re \equiv& \frac{\rho V_0 L_0}{\eta}\end{aligned}$$

The Reynolds number, Re, is a dimensionless number representing the ratio between viscous and inertial forces, and as is evident from Equation (3.2), $Re \ll 1$ results in the linear Stokes equation:

$$\boldsymbol{0} \approx -\boldsymbol{\nabla}p + \eta\boldsymbol{\nabla}^2\boldsymbol{v} \quad (3.3)$$

As long as the system we are describing has $Re \ll 1$ (is predominantly influenced by viscosity effects), we may use Equation (3.3) for finding analytical solutions. Two typical solutions to Equation (3.3) are given in Figure 3.1. Furthermore, in this regime, the flow is *laminar*, meaning that the an unchanging system will result in a flow in steady state. In laminar flow, streamlines, representing the direction of the velocity field, coincides with the path lines of individual fluid particles (since the velocity field is unchanged in time). In Chapter 7 on page 97, we will model water-in-oil droplets and see that pathlines deviating from streamlines is a proxy for external forces (gravity). Two important examples of laminar flow are the so-called Couette flow and Poiseuille flow. The linear Stokes equation and boundary conditions are presented and solved in Figure 3.1.

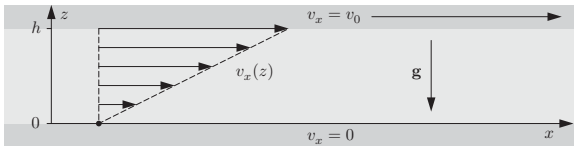

$$\eta \partial_z^2 v_x(z) = 0 \tag{3.4}$$
$$v_x(0) = 0$$
$$v_x(h) = v_0$$
$$v_x(z) = v_0 \frac{z}{h} \tag{3.5}$$

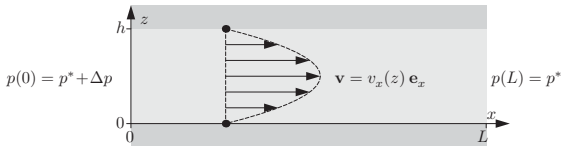

$$\eta \partial_z^2 v_x(z) = -\frac{\Delta p}{L} \tag{3.6}$$
$$v_x(0) = 0$$
$$v_x(h) = 0$$
$$v_x(z) = \frac{\Delta p}{2\eta L}(h - z)z \tag{3.7}$$

Figure 3.1: (left) Coutte flow: A liquid is suspended between two infinite, parallel plates. The plates are moving with constant speed, v_0, relative to each other, while keeping the separation distance, h, constant. The Stoke's equation then takes the form of Equation (3.4). Utilising the Dirichlet boundary conditions, Equation (3.4) solves to give Equation (3.5). (right) Poiseuille flow: A liquid is suspended between two stationary, infinite, parallel plates. A pressure difference, Δp, exists over the section of length L in the x direction, driving the fluid flow. Again, by using Dirichlet boundary conditions, the Stokes equation, Equation (3.6), solves to give Equation (3.7). Figures are adapted from Bruus (2008)[152].

3.2 Surface effects

To understand the implications of interface effects such as capillary effects in a microfluidic system, we must first understand the fundamental principle of surface tension, γ. In a bulk liquid, the molecules constantly interact with their neighbours through temporary bonds such as hydrogen bonds, van der waals interactions (induced dipole - induced dipole) or ionic interactions. The molecules close to the interface will have fewer (or less energetic) interactions, and their Gibbs free energy is therefore increased. See Figure 3.2.

A system will seek to minimise its Gibbs free energy, and we may assume this to be

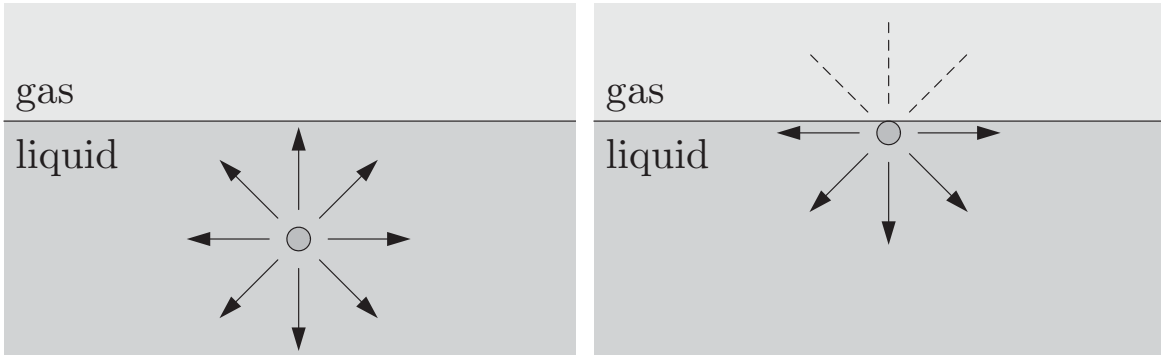

Figure 3.2: (left) A molecule submerged into the bulk part of the liquid can interact with with neighbouring species in all directions (arrows). (right) When closed to the surface, the number of possible interactions are reduced (dashed lines). Figures are adapted from Bruus (2008)[153].

accomplished for a system in equilibrium. From this, we may define the surface tension:

$$\gamma \equiv \left(\frac{\partial G}{\partial A}\right)_{T,p}$$

Typical values for surface tension relevant for this project:

- Water/vapour[153]: $\gamma = 72.9$ mJ/m^2.
- Octanol[b]/water[2]: $\gamma = 8.02$ mJ/m^2.
- Octanol + 3% (w/w) Abil EM90[c]/water[2]: $\gamma = 5.46$ mJ/m^2.

3.2.1 Laplace pressure

An alternative interpretation of surfaces tension may be made by rewriting its units:

$$[\gamma] = \text{J m}^{-2} = \text{N m}^{-1} = \text{Pa m}$$

N m^{-1} may be interpreted as the force required to expand a rectangular region of surface by pulling in a side of unit length. Using this interpretation, we may observed a curved interface such as the one depicted in Figure 3.3.

If the surface has a positive surface tension and therefore assumes minimum surface area in equilibrium, we can conclude that a finite pressure difference exists across the surface (like a balloon contracts, compressing the inflating air). We can calculate this

[b] An octanol droplet submerged in water. Phases were mutually saturated prior to measuring. Please see Supplementary Information of Paper 4 on page 112 for further details.

[c] A *surface active agent* (surfactant): ABIL EM90 surfactant, cetyl dimethicone copolyol, Rose Chemicals, U.K.
Surfactants are amphiphilic molecules, harvesting both hydrophilic and hydrophobic constituents. This results in an energy minimum when placed at the surface or when forming micelles.

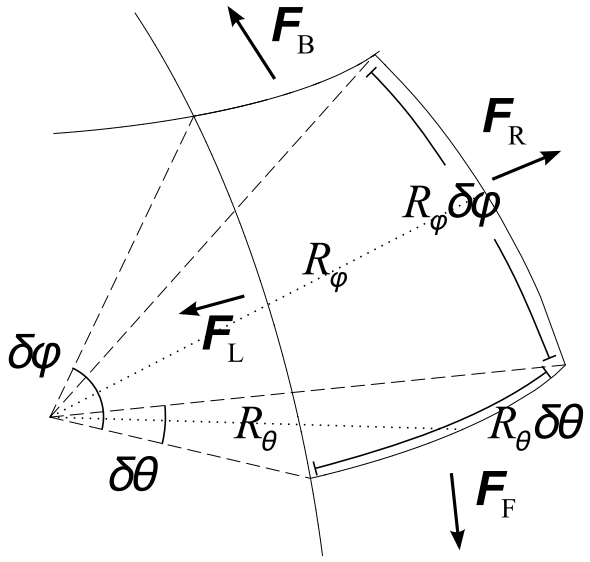

Figure 3.3: Infinitesimal section of a curved surface. $\boldsymbol{F}$ denotes forces acting on sides. L, R, F and B denote component, left, right, forward and backward, respectively. Figure is modified from Bruus (2008)[153].

pressure difference by calculating the net radial forces on this section of the surface. Assuming that the angles, θ and ϕ, are small, the area of the observed interface, $A \approx R_\phi \sin(\delta\phi)\, R_\theta \sin(\delta\theta) \approx R_\phi \delta\phi R_\theta \delta\theta$, and the radial net force is given by

$$0 = A\Delta p - F_{r,L} - F_{r,R} - F_{r,F} - F_{r,B}, \tag{3.8}$$

where force indices r, L, R, F and B denote radial component, left, right, forward and backward, respectively, as indicated on Figure 3.3. The magnitude of these forces are given by

$$\begin{aligned} F_{r,L} = F_{r,R} &= \gamma R_\phi \delta\phi \sin\left(\frac{\delta\theta}{2}\right) \approx \gamma R_\phi \delta\phi \frac{\delta\theta}{2} \\ F_{r,F} = F_{r,B} &= \gamma R_\theta \delta\theta \sin\left(\frac{\delta\phi}{2}\right) \approx \gamma R_\theta \delta\theta \frac{\delta\phi}{2}. \end{aligned} \tag{3.9}$$

Inserting this in Equation (3.8), we obtain the Young-Laplace equation, yielding the Laplace pressure of the interface:

$$\Delta p = \gamma \left(\frac{1}{r_\theta} + \frac{1}{r_\phi}\right) = \gamma\left(\kappa_1 + \kappa_2\right) \tag{3.10}$$

where κ_1 and κ_2 are the curvatures of the interface.

From Equation (3.10) we may identify that higher curvatures (e.g. a small droplet) results in a higher Laplace pressure. A simple way to reduce interactions (be it droplet-droplet or droplet-surface) is therefore to reduce the droplet size, making the droplets "harder" and their interfaces less deformable. Additionally, the increased pressure by the Laplace pressure results an increased vapour pressure, which in turn explains why small droplets spontaneously evaporate even in with close to 100% humidity.[d]

3.2.2 Contact angle

In a multiphase system such as the one shown in Figure 3.4, so called *contact lines* exists, where all three phases meet. The system shown in Figure 3.4 contains three phases: gas, liquid and solid, and therefore three surface tensions: γ_{LG}, γ_{SG} and γ_{SL} representing the liquid-gas, solid-gas and solid-liquid interfaces, respectively. The contact angle, θ_C, is defined as the angle between the γ_{LG} and γ_{SL} interfaces, measured on the liquid side.

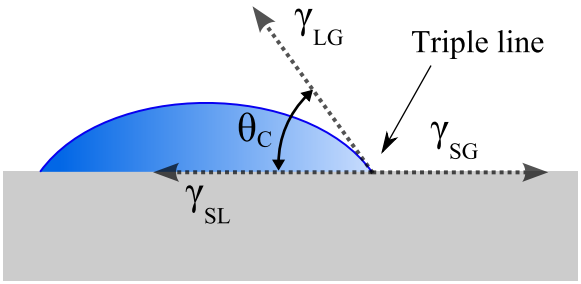

Figure 3.4: Annotation of contact angle and triple line in a triple phase system. The figure is downloaded from Wikimedia.org and is used under a creative commons license[155].

As when deriving the Young-Laplace equation, we may calculate the net force on the contact line from the surface tension of the three interfaces. In equilibrium, this line is steady, and the net force is zero, and from a simple geometric contemplation, we get

$$0 = -\gamma_{SL} - \gamma_{LG}\cos\theta_C + \gamma_{SG}.$$

This expression may be rearranged into Young's equation for the contact angle:

$$\cos\theta_C = \frac{\gamma_{SL} + \gamma_{LG}}{\gamma_{SG}}. \tag{3.11}$$

[d] This is calculated from the fact that the two phases are in equilibrium, which imply that the chemical potentials are equal. Increasing the pressure will perform PV work on the gas thus increasing said chemical potential. To re-establish equilibrium, molecules escape to the gas phase, increasing the vapour pressure. Derivation is found in Atkins *et al.* (2006)[154] on page 125.

A system of this type is denoted hydrophilic if the contact angle i $< 90°$, hydrophobic if $\theta_C > 90°$, and super hydrophobic if $\theta_C > 160°$. For highly wetting surfaces, the concept of a contact angle may be meaningless (if the liquid completely wets the surface, and no contact line exists), and it may be more useful to simply calculate the energy difference of the solid, before and after wetting:

$$S = \gamma_{SG} - (\gamma_{SL} + \gamma_{LG}) .$$

Here, S is termed the *spreading parameter*, and as is obvious from inserting S in Equation (3.11), $S < 0$ is required to have partial wetting, and hence a meaningful solution for the contact angle: $S = \gamma_{LG} (\cos\theta_C - 1)$.[156]

These two phenomena, Laplace pressure and contact angle, give rise to numerous effects discussed in this thesis, including droplet formation and micro capillary valves.

3.3 Droplet microfluidics

Taking a simple, macroscopic viewpoint, the origin of droplet formation in microfluidics may be explained from an energy consideration[157]: From the very definition of the surface tension (Section 3.2), we know that in order to minimise the Gibbs free energy, a multiphase system will stride to minimise is surface area. Disregarding the ends, the energy contribution from surface tension of a cylindrical rod is

$$E_C = 2\pi R L \gamma.$$

Similarly, the energy of N droplets of radius R' is

$$E_D = 4\pi R'^2 N \gamma.$$

By conserving the total volume of the dispersed phase these expressions may be rewritten in terms of the total volume V:

$$E_C = \frac{2\pi\gamma V}{R},$$
$$E_D = \frac{3\gamma V}{R'}.$$

For droplets to form, we require $E_D \leq E_C$, and therefore

$$R' \geq R\frac{3}{2\pi} \approx 0.48R, \tag{3.12}$$

We may conclude that *any* instability of the water stream may cause it to form droplets since Equation (3.12) is essentially always fulfilled. What this equation also tells us is that the formed droplets can have any size, only limited by the minimum size $R' \geq$

$R\frac{3}{2\pi} \approx 0.48R$. The formed sizes are however not arbitrary, as we shall see in the following.

An initial perturbation in the stream is required for the onset of instability and droplet formation, which, in a simple example may be in the form of waves. Assuming that initially, an equal proportion of waves of every different wave number is present, then the perturbation with the fastest growth (in time) will dominate the droplet formation. The growth rate of a particular wave will depend on the Young-Laplace pressure arising from the curvature of the stream and the wave itself. Figure 3.5 illustrates the terminology with the *stream* component highlighted in blue, and the *wave* component highlighted in red. Analysing Figure 3.5 with the Young-Laplace Equation (3.10) in mind, we see that the streams radius of curvature in the trough (T) is smaller than at the peak (P), inducing a higher Laplace pressure in the trough than in the peak. On the contrary, the radius of curvature from the wave (red) will have the opposite effect on the Laplace pressure. Since shorter wave lengths (λ) cause the interface to curve more, the stream stabilising effect is enhanced, the perturbation (wave) is damped, and the stream does not break. An in-depth mathematical analysis of this phenomenon is beyond this thesis, but it has been shown by Bush (2004)[158], for a wave to grow in an inviscid fluid, it is required that $kR < 1$, where R is the initial radius of the stream and k is the wave number. Infinitely long wavelengths naturally has no such dampening, however, shaping the stream into droplets obviously requires the fluid to move, which introduces inertial effects, which in turn dampens/slows the droplet formation of big droplets. These two opposing effects lead to a maximum growth rate[e] at $\lambda_{max} = 9.02R$.[158]. Since each period leads to exactly one droplet, by conservation of mass we may deduce that, $R' = 1.89R|_{\lambda=9.02R,H_2O}$, which agrees well with Equation (3.12).

[e] As shown by Bush (2004)[158], the growth rate ω of wavenumber k is $\omega^2 = \frac{\gamma}{\rho R^3} kR \frac{I_1(kR)}{I_0(kR)} \left(1 - k^2R^2\right)$ where γ is the surface tension, ρ is the density, R is the initial radius of the stream, and I_0 and I_1 are the modified Bessel function.

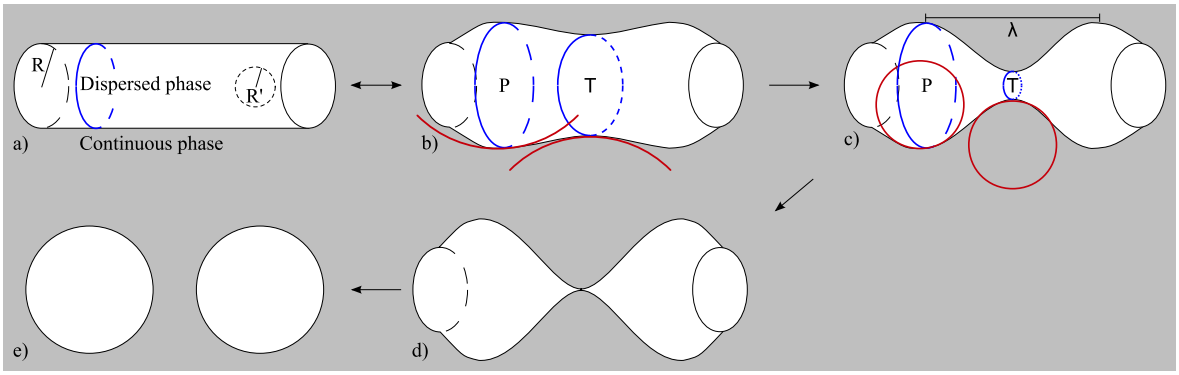

Figure 3.5: Plateau-Rayleigh instability: Droplet formation from a cylindrical rod of to-be dispersed phase submerged in a continuous phase. (a) Cylinder with R and R' annotated from Equation (3.12). Note that from a perspective of surface tension, droplets bigger than R' are energetically favourable. (b) Waves along the length of the cylinder introduce curvatures along the cylinder (red), and cause the stream curvatures (blue) to be higher in troughs (T) than in peaks (P). (c) If the stream component dominates, water flow from the high pressure at T to the lower pressure at P, escalating the effect. (d) This effect continues until the stream has collapsed, and (e) two new droplets have been formed. The figure is modified and downloaded from Wikimedia.org and is used under a creative commons license[155].

3.3.1 Dynamical systems: dripping, jetting and squeezing

Plateau-Rayleigh instability describes *why* droplets form, but in the estimate of droplet sizes presented, it was assumed that the surface of the stream was not influenced by shear stress from the continuous phase. Also, the model by Bush (2004)[158] does not include the viscosity of both phases, nor the density of the continuous phase, and may be assumed to work primarily with liquid in gas systems such as a dripping kitchen tap. Including these effects makes it difficult to create good analytical models to correlate to experimental data - even for axial symmetric models[159]. Instead, since once the droplet chip has been fabricated, multiple different experimental settings[f] may be explored and the droplet generation characteristics obtained, experimental correlations are widely used for experimental planning[160–163]. In this context, the two dimensionless numbers, the capillary number and the Weber number are often applied for enabling interexperiment comparison[160]. The capillary number is ratio between the effect of viscous forces and surface tension, and is given by $Ca = \eta V_0/\gamma$, with η being the viscosity, V_0 being the flow velocity, and γ being the surface tension[153]. The Weber number is the ratio between effects from inertial forces and surface tension, and is given by $We = \rho L_0 V_0^2/\gamma$, ρ being the viscosity, and L_0 being the characteristic length scale of the system. It has been experimentally observed[160,161], that if surface tension dominates and $Ca+We < 1$, droplet will be formed in a "dripping" manner (illustrated in Figure 3.6a), and if $Ca + We > 1$ droplets will be produced in a so-called "jetting" manner (Figure 3.6a). There are several scenarios, which cause jetting, but common is that the time scale of the surface tension breaking up the stream is larger than

[f] Surface tension, flow rate of dispersed phase, flow rate of continuous phase, viscosities, etc.

the time scale of the stream moving through the channel: either because of low surface tension, high flow velocity, high viscosity, or high density. A phase diagram of dropping and jetting is plotted in Figure 3.6c. Less dynamic modes of droplet formation is by using a T-junction or low flow rates in a droplet junction, causing it to for droplets by "squeezing". The latter is has similarities to droplet formation by using a gradient of confinement 3.6b.

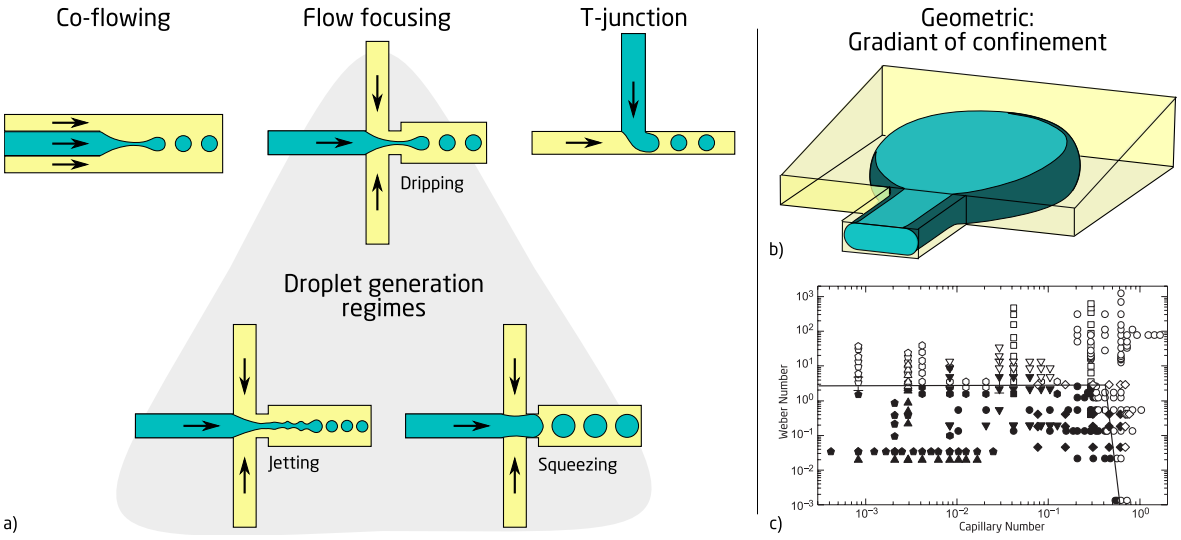

Figure 3.6: Examples of droplet forming strategies and droplet generation regimes. (a) By using co-flowing fluids to achieved droplet, dripping or squeezing (explained in the main text), or (b) by using a gradient of confinement, to cause the Laplace pressure to birth the droplet from the stream. (c) Phase diagram of droplet formation with capillary number (CA) plotted versus Weber number (We). Empty symbols represent jetting. Shapes represent different ratios of viscosity between the continuous and dispersed phase and different geometries. η_d/η_c: $\diamond = 0.01$, $\hexagon = 0.1$, $\bigcirc = 0.1$, $\pentagon = 1$, and $\triangle = 10$. Figures a and b are adapted Dangla *et al.* (2013)[66] and inspired by Christopher *et al.* (2007)[65], respectively, and Figure c is adapted from Utada *et al.* (2007b)[160].

4

Paper 1: Numerical predictions of capillary microvalve burst pressures

Rapid prototyping is always desirable when developing a microfluidic device, and with the chip fabrication work flow described in Section 2.2 on page 27 which allowed for a microfluidic device to be sketched and milled in the morning, injection moulded in the afternoon, and tested in the evening, ideas could quickly be realised and tested. Since materials, machine time and man hours are precious, one should always thoroughly estimate the important parameters of the system and strive to optimise the amount of information gained from the experiment. If good mathematical models and tools exist, the number of iterations required for achieving a working design may be reduced. As elaborated in Chapter 3, the mathematics of microfluidics (low Reynolds number) are "simpler", which allows for exact analytical expressions to be constructed to estimate values for hydro dynamic resistance, flow velocity profiles, back pressures, etc[151]. However, due to the introduction of interface forces and boundary conditions at the interface, the mathematics of multiphase flows are significantly more complicated than those of single phase flow[164], and for studying microfluidic droplet formation, numerical simulations may be the only option for obtaining an estimate for characteristics such as droplet size[165].

Due to all of the above, we decided to develop a numerical model for prediction droplet production characteristics for a given combination of viscosities, surface energies, flow rates and geometries. Further, to break the model development into manageable and widely applicable milestones, the first multiphase model was of a more stable and less dynamic system (making it less computational demanding): the capillary microvalve.

4.1 Capillary microvalves

A capillary microvalve is geometric feature which functions to locally increase the capillary pressure required to further advance an interface in a multiphase microfluidic system (device-gas-liquid, device-liquid-liquid). The maximum capillary pressure which can be retained by a specific capillary microvalve is termed the burst pressure. An advancing interface, subjected to a pressure drop larger than the capillary pressure of

the channel (hence the advancement), but less than the burst pressure of the capillary microvalve will pause on the capillary microvalve in a so-called "pinned" state. If the applied pressure drop is increased above the burst pressure, the microvalve will "burst", and the interface advances beyond the capillary microvalve.

Since the purpose of the microvalve is to increase the Laplace pressure (Equation 3.10), it is reasonable that the curvature of the interface must be increased[a]. As elaborated in our journal article below, an increase in interface curvature for achieving the pinned state is most often acomplished by introducing a local chemical modification on the channel wall which exercises a higher contact angle than the preceding channel walls. Alternatively, a capillary microvalve may be constructed geometrically by expanding the channel, reducing the apparent contact angle. This principle is sketched in Figure 1 on page 50. A minor detail that must be added with regards to this figure is that the change in contact angle is not strictly required to be abrupt (a zero tolerance for imperfections would otherwise make fabrication extremely difficult). The motivation for employing an abrupt change in contact angle for constructing a capillary microvalve in this study was to make the pinned interface as static as possible[b].

4.2 Description of contribution

For this journal article, I was responsible for developing, testing, automating and verifying the numerical model, and co-author the paper. The model is nicely described in the paper below (page 53 of this thesis), however, I must emphasise the generality of the introduced COMSOL model coupling; When studying an abruptly changing system such as a capillary microvalve, convergence of the model solver is frequently compromised if the model is not relaxed properly, and allowed to progress slowly. This is the reason for the necessity of using time dependent models with time dependent (growing) back pressure contrary to stationary models; Stationary models never converged if the applied back pressure was on the same order of magnitude as the expected bursting pressure. Further, the task of estimating *the* pressure value, which caused the system to escalate, may be difficult because of inertial effects masking the exact point of bursting. In our model, the model coupling simply served to slightly decrease the applied pressure drop linearly with the fraction of the model occupied by water. By appropriate choice of coupling constants, the rapid advancement of the interface during bursting resulted in the dampening term dominating the "time dependent linear increase" term, decreasing the applied pressure drop, resulting in a notable peak in the recorded pressure drop (See Figure 4 on page 54). Since the capillary pressure required to advance the interface *after* bursting is *lower* than the burst pressure, the interface continues to advance until the evaluation is terminated (more on that in the supplementary information of the paper, page 62). The model coupling may be formulated

[a] Theoretically, the Laplace pressure may also be altered by increasing the surface tension of the interface. This is however the least practical choice if a passive device is desired

[b] An interface pinned on a "gradual" capillary microvalve will advance according to the increasing (applied) back pressure until bursting.

as

$$\Delta p\left(t\right) = \underbrace{p_{start} + \alpha t}_{\text{Time dependent}} - \underbrace{\beta \frac{V_{water}\left(t\right)}{V_{model}}}_{\text{Dampening}} \tag{4.1}$$

where the applied pressure drop, Δp, of the model is linearly growing in time (scaled by a factored of α), but is in term dampened by the fraction of water occupying the model (scaled by a factor of β).

4.3 Remarks

4.3.1 Numerical model

The successful modelling of a bursting capillary microvalve enabling the prediction of experimental burst pressures was only possible due to the introduction of a model coupling dampening term, Equation (4.1). However, for modelling the generation of droplets, the system cannot be dampened, and the inlet flow must be set to constant flow rate (simulating a syringe pump), or constant pressure (simulating a pressure pump). Based on the experiences accumulated to develop the presented model, it is (1) highly doubtful that a model of continuous flow would be able to complete uninterrupted evaluation. Further, (2) the presented simulations required between 1,000 and 10,000 seconds of computational time. If proper droplet generation statistics are desired, tens or hundreds of droplets should be analysed, and the computational time would explode. Lastly, (3) as mentioned in the paper, it was found that poor mass conservation was observed which, in the context of droplets, would result in spontaneous changes to the volume. An example of this is illustrated in Figure 4.1.

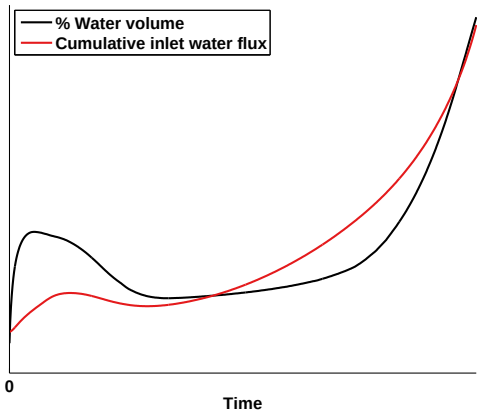

Figure 4.1: Plot of the ratio of water volume to the total model volume developing in time, and the cumulative inlet water flux developing in time[a]. It is noteworthy that though the two graphs have resemblances, it is evident, that they are not identical.

[a] Or in other words: Plot of water as measured by the interior of the model, and plot of sum of water flowing into the model through the boundaries.

4.3.2 Ultrasonic welding

One observation made in the presented paper of major importance to droplet generation is the fact that capillary microvalves of 100 by 100 μm^2 could not be produced in a reproducible manner due to polymer from ultrasonic welding flowing into the channels. It was therefore desired to develop a new type of energy director which would allow for bonding of smaller microstructures. We developed two types, and these are presented in Chapters 5 and 6.

IOP Publishing Journal of Micromechanics and Microengineering
J. Micromech. Microeng. **24** (2014) 125007 (10pp) doi:10.1088/0960-1317/24/12/125007

Fabrication and modelling of injection moulded all-polymer capillary microvalves for passive microfluidic control

Kasper Kistrup[1,3], Carl Esben Poulsen[1,3], Peter Friis Østergaard[1], Kenneth Brian Haugshøj[2], Rafael Taboryski[1], Anders Wolff[1] and Mikkel Fougt Hansen[1,4]

[1] Department of Micro- and Nanotechnology, Technical University of Denmark, DTU Nanotech, Building 345 East, DK-2800 Kongens Lyngby, Denmark
[2] Centre for Microtechnology and Surface analysis, Danish Technological Institute, Gregersensvej, DK-2630 Taastrup, Denmark

E-mail: mikkel.hansen@nanotech.dtu.dk

Received 15 May 2014, revised 8 August 2014
Accepted for publication 17 September 2014
Published 12 November 2014

Abstract
Rapid prototyping is desirable when developing products. One example of such a product is all-polymer, passive flow controlled lab-on-a-chip systems that are preferential when developing low-cost disposable chips for point-of-care use. In this paper we investigate the following aspects of going from rapid prototyping to pilot (mass) production. (1) Fabrication of an all-polymer microfluidic system using a rapid prototyped master insert for injection moulding and ultrasonic welding, including a systematic experimental characterisation of chip featured geometric capillary microvalve test structures. (2) Numerical modelling of the microvalve burst pressures. Numerical modelling of burst pressures is challenging due to its non-equilibrium nature. We have implemented and tested the level-set method modified with a damped driving term and show that the introduction of the damping term leads to numerically robust results with limited computational demands and a low number of iterations. Numerical and simplified analytical results are validated against the experimental results. We find that injection moulding and ultrasonic welding are effective for chip production and that the experimental burst pressures could be estimated with an average accuracy of 5% using the presented numerical model.

Keywords: injection moulding, capillary stop, polymer microfluidics, microvalve, ultrasonic bonding, finite element analysis

S Online supplementary data available from stacks.iop.org/JMM/24/125007/mmedia

(Some figures may appear in colour only in the online journal)

1. Introduction

Ever since Manz *et al* coined the term 'miniaturized total analysis system' (μTAS), that laid out the fundamental requirements for lab-on-a-chip systems, it has been recognized that microfluidics plays a central role as the mediator linking all the components of a μTAS (Manz *et al* 1990). It is clear that precise control of fluids on-chip is critical for the success of such a microfluidic device. An idealised μTAS is low-cost and easy-to-fabricate, which by today's standards is preferably a single-use all-polymer system, often realised using rapid prototyping (Giboz *et al* 2007, Becker and Gärtner 2008, Waldbaur *et al* 2011). Capillary microvalves are essential components in many lab-on-a-chip systems and are also sensitive to dimensions. They are

[3] These two authors contributed equally to this article.
[4] Author to whom any correspondence should be addressed.

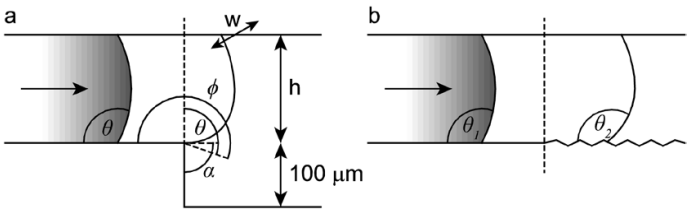

Figure 1. Cross sectional view of capillary microvalve types. (*a*) Geometric capillary microvalve, where pinning is achieved through a sudden change in geometry. θ, α and ϕ denote the channel contact angle, expansion angle and effective contact angle, respectively. w and h denote width and height of the channel. (*b*) Hydrophobic capillary microvalve, where pinning is achieved by abrupt changes in the wetting properties of one or more channel walls. θ_1 and θ_2 denote the contact angles of the smooth and rough channel area, respectively.

therefore chosen to illustrate the applicability of the methods presented here.

An important aspect of lab-on-a-chip systems is the fabrication process itself. When developing a disposable chip for commercial use, it is highly desirable to apply rapid prototyping technologies that are directly compatible with mass production. Lab-on-a-chip systems presented in the scientific literature often consist of different materials that need to be carefully aligned prior to assembly (Begolo *et al* 2011). While this is no hindrance for prototyping, a redesign is needed for implementation into an assembly line or to reduce fabrication costs. Furthermore, the fabrication of a single chip is laborious for silicon chips, glass etched chips and to some extent polydimethylsiloxane (PDMS) chips leading to long production times for each chip.

Injection moulding of thermoplastics is well established as a commercial production technique and serves well to reliably replicate structures down to nanometer size (Attia *et al* 2009, Tanzi *et al* 2012) at turn-around times of ca. 1 min per chip (Matteucci *et al* 2013). Ultrasonic welding is also widely used in production around the world, though its usage for lab-on-a-chip systems is limited (Truckenmüller *et al* 2006a, 2006b). Ultrasonic welding functions without the need of additional adhesives or substrates and only applies a localised friction heating at the welding seam. This is advantageous when working with lab-on-a-chip systems where interactions of chip reagents or sample with the bonding material might dissolve the chip or contaminate the sample.

Passive on-chip fluid management can be realised by utilising the capillarity available due to the large surface-to-volume ratio of microsystems. This approach is known as passive or autonomous flow control. Two examples include capillary pumps and capillary microvalves (Zimmermann *et al* 2008). Active and passive flow control have their benefits and disadvantages. A major drawback of active control is that it adds complexity to the system. Passive components are inexpensive to incorporate, yet they are single-use and most often unidirectional, and are sensitive to surfactants altering the surface and wetting properties. Depending on the desired application one should carefully choose the appropriate components to include in a given μTAS.

Two strategies for creating capillary microvalves exist (figure 1): (a) an abrupt geometry change, and (b) areas of altered wetting properties. A geometric capillary microvalve consists of an abrupt expansion of a micro channel, with expansion angle, α, see figure 1(*a*). From geometric considerations, it is evident that when the interface reaches the edge of the expanded region, the interfacial contact angle to the expanded region, ϕ, is smaller than the expanded region advancing contact angle, θ, and the interface is thus pinned as long as $\phi \leq \theta + \alpha$ (Cho *et al* 2007). A similar pinning effect may be achieved in a hydrophobic capillary microvalve. Here, pinning is achieved by an abrupt change in the wetting properties, increasing the contact angle, see figure 1(*b*). In several studies, this pinning effect have been exploited to create 'virtual walls', guiding the liquid phase (Zhao *et al* 2002, Bouaidat *et al* 2005, den Dulk *et al* 2012).

Passive capillary microvalves have previously been demonstrated in a variety of materials, including, silicon and PDMS (Zimmermann *et al* 2008), PDMS (Duffy *et al* 1999), Polycarbonate (PC)-PDMS (Cho *et al* 2007), and micro machined poly(methyl methacrylate) and pressure adhesive tape (Thio *et al* 2013), for both disc based and conventional planar microfluidic systems. All of these systems are fairly complex in the sense that they are constructed from multiple materials, some require clean room work, and some need careful alignment of the parts during fabrication. They are therefore not applicable for commercial scale chip fabrication.

Since passive flow control is promising for many applications, it is interesting to investigate the relations between analytical expressions and numerical evaluations that predict the rheology of microfluidics, and the performance of on-chip passive flow control components. Previous studies have shown that the finite interface thickness of the volume of fluid (VOF) does not influence the pinning of the interface until the interface width is of comparable to the size of the obstacle, suggesting that this approach may be applicable for estimating the pressure drop on pinned interfaces (Chibbaro *et al* 2009). However, one major disadvantage of VOF is the difficulty to calculate local surface curvatures (Sussman and Puckett 2000) and hence surface tension effects (Gerlach *et al* 2006). Opposed to that, using the level-set (LS) method for the calculation of the surface curvature is simple, but good conservation of mass is lacking (Sussman and Puckett 2000). Therefore, numerical methods combining VOF and LS have been created (Sussman and Puckett 2000, Olsson and Kreiss 2005) and implemented in commercial software.[5]

In this paper we look into two challenges of going from rapid prototyping to pilot (mass) production: (1) fabrication of a

[5] COMSOL v4.3 computer software 2012 (www. comsol.com).

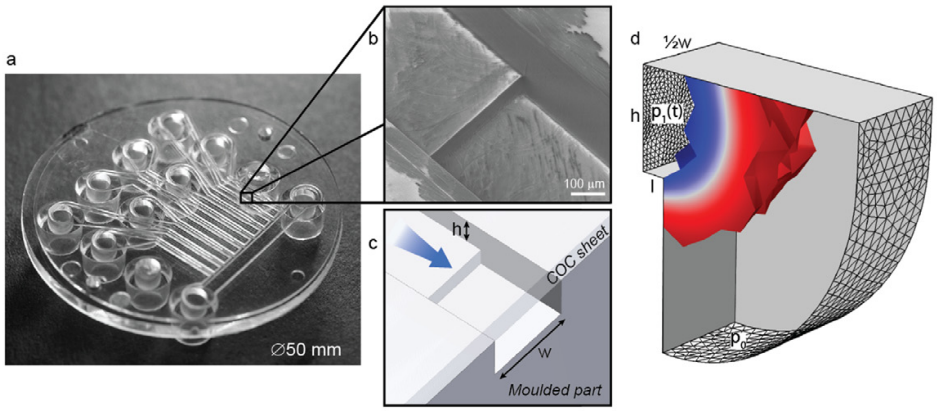

Figure 2. Overview of chip dimensions (*a*) Photograph of the injection moulded main chip part (pre-welding) showing the overall parallel lay-out of the channels containing the capillary stops. The location of a single capillary stop has been marked (box) along with two insets; (*b*) a SEM image showing the actual capillary stop (pre-welding) and (*c*) a 3D representation of the same capillary stop on which dimensions (height and width), flow direction (blue arrow) and a COC sheet has been depicted. (*d*) Geometry used in the COMSOL Multiphysics finite element calculations. The symmetry plane is the transparent face of the figure and an advancing interface is illustrated as filled elements in a blue–white–red gradient going from 75%–50%–25% water content. ½*w*, *h*, $p_1(t)$ and p_0 indicate half width, height, inlet channel length, inlet pressure and outlet pressure, respectively.

microfluidic chip using mass-production techniques from a rapid prototyped master insert; (2) reducing the number iterations by addressing the feasibility of using the LS + VOF method as a numerical tool to predict fluid behaviour in a surface tension controlled all-polymer system. We present a systematic comparison between experimentally measured, numerically estimated and analytically calculated burst pressures of a selection of geometrical capillary microvalves. Our experimental model system is an all-polymer injection moulded chip, made using a rapid prototyped master insert. It consists of two pieces of polymer, which have been thin film coated to increase the hydrophobicity. The chip parts are bonded using ultrasonic welding. All parts of the chip fabrication are directly applicable to mass production and require no careful alignment during assembly.

2. Theory

The theoretical pressure drop required for forcing a liquid through an expanding microfluidic structure such as a capillary microvalve may be estimated analytically for simple geometries. Cho *et al* assumed that the liquid interface will pin to the corner of the expansion forming an angle α (figure 1(*a*)) if the interface angle to the expanded wall, ϕ, is smaller than the expanded region advancing contact angle, θ, leading to the pinning condition (Cho *et al* 2007)

$$\theta \leq \phi \leq \theta + \alpha \tag{1}$$

also known as Gibbs' inequality condition (Gibbs 1906, Dyson 1988).

By geometric considerations, the curvature of the pinned surface can be described and used for calculating the Young–Laplace pressure of the interface (equation (2)) of the capillary microvalve illustrated in figure 1(*a*) (Delamarche *et al* 1998, Huang *et al* 2006, Cho *et al* 2007)

$$\Delta p = -\gamma\left(\frac{2\cos\theta}{w} + \frac{\cos\phi}{h} + \frac{\cos\theta}{h}\right) \tag{2}$$

where γ is the surface tension of the gas–liquid interface, and w and h are the dimensions of the microvalve geometry, see figure 1(*a*). Maximising the pressure drop with regards to ϕ expressed in terms of equation (1) yields the theoretical burst pressure,

$$p_{\text{burst}} = -\gamma\left(\frac{2\cos\theta}{w} + \frac{\cos\left(\min\left\{\theta+\alpha; 180°\right\}\right)}{h} + \frac{\cos\theta}{h}\right). \tag{3}$$

This expression may also be obtained by considering the change in total interfacial energy of the system as a result of the change in volume (Andersson *et al* 2001, Huang *et al* 2006).

3. Experimental

3.1. Chip fabrication and design

The polymer chip consists of two parts: an injection moulded main part of cyclic olefin-copolymer (COC) polymer (TOPAS grade 5013L-10) and a 0.254 mm extruded COC sheet (TOPAS grade 5013S-04) both from TOPAS Advanced Polymers GmbH, Frankfurt–Höchst, Germany. The main part features capillary microvalves laid out in parallel, each with its own luer-fitted inlet, see figure 2(*a*) for an overview photograph of the injection moulded chip part. Injection moulding was conducted on an Engel Victory 80/45 Tech injection moulder (ENGEL, Schwertberg, Austria). It was fitted with a rapid prototyped computer numerical control (CNC) milled aluminium master insert featuring the negative counter-part of the channel layout on one side of the injection moulding tool and a luer-layout counter-part with through-holes (Andresen *et al* 2010) on the other. To complete the chip, the injection

Table 1. Nominal geometries compared to the post fabrication geometries as determined by chip characterisation performed on a single chip. Note that the heights contain the added height of 23.9 μm from the welding process. See figure 2(*c*) for the schematic lay-out of the capillary microvalve.

	w [μm]		h [μm]	
Valve #	Nominal	Actual	Nominal	Actual
100/100	100	92	100	135
200/100	200	202	100	134
300/150	300	286	150	182
500/150	500	486	150	181
500/250	500	447	250	281

moulded part was bonded to the COC sheet using a Telsonic USP4700 ultrasonic welder (Telsonic, Erlangen, Germany).

The channel layout features eight sets of channels with capillary microvalves connecting separate luer fittings to a collective outlet, see figure 2(*a*). Each channel has a unique width and height (see table 1) and a capillary microvalve constructed by a 90° expansion towards the floor of the channel. See figure 2(*b*) for an SEM image of an injection moulded capillary microvalve and figure 2(*c*) for a 3D representation of a capillary microvalve. Energy directors used for the ultrasonic welding were 130 μm wide triangular prism shaped protrusions (apex angle = 60°) centered 500 μm from the channel sidewalls. The chip topography characterization was carried out using a Nova 600 NanoSEM (FEI, Eindhoven, Netherlands) for images and a PLu Neox 3D Optical Profiler (Sensofar-Tech, S.L, Terrassa, Spain) for topographic data.

3.2. Chip coating

To increase the robustness of the system when performing burst pressure measurements, the hydrophobicity of the COC was increased by coating both the injection moulded part and the COC sheet with a hydrophobic 1H,1H,2H, 2H-perfluorodecyltrichlorosilane (FDTS, CAS No 78560-44-8) layer using a gas phase multi-step deposition process, prior to bonding. While FDTS and analogous perfluoroalkylsilanes alone provide a hydrophobic coating on silicon (Mayer *et al* 2000, Ashurst *et al* 2003, Ashurst *et al* 2004), polymers require a metal oxide adhesion layer prior to deposition of FDTS (Kobrin *et al* 2005, Kobrin *et al* 2007). Otherwise, the contact angle with water may be rather low, depending on the substrate. For the present work, silicon dioxide was used as the adhesion layer. The deposition was performed at 35 °C in a MVD100 system from Applied Microstructures (San Jose, California). In brief, the system consists of a deposition chamber, vaporization chambers for the precursors and cylinders housing the different precursors, where the connections between precursor cylinders, vaporization chambers and deposition chamber are controlled by valves. The system is connected to a pump via the deposition chamber. Precursor is vaporized from the cylinders into the vaporization chambers. Once a set pressure in the vaporization chamber is reached, the precursor vapour is introduced into the deposition chamber by means of the pressure difference between vaporization chamber and deposition chamber. During the precursor introduction step and the subsequent reaction, no pumping on the chamber is performed. After the reaction is finished, the reaction chamber is pumped down and purged several times with nitrogen. Prior to the deposition, the sample surface is activated using a remote oxygen plasma generated from a plasma source in the MVD100 system. Subsequently, silicon dioxide and FDTS are deposited at 35 °C in two consecutive process steps. Silicon tetrachloride and water were used as precursors for silicon dioxide. The two precursors are introduced simultaneously and allowed to react for a given time. The simultaneous presence of the two precursors means that the layer thickness obtained in one reaction cycle depends on the partial pressures of the two precursors and the reaction time (Kobrin *et al* 2005). For formation of the FDTS-layer, FDTS and water are introduced simultaneously. The simultaneous action of FDTS and water allows for the deposition of a self-assembled monolayer (SAM) of the perfluoroalkylsilane (Mayer *et al* 2000). The advancing contact angle of water to FDTS-coated COC sheets was measured on a Krüss DSA10 Contact Angle Measuring System (Krüss GmbH, Hamburg) to 120 ± 2°. The advancing contact angle for uncoated COC is 96 ± 3°.

3.3. Bonding by ultrasonic welding

Ultrasonic welding is performed by applying vibrations through a transducer to an energy director that melts and welds two layers together, as illustrated in figure 3. Depending on the success of the welding there are two main outcomes; if too much energy is applied, polymer may flow into cavities, known as flash (figure 3 bottom left). Conversely if too little energy is deposited, the energy directors will not completely melt, leaving small gaps (figure 3 bottom right). In either case, there will be an increase in height due to the presence of the polymer welding seam. This height was estimated by first calculating the cross-sectional area of the triangular shaped energy directors pre-welding and correlating it to the cross-sectional area of the welded energy director, assuming that the volume of the polymer was conserved during welding. Dimensions of the pre- and post-welding energy directors were measured using a PLu Neox 3D Optical Profiler and an optical microscope, respectively. The post-welding height was calculated to be 23.9 ± 1.7 μm, assuming a square cross-sectional area of the welded energy director.

Ultrasonic welding was chosen over thermal bonding because thermal bonding is not applicable with the hydrophobic coating and because ultrasonic welding allows for easy bonding of large area channels. While large area bonding is possible with thermal bonding, e.g. by using a custom pressure plate (Kim *et al* 2007), it requires a custom pressure plate for each design and an aligning step for each chip, which makes this process more complicated.

3.4. Burst pressure measurements

Hydrostatic burst pressures were determined by slowly raising a water column (50 mL syringe without piston) above chip level using a Thorlabs LTS150 motorized stage (Thorlabs, Newton,

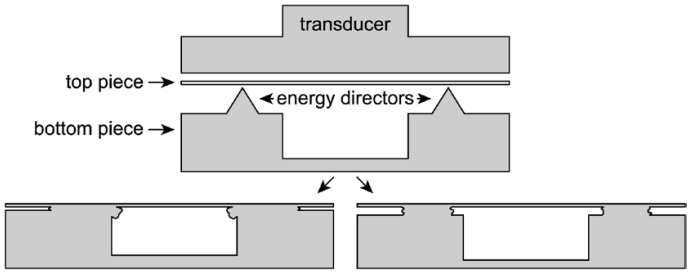

Figure 3. Cross sectional schematic of a channel before (top) and after ultrasonic welding (bottom left and right). The top part of the chip is pressed onto the bottom part with an ultrasonic transducer, which then vibrates to melt the energy directors. Depending on the amount of energy that is deposited via the transducer different outcomes will arise: Too much energy causes flash to form (bottom left) while too little energy causes a gap in the upper part of the channel (bottom right). In both cases, an added height results from the welding process.

NJ, USA). The water column was connected to the chip via tubing with luer fittings, resulting in a stable hydrostatic pressure. Before initiating a measurement, the chip was positioned so the surface vertical position matched that of the water surface. The syringe was then raised at 1 mm s^{-1} while the capillary microvalve was carefully monitored. Once the water advanced into the channel leading to the capillary microvalve, the stage was paused and the fluid allowed to pin at the capillary microvalve after which the stage was re-engaged. When the water burst through the capillary microvalve, the stage was stopped immediately and the height recorded. The syringe vertical position was then reset and after the meniscus had retracted past the capillary microvalve and the process was repeated for a total of three measurements per capillary stop. The chip was then rinsed and dried before another set of measurements was conducted amounting to a total of 6 measurements per chip. For every capillary microvalve, this experiment was repeated on 2–3 chips, resulting in a total of 12–18 measurements per capillary microvalve. An example of a single measurement can be seen in supplementary video 1 (stacks.iop.org/JMM/24/125007/mmedia). The burst pressures were calculated using $p = \rho g H$, where p is the calculated pressure, $\rho = 998\,\mathrm{kg\,m^{-3}}$, $g = 9.82\,\mathrm{m\,s^{-2}}$ and H is the measured height.

3.5. Numerical simulations

3.5.1. Model design. A numerical model for determining the capillary microvalve burst pressures was constructed on the basis of the geometry of the microfluidic chip with a pressure drop applied across the geometry (see figure 2(*d*)). Since steady state models with constant pressure drop was found to have convergence problems when the pressure drop was set to the approximate analytic burst pressure, a different approach had to be taken. The simulation was instead run in time-dependent mode with the initial interface position set at the channel expansion with a pressure drop increasing over time until bursting occurred. Because a capillary microvalve is an abruptly changing system when the valve bursts, a model coupled damping term was included in the expression for the pressure drop. This ensured that the unstable state was approached at a rate that minimized viscous and inertial effects, whilst elucidating the minimum pressure required for bursting (i.e. the burst pressure). Since a higher percentage of the model volume will be occupied with water as the pressure drop increases, the pressure drop dampening term was negatively proportional to the average water content.

The rationale of the model coupling is that the pressure drop increases more slowly when the interface expands; as the burst pressure is reached and the valve starts bursting, the pressure drop is reduced as a result of the increasing volume fraction occupied by water. Yet, regardless of the reduced pressure, the interface will continue to grow due to the smaller pressure required to expand the now larger (and less curved) interface.

3.5.2. Model description. The numerical analysis of the capillary microvalves was conducted using the 'Laminar Two-Phase Flow, Level-Set' package in COMSOL Multiphysics 4.3a (COMSOL A/S, Kgs. Lyngby, Denmark). The governing equations were the Navier–Stokes equation and the reinitialized LS function, $\phi_{\mathrm{ls}}(r)$, used to track the interface and interpolate the material properties (Olsson and Kreiss 2005, COMSOL 2012). The reinitialized LS function operates on an interface of finite thickness with intermediate properties of the two phases. This makes the LS method ideal for calculating curvatures which is crucial for estimating the Young–Laplace pressure, but weak at conserving mass and tracking the meniscus position (e.g. the dynamic contact angle). Properties, such as the density is determined by $\rho = \phi_{\mathrm{ls}}(r)\,\rho_{\mathrm{air}} + \left(1 - \phi_{\mathrm{ls}}(r)\right)\rho_{\mathrm{water}}$, where $\phi_{\mathrm{ls}}(r) = 1$ for 0% water and $\phi_{\mathrm{ls}}(r) = 0$ for 100% water (COMSOL 2012).

The time-dependent pressure drop across the geometry (see figure 2(*d*)) was defined as $p_1(t) = \Delta p(t) + p_0$ where

$$\Delta p(t) = p_{\mathrm{start}} + \alpha t - \beta \overline{\phi_{\mathrm{ls}}}(t) - p_0\,. \tag{4}$$

Here, p_{start} was set larger than the capillary pressure of the inlet channel of the geometry to avoid backwards interface movement. Effectively, $\overline{\phi_{\mathrm{ls}}}(t) = \mathrm{Volume}_{\mathrm{water}}(t)\,/\,\mathrm{Volume}_{\mathrm{geometry}} = \int_V \phi_{\mathrm{ls}}(r,t)\,\mathrm{d}r \Big/ \int_V \mathrm{d}r$. The pressure drop is thus reduced as more volume is occupied by water, resulting in a dampening of the interface advance. The ambient pressure, p_0, was set to 0, since it cancels out and hence has no contribution to the pressure drop. As shown in the supplementary information (stacks.iop.org/JMM/24/125007/mmedia), appropriate

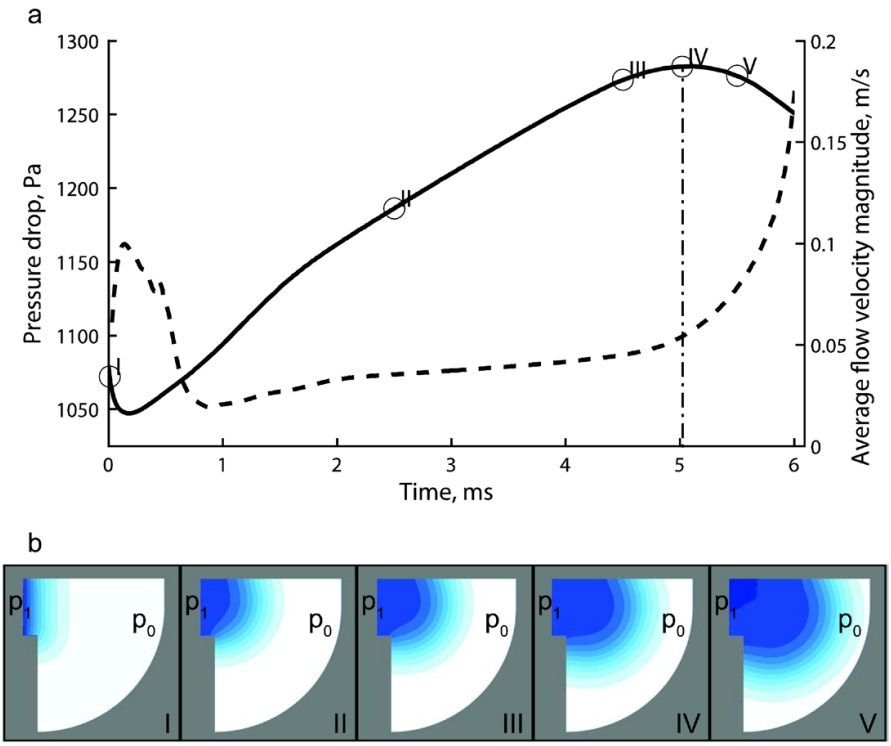

Figure 4. (*a*) Pressure drop, controlled by the model coupling equation (4), and average flow velocity magnitude developing over time. The burst pressure is marked by a vertical dash-dot line. (*b*) (I–V) Contour plots of fraction of water (ϕ_{ls}) spanning [0:1] in steps of 0.1, dark blue being 100% water. (*b*)(I) Initial flat interface with forced contact angle = 90° relaxes rapidly. (*b*)(II) Stabilised and linearly growing interface. (*b*)(III) Interface immediately prior to bursting. (*b*)(IV) Bursting meniscus. Note the concentration of water at the pinning corner is >90%. (*b*)(V) Rapidly expanding meniscus, where the damping term reduces the pressure drop.

values for the pressure ramping rate (α) and the damping range (β) were found to be 50.000 Pa s^{-1} and 200 Pa, respectively. The model was generally found to be robust in terms of these parameters (see table S2 in the supplementary information (stacks.iop.org/JMM/24/125007/mmedia)). However, the simulation time could be significantly prolonged if the α / β ratio was decreased in equation (4). On the other hand, a too high ratio would cause the dampening term to be negligible, complicating the determination of the burst pressure.

To achieve faster convergence, 'transformer oil' ($\rho = 0.879$ g cm^{-3}, $\eta = 20.8$ mPa s) with surface tension equal to that of an air–water interface $(\gamma_{water/air} = 72.89$ mN m$^{-1})$ was used as a substitute for air. This does not take into account the compressibility of air, however, due to the nature of the simulation it is not expected to affect the results. Additionally, the increased density and viscosity of oil will affect the inertial component, however, since the model is already dampened by equation (4) this is not expected to influence the burst pressure. Parameters not listed above used in the COMSOL model are stated in the supplementary information (stacks.iop.org/JMM/24/125007/mmedia), section 1.4.

The inlet channel length, l, was chosen to accommodate the relaxation of the initial (flat) interface (see figure 2(*d*)). Likewise, the outlet chamber was made sufficiently large for the meniscus to burst without interacting with the outlet boundary. The central symmetry plane was exploited to minimise computational demands, see figure 2(*d*).

4. Results and discussion

First a validation of the numerical model including the *modus operandi* of determining the burst pressure is presented. Then, the fabrication process is evaluated and finally the experimental burst pressures are presented and compared to the numerically simulated and analytically calculated results.

4.1. Numerical model analysis

To elucidate that the model coupled dampening term, equation (4), used to control the pressure drop in the simulation, functioned as intended, the pressure drop developing over time is plotted in figure 4(*a*). As evident, the two opposing terms in equation (4) result in three stages: interface relaxation (figure 4(*a*)(I)), linear pressure rise (figure 4(*a*)(II + III)) and bursting (figure 4(*a*)(IV)). To study the behaviour of the virtual interface during the simulation and its interaction with the model geometry, contour plots of fraction-of-water on the symmetry

plane (see figure 2(*d*)) are plotted for the selected times in figure 4(*b*). The readily recognisable peak in figure 4(*a*) and the on-going bursting illustrated figure 4(*b*)(V) confirm that the constructed model coupling works as intended and does not prevent continued bursting of the valve.

The fact that the interface has a finite width that spans to both sides of the pinning corner at all times may seem counter intuitive from an experimentalists point of view, but this is intrinsic for the LS method . In most analytical expressions, the temporal meniscus position defines the burst pressure, whereas in simulations using the LS method, the exact meniscus position is not available (figures 2(*d*) and 4(*b*)). Therefore a different approach for determining the burst pressure has to be taken. In this study, the maximum pressure drop that can be applied without causing a rapid expansion of the interface defines the burst pressure (full line in figure 4(*a*)). To further illustrate the interface dynamics, the average flow velocity magnitude is plotted versus time (dashed line in figure 4(*a*)). It is evident that the interface has rapid movements during the initial interface relaxation and again when bursting occurs. These steep changes in flow velocity within a single ms support the assumption that the added inertia of the transformer oil does not influence the simulation. To stress the importance of the dampening term, an identical simulation was run with no dampening ($\beta = 0$). From the data (figure S1 (stacks.iop.org/JMM/24/125007/mmedia)) it is clear that no burst pressure can be determined either from $p(t)$ or from the average flow velocity magnitude. Without dampening, the burst pressure could not be estimated in a reproducible manner. We propose that this approach may generally assist when determining critical variables in abruptly changing systems.

To validate the numerical model, a set of simple axial symmetrical geometries was analysed. Contrary to the complex rectangular geometries, the burst pressures of the cylindrical geometries have a closed-form analytical solution, see supplementary information (stacks.iop.org/JMM/24/125007/mmedia). From supplementary figure S3 (stacks.iop.org/JMM/24/125007/mmedia) it is evident that the numerical simulations consistently underestimate the analytically calculated burst pressures by 6.7%. As discussed by Olsson and Kreiss, the diffusive representation of the interface results in an attraction between the interface and the walls when the distance is close to the interface thickness (Olsson and Kreiss 2005). This effect may be the cause of the consistent burst pressure undershooting of the LS based model. Obviously, this effect depends in part on the geometry and the impact on the numerical burst pressure varies accordingly. In light of the intrinsic limitations of the LS method, such as the diffuse interface definition and the poor conservation of mass which may destabilise the pinned interface, the consistent underestimation of the burst pressure by 6.7% is acceptable for most applications.

Figure 5 shows numerical simulations as well as analytical calculations (equation (3)) of the burst pressure in structures illustrated in figures 1(*a*) and 2(*c*) for $50\,\mu\text{m} \le w \le 500\,\mu\text{m}$ and $25\,\mu\text{m} \le h \le 281\,\mu\text{m}$ (details given in the supplementary information (stacks.iop.org/JMM/24/125007/mmedia)). Again, a consistent underestimation of the numerical burst pressure is observed compared to the analytically calculated result,

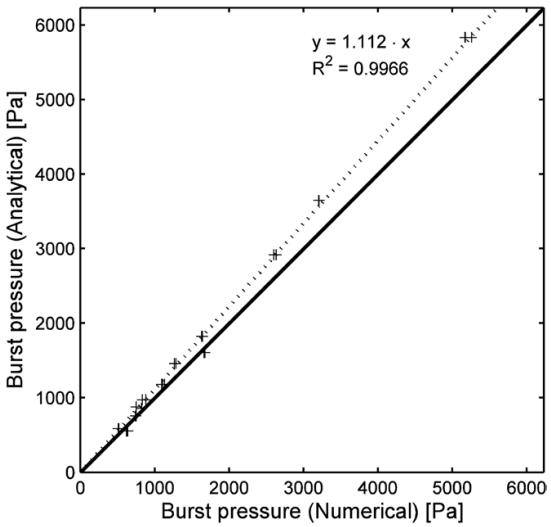

Figure 5. Analytically calculated burst pressures of all nominal and measured geometries plotted versus numerically determined burst pressures (+) of the same geometries (see supplementary information (stacks.iop.org/JMM/24/125007/mmedia), for a complete list of geometries and results). The solid line represents $y = x$ and the dashed line is a linear fit to the data points.

except that the difference is larger (11.2%). This behaviour can be explained by the more complex geometry, which is more taxing for the numerical simulations and also causes the analytical predictions to be less accurate, since a complete solution does not exist. As stated above, we believe that this is an acceptable error for most applications, such as modelling burst pressures of complex microfluidic systems prior to fabrication.

The R-squared values (>0.995) for the linear fits of the correlations between the numerically modelled and analytically calculated burst pressures (see figures 5 and S3 (stacks.iop.org/JMM/24/125007/mmedia)) suggest that the model is robust and precise for a wide range of geometries. Furthermore, the similarity in underestimating between the cylindrical and rectangular geometries shows that the model performs equally well with simple and complex problems.

4.2. Geometrical characterisation of chips

A total of eight capillary microvalve geometries (nominal width/nominal height in μm) were chosen for investigation; 50/25, 50/50, 100/50, 100/100, 200/100, 300/150, 500/150 and 500/250, see figure 2(*b*) for an SEM image and figure 2(*c*) for the schematic lay-out of a single capillary microvalve. It was not possible to conduct experiments on the smallest geometries (50/25, 50/50 and 100/50) due to polymer blocking the channels after ultrasonic welding.

The micro milling and injection moulding added some error to the nominal geometries chosen, but for clarity the labels for the different capillary stops have been kept in the 'nominal width/nominal height' format. The actual widths

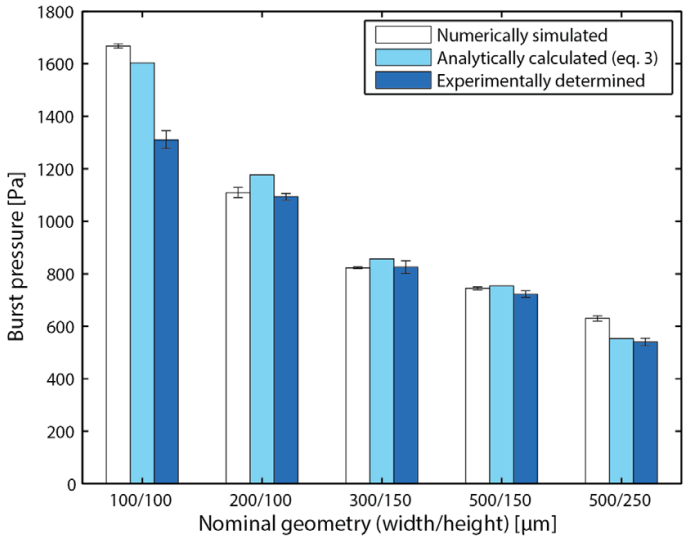

Figure 6. Numerically simulated, analytically calculated, and experimentally determined burst pressures of the selected capillary microvalve geometries. Light blue columns represent the burst pressures calculated from the analytical expression (equation (3)). White columns denote the numerically simulated burst pressures, n = 2, 3, 2, 3 and 3 for 100/100, 200/100, 300/150, 500/150 and 500/250, respectively. Dark blue columns denotes the experimentally determined hydrostatic burst pressures, n=18 for 100/100 and 500/250 and n = 12 for 200/100, 300/150 and 500/150. Error bars represent the sample standard deviation.

and heights deviate 1.2–10.7% from their nominal values as determined by the chip characterisation (see table 1 for geometries). The majority of the error comes from the milling process, which was confirmed by confocal microscopy measurements of the master insert. The master insert dimensions differed on average less than 1 μm from the dimensions measured on the moulded chip. The polymer filling/shrinkage associated with injection moulding of 5013L-10 is negligible (Tanzi *et al* 2012), which is also evident from the SEM image in figure 2(*b*). The average arithmetic mean roughness (Sa) of the chip bottom part surface was measured to 0.6 μm.

The actual widths and heights have been used as input in the analytical expressions as well as the numerical simulations when comparing with the experimentally determined burst pressures.

4.3. Fabrication process

The fabrication process can be split in two. First there is the rapid prototyping, which takes 3–4 h of CNC milling on average per design. Then there is the two-step manufacturing of the chip itself, which consists of injection moulding and ultrasonic welding. The injection moulder has an isothermal cycle time of about 50 s per chip and the (manual) ultrasonic welding takes 30 s on average per chip. The welding itself takes about 5 s, the rest is mounting, removal of protective films and release of the chip. This amounts to 80 s for a standard chip fabricated using this process. For the chip presented in this paper a coating of the COC parts was needed, to be able to get robust measurements. This is a batch process that takes about 60 min. The MVD holds 48 chips at a time amounting to 85 s/chip. The total average fabrication time for the chip presented in this study is thus about 155 s per chip. We typically fabricated about 100 chips per run.

Injection moulding is very fast compared to many other published systems, where each chip is often custom CNC milled or cast in PDMS, which takes up to 4 h, and on par with other micro moulding techniques such as thermoforming and hot embossing. Ultrasonic welding is rapid compared to, e.g. thermal bonding and more durable and less prone to decay than, e.g. bonding using adhesive layers. As the bulk of the chip is not heated, pre-loading of dried or jellified reagents is possible, which is of high relevance to Point-of-Care devices (Sun *et al* 2013). The local heating is applied for ~0.1 s leading to turn-over times of ca. 5 s per welding (excluding mounting and release), which is considerably shorter than other common bonding processes such as thermal bonding and plasma assisted bonding (Bu *et al* 2013). This makes ultrasonic welding very desirable for μTAS rapid prototyping and mass production. The added height imposed by the ultrasonic welding and milling process may be of concern; however, this undesired addition can be avoided by optimising the milling process and energy director design and welding process. Since ultrasonic welding does not have the same cross material compatibility as, e.g. adhesive bonding, the most common practise is to weld together like materials. It does, however, allow for bonding through thin-film layers (e.g. Teflon coatings as demonstrated in this study) or thin sheets of other polymer types (Truckenmüller *et al* 2006a, Bu *et al* 2011).

4.4. Experimental burst pressures

Figure 6 shows the average determined hydrostatic burst pressures for each microvalve geometry compared to the

analytically calculated and numerically simulated values. In general, the experimentally determined burst pressures are lower than the analytically calculated results with larger relative deviations for larger burst pressures, ranging from 2.2% to 18%. There is good reproducibility of the experimental data with regards to repetitions on the same chip and repetitions in-between chips, with a mean coefficient of variation of 2.2%. The large deviation from the analytical and numerical values for the 100/100 capillary microvalve can be explained by incomplete polymer melting during ultrasonic welding: The small gaps left by ultrasonic welding (see figure 3 bottom right) were observed to have lower capillary pressure than the actual capillary microvalve. This led to a premature bursting of the microvalve and hence a lower than expected capillary burst pressure (see figure 6). Disregarding the 100/100 microvalve, a good correlation between the experimentally determined and analytically calculated burst pressures is observed with an average deviation of 4.5%.

Although the analytically calculated results deviate slightly from the experimentally determined burst pressures, they do show that over the investigated aspect ratios and dimensions, equation (3) can on average predict the experimentally determined burst pressures with an accuracy of 4.5%. The small standard deviations on the experimental results demonstrate that injection moulded and ultrasonically welded chips provide excellent reproducibility and stable results. For the smallest geometries it was not possible to produce functional channels due to polymer blocking the channels after bonding by ultrasonic welding (figure 3 bottom left). However, as mentioned it is expected that this can be avoided by optimising the chip design, master insert quality, the energy director geometry and bonding parameters. The chip design used in this study had a high local density of energy directors, which complicates the ultrasonic welding. Micromilling is also not ideal for producing small (~50 μm) structures, because it is difficult to maintain precise alignment upon tool switching with the machines used in the present work.

4.5. Numerically simulated burst pressures

As previously described, the numerical simulations were carried out for both nominal- and actual (measured) chip dimensions using starting pressures (p_{start}) lying in-between the analytically calculated capillary pressure of the inlet channel and the analytically calculated capillary burst pressure. For each of the geometries, two additional control simulations were conducted by using starting pressures of approximately 90% and 70% of the predicted burst pressure of the preceding simulation.

As can be observed in figure 6, the numerical estimates fit well with the experimental values, except for the 100/100 geometry. The numerical model does, however, show good agreement with the analytical estimate for this geometry. When comparing figures 5 and 6, there is a general trend of the numerical simulations to deviate more from the analytically calculated results for large burst pressures, while for small burst pressures there is a better correlation. From the linear fit in figure 5 it can be seen that the numerical model is a good alternative to the analytical expression. It is also evident that the width/height aspect ratio does not influence the results for the investigated range of geometries.

In summary, the numerical model overestimated the experimental burst pressures by 5.2% on average, which, together with the demonstrated robustness of our numerical model indicates that the LS method is promising for burst pressure predictions of more complicated geometries. However, further studies need to be undertaken to confirm this.

5. Concluding remarks

In this work, two aspects of going from rapid prototyping to pilot (mass) production were investigated:

(1) We have presented an all-polymer chip system fabricated using a rapid prototyped master insert for injection moulding and ultrasonic welding, which can be directly implemented in mass production. The chip has a short production time of 80 s per chip (155 s including coating assuming a batch of 48 chips).
(2) A numerical tool was developed to aid in rapid prototyping by predicting geometries required to achieve capillary microvalves with a desired burst pressure.

The fabrication process and numerical tool were validated via investigations of geometrical capillary microvalves. In both cases the numerically simulated and analytically calculated burst pressures were found to be within 5.2% and 4.5% of the experimentally determined burst pressures, respectively. The numerical model was further validated, by modelling a more simple geometry for which a complete analytical expression exists. The LS approach was found to be precise and robust with regards to geometry and model parameters and The included dampening term may also be beneficial to others when simulating unstable or abruptly changing systems. The data presented in this study supports the idea of using numerical simulations as a tool in rapid prototyping to predict burst pressures of complex geometries before physically crafting the prototypes, ideally reducing the number of iterations needed from idea to functioning prototype to final product.

The ability to tailor and mass-produce capillary microvalves with a quantitatively predictable behaviour in all-polymer microfluidic systems is important and beneficial for many medical, biological and chemical applications.

Acknowledgments

This work is supported by the Danish Council for Strategic Research through the Strategic Research Center PolyNano (Grant No. 10-092322/DSF).
We would like to acknowledge Minqiang Bu, Department of Photonics Engineering, Technical University of Denmark, and Ivan R Perch-Nielsen, DELTA, Hørsholm, Denmark, for sharing experience in micro-fabrication and ultrasonic welding, and Fridolin Okkels, Department of Micro- and Nanotechnology for discussions on COMSOL related topics.

References

Abhari F, Jaafar H and Yunus N A 2012 A comprehensive study of micropumps technologies *Int. J. Electrochem. Sci.* **7** 9765–80

Andersson H *et al* 2001 Hydrophobic valves of plasma deposited octafluorocyclobutane in DRIE channels *Sensors Actuators* B **75** 136–41

Andresen K Ø *et al* 2010 Injection molded chips with integrated conducting polymer electrodes for electroporation of cells *J. Micromech. Microeng.* **20** 055010

Ashurst R W *et al* 2004 Improved vapor-phase deposition technique for anti-stiction monolayers *Proc. SPIE* **5342** 204–11

Ashurst W R, Carraro C and Maboudian R 2003 Vapor phase anti-stiction coatings for MEMS *IEEE Trans. Device Mater. Reliab.* **3** 173–8

Attia U M, Marson S and Alcock J R 2009 Micro-injection moulding of polymer microfluidic devices *Microfluid Nanofluidics* **7** 1–28

Becker H and Gärtner C 2008 Polymer microfabrication technologies for microfluidic systems. *Anal. Bioanal. Chem.* **390** 89–111

Begolo S, Colas G, Viovy J-L and Malaquin L 2011 New family of fluorinated polymer chips for droplet and organic solvent microfluidics *Lab Chip* **11** 508–12

Bouaidat S *et al* 2005 Surface-directed capillary system; theory, experiments and applications *Lab Chip* **5** 827–36

Bu M *et al* 2013 A temperature control method for shortening thermal cycling time to achieve rapid polymerase chain reaction (PCR) in a disposable polymer microfluidic device *J. Micromech. Microeng.* **23** 074002

Bu M, Perch-Nielsen I R, Sun Y and Wolff A 2011 A microfluidic control system with re-usable micropump/valve actuator and injection moulded disposable polymer lab-on-a-slide *Proc. 16th Int. Solid-State Sensors, Actuators Microsystems Conf. IEEE (Beijing, Jun. 2011)* pp 1244–7

Chibbaro S *et al* 2009 Capillary filling in microchannels with wall corrugations: a comparative study of the Concus–Finn criterion by continuum, kinetic, and atomistic approaches *Langmuir* **25** 12653–60

Cho H, Kim H-Y, Kang J Y and Kim T S 2007 How the capillary burst microvalve works *J. Colloid. Interface Sci.* **306** 379–85

Delamarche E *et al* 1998 Microfluidic networks for chemical patterning of substrates: design and application to bioassays *J. Am. Chem. Soc.* **120** 500–8

den Dulk R C *et al* 2012 Magneto-capillary valve for integrated purification and enrichment of nucleic acids and proteins *Lab Chip* **13** 106–18

Duffy D C *et al* 1999 Microfabricated centrifugal microfluidic systems: characterization and multiple enzymatic assays *Anal. Chem.* **71** 4669–78

Dyson D C 1988 Contact line stability at edges: comments on Gibbs's inequalities *Phys. Fluids* **31** 229

Gerlach D, Tomar G, Biswas G and Durst F 2006 Comparison of volume-of-fluid methods for surface tension-dominant two-phase flows *Int. J. Heat Mass Transf.* **49** 740–54

Gibbs J W 1906 *Scientific Papers of J. Willard Gibbs...: Thermodynamics* (Longmans, Green and Company)

Giboz J, Copponnex T and Mélé P 2007 Microinjection molding of thermoplastic polymers: a review *J. Micromech. Microeng.* **17** R96–109

Huang W, Liu Q and Li Y 2006 Capillary filling flows inside patterned-surface *Microchannels. Chem. Eng. Technol.* **29** 716–23

Kim D S *et al* 2007 Collapse-free thermal bonding technique for large area microchambers in plastic lab-on-a-chip applications *Microsyst. Technol.* **14** 179–84

Kobrin B, Dangaria N and Chinn J 2007 Low temperature nanolayers of metal oxides by MVD™ *Tech. Proc. 2007 NSTI Nanotechnol. Conf. Trade Show* vol **4** pp 575–7

Kobrin B, Nowak R, Yi R C and Chinn J 2005 Controlled deposition of silicon-containing coatings adhered by an oxide layer *US Patent* US20050271809 A1

Manz A, Graber N and Widmer H M 1990 Miniaturized total chemical analysis systems: a novel concept for chemical sensing *Sensors Actuators* B **1** 244–8

Matteucci M *et al* 2013 Fabrication and characterization of injection molded multi level nano and microfluidic systems *Microelectron. Eng.* **111** 294–8

Mayer T M *et al* 2000 Chemical vapor deposition of fluoroalkylsilane monolayer films for adhesion control in microelectromechanical systems *J. Vac. Sci. Technol. B Microelectron. Nanom. Struct.* **18** 2433

Oh K W and Ahn C H 2006 A review of microvalves *J. Micromech. Microeng.* **16** R13–39

Olsson E and Kreiss G 2005 A conservative level set method for two phase flow *J. Comput. Phys.* **210** 225–46

Sun Y *et al* 2013 Pre-storage of gelified reagents in a lab-on-a-foil system for rapid nucleic acid analysis *Lab Chip* **13** 1509–14

Sussman M and Puckett E G 2000 A coupled level set and volume-of-fluid method for computing 3D and axisymmetric incompressible two-phase flows *J. Comput. Phys.* **162** 301–37

Tanzi S *et al* 2012 Fabrication of combined-scale nano- and microfluidic polymer systems using a multilevel dry etching, electroplating and molding process *J. Micromech. Microeng.* **22** 115008

Thio T H G *et al* 2013 Theoretical development and critical analysis of burst frequency equations for passive valves on centrifugal microfluidic platforms *Med. Biol. Eng. Comput.* **51** 525–35

Truckenmüller R *et al* 2006a An ultrasonic welding based process for building up a new class of inert fluidic microsensors and -actuators from polymers *Sensors Actuators* A **132** 385–92

Truckenmüller R *et al* 2006b Micro ultrasonic welding: joining of chemically inert polymer microparts for single material fluidic components and systems *Microsyst. Technol.* **12** 1027–9

Waldbaur A, Rapp H, Länge K and Rapp B E 2011 Let there be chip—towards rapid prototyping of microfluidic devices: one-step manufacturing processes *Anal. Methods* **3** 2681

Zhao B, Moore J S and Beebe D J 2002 Principles of surface-directed liquid flow in microfluidic channels *Anal. Chem.* **74** 4259–68

Zimmermann M, Hunziker P and Delamarche E 2008 Valves for autonomous capillary systems *Microfluid Nanofluidics* **5** 395–402

Fabrication and Modelling of Injection Moulded All-Polymer Capillary Microvalves for Passive Microfluidic; Journal of Micromechanics and Microengineering; K. Kistrup, C.E. Poulsen, P.F. Østergaard, K. B. Haugshøj, R. Taboryski, A. Wolff and M. F. Hansen, Department of Micro- and Nanotechnology, Technical University of Denmark, mikkel.hansen@nanotech.dtu.dk

1 Supplementary information

1.1 Dimensions of simulated geometries

Table S1 contains a list of all capillary microvalve geometries simulated using the constructed COMSOL model, the starting pressures, the simulated burst pressures and the analytically calculated burst pressures.

Table S1 Geometries used for numerical calculations. Note that both nominal geometries and post fabrication geometries are included. The configurations are sorted by the analytically calculated burst pressure.

Width [µm]	Height [µm]	Starting pressure [Pa]	Numerical burst pressure [Pa]	Analytical burst pressure [Pa]
447	281	300,0	620,0	552,8
447	281	400,0	640,0	552,8
447	281	400,0	630,0	552,8
500	250	400,0	508,9	583,2
500	250	450,0	518,2	583,2
500	250	300,0	508,1	583,2
486	181	400,0	748,0	753,9
486	181	500,0	738,0	753,9
486	181	400,0	748,0	753,9
286	182	500,0	820,0	857,0
286	182	600,0	825,0	857,0
500	150	600,0	748,0	874,8
500	150	600,0	748,0	874,8
500	150	500,0	748,0	874,8
300	150	800,0	831,1	972,0
300	150	700,0	878,0	972,0
202	134	1000,0	1130,0	1176,8
202	134	900,0	1108,0	1176,8
202	134	800,0	1091,0	1176,8
200	100	1050,0	1265,8	1458,0
200	100	1100,0	1282,7	1458,0
92	135	1400,0	1673,7	1603,9
92	135	1200,0	1662,0	1603,9
100	100	1600,0	1630,2	1822,5
100	100	1500,0	1630,3	1822,5
100	100	1650,0	1643,3	1822,5
100	50	2200,0	2601,7	2916,0
100	50	2200,0	2631,8	2916,0
50	50	2850,0	3205,3	3645,0
50	50	2800,0	3210,0	3645,0
50	25	4700,0	5177,0	5832,0
50	25	4500,0	5172,0	5832,0
50	25	4700,0	5258,0	5832,0

1

Fabrication and Modelling of Injection Moulded All-Polymer Capillary Microvalves for Passive Microfluidic; Journal of Micromechanics and Microengineering; K. Kistrup, C.E. Poulsen, P.F. Østergaard, K. B. Haugshøj, R. Taboryski, A. Wolff and M. F. Hansen, Department of Micro- and Nanotechnology, Technical University of Denmark, mikkel.hansen@nanotech.dtu.dk

1.2 Undampened model simulation

To elucidate the importance of the dampening term an identical simulation to the one run in Fig. 4a was conducted, where β = 0 *i.e.* without the dampening term (Fig. S1). It is evident that there is no correlation between the bursting pressure and the average flow velocity magnitude (*cf.* Fig. 4a). The burst pressure could not be determined from Fig. S1 in a reproducible fashion.

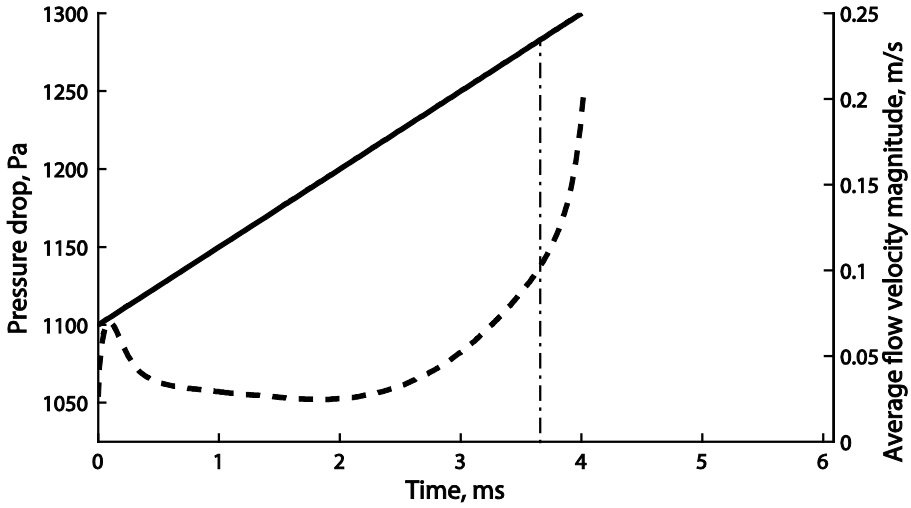

Fig. S1 Pressure drop, controlled by the model coupling Equation (3.1) with β = 0, and average flow velocity magnitude developing over time. The bursting pressure estimated with dampening is marked by a vertical dashed-dot line in the figure.

1.3 Model validation using an axial symmetrical geometry

To validate the developed COMSOL model and the applicability of the Level-Set method for burst pressure determination, simulations were conducted on geometries having axial symmetry. The two major differences between the rectangular capillary microvalves characterised in this study and these cylindrical geometries are the lack of corners on the pinning edge and the fact that an exact analytical expression can be constructed for the cylindrical microvalves. The analytical burst pressures, $p_{burst,cyl}$, can by geometric considerations be expressed using the Young-Laplace equation as

$$p_{burst,cyl} = -4\gamma \frac{\cos(\min\{\theta + \alpha; 180°\})}{D}. \qquad \textbf{(1.1)}$$

where D is the diameter of the capillary. Similarly to the rectangular capillary microvalves characterised in this paper, the expansion angle, α, was kept constant at 90°and the contact angle, θ, was set to 120°. Fig. S2 shows the axial symmetrical COMSOL model. The inlet and outlet are denoted by wireframes, walls are shown in grey and the isosurface represents 50% water content ($\phi_{ls} = 0.5$).

Fabrication and Modelling of Injection Moulded All-Polymer Capillary Microvalves for Passive Microfluidic; Journal of Micromechanics and Microengineering; K. Kistrup, C.E. Poulsen, P.F. Østergaard, K. B. Haugshøj, R. Taboryski, A. Wolff and M. F. Hansen, Department of Micro- and Nanotechnology, Technical University of Denmark, mikkel.hansen@nanotech.dtu.dk

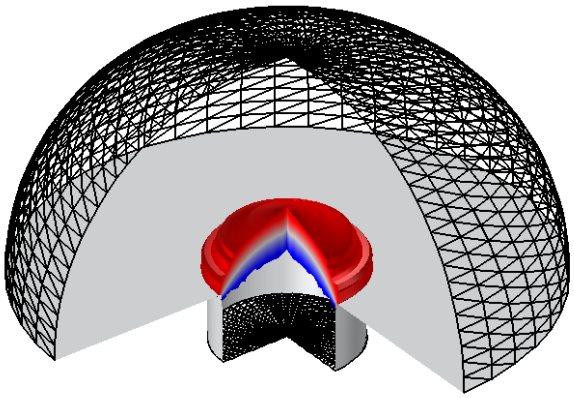

Fig. S2 Cylindrical capillary microvalve. Fine and coarse wireframes are inlet and outlet, respectively, grey surfaces are walls with contact angle θ and the volume filling denotes elements with $\phi_{ls} = [0.25, 0.75]$ where the blue colour denotes higher water content.

Simulation data for 24 geometries of diameter 30 µm to 260 µm is plotted in Fig. S3.

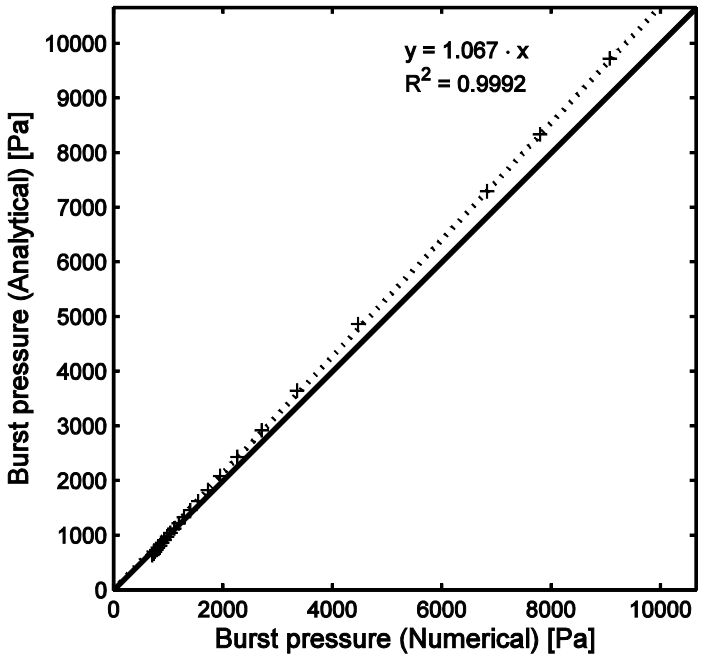

Fig. S3 Analytically calculated burst pressures of cylindrical geometries plotted versus numerically determined burst pressures (+) of the same geometries. The solid line represents $x = y$ and the dashed line is a linear fit of the data points.

It is evident that the trend of underestimating at higher burst pressures is similar to that observed for the rectangular geometries, see Fig. S3 and Fig. 5.

Fabrication and Modelling of Injection Moulded All-Polymer Capillary Microvalves for Passive Microfluidic; Journal of Micromechanics and Microengineering; K. Kistrup, C.E. Poulsen, P.F. Østergaard, K. B. Haugshøj, R. Taboryski, A. Wolff and M. F. Hansen, Department of Micro- and Nanotechnology, Technical University of Denmark, mikkel.hansen@nanotech.dtu.dk

The R-squared value of 0.9992 for the linear fit of the correlation between the numerically modelled and analytically calculated burst pressures suggests that the model is robust and precise for a wide range of geometries. Furthermore, the similarity in underestimating between the cylindrical and rectangular geometries shows that the model performs equally with simple and complex problems. As mentioned in Section 4.1, the diffusive representation of the interface results in an attraction between the interface and the walls when the distance is close to the interface thickness (Olsson and Kreiss 2005).

1.4 Additional model parameters

To avoid interactions between the pinned interface and the outlet of the model, the circular section, centered on the pinning corner (see Fig. 2d), was set to be larger than$2.2 \times h$ (diameter for cylindrical model). Similarly, the inlet capillary length, *l*, was set to 25 µm. The interface thickness parameter was set to half of the maximum element size (default setting in COMSOL), resulting in an interface thickness of 15.65 µm. Memory consumption and computational demands were minimised by using a minimum mesh element size of 7.83 µm and applying stop condition to terminate the simulation as soon as the average water content on the outlet boundary exceeded 50%, $\overline{\phi_{ls,outlet}} \geq 0.5$. The time dependent solver was set to extract data every 10 µs and was allowed to run for a total of 50 ms. In this time span, bursting always occurred, and the model was hence terminated by the stop condition.

As mentioned in the main text, the values used for the pressure ramping rate (α) and the damping range (β) were 50.000 Pa/s and 200 Pa, respectively. Examples simulations with other values for these two parameters are listed in Table S2.

Table S2 Twin simulations of the rectangular geometry using alternative values for α and β and the resulting numerical pressure.

α [Pa/s]	β [Pa]	Numerical burst pressure [Pa]	Analytical burst pressure [Pa]
50000	300	831.1	728.9
75000	300	878.0	728.9
25000	200	1586.8	1457.8
50000	200	1604.2	1457.8
50000	100	3205.3	2915.6
75000	100	3210.0	2915.6

5

Paper 2: Tongue-and-groove energy directors for microfluidics

Motivated by the relatively high variation in bursting pressure of the capillary microvalves presented in Chapter 4, and to further improve on the applicability of ultrasonic welding for microfluidic systems, an additional energy director type was developed. Specifically, tongue-and-groove energy directors (ED) were adapted and miniaturised for bonding a multiphase sample preparation system[4]. Tongue-and-groove EDs are a special case of butt-joint energy directors and have been extensively applied for polymer fusion of macroscopic pieces due to their high strength[166]. For microfluidics another significant advantage of the tongue-and-groove EDs is that that "height" of the fused piece is easily controlled and is not affected by variations in the bonding process to the same degree as the butt-joint EDs. Additionally, since the tongue-and-groove pieces is complimentary with high precision, the tongue-and-groove bonding has build in alignment with equally high precision. The two ED designs and welding seams are compared in Figure 5.1.

One limitation of tongue-and-groove EDs compared to butt-joint EDs is the fact that a structured piece is used for lidding, which also needs to be fabricated (injection moulded) specifically to mate with the main polymer piece. This is undoubtedly more expensive than using a roll-to-roll extruded foil. To circumvent this, a new independent tongue-and-groove EDs is proposed[a] which allows for using foil as one half of the tongue-and-groove fusion. As illustrated in Figure 5.2, the independent tongue-and-groove EDs work by combining the tongue and grove in one unified structure. Obviously, since no complimentary parts are used in the fusion, the independent tongue-and-groove EDs do not have included alignment of the fused pieces.

[a] We have yet to realise and test this design.

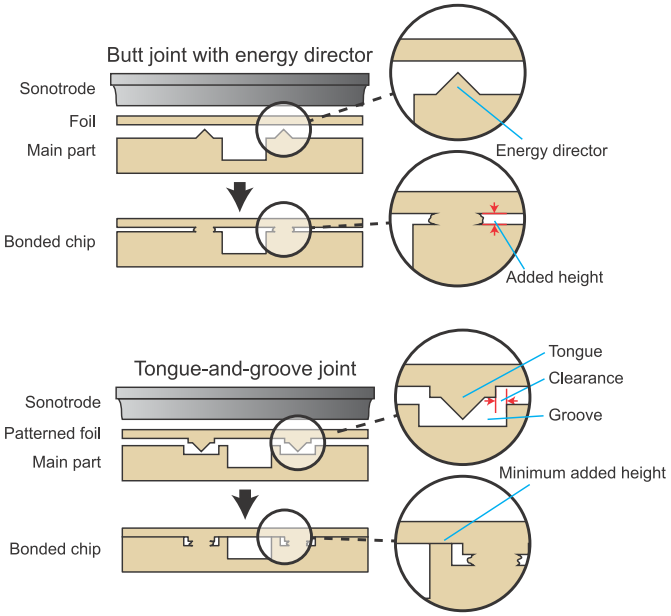

Figure 5.1: (top) Scheme of the standard butt joint. Please note the added height and gap from welding. (bot) Scheme of tongue-and-groove joint. No additional height is added from the fusion. Figures are adapted and modified from Kistrup *et. al* 2014[4].

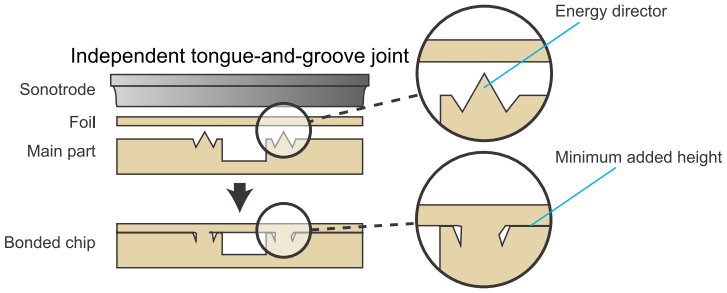

Figure 5.2: Proposed independent tongue-and-groove EDs. Figure is created from figures adapted from Kistrup *et al.* (2015)[4].

5.1 Description of contribution

Except from presenting the tongue-and-groove EDs in a microfluidic context, paper 2 also demonstrated ultrasonic welding (butt joint EDs) of a large area shallow chamber (1.8 $cm^2 \times 150$ µm) for storing, thermo-cycling and imaging of droplets. As with other devices of this PhD-project, for microfluidic fabrication, methods relevant to industrial mass production and commercialisation was applied: injection moulding and ultrasonic welding. The chip was designed to enable single or multiple fluorescence signals to be detected using a common fluorescence microscope. The design concept and the channel layout of the droplet incubation chip are shown in Figure 5.3.

The droplet incubation chamber of the chip was designed to exploit the positive buoy-

ancy of the droplets to facilitate optimal droplet packing regardless of the droplet production rate and water-to-oil flow-rate ratio. The height of the chamber restricts the droplets to pack into a single monolayer enabling read out of fluorescence signals of the entire droplet population by fluorescence microscopy. In addition, the thin sealing foil of the chip allows for thermo-cycling for PCR amplification. Since all the steps of ddPCR such as droplet imaging, droplet thermo-cycling and reimaging were performed in one disposable injection moulded chip, the droplet handling was greatly reduced.

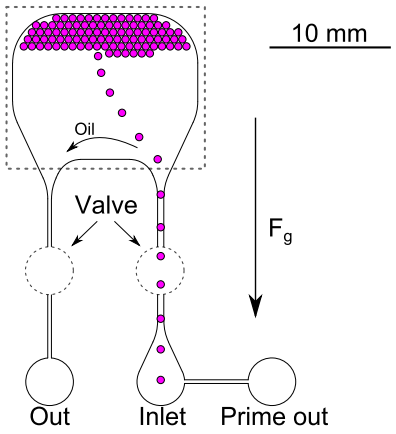

Figure 5.3: Schematic channel layout of the disposable injection moulded chip. (box) Incubation and imaging chamber. Tight droplet packing is achieved by confinement and gravity (F_g). PDMS squeeze valves are indicated by dashed circles. *Prime Out* is an additional outlet used when priming the upstream system of air.

5.1.1 Experimental

5.1.1.1 Device fabrication

The droplet chip was fabricated using the common fabrication scheme of this PhD-study, described in Section 2.2. Specifically for this device, the energy directors were micromilled to a height of 150 µm with a 550 µm offset to the channel walls. Also, the final mould insert was carefully polished to reduce roughness since it was found that this reduced bubble formation (more on bubbles below). The devices were injection moulded in COC 5013L-10 (TOPAS Advanced Polymers). Injection temperature of the polymer was 270 °C and the mould (and demoulding) temperature was kept stable at 120 °C resulting in a turnaround time of approximately 45 seconds. The injection moulded part is sketched in Figure 5.4 (left). To seal the microfluidic chip, a 152 µm thick COC sheet (TOPAS grade 5013S-04, TOPAS Advanced Polymers) was bonded to the injection moulded part using ultrasonic welding. The chip welding was conducted by depositing 60 J at 100% amplitude, 20 kHz and with a trigger force of 500 N. The sealed microfluidic chip loaded with fruit dye for channel highlight is photographed in Figure 5.4 (right). Including ultrasonic welding, the total turn-around time per chip was <1 min including handling.

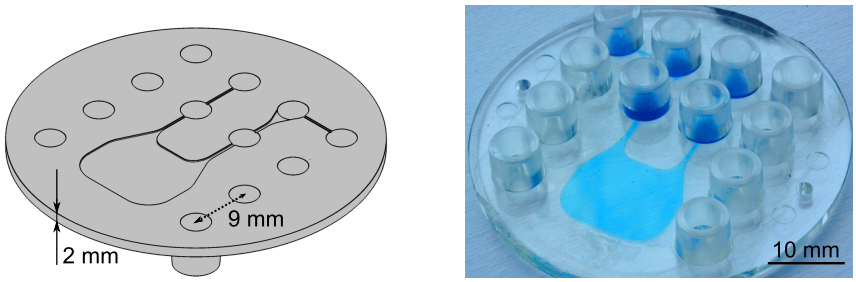

Figure 5.4: (left) Scheme of the injection moulded chip (cover plate not shown). (right) A bonded chip loaded with 10% brilliant blue dye for channel highlight.

5.1.1.2 Droplet generation

Droplets were generated using a Droplet Junction Chip, Hydrophobic, Part #3000301 (Dolomite). 2% of Pico-Surf® 1 in FC40 (Dolomite) was used as the continuous phase and the dispersed phase consisted of PCR master mixture for detection of *Campylobacter* spp using universal Campylobacter primers targeted a 300 bp of 16sRNA gene described previously[167]. 1 pm/µL TaqMan probe labelled with 5'6-FAM and 3' BBQ (DNA Technology Århus, Denmark) was added to the PCR mixture to detect DNA amplification. 10 µM Sulphorhodamine 101 was also added for improved droplet detection and size statistics. Target DNA samples were chromosomal DNA isolated from *Campylobacter jejuni*, strain NCTC-11284, using QIAamp DNA mini kit (Qiagen Germany)[167]. The final target concentration used was 7.2 fM, derived from 7.2 pg/µL of genomic DNA (Assuming one target per genome, and a genome size of 1.64 Mbp[168]).

Prior to experimentation, the continuous phase was degassed overnight at 5 mbar to limit bubble formation during thermo-cycling. The droplets were formed using syringe pumps (55 – 2222, Harvard Apparatus) with flow rates of 2 and 18 µL/min for the dispersed and continuous phase, respectively.

5.1.1.3 Droplet imaging

Droplets collected in the incubation chamber were imaged using a LaVision BioAnalyzer 4F/4S Scanner (LaVision Biotech Germany) fitted with Cy3 and FITC filter cubes using exposure times of 20 and 50 ms, respectively. After acquisition, the images were stitched using the concomitant software FIPS (LaVision Biotech Germany) before being analysed using a custom made MATLAB code applying a hough transformation for droplet detection. This protocol was repeated after thermo-cycling:

Table 5.1: PCR thermo-cycling protocol for amplification of the target 300 bp 16sRNA gene fragment[167].

Step	Temperature, °C	Time, s	Repeats
Hot start	96	300	x 1
Melting	94	15	
Annealing	54	15	x 40
Extension	72	8	
Final extension	72	60	x 1

5.1.1.4 Thermo-cycling

After loading and droplet imaging, the chip was transferred to a commercial flatbed PCR thermo-cycling (DNA Engine, Bio-Rad, USA) controlled using a custom LabVIEW script and a GPIB interface (NI GPIB-USB-HS, National Instruments). The chip was fixed using a custom made clamping piece that also harvested the bolts for applying pressure on two cylindrical PDMS plugs, effectively sealing the chamber during thermo-cycling (see Figure 5.5). To achieve better thermal contact and avoid damaging the sealing COC sheet, a 1 mm copper plate with Heat Sink Compound (RS) applied to the bottom was mounted on the flatbed PCR machine below the COC chip.

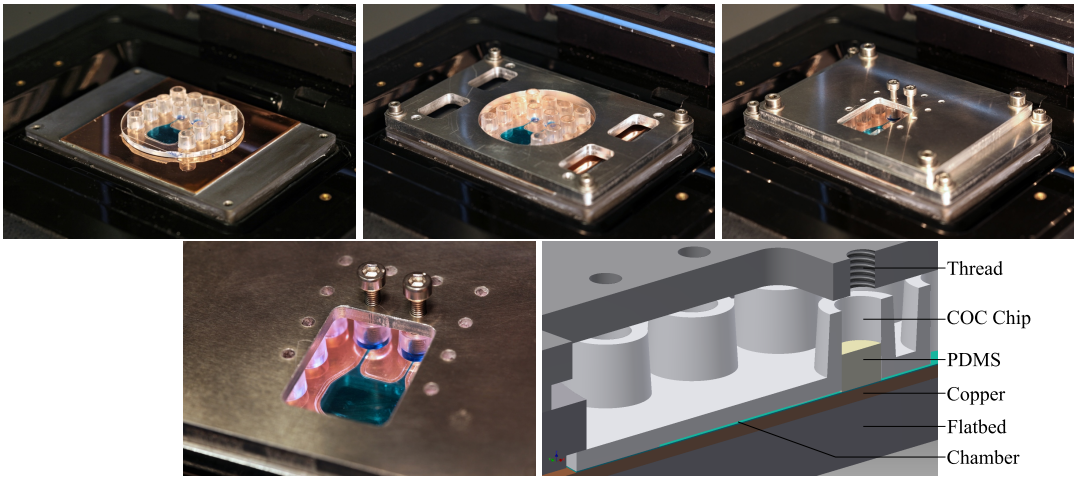

Figure 5.5: (left to right) Stepwise mounting of the injection moulded droplet chip on the commercial flatbed PCR machine. (Last) Schematic cross section of mounted chip. For easier identification, the sealing COC sheet and the PDMS valve are highlighted in turquois and ivory, respectively.

The heating strategy employed for thermo-cycling the device and droplets was optimised using a chip fitted with a 125 µm unsheathed bead-welded thermo coupler (K-Type, Omega, part #CHAL-005) in the droplet incubation chamber and the above mentioned LabVIEW script targeting the PCR protocol of Table 5.1.

The robustness of the optimised heating strategy was tested with air, water and FC40 in the incubation chamber prior to droplet loading and PCR amplifying.

5.1.1.5 Gel electrophoresis

To confirm successful droplet PCR amplification, the PCR product was analysed using 2% agarose gel electrophoresis. As preparation, the emulsion of droplets within a chip was broken by adding an equal volume of FC40 with 10% 1H,1H,2H,2H-perfluoro-1-decanol (Apollo Scientific) followed by vigorous vortex for 5 minutes. After extraction, 1 µL of the aqueous phase was loaded on a 2% w/v agarose gel (Cat: A9539, Sigma-Aldrich) in UltraPure® TAE buffer (Cat: 15558-026, Invitrogen) and run for 15 minutes at 100 V. The gel was stained with SYBR® Safe DNA Gel Stain (Invitrogen).

5.1.2 Results and Discussion

5.1.2.1 Droplet generation

The droplets collected in the incubation chamber and imaged using Cy3 filter cube and 20 ms exposure are illustrated in Figure 5.6. Subsections of these images are presented in Figure 5.7.

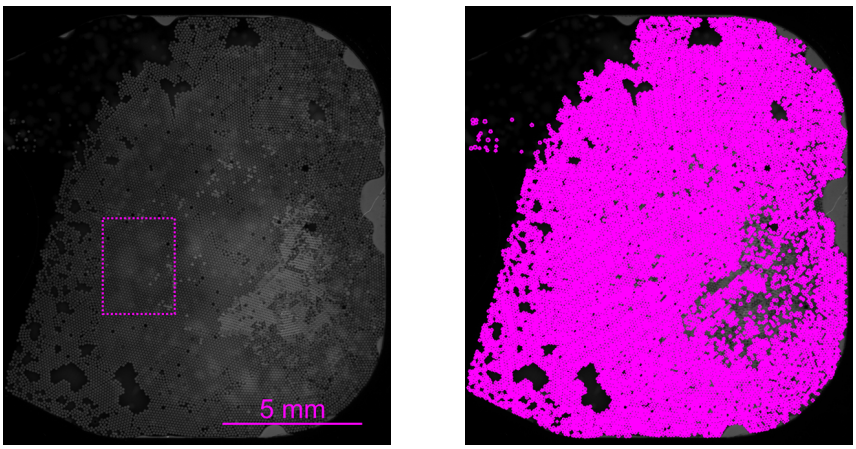

Figure 5.6: Droplets imaged using Cy3 filter cube and 20 ms exposure. (left) Overview. Magenta region is analysed in MATLAB. (right) Droplets with fitted diameter marked in magenta. 13438 droplets have been detected.

As seen in Figure 5.6, a nearly perfect monolayer is formed by the droplets with few voids and ”stacking areas”. A closer examination (Figure 5.7) shows that the droplet detection algorithm correctly discards voids and overlapping circles.

Size statistics of the 13438 droplets visualised in Figure 5.6 have been plotted in Figure 5.8.

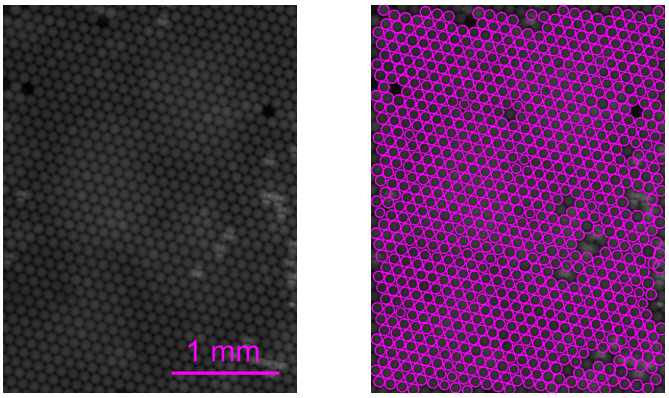

Figure 5.7: Enlargement of sub area highlighted in Figure 5.6. (right) Fitted circles (hough transform) are overlaid in magenta.

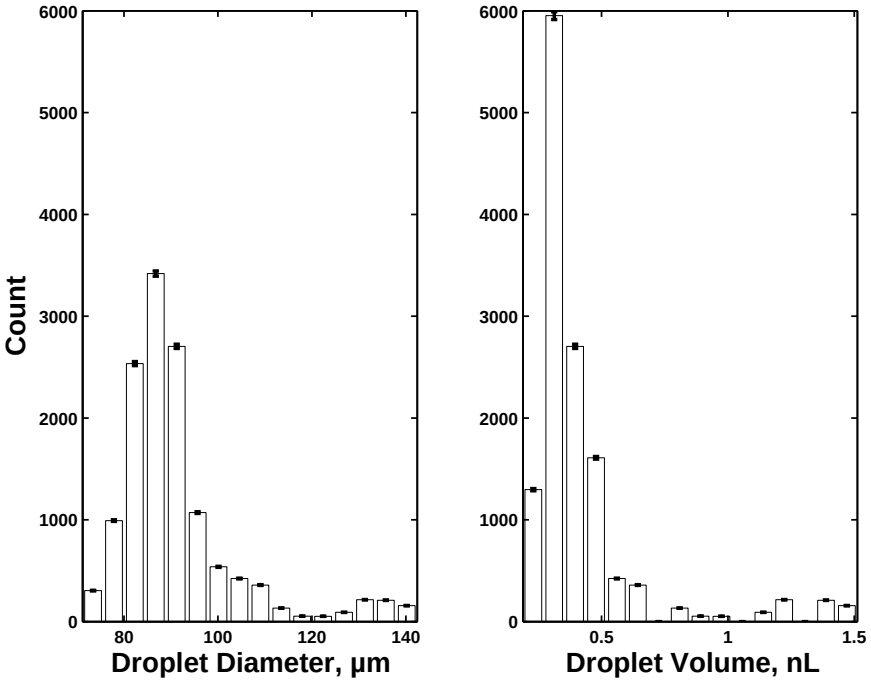

Figure 5.8: Droplet size statistics of 13438 droplets imaged in a single chip. Error bars represent standard deviation estimated by an "in-or-out" binomial distribution. The droplet volume is estimated to 0.51 ± 0.096 nL and the diameter to 98.72 ± 6.0 µm. Since droplet diameter detection [pixels] is limited to integers, bin width is equidistant with one pixel in droplet diameter.

5.1.2.2 Thermo-cycling

Temperature measurements of the droplet incubation chamber during the first three rounds of thermo-cycling are illustrated in Figure 5.9. Since it was not possible to load droplets while conducting temperature measurement, water, FC40 and air has been measured independently.

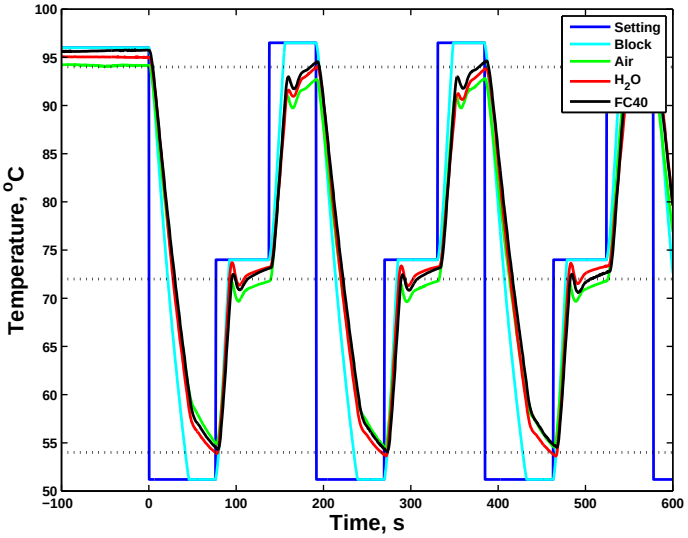

Figure 5.9: Temperature profiles measured in the incubation chamber during thermo-cycling. *Setting* denotes block target, *Block* denotes block temperature measured by the PCR machines built in probe, and *Air*, H_2O and *FC40* denote temperature readout of the k-type thermo coupler embedded in the chamber (name refering to chamber content). Dashed horizontal lines indicate PCR target temperatures.

The temperature profiles for the incubation chamber filled with air, water, or FC40 are observed to largely reflect the thermal conductivity of their respective medium: FC40 and water having thermal conductivity coefficients of 0.065 and 0.58 W/m·K, respectively, are observed to follow the temperature profile of the block closer than the air (0.024 W/m·K). With about half the thermal conductivity and -capacity compared to water (0.21 W/m·K and 2000 J/kg·K, respectively)[169], the top COC layer of the chip (2 mm) is observed to add significant thermal mass to the system. During ramping of the temperature for the extension phase (72 °C), the chamber temperature is observed to drop briefly as a result of reduced heating by the flatbed PCR machine and cooling by the chips thermal mass. Likewise, the cooling rate is slightly reduced as the block reaches its setting temperature. These fluctuations are also commonly observed when conducting PCR in tube using commercial PCR instruments, and fluctuations of 1 to 2 degrees are acceptable, even for multiplex reactions[170].

5.1.2.3 Gel electrophoresis

Gel-electrophoretic analysis of a reference PCR reaction thermo-cycled in tube on a conventional thermo-cycler, on-chip PCR and on-chip droplet PCR are depicted in Figure 5.10.

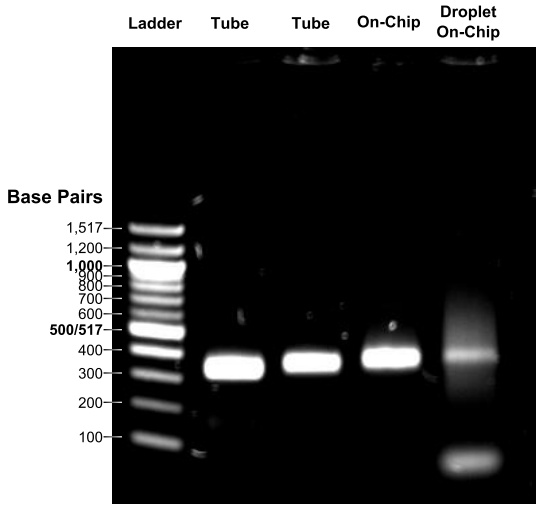

Figure 5.10: 2% agarose gel electrophoresis of PCR products. *Tube* refers to in tube conventional thermocycling. *On-Chip* refers to bulk PCR sample in the chip chamber. *Droplet On-Chip* refers to droplets loaded to chip and thermo-cycled. *Ladder* is a 100 bp DNA Ladder (NEW ENGLAND BioLabs®).

From the gel electrophoresis, it is evident that the target DNA has been amplified in all the samples. However, higher levels of primer dimers are identified in the droplet-on-chip lane (band $\ll$ 100 bp). The increased amount of primer dimer observed in the gel electrophoresis (Figure 5.10) corresponds well with what could be expected from compartmentalising a PCR reaction: Whereas a bulk PCR reaction, such as the samples conducted in tubes (lanes 1 + 2) and the bulk chamber on-chip-PCR (lane 3), will amplify the entire sample and deplete the reagents by producing copies of the target, the portion of the droplets that harvest no target DNA may eventually start forming primer dimers. The fact that the PCR target must successfully start amplifying before the onset of primer dimer formation hence favours primer dimers in droplets compared to bulk PCR reactions[171]. This may explain why using TaqMan propes for ddPCR is the much more used[4,47,57,58,70–72,75,76,79,85,92,93,96,109,110,116] than unspecific nucleic acid staining such as EvaGreen®[172].

5.1.2.4 Droplet imaging

From a single image (Figure 5.6), the size statistics reveal a volume of 0.51 ± 0.096 nL. For the purpose of assessing the hydrolysis of the TaqMan probes and hence the completion of the PCR reaction, the FAM (FITC) fluorescence intensity was imaged after the thermo-cycling had been completed, see Figure 5.11.

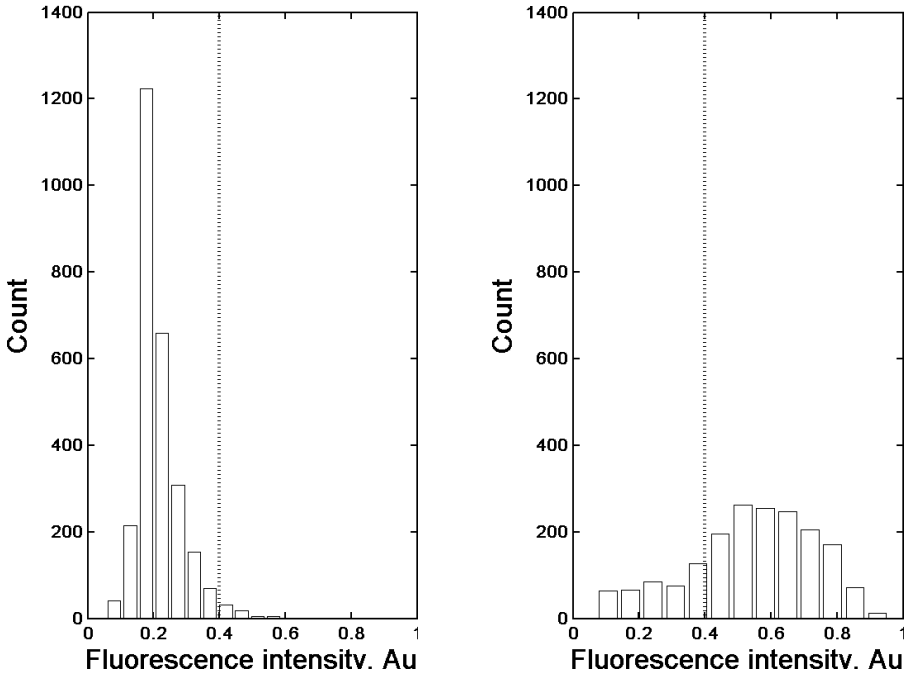

Figure 5.11: Droplet average pixel intensity populations imaged using FITC filter cube and 50 ms exposure. (left) Fluorescence intensity prior to thermo-cycling. 1.9% of the droplet population display intensity higher than 0.4. (right After thermo-cycling (40 cycles). 79% of the droplets are now above 0.4.

As observed, the fluorescence intensity in the FITC channel is shifted in the thermo-cycled population compared to the non-thermo-cycled droplets. Defining an intensity threshold of 0.4 AU it is observed that only 1.9% of the droplets reach intensity levels equal to or higher than the threshold, whereas this number is 79% when the droplets have been thermo-cycled 40 times.

5.1.2.5 Droplet analysis

Before describing the droplet analysis of this paper, I would like to emphasise that the work presented in this chapter (and paper) were conducted prior to the development of the improved estimators[b] presented in Paper 5 (Chapter 8 on page 115). Droplet statistics were therefore done using the state-of-the-art estimator which is based on the assumption that the targets enter the droplets via a *Poisson* process (e.i. (1) the events of a target entering a droplet are in no way correlated and (2), the probability of a target entering a droplet i constant in time, given the constant concentration) and that the droplet size distribution is monodisperse[82].

If the targets enter the droplets in a *Poisson* process, the probability of a droplet of volume V to contain k droplets, given the loading concentration c^* is

[b] The concept of estimators is elaborated in the box 8.1 on page 116.

$$P_k(\mu) = \frac{\mu^k}{k!} e^{-\mu},$$

where $\mu = c^* V$ is the expected value of the occupancy ($\mu = \langle k \rangle$). Using this, we may calculate the probability of obtaining a positive droplet ($k > 0$) by subtracting $P_0(\mu)$ from 1:

$$P_+(\mu) = \sum_{k=1}^{\infty} \frac{\mu^k}{k!} e^{-\mu} = 1 - P_0(\mu) = 1 - e^{-\mu}.$$

Assuming that the percentage of positive droplets approaches the probability of obtaining a positive droplet when the sample size increases,

$$\begin{aligned} \lim_{N \to \infty} \frac{N_1(\mu)}{N} &= P_+(\mu) \\ &= 1 - e^{-\mu}, \end{aligned}$$

and we may solve for, μ,

$$\hat{\mu} = -\ln\left(1 - \frac{N_1}{N}\right).$$

The template concentration can be estimated from the fraction of positive droplets from $\hat{c} = \hat{\mu}/V$.

When calculating the average number of targets per drop, μ, using the added target concentration of 7.2 fM and the identified droplet volume of 0.51 nl, $88.6 \pm 0.7\%$ of the droplets are expected to be positive. With 79% positive droplets, the initial template concentration is estimated to 5.2 fM, an underestimation of 28%. Comparing this observation to previous studies, a fewer percent positive droplets observed than expected is very common, and may be ascribed to the sensitivity of the PCR reaction and sample loss in the upstream microfluidic system[75,82,90].

Considering that quantitative PCR methods based on real-time measurements and Ct values may require dozens of parallel samples to achieve a comparable confidence interval[173], obtaining this result from a single sample end point image is acknowledgeable. Additionally, no "standard-curve" samples were needed for the preparation of the demonstrated results, and only 20 µL of PCR reagents were used. As mentioned in the experimental section, a cycle time of <1 min/chip was achieved without any optimisation. An important point to stress in this aspect is that no surface modification of the

COC was needed prior to experimentation. This is in contrast to PDMS based droplet (water in oil) systems which are always surface modified to enhance hydrophobicity: the most common method is by plasma activation followed by covalent silanisation to fluor-containing compounds[41,45,46,49,53,82,84,174–183].

5.2 Remarks

The reason for the somewhat limited data presented above is due to an extremely high failure rate of the experiments - the main reason being the formation of bubbles. The solubility of atmospheric gasses in fluorinated oils like FC40 is an order of magnitude higher than that of water[184]. This is very useful when incubating cells or multicellular organisms[175], however (to my regret), it was observed that when heated to ~ 95 °C, bubbles would form in the oil phase. This effect was reduced by degassing the oil prior to use, but decreasing degassing pressure further resulted in evaporation of the oil. After the bubbles had formed, they would be present until the end of the experiment, and they were observed to expand and contract, disrupting the droplets[185]. Figure 5.12 show two examples of experiments failed due to bubble formation.

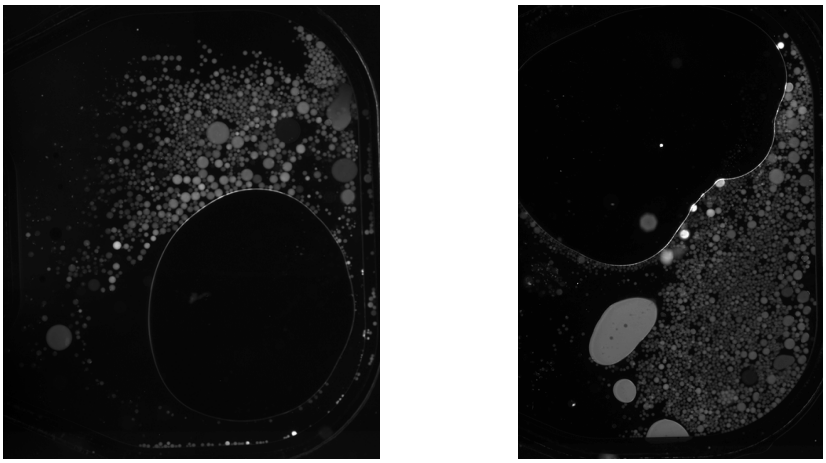

Figure 5.12: Two examples of bubble formation during ddPCR. Note the high polydispersity in diameters from the merging of droplets during thermo-cycling. For comparison, Figures 5.6 and 5.7 on page 69 show a ensemble of droplets prior to thermo-cycling.

The issue of bubble formation from fluorinated oil is almost absent in literature - probably because the studies almost exclusively employ one of two thermo-cyclic schemes; (1) Thermo-cycling on-chip using PDMS[47,74,75,77], which conducts gasses very well, or (2) thermo-cycling off-chip in an "open" device such as a PCR-tube or a titer plate[58,68–72,78,79,82,174]. Alternatively (published after this work), the bubbles may be expelled by using gradients of confinement[73].

After several failed attempts to improve the chip design to accommodate the droplet formation, focus was changed to finding an alternative to the fluorinated oil. Octan-1-ol

(octanol) was identified as a promising candidate due to it's multiple uses in other fields of research (see Chapter 7 for liquid-liquid extraction), its low price, its compatibility with COC (after annealing, see page 114) and the fact that it is far less toxic and bio-accumulating than fluorinated compounds[186–188].

Further, an alternative to the PCR reaction was desired since the thermo-cycling were highly time-consuming and required careful calibration and precise temperature control. As presented in Section 9.1, we are at the time of writing working on a droplet based loop-mediated isothermal amplification (LAMP) system for detecting *Salmonella* spp. in food samples. The work is a continuation of the methods presented by Yi Sun *et al.* (2015)[189].

Lab on a Chip

TECHNICAL INNOVATION

View Article Online
View Journal | View Issue

Cite this: *Lab Chip*, 2015, **15**, 1998

Ultrasonic welding for fast bonding of self-aligned structures in lab-on-a-chip systems†

K. Kistrup, C. E. Poulsen, M. F. Hansen and A. Wolff*

Received 12th February 2015,
Accepted 10th March 2015

DOI: 10.1039/c5lc00174a

www.rsc.org/loc

Ultrasonic welding is a rapid, promising bonding method for the bonding of polymer chips; yet its use is still limited. We present two lab-on-a-chip applications where ultrasonic welding can be preferably applied: (1) self-aligned gapless bonding of a two-part chip with a tolerance of 50 μm; (2) bonding of a large area shallow chamber (1.8 cm^2 × 150 μm). Using injection moulding combined with ultrasonic welding we achieved a total production and bonding time of 60 s per chip, and a batch of chips could be produced within a day going from design to finished chips. We believe that the technical solutions offered here can significantly help bridge the gap between academia and industry, where the differences in production methods and materials pose a challenge when transferring technology.

Introduction

In industry, ultrasonic welding is one of the leading fusion processes for thermoplastics and is ubiquitously used, historically moving from commodities, to the automotive industry, to medical devices.[1,2] Ultrasonic welding has had great impact on the plastics industry, because it is fast (rapid welding process, no curing or solvent that needs to dry), requires no soldering materials and is easy to automate. Moreover, it can be used for a range of applications, including welding of wires in electronics, embedding metal objects in plastics and fusion of virtually any thermoplastic with some cross-material compatibility.[1] A general rule of thumb is that materials of similar molecular structures and melting temperatures are compatible.[3–6]

As noted by Tsao *et al.*,[5] thermoplastics are well suited for microfluidic systems. However, bonding remains a critical and non-trivial step. The use of ultrasonic welding within the lab-on-a-chip research field is very limited,[7–12] perhaps, because the technique is thought to have a low depth resolution and requires special chip designs with energy directors to enable reproducible ultrasonic welding.[5,13] We believe that ultrasonic welding will be a key technology, also in the lab-on-a-chip field for the following reasons: (1) it is rapid and well suited for all-polymer rapid prototyping, (2) it generates high-strength hermetic bonds, (3) the ultrasonic energy is focused on the contact points between the parts allowing the energy director to penetrate thin films[14] or membranes,[11] and it prevents heating and destruction of pre-loaded reagents.[15] Moreover, combining ultrasonic welding with other mass production techniques such as injection moulding or embossing in the research phase on a lab-on-a-chip system substantially eases the transfer to commercial production of chip systems. An additional advantage is that a large number of truly single use chips can be made available in the research phase while maintaining a short time from design to prototype.

In this work, we show that ultrasonic welding can efficiently be applied to microfluidic systems and that energy directors can easily be incorporated in prototypes with parts fabricated using injection moulding.[14,16] Specifically, we demonstrate two novel aspects, where ultrasonic welding can be taken advantage of in microfluidic systems: (1) self-aligned gapless bonding of a two-part chip, and (2) sealing of low aspect ratio, large area chambers.

Ultrasonic welding of polymer chips

Ultrasonic welding is a simple thermal fusion process, where two parts are melted together by inducing vibrational friction heating at their interface. Using energy director structures the welding is localized to predefined areas of the part. Fig. 1a and b show two types of energy directors that both rely on an apex to focus the applied energy. Briefly, an ultrasonic welding machine consists of five core components: (1) a kHz range power supply, (2) a piezoelectric transducer that converts the signal to mechanical vibrations, (3) a booster horn that helps amplify and shape the vibrations, (4) a welding horn (sonotrode) that provides pressure and a contact point to pass the vibrations onto the parts to be fused, (5) a fixture that prevent the parts from moving during

Department of Micro- and Nanotechnology, Technical University of Denmark, DTU Nanotech, Building 345 East, DK-2800 Kongens Lyngby, Denmark.
E-mail: Anders.Wolff@nanotech.dtu.dk

† Electronic supplementary information (ESI) available: Additional micrographs of ultrasonic welded parts and droplet PCR protocol. See DOI: 10.1039/c5lc00174a

View Article Online

Lab on a Chip Technical Innovation

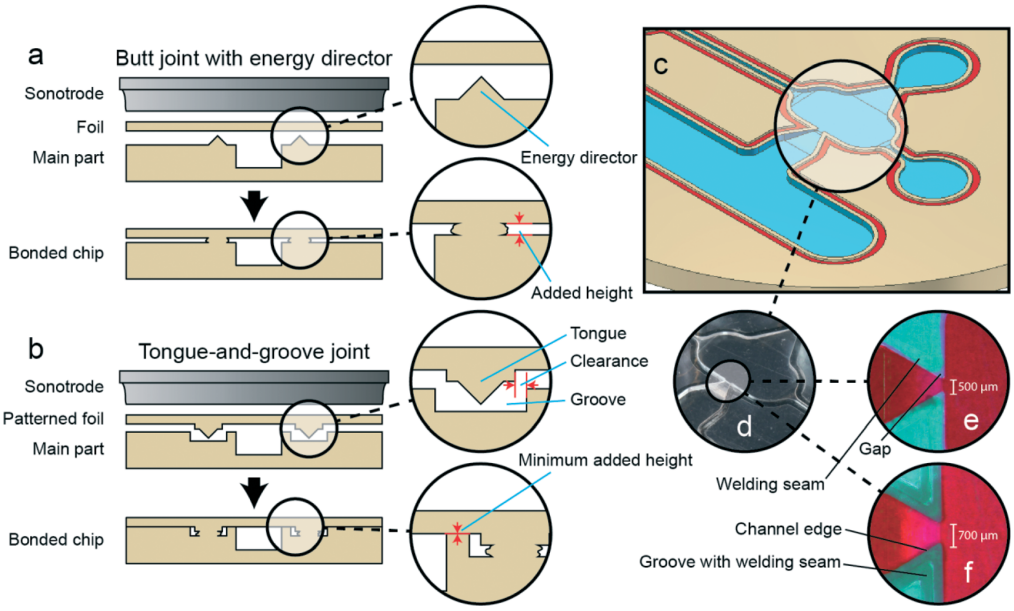

Fig. 1 Sketches of two joint types for ultrasonic welding and presentation of chip systems with like joints. (a) Sketch of butt joint energy director pre and post welding. The energy director material results in an added channel height. (b) Sketch of a tongue-and-groove joint pre and post welding. The energy director material is contained within the groove resulting in no added height. (c) Sketch of the microfluidic main part of Design A2 showing the channel system (blue) and the groove (red). (d) Photograph of ultrasonically welded chip with the same channel system featuring a butt joint. The width of the capillary microvalve is 500 µm. Parts (e) and (f) show micrographs of Design A1 and A2 capillary microvalves, respectively, filled with a 1.3% (V/V) sarkosyl Rhodamine B fluorescent dye solution. For the butt joint, the liquid extends outside the channel because of the added height between the chip and foil (panel (e)), whereas no liquid is observed outside the channel for the tongue-and-groove joint (panel (f)). Contrast and colour was adjusted for clarity. The darker tint of turquoise is a welding phenomenon known as flash that changes the refractive properties of the polymer. Supporting micrographs are provided in the ESI† Fig. S3.

welding. The most important parameters influencing the process are: polymer type, transducer amplitude, welding pressure and welding time/energy. Welding time is typically less than 1 second, and production rates of 20 to 60 parts per minute are routinely achievable.[1]

Fabrication of polymer chips

Three chip designs (Design A1, A2, and B) are presented in this work. They are all disc shaped (∅ = 50 mm), fitted with 12 Luer-Slip connectors,[17] and are made by fusing an injection moulded main part (featuring the fluidic system) with a foil part.

Designs A1 and A2 were designed for magnetic bead-based solid phase extraction of biological targets using immiscible phase filtration as described in ref. 16. They have the general design shown in Fig. 1c where a critical capillary microvalve structure is highlighted. Designs A1 and A2 differ by having different capillary microvalve dimensions (width = 500 and 700 µm, respectively) and by their energy director design and bonding process. Design A1 was fused *via* a butt joint to a flat 152 µm thick extruded foil by ultrasonic welding, see Fig. 1a. Design A2 was fused *via* a tongue-and-groove joint to a custom made 530 µm thick injection moulded foil, see Fig. 1b. Prior to welding, the chip parts were put together manually by visual alignment of the tongue-and-groove structures and by applying a small pressure until the two parts "clicked" together.

Design B was designed for imaging, incubation and thermal cycling of droplets and is shown in Fig. 2a. It features a

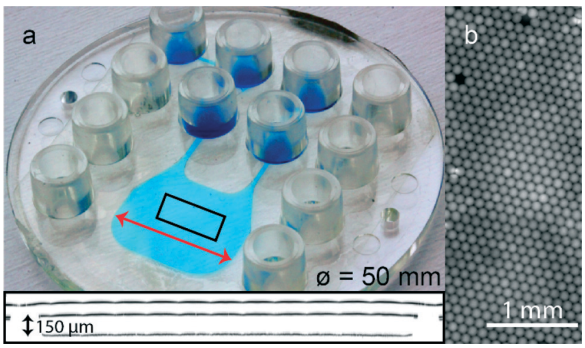

Fig. 2 (a) photograph of an ultrasonic welded polymer chip with a large area, low aspect ratio chamber for ddPCR. Inset: chamber cross section (red arrow) imaged using confocal microscopy. The three lines (top to bottom) show the outer foil surface, the inner foil surface (broken where welding has occurred), and the chip main part surface. The black double arrow denotes the channel height of 150 µm. (b) Fluorescence image of droplets for size statistics and PCR read-out.

critical large (15 mm × 11.8 mm × 0.15 mm) chamber. It was fused *via* a butt joint to the 152 μm thick extruded foil.

Custom mould inserts for the injection moulder were CNC micro machined from Al sheets (grade 2017, MetalCentret, Denmark). The milling process took approx. 3–5 hours per mould insert, depending on the complexity of the design. Dimensions of the tongue-and-groove joint of Design A2 are illustrated in Fig. S1 in the ESI.†

All the main chip parts and the foil for Design A2 were injection moulded in cyclic olefin copolymer (COC, TOPAS 5013L-10) as described in ref. 14 with a cycle time of 40–50 s per part. The 152 μm thick extruded COC foil was of grade TOPAS 5013S-04.

Ultrasonic welding was manually performed on a Telsonic USP4700 20 kHz ultrasonic welder (Telsonic, Erlangen, Germany). The chips were mounted in a custom fixture with the foil placed on top. Design A1 was welded using a 850 N trigger force with a 0.35 s hold time. 85 J was deposited during the welding running at 80% vibrational amplitude. Design A2/B settings differed at the following parameters: Trigger force = 515/500 N; energy = 40/60 J; amplitude = 55/100%, respectively. The average welding time per chip was 30 s including mounting of chip and foil. Once the processes were optimised, the yield of the entire process was higher than 95%. Most failures pertained to the welding process where cracking of the foils occurred due to resonances in the chip.

The bonding strength was assessed by applying pressurised air to Design A1 and A2. Design A1 failed at 3.5 bar where the 152 μm thick foil burst, see Fig. S2 in the ESI.† Design A2 remained intact after exposure to 8.5 bar, which was the highest pressure available for testing.

Design A: Gapless ultrasonic welding with possibility for self-aligning using energy directors

Two joint types are presented to highlight the versatility of ultrasonic welding.

Design A1 features a simple butt joint, which is the most common joint type (illustrated in Fig. 1a (schematic) and Fig. 1e (a post-welding photograph)). Butt joints are simple to integrate and require only a peripheral pattern of small energy directors to be included in the chip main part design (Fig. 1b). Moreover, no alignment is needed. However, the material from the molten energy director inevitably results in an added height to the channel. We have previously published systems featuring this type of energy director.[14,16]

Design A2 features a tongue-and-groove joint. Such joints are common for macroscale objects but have until now not been implemented on microscale in lab-on-a-chip systems. Here, the energy director is situated on the foil (the tongue) and a matching peripheral groove is introduced on the chip main part, see Fig. 1b (schematic) and Fig. 1c (schematic with groove in red). The tongue-and-groove joint makes it possible to self-align the foil to the chip main part by "clicking" the two parts together prior to welding. This allows for inclusion of other features requiring alignment such as local coatings, spotted biomaterial or reagents, electrodes, and channel structures. The groove clearance of 50 μm sets the alignment tolerance of Design A2. The added channel height is eliminated, because the groove underneath the tongue contains the molten polymer from the energy director (Fig. 1b). Tongue-and-groove joints limit the choice of foils, since they have to be custom designed with appropriate structural features. However, these can be fabricated with embossing/moulding techniques, such as injection moulding, as is the case in this work.

To illustrate the performance difference of the two joint types, Designs A1 and A2 were filled with a 1.3 (V/V)% detergent (*N*-lauroylsarcosine, #L7414, Sigma-Aldrich, MO, USA) containing Rhodamine B (#R6626, Sigma-Aldrich, MO, USA) solution and micrographs were taken using a Leica ZMFL III microscope. Detergent was added to ensure filling of the device, since COC is hydrophobic. Fig. 1e shows the solution flowing into the small gap of Design A1 resulting from the added height of the butt joint. In contrast, the welding seam of Design A2 perfectly follows the edge of the channel because, in addition to the welding at the tongue-and-groove welding seam, the foil and channel edge are in contact and have fused together (Fig. 1f). To further characterise the added height, the chips were investigated using a confocal microscope, see ESI† Fig. S3 for details. For Design A1, an added height of 15 μm was found. Depending on the tolerance of the microfluidic system and its application, this added height can modify the behaviour compared to a system with no added height and may compromise the function of the system. No added height was detectable for Design A2.

Design B: bonding of large area, low aspect ratio chambers

Large area, low aspect ratio (height/width) chambers have numerous uses, *e.g.*, for cell culturing and parallelised droplet interrogation by wide field imaging.[18] Because ultrasonic welding relies on localised forces and energy deposition, it is useful for sealing large area shallow chambers, *i.e.*, chambers with low aspect ratio geometries. Such chambers are not easily bonded thermally due to the risk of collapse of the chamber and special precautions have to be taken, for example, by selectively applying bonding pressure using a custom made bonding tool.[19] Moreover, since no new materials, such as glues or adhesives, are introduced, the temperature working range of the microfluidic system is not limited by differences in thermal expansion. To demonstrate these capabilities in a microfluidic setting, we present an all-polymer ultrasonic welded microfluidic chip featuring a single 15 mm × 11.8 mm × 0.15 mm chamber for Droplet Digital™ PCR (ddPCR), see Fig. 2a. The chamber allows for droplet packing into a single monolayer, imaged by fluorescence microscopy (Fig. 2b).

Using a single chip, 13 438 droplets were simultaneously analysed, and a target concentration of 7.2 fM was determined with 28% underestimation. More details on this application of ultrasonic welding are found in the ESI.†

Discussion and conclusion

Bonding is still a recurring challenge and unsolved issue in microfluidics, where most systems are based on two or more parts that need to be fused together or interfaced with other components. This work encourages the use of ultrasonic welding for bonding of lab-on-a-chip systems, where applicable. Ultrasonic welding provides a strong fusion with foils over a range of thicknesses (at least 100 μm to 2 mm, data not shown) and needs no special pre-treatment. It is also devoid of chemicals that may interfere with the chip application or change chip properties over time. As demonstrated in this paper, tongue-and-groove joints add a simple alignment step to the fusion process. In addition ultrasonic welding can be utilized for bonding of large area shallow chambers, expanding the applications of ultrasonic welding within microfluidics.

In spite of these advantages, ultrasonic welding has not yet gained wide academic popularity, which may be ascribed to the fact that energy directors are required and ultrasonic welding is not compatible with thermosetting polymers such as polydimethylsiloxane (PDMS). From an industrial viewpoint, thermosetting polymers are far less attractive than thermoplastics, and it is recommended that prototypes are designed with manufacturability kept in mind for the easy implementation of larger scale testing and for future potential commercial production.[20,21] Most research in the field of microfluidics is, after all, application driven, and commercialization is often highlighted as the objective.

The chip fabrication process described here is rapid and allows for fast design iterations using commercially relevant fabrication techniques. It is possible to go from design to a 'bag of chips' within a day for Designs A1 and B; 3–5 hours micro machining, 1–2 hours injection moulding, and 1–2 hours of back-end ultrasonic welding can easily yield up to 50 ready-to-use chips. For Design A2 a second milling and injection moulding step must be included.

The bonding strength of Design A1 and A2 was assessed by applying air pressure to the chips. Design A2 was able to withstand pressures up to 8.5 bar (maximum tested), whereas Design A1 burst at 3.5 bar. As can be seen in Fig. S2† the mode of failure pertained to the bursting of the 152 μm thick foil over the channel and not the welding seam, which remained intact. This correlates well with the observation of no failure for the 500 μm thick foil of Design A2.

Design A2 has a clearance of 50 μm, see Fig. 1b and S1,† which limits the alignment precision. We remark that an alignment precision of 50 μm may be sufficient for most microfluidic applications and note that no optimization was performed to minimize the clearance. If needed, this clearance can likely be further reduced.

Acknowledgements

The authors of this work would like to acknowledge Professor Dang Duong Bang for supplying PCR reagents and template DNA for the ddPCR and Marco Matteucci for help with injection moulding. This work is funded by the Danish Council for Strategic Research through the Strategic Research Centre Poly-Nano (grant no. 10-092322/DSF) and The Danish Council for Independent Research (grant no. 09066477).

References

1 J. Rotheiser, *Joining of plastics*, 2004.
2 R. S. Soloff and S. G. Linsley, Sonic method of welding thermoplastic parts, *US Pat.*, US 3224916 A, 1965.
3 M. J. Troughton, in *Handbook of Plastics Joining - A Practical Guide*, William Andrew Publishing, Boston, 2009, 2nd edn., pp. 1535.
4 A. Weber, *Assembly*, 2007.
5 C.-W. Tsao and D. L. DeVoe, *Microfluid. Nanofluid.*, 2008, **6**, 1–16.
6 C. Ageorges, L. Ye and M. Hou, *Composites, Part A*, 2001, **32**, 839–857.
7 R. Truckenmüller, Y. Cheng, R. Ahrens, H. Bahrs, G. Fischer and J. Lehmann, *Microsyst. Technol.*, 2006, **12**, 1027–1029.
8 R. Truckenmüller, R. Ahrens, Y. Cheng, G. Fischer and V. Saile, *Sens. Actuators, A*, 2006, **132**, 385–392.
9 Y. Luo, Z. Zhang, X. Wang and Y. Zheng, *Microelectron. Eng.*, 2010, **87**, 2429–2436.
10 Z. Zhang, Y. Luo, X. Wang, S. He, F. Meng and L. Wang, *Microsyst. Technol.*, 2010, **16**, 2043–2048.
11 M. Bu, I. R. Perch-Nielsen, Y. Sun and A. Wolff, in *2011 16th International Solid-State Sensors, Actuators and Microsystems Conference, IEEE*, 2011, pp. 1244–1247.
12 K. G. Lee, S. Shin, B. Il Kim, N. H. Bae, M.-K. Lee, S. J. Lee and T. J. Lee, *Lab Chip*, 2015, **15**, 1412–1416.
13 H. Becker and C. Gärtner, *Anal. Bioanal. Chem.*, 2008, **390**, 89–111.
14 K. Kistrup, C. E. Poulsen, P. F. Østergaard, K. B. Haugshøj, R. Taboryski, A. Wolff and M. F. Hansen, *J. Micromech. Microeng.*, 2014, **24**, 125007.
15 Y. Sun, J. Høgberg, T. Christine, L. Florian, L. G. Monsalve, S. Rodriguez, C. Cao, A. Wolff, J. M. Ruano-Lopez and D. D. Bang, *Lab Chip*, 2013, **13**, 1509–1514.
16 K. Kistrup, K. Skotte Sørensen, A. Wolff and M. Fougt Hansen, *J. Magn. Magn. Mater.*, 2014, **100**, 1–6.
17 K. Ø. Andresen, M. Hansen, M. Matschuk, S. T. Jepsen, H. S. Sørensen, P. Utko, D. Selmeczi, T. S. Hansen, N. B. Larsen, N. Rozlosnik and R. Taboryski, *J. Micromech. Microeng.*, 2010, **20**, 055010.
18 A. C. Hatch, J. S. Fisher, A. R. Tovar, A. T. Hsieh, R. Lin, S. L. Pentoney, D. L. Yang and A. P. Lee, *Lab Chip*, 2011, **11**, 3838–3845.
19 D. S. Kim, H. S. Lee, J. Han, S. H. Lee, C. H. Ahn and T. H. Kwon, *Microsyst. Technol.*, 2007, **14**, 179–184.
20 E. K. Sackmann, A. L. Fulton and D. J. Beebe, *Nature*, 2014, **507**, 181–189.
21 H. Becker, *Lab Chip*, 2010, **10**, 271–273.

Electronic Supplementary Material (ESI) for Lab on a Chip.

Ultrasonic welding for fast bonding of self-aligned structures in lab-on-a-chip systems

K. Kistrup C.E. Poulsen M.F. Hansen and A. Wolff

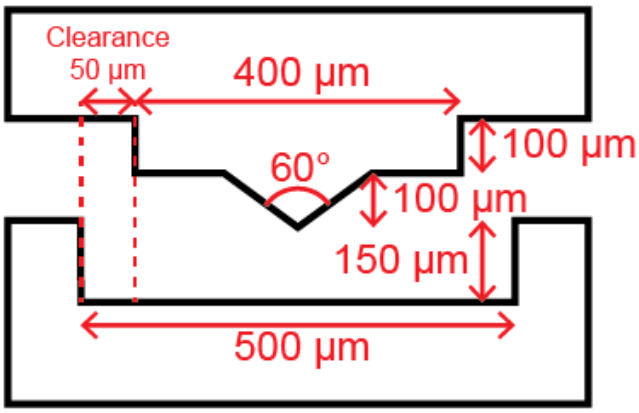

Fig. S1 Technical drawing of the tongue-and-groove joint used in Design A2. The overall design was based on the guides made available by Dukane's "Guide to Ultrasonic Plastics Assembly" (http://www.dukane.com/us/DL_DesignGuides.asp, accessed March 03, 2015). The features themselves were generated by CNC micromachining in aluminium.

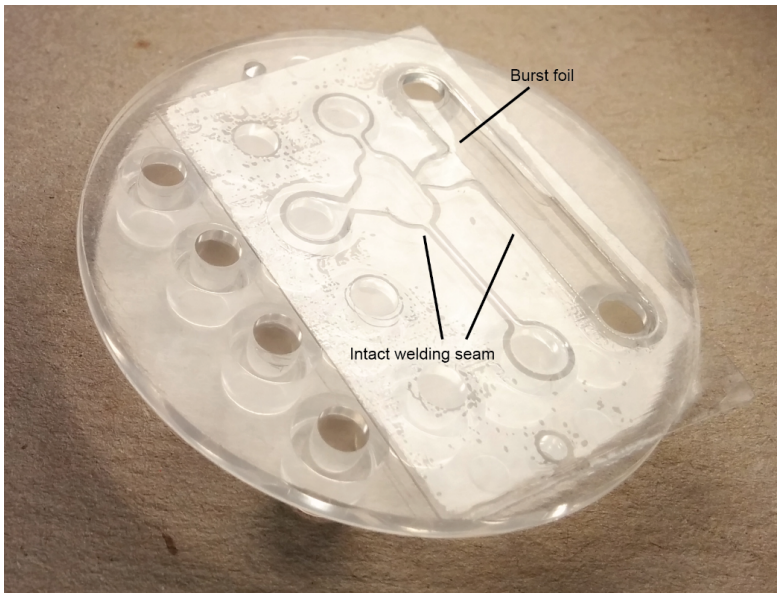

Fig. S2 Chip failure during pressure testing. To investigate the bonding strength of the welding seams pressurised air was applied to the chip inlet, while the other connectors were blocked. Design A1 failed after applying 3.5 bar (see photograph). The mode of failure was bursting of the 152 µm thick foil. Note that the welding seam is intact, as is visible by the darker surface. Design A2 with the 500 µm thick foil did not fail within the testing limits, which was up to 8.5 bar.

Ultrasonic welding for fast bonding of self-aligned structures in lab-on-a-chip systems
K. Kistrup C.E. Poulsen M.F. Hansen and A. Wolff

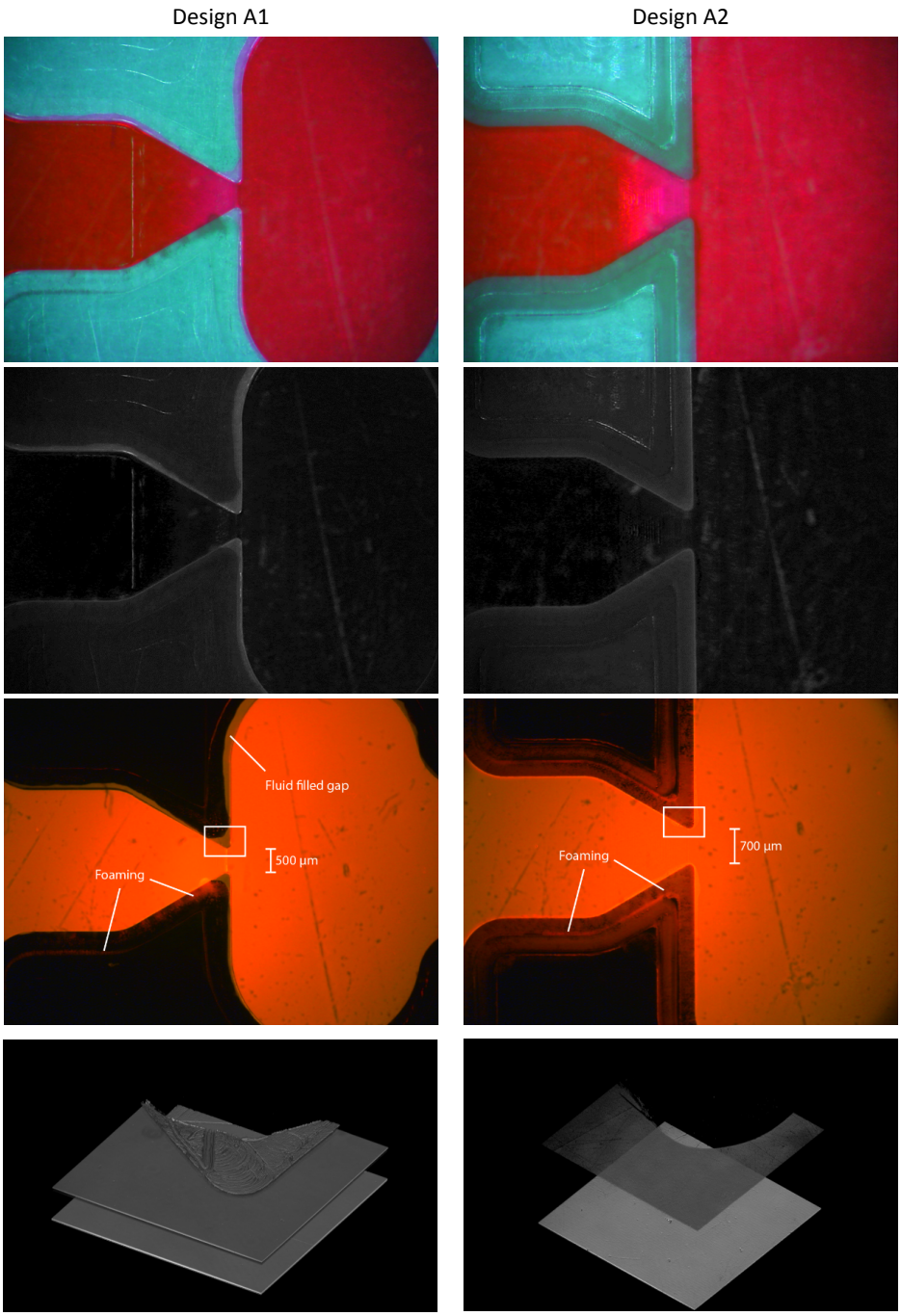

Fig. S3 Various micrographs of the capillary microvalve of Design A1 and A2. First two rows are standard bright field images, with the contrast and colour adjusted for clarity. Third row is taken with fluorescence microscopy. Note that the foaming, especially present in Design A2, reflects the light emitted from the rhodamine B solution; however, this is distinctly different from where actual fluid is present around the edges of Design A1. Row four shows a 3D representation of confocal micrographs taken at the upper corner of the capillary microvalve as marked with the white squares in row three (Zeiss LSM 700 confocal microscope (20x/0.5, z-stack images, 1.590 µm sections). The bottom plane shows the outer foil surface and the upper plane the inner foil surface. Note that for Design A1 the corner of the main chip part is also visible due to the gap, whereas for Design A2, no such surface exists.

Ultrasonic welding for fast bonding of self-aligned structures in lab-on-a-chip systems
K. Kistrup C.E. Poulsen M.F. Hansen and A. Wolff

Droplet PCR

Droplets were produced off-chip using a Droplet Junction Chip (#3000301, Dolomite, UK) using 2 % (V/V) Pico-Surf™ 1 (Dolomite, UK) in 3M FC40 oil (Walbom A/S, Denmark) as the continuous phase. The dispersed phase consisted of PCR master mixture for detection of *Campylobacter* species using universal Campylobacter primers targeting a 300 bp of 16sRNA gene described previously[1]. 1 pm/µl TaqMan probe labelled with 5´6-FAM and 3' BBQ (DNA Technology, Denmark) was added to the PCR mixture to detect DNA amplification. 10 µM Sulphorhodamine 101 (Cat 80101, Biotium, VWR, Denmark) was also added for improved droplet detection and size statistics. Target DNA samples were 7.2 fM chromosomal DNA isolated from *Campylobacter jejuni*, strain NCTC-11284, using QIAamp DNA mini kit (Qiagen, Germany)[1]. Thermo-cycling was performed on a Bio-Rad DNA Engine PTC-200 flat-bed PCR thermo-cycler with the COC lid contacting the hot-plate, see Fig. S1. Temperature steps used were as described previously[1].In brief, 5 minute hot start of 96 °C followed by 40 cycles consisting of a melting step at 94 °C for 15 seconds, an annealing step a 54 °C for 15 seconds and extension step at 72 °C for 8 seconds. The final extension was run for 60 seconds.

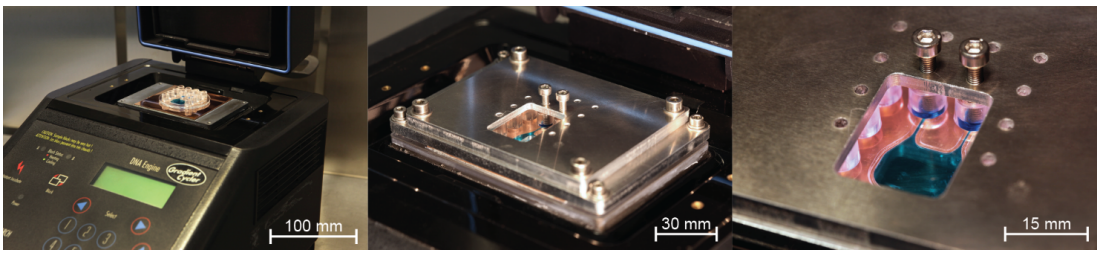

Fig. S4 Mounting of chip B on flat-bed PCR thermo-cycler.

Using circular Hough transformation, 13438 droplets were analysed in a single chip to have a diameter of 98.7 ± 6.0 µm which fits well with the observed monolayer. After thermal cycling, 79% of the droplets were observed to fluoresce from the TaqMan probe (FAM/FITC channel), which corresponds to a concentration of 5.2 fM, estimated using the *Poisson* distribution. As discussed in other ddPCR studies, this underestimation of 28% may be ascribed to the sensitivity of the PCR reaction and sample loss in the upstream microfluidic system[2–4].

1 Y. Sun, J. Høgberg, T. Christine, L. Florian, L. G. Monsalve, S. Rodriguez, C. Cao, A. Wolff, J. M. Ruano-Lopez and D. D. Bang, *Lab Chip*, 2013, **13**, 1509–14.

2 M. M. Kiss, L. Ortoleva-Donnelly, N. R. Beer, J. Warner, C. G. Bailey, B. W. Colston, J. M. Rothberg, D. R. Link and J. H. Leamon, *Anal. Chem.*, 2008, **80**, 8975–81.

3 L. Mazutis, A. F. Araghi, O. J. Miller, J.-C. Baret, L. Frenz, A. Janoshazi, V. Taly, B. J. Miller, J. B. Hutchison, D. Link, A. D. Griffiths and M. Ryckelynck, *Anal. Chem.*, 2009, **81**, 4813–21.

4 G. Jenkins, H. Zhang, Y. Zou, X. Leng, W. Zhang and C. Yang, *rsc.org*, 2011, 945–947.

6

Paper 3: Laser ablated micropillar energy directors

While exploring alternative methods for introducing groves in injection moulding tools for replicating EDs in microfluidic systems, we invented a new type of energy director: the micropillar energy directors. These EDs were formed by introducing cone like protrusion structures (CLP)[190] into replication moulds using a picosecond laser.

The CLP-EDs are advantageous over conventional apex-shaped energy directors (Figure 1 on page 87) in that (1) they can be freely and selectively added to mould surfaces accessible to a laser beam[a] in full 3D, (2) the height and width of the ED is not linked as is the case with the conventional ED (Figure 5c-f on page 90) and (3) the use of EDs of lower aspect ratio (height/width) gives good polymer flow control since the polymer is more evenly distributed pre welding (Figure 5g-h on page 90).

6.1 Remarks

6.1.1 Particle formation

As addressed in the supplementary information of the paper, we speculated that the CLP-EDs would be less prone to generating particulate. Particulate is dust-like particles which is generated by the rapid scrubbing of surfaces during the ultrasonic welding process[191–193], and can in the worst case contaminate the fabricated device[191,193]. As discussed in the supplementary information, we did not observe a significant difference between the number of particles before and after ultrasonic welding using conventional and CLP-EDs, suggesting that the amount of particulate generated by ultrasonic welding is generally low. Interestingly, we observed that samples observed to have moved laterally during welding (skating) contained 28.5 ± 7.8 particles (not subtracting background level) whereas non-skating specimens contained 3.8 ± 4.5 particles. An example of one of a skated sample is seen in Figure 6.1.

[a] Which is generally the case since the mould must allow for demoulding of the polymer piece.

This emphasises the importance of proper fixation of the two polymer pieces during welding. We have since implemented further fixation of the devices by adding a padding layer of adhesive tape (Semiconductor Wafer Tape SWT 20P+, Nitto) on the lower side of the sonotrode and on the fixation at surfaces contacting the lower polymer piece. The flexibility of this PVC based film adds traction to the assembly, while allowing for ultrasonic energy to be transferred[b]. Interestingly, Branson (now owned by Emerson) have presented the use of textured surfaces opposite the (conventional) energy director[150]. Apparently, welding to these surfaces reduces skating *and* particulate - supporting the hypothesis of a causal relation.

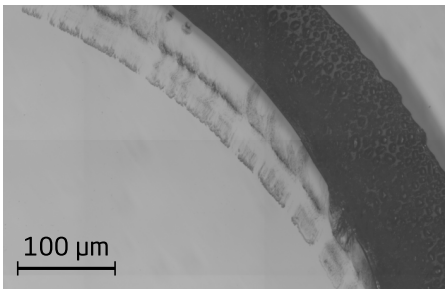

Figure 6.1: Micrograph of specimen which skated during ultrasonic welding. Imaging is conducted from the lid side looking down on the CLP-EDs. Note the visible periodic imprints in the lid from the energy directors. The welding is also incomplete since the microstructures have not completely collapsed.

6.1.2 Elevated channel walls

An unexpected advantage of bonding high aspect ratio, free standing structures were that it was significantly easier to achieve a uniform and consistent welding compared to when bonding devices with only the energy directors protruding. By defining the channel with protruding walls, the plane of welding is raised, and interference from moulding defects elsewhere on the device is thereby less catastrophic. Particularly, the ultrasonic welding energy required for welding is more consistent since energy is not absorbed into unwanted areas of the device. See Figure 6.2.

6.2 Additional applications of microstructures

The microstructuring method and the replicated microstructures were not only well suited for ultrasonic welding, but we also found that replicating large surfaces in a hydrophobic material (e.g. polypropylene) enabled us to produce superhydrophobic surfaces. The novelty and high commercial relevance of this microstructuring method persuaded us to patent the technology and raise funding for (and start) a ”spin-out

[b] It has not been necessary to update the welding parameters/settings after adding the tape, and we have not observed a decrease in welding quality.

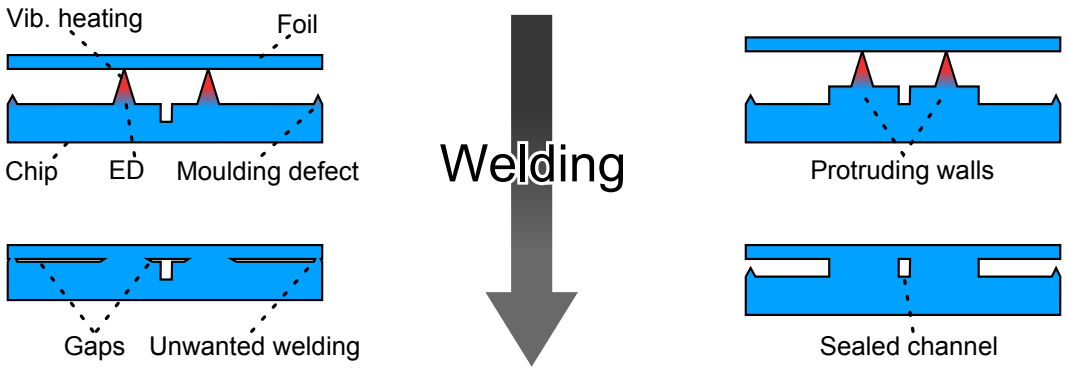

Figure 6.2: Comparison of ultrasonic welding using different channel defining strategies. (top row) Pre welding. (bottom row) Post welding. (left column) Conventional layout with only the energy directors and moulding defects protruding above the bulk plane of the device. (right column) Layout with raised walls. Note that the moulding defects are less interfering with the welding process.

project" called TransForm-Technologies. 725.000 DKK was raised and spent on maturation of the technology, incorporating and testing it in a commercial setting, formulating a business plan and composing patent applications. TransForm-Technologies and the associated patent applications are presented in Appendices A and B-D, respectively.

IOP Publishing Journal of Micromechanics and Microengineering
J. Micromech. Microeng. **00** (2016) 000000 (7pp) UNCORRECTED PROOF

Technical Note

Laser ablated micropillar energy directors for ultrasonic welding of microfluidic systems

AQ1

Carl Esben Poulsen, Kasper Kistrup, Nis Korsgaard Andersen, Rafael Taboryski, Mikkel Fougt Hansen and Anders Wolff

Department of Micro- and Nanotechnology, Technical University of Denmark, DTU Nanotech, Building 345 East, DK-2800 Kongens Lyngby, Denmark

E-mail: anders.wolff@nanotech.dtu.dk

Received 19 November 2015, revised 10 February 2016
Accepted for publication 29 February 2016
Published

Abstract

We present a new type of energy director (ED) for ultrasonic welding of microfluidic systems. These micropillar EDs are based on the replication of cone like protrusion structures introduced using a pico-second laser and may therefore be added to any mould surface accessible to a pico-second laser beam. The technology is demonstrated on an injection moulded microfluidic device featuring high-aspect ratio ($h \times w = 2000\ \mu\text{m} \times 550\ \mu\text{m}$) and free-standing channel walls, where bonding is achieved with no detectable channel deformation. The bonding strength is similar to conventional EDs and the fabricated system can withstand pressures of over 9.5 bar.

Keywords: ultrasonic welding, polymer fusion, microfluidics, bonding, injection moulding

S Online supplementary data available from stacks.iop.org/JMM/00/0000/mmedia

AQ2 (Some figures may appear in colour only in the online journal)

1. Introduction

In academia, soft imprint lithography with polydimethylsiloxane (PDMS), sealed using plasma activated bonding, is by far the most-used route for the rapid prototyping of microfluidic systems [1]. The high elasticity of PDMS allows for the fabrication of advanced valves and gates, and its good solvent compatibility enables the use of multiphase liquid systems [2]. For commercial production, however, hot embossing or injection moulding (IM) combined with ultrasonic welding (UW) are more common for high throughput fabrication of low-cost disposable devices [3]. Since the physical and chemical properties of thermoplastics differ significantly from those of PDMS, the transfer of the technology from academia to industrial production may prove unfeasible or require the fabrication process to be completed redesigned [3]. Moreover, PDMS has fabrication limitations compared to thermoplastics [4]; for example, its the high elasticity and self-adhesion may induce the collapse of high- [5] and low- [6] aspect ratio channels and structures via self-adhesion. Thermoplastics, on the other hand, are generally stiffer and less self-adhering. Recently, we presented ultrasonically welded, injection moulded, large area, low-aspect ratio cyclic olefin copolymer (COC) devices [7, 8], where the fabrication in PDMS of similar devices has traditionally relied on embedded glass slides to achieve sufficient rigidity [9]. Similarly, high-aspect ratio features in PDMS devices can only be realised by the use of sacrificial moulding methods [10], where these features have to be structurally supported by a solid bulk part [11]. Many techniques for the bonding of thermoplastic devices require elevated temperatures and/or high pressures [12–15], which may cause structural

AQ3

JNL:JMM PIPS: AA1A1D TYPE: TEC TS: NEWGEN DATE:22/3/16 EDITOR: IOP SPELLING: US

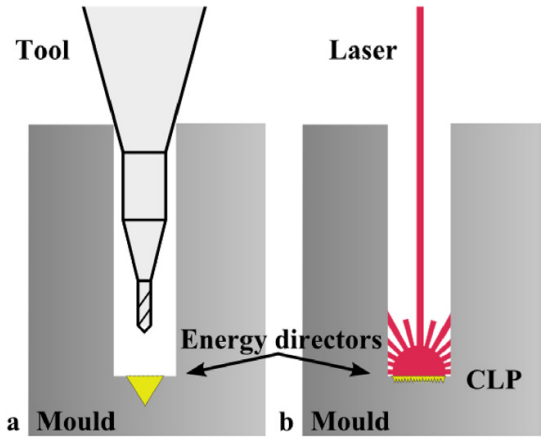

Figure 1. Schematics of methods for introducing ED forming grooves in moulds. (a) Conventional EDs introduced by micro-milling (or electric discharge machining). (b) Laser ablated CLPs. Removed material is highlighted in yellow.

deformation, and the bonding of high-aspect ratio structures is therefore not easily realized. UW, on the other hand, is a fast back-end bonding process, and may be conducted at relatively low pressures and at room temperature. However, it requires the addition of energy director (ED) structures protruding on top of the channel walls. For device fabrication based on replication techniques (e.g. hot embossing and injection moulding), the tool has the inverse structure and the ED structures thus have to be realized as depressions in the bottom of the cavity structure used to define the channel wall. ED structures can be realized, e.g. by micro-milling, which is a rapid mould tool fabrication process, but the size of the milling tool limits their dimensions. Milling tools are made as small as 10–50 μm, yet it is often not feasible to make EDs on high-aspect ratio wall structures in this way, since the drill aspect ratio is often limited to 1:3, and the micro mills are short and mounted on large shanks (figure 1(a)).

In this paper, we present a new type of micropillar EDs for UW of microfluidic systems. These EDs are formed by introducing cone-like protrusion structures [16] as a back-end process into replication moulds using a picosecond laser. They have the substantial advantage over traditional EDs that they can be defined on any surface accessible to a high energy picosecond laser beam (figure 1(b)). Moreover, these EDs can be introduced in designated areas on the tool, and the width of these areas can be chosen independently from the heights of the EDs. This is in contrast to traditional EDs, where larger widths are accompanied by higher structures. The CLPs are formed stochastically within the designated area, so only ablation of the general ED shape is required, not the individual CLPs. We demonstrate the technology in an aluminium mould, but also verify the CLP formation in tool steel used for industrial moulds. To characterise the performance of this new type of EDs, we compare CLP-EDs to micromilled EDs with respect to (1) welding strength, (2) structural deformation of a free-standing high-aspect structure, and (3) formation of particles during welding (any formed particles may interfere with the function of the microfluidic device [17]). The results of particle forming are presented in the supplementary information (stacks.iop.org/JMM/00/000/mmedia).

2. Materials and methods

2.1. Chip fabrication

Injection moulding was carried out using a custom-made moulding tool comprising a 50 mm diameter disk cavity with 12 luer inlets [7, 8, 12, 13, 18, 19]. The tool could be combined with mould inserts with structures machined in aluminium 2017 (al2017) [19]. Prior to injection moulding, two types of ED structures were introduced: (1) Traditional EDs introduced by micro-milling using a 60° helical engraving tool (#7025, DIXI Polytool, Le Locle, Switzerland). An apex depth of 100 μm was used (width = 115 μm). (2) Microstructured CLP-EDs written using a FUEGO 1064 nm, 50 W picosecond laser (Time Bandwidth, 3D-Micromac AG, Chemnitz, Germany) mounted in a microSTRUCT vario (3D-Micromac AG). CLPs were introduced by scanning designated areas with parallel lines (10 μm spacing), which was repeated 20 times at 50% power and 1000 mm s^{-1} with the focus plane 1.3 mm above the surface (green lines in figure 3). The writing time was 200 s cm^{-2}. These settings were similar to the work by Brüning *et al* in 2014 [16], but the tuning of parameters was conducted towards higher roughness. As demonstrated by Wu *et al* [20], the dimensions of the CLPs may be tailored by the laser parameters. In this study, we aimed for CLPs slightly higher than 10 μm, since smaller EDs generally require specialised levelling systems to achieve satisfactory welding [21].

To confirm the commercial relevance of the technology, we also demonstrated the writing of CLPs in high performance tool steel Orvar2343 (MetalCentret, Glostrup, Denmark). Al2017 was preferred for mould making in this low-volume academic setting study due to its ease for machining.

The injection moulding was carried out on a Victory 80/45 Tech hydraulic injection moulding machine (Engel, Schwertberg, Austria) using COC grade 5013L-10 (TOPAS Advanced Polymers GmbH, Frankfurt-Höchst, Germany) with injection and mould temperatures of 270 °C and 120 °C, respectively. Injection pressure was 1766 bar and the process cycle time was 45 s per part.

Fabricated chips were bonded to a 500 μm thick foil of COC grade 5013S-04 (TOPAS Advanced Polymers GmbH) by UW. This was performed at ambient temperature using a Telsonic-USP4700 ultrasonic welder (Telsonic, Erlangen, Germany), depositing 25 J with 75% vibrational amplitude, a trigger force of 400 N and 0.5 bar vertical welding pressure. With the fitted 2 × booster and flat sonotrode (78 × 115 mm^2), the vibrational amplitude normal to the sample surface was approximately 44 μm. See figure 2 for schematics of the ultrasonic welding process utilised. A video of the UW process described is found in the supplementary information.

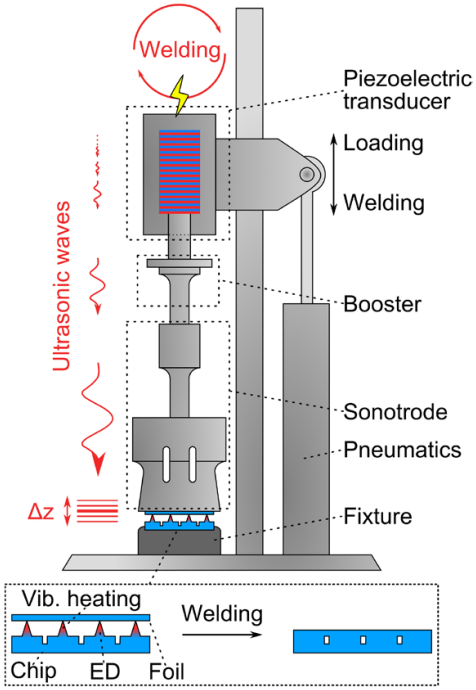

Figure 2. Schematic of the ultrasonic welding machine used in this study. Prior to welding, the pneumatic cylinder is set to the welding pressure (0.5 bar), clamping the foil and chip together vertically. Next, the piezoelectric transducer generates a downward 20 kHz pulse of ultrasonic waves which is then amplified and shaped to a planar wave in the booster and sonotrode. Finally, the ultrasonic waves are transferred from the vibrating underside of the sonotrode to the polymer foil (sonotrode amplitude, $\Delta z = 44$ μm. Here they cause local heating and melting of the EDs due to the high energy density caused by the low contact area. As the foil and chip fuse, the contact area increases and the heating terminates. (Inset) close-up (not to scale) of polymer chip with EDs (not to scale) pre welding (left) and post welding (right). Vibrational heating is highlighted in red.

2.2. Bonding strength

The bonding strength was assessed using the *razor-blade test* based on fracture propagation developed by Maszara *et al* [22], and employed by Matteucci *et al* [13] to assess the strength of thermal bonding in similar chips. To perform the test, two flat mould inserts with a milled $5.15 \times 42.5 \times 0.25\,\text{mm}^3$ cavity were fabricated by micro-milling. In this cavity, the first insert further featured a 40.5 mm long conventional ED made by conventional milling and the second insert featured a laser micromachined ED with CLPs on an area of $40.5 \times 0.2\,\text{mm}^2$. The resulting injection moulded parts thus featured 0.25 mm high plateaus with the respective EDs on top. The parts were bonded to a COC foil as described above. Details of the razor-blade testing as well as the results on all chips are given in the supplementary material.

2.3. High-aspect ratio microfluidic system

UW of free-standing structures was demonstrated on an intertwining microfluidic system consisting of two 400 μm wide channels. These channels are separated by 2000 μm high, 550 μm wide, free-standing walls with a 200 μm-wide band of micropillar EDs on top (figure 3). Note that these EDs cannot be fabricated by conventional methods due to the small size of the structures and the large aspect ratio. The microfluidic system spanned a $36.3 \times 25.8\,\text{mm}^2$ rectangle. Note that the 200 μm wide ED structure in expanding regions was separated into two bundles of ten lines, keeping a constant wall-to-edge distance of 180 μm (figure 3(c)).

Channel deformation was characterised along four cross sections using confocal microscopy, with a Zeiss LSM 700 with voxel sizes of $X \times Y \times Z = 0.313 \times 0.313 \times 5.387$ μm^3. The location of the cross sections and the bonded chip are shown in figures 3(a) and (b), respectively.

3. Results and discussion

3.1. CLP and ED structures

Figures 4(a) and (b) show scanning electron microscopy (SEM) images of the CLPs written in the al2017 mould. It is of note that although the laser scanning is conducted in bundles of parallel lines, the formed CLPs are stochastically formed within the laser ablated area. This may be ascribed to the fact that the microphase explosions causing the CLPs are caused by a combination of metal impurities (alloy) picking up the energy, the pulsing nature of the laser beam and non-uniformity of the laser fluence distribution [20]. The CLPs have a typical height and spacing of 10 μm and 10 μm, respectively. On average, the CLP area protrudes 47 μm from the plane of the part wall (figure 5(g)). Note that the CLPs are locally convex depressions in the mould which therefore facilitate easy demoulding during replication. Figure 4(c) shows a SEM image of a COC cast of the mould. The replicated structures are observed to have rounded tops due to imperfect filling during replication. We found that operating at conditions yielding higher fidelity replication resulted in more difficult demoulding, due to stronger adhesion between the mould and its replica. This rounding did not affect the performance of the EDs and attempts to achieve more pointed structures and better replication in the z-direction were therefore not pursued. Figure 4(d) shows tool steel Orvar2343 ablated to produce CLPs similar to those demonstrated in al2017.

Figures 5(a) and (b) show SEM images of the CLP-EDs in the al2017 mould for fabrication of the high-aspect ratio microfluidic system. The images clearly show the feasibility of writing CLP-ED structures at the bottom of the trenches in the mould. Note that the separation and joining of bundles of laser lines do not alter the pattern and formation of CLPs. Thus, CLP-EDs can be formed in any pattern or geometry. Corresponding SEM images of the injection moulded COC part (figures 5(c) and (d)) clearly show that micropillar structures are well reproduced laterally on the top of the high-aspect ratio wall.

Figures 5(e) and (f) show optical micrographs of a section of the wall of a moulded part pre and post UW. Due to the structure of the CLPs, the final micropillar CLP-EDs of the polymer chip are opaque (figure 5(e)). However, like

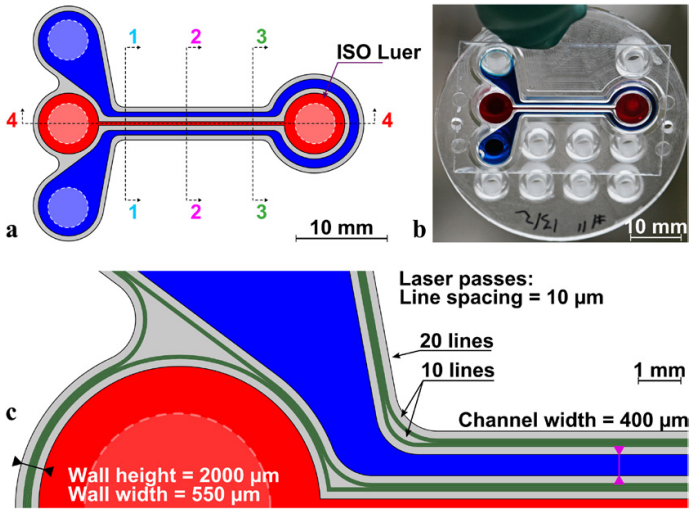

Figure 3. (a) Schematic drawing of high aspect ratio chip. Blue: outer channel, red: inner channel, and gray: walls. Cross sections 1–4 for confocal imaging are indicated. (b) Image of bonded chip filled with dye solutions for highlighting channels. Note that the sealing lid only contacts the walls. (c) Chip with laser patterning lines added (green). Note that the 20 lines are separated into two bundles at the corners, to keep a constant edge distance (180 μm).

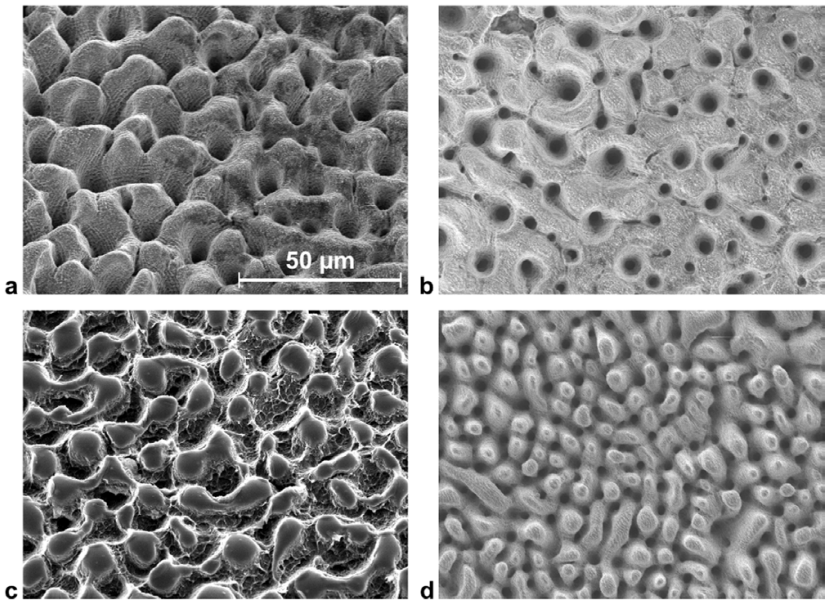

Figure 4. (a) and (b) SEM images of CLPs in al2017 moulds (30° and 0° tilt, respectively) and (c) replicated COC (30° tilt). (d) Industrial mould making steel Orvar2343 modified using the presented technology (0° tilt).

conventional butt joint EDs [8], the joints are transparent post welding (figure 5(f)). It is worth noting that no signs of trapped or compressed air are observed in the corner section, where the CLP-EDs are split (figure 5(e)). Little or no gap is observed post UW in figure 5(f). This indicates that the micropillar structure does not trap air during UW, which would otherwise lead to hazy and weakened bonds. SEM images in figures 5(g) and (h) show an unbonded and bonded chip, respectively, cleaved to show a cross section of the top of the walls. Good polymer control was achieved, evident by the position of the polymer comprising the CLP-EDs pre and post welding, as little or no flash formed (polymer spilling into the channel).

3.2. Bonding strength

Bonding strengths in terms of the surface energy, γ, calculated from razor-blade tests are listed in table 1. Bonding strengths

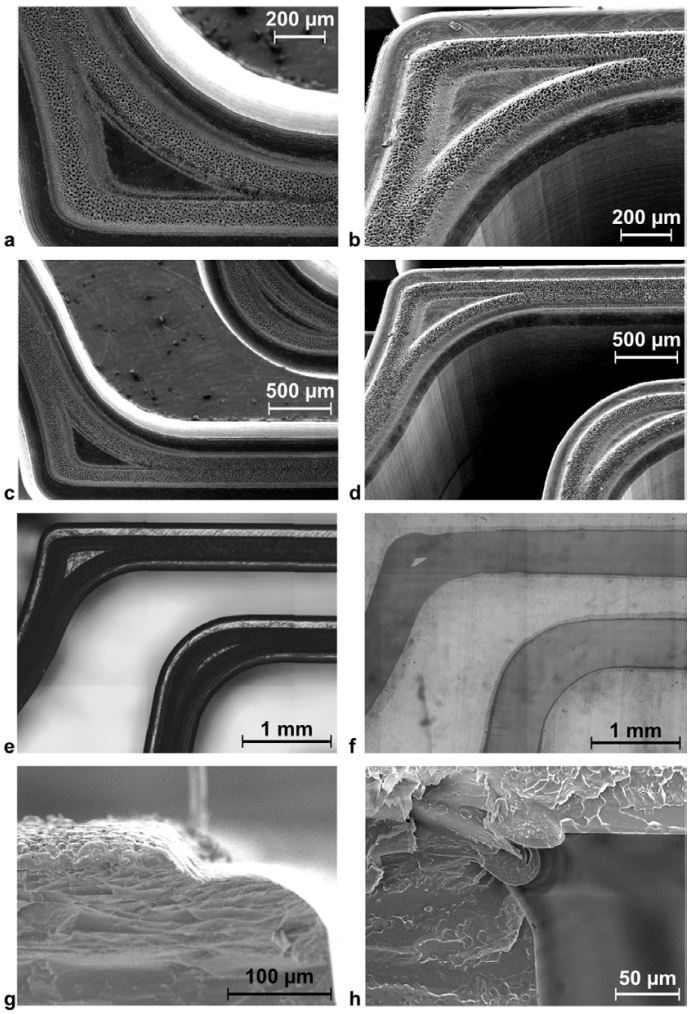

Figure 5. (a) and (c) SEM images of modified mould on indicated length scales. (b) and (d) SEM images of injection moulded piece, 30 degrees tilt. (e) Micrograph of unbonded micro pillar EDs and (f) bonded. Note the transparent welding seam. (g) Cross-sectional SEM images in direction 2 of figure 3(a) of unbonded, cleaved, and (h) bonded, cleaved, chips. Note the solidified polymer from the welding process in (h).

for other materials and bonding methods commonly used in microfluidics are also listed. These were calculated from channel dimensions and channel burst pressures. The bonding strength measurements and calculations are given in the tables S1 and S2 in the supplementary information.

Table 1 clearly shows that the bonding strength for thermoplastics is largest for structures bonded using UW. No significant difference is observed between conventional EDs and CLP-EDs. UW likely provides the strongest bonding because the substrate is not chemically altered (e.g. bond breakage by UV radiation or plasma activation for thermal bonding), and the bonding strength is thus limited by the bulk strength of the substrate. In high-pressure applications, it is important to note that the upper limit pressure (burst pressure) of a device is determined by two additional factors: the geometry and Young's modulus [27]. A softer material will flex more and result in larger forces in junctions (cracks) [27]. This explains why most PDMS devices burst at pressures lower than 6 bar [25, 26], even when covalent bonding methods are used [25].

3.3. High-aspect ratio microfluidic system

The performance of CLP-ED structures were tested in the described high-aspect ratio microfluidic system. First, we verified that the microfluidic channels were leak-tight (see figure 3(b)). Further, pressure testing with gas applied to the outer channel while leaving the inner channel at ambient pressure showed that the devices (three were tested) could sustain pressure of up to at least 9.5 bar (the maximum pressure available in our laboratory).

Figure 6 shows confocal scans of the free-standing wall structures of the device along the cross sections 1–4 (see

Table 1. Bonding strength results expressed in terms of surface energy, γ.

Bonding method	Material	γ (J m^{-2})
UW, conventional EDs (this study)	COC Topas 5013 L-10	100 ± 30[b]
UW, CLP-EDs (this study)	COC Topas 5013 L-10	122 ± 23[b]
UV activated thermal bonding [13]	COC Topas 5013 L-10	61
UV/ozone thermal bonding [14]	COC Zeonor 1020 R	8.1
Solvent bonding, cyclohexane [23]	COC Topas 8007	6.2[a]
Plasma + thermal bonding [15]	COP ZEONEX	8
Solvent bonding, 75% acetone [24]	PMMA	13.6
Oxygen plasma [25, 26]	PDMS	44.4 ± 2[a]
Uncured PDMS as adhesive [25]	PDMS	227[a]

[a] These surface energies from the literature are calculated from the channel dimensions, Young's modulus, and bursting pressure. See supplementary information for calculations.
[b] A two-sample (unpaired) T-test showed no significant difference in the bonding strength between conventional EDs and CLP-EDs: $t(10) = -1.84$, $p = 0.084$.

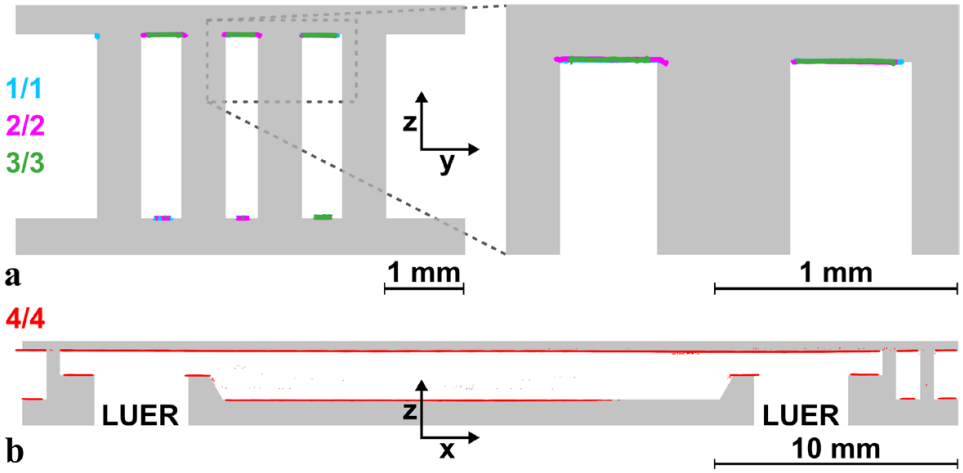

Figure 6. 2D cross-sections 1–4 of bonded chips. The cross sections are denoted by labels and colour identical to figure 3. These 2D images are generated from the confocal image stacks by averaging 100 cross-sections along the x-axis (top figures) or y-axis (bottom figure). This corresponds to averaging over a length of 31.3 μm. The data is overlaid on the chip CAD file (grey). Dashed box: close-up of the data.

figure 3(a)). The images are overlaid with the corresponding CAD file used for the mould fabrication. From the confocal scans, we find that the channel height of the welded structure matches that of the design (2000 μm) with a tolerance of ± 4.2 μm. This value is smaller than the confocal image voxel height and we conclude that any height difference is below our detection limit.

4. Conclusion

We presented a new type of ED for ultrasonic welding (UW) of microfluidic systems based on micropillar EDs. These are based on replication of CLPs in aluminium, formed using a picosecond laser, and can be added to any mould surface accessible to a high power pico-second laser. We have demonstrated the technology by injection moulding microfluidic devices featuring high-aspect ratio structures and shown that UW of the devices is possible with no detectable channel deformation. This would be impossible using conventional bonding methods that involve high pressures and temperatures. We have characterised the performance of the CLP-EDs and found that bonding strength is similar to conventional EDs, with no particle formation. The bonded devices could withstand 9.5 bar of pneumatic pressure without fracturing.

Most importantly, the technology has been demonstrated to work with high endurance tool steel used for making high performance injection moulding tools, which is a necessity for commercial applications. In addition, with a modification rate of 200 s cm^{-2} and full 3D capabilities, the technology is fast and allows for the addition of CLP-EDs in existing moulds regardless of their origin, be it electric discharge machining, micro-milling or cleanroom fabrication (electroforming).

Acknowledgments

This work is funded by DTU Nanotech and the Danish Council for Strategic Research through the Strategic Research Centre PolyNano (Grant no. 10-092322/DSF). AQ4

AQ5 **References**

[1] Waldbaur A, Rapp H, Länge K and Rapp B E 2011 Let there be chip—towards rapid prototyping of microfluidic devices: one-step manufacturing processes *Anal. Methods* **3** 2681

[2] Sia S K and Whitesides G M 2003 Microfluidic devices fabricated in poly(dimethylsiloxane) for biological studies *Electrophoresis* **24** 3563–76

[3] Becker H 2010 Mind the gap! *Lab Chip* **10** 271–3

[4] Mukhopadhyay R 2007 When PDMS isn't the best *Anal. Chem.* **79** 3248–53

[5] Roca-Cusachs P, Rico F, Martínez E, Toset J, Farré R and Navajas D 2005 Stability of microfabricated high aspect ratio structures in poly(dimethylsiloxane) *Langmuir* **21** 5542–8

[6] Huang Y Y, Zhou W, Hsia K J, Menard E, Park J U, Rogers J A and Alleyne A G 2005 Stamp collapse in soft lithography *Langmuir* **21** 8058–68

[7] Kistrup K, Poulsen C E, Hansen M and Wolff A 2015 Ultrasonic welding for fast bonding of self-aligned structures in lab-on-a-chip systems *Lab Chip* **15** 1998–2001

[8] Poulsen C E, Wootton R C R, Wolff A, DeMello A J and Elvira K S 2015 A microfluidic platform for the rapid determination of distribution coefficients by gravity-assisted droplet-based liquid–liquid extraction *Anal. Chem.* **87** 6265–70

[9] Hatch A C, Fisher J S, Tovar A R, Hsieh A T, Lin R, Pentoney S L, Yang D L and Lee A P 2011 1-million droplet array with wide-field fluorescence imaging for digital PCR *Lab Chip* **11** 3838–45

[10] Kung Y-C, Huang K-W, Fan Y-J and Chiou P-Y 2015 Fabrication of 3D high aspect ratio PDMS microfluidic networks with a hybrid stamp *Lab Chip* **15** 1861–8

[11] Natarajan S, Chang-Yen D A and Gale B K 2008 Large-area, high-aspect-ratio SU-8 molds for the fabrication of PDMS microfluidic devices *J. Micromech. Microeng.* **18** 045021

[12] Tanzi S, Østergaard P F, Matteucci M, Christiansen T L, Cech J, Marie R and Taboryski R 2012 Fabrication of combined-scale nano- and microfluidic polymer systems using a multilevel dry etching, electroplating and molding process *J. Micromech. Microeng.* **22** 115008

[13] Matteucci M, Christiansen T L, Tanzi S, Ostergaard P F, Larsen S T and Taboryski R 2013 Fabrication and characterization of injection molded multi level nano and microfluidic systems *Microelectron. Eng.* **111** 294–8

[14] Tsao C W, Hromada L, Liu J, Kumar P and DeVoe D L 2007 Low temperature bonding of PMMA and COC microfluidic substrates using UV/ozone surface treatment *Lab Chip* **7** 499–505

[15] Mizuno J, Ishida H, Farrens S, Dragoi V, Shinohara H, Suzuki T, Ishizuka M, Glinsner T, Lindner F P and Shoji S 2005 Cyclo-olefin polymer direct bonding using low temperature plasma activation bonding *13th Int. Conf. Solid-State Sensors, Actuators Microsystems, 2005. Digest Technical Paper (TRANSDUCERS)* vol 2 pp 1346–9

[16] Brüning S, Jenke G, Du K and Gillner A 2014 High Precision laser processing of steel surfaces with sub-ns-lasers *Phys. Proc.* **56** 919–26

[17] Branson X X 1975 Part Design for ultrasonic welding *Technical Information PW-3* vol 1 (Branson Ultrasonics) AQ6

[18] Andresen K Ø *et al* 2010 Injection molded chips with integrated conducting polymer electrodes for electroporation of cells *J. Micromech. Microeng.* **20** 055010

[19] Kistrup K, Poulsen C E, Østergaard P F, Haugshøj K B, Taboryski R, Wolff A and Hansen M F 2014 Fabrication and modelling of injection moulded all-polymer capillary microvalves for passive microfluidic control *J. Micromech. Microeng.* **24** 125007

[20] Wu B, Zhou M, Li J, Ye X, Li G and Cai L 2009 Superhydrophobic surfaces fabricated by microstructuring of stainless steel using a femtosecond laser *Appl. Surf. Sci.* **256** 61–6

[21] Lee K G, Shin S, Kim B I, Bae N H, Lee M-K, Lee S J and Lee T J 2015 Ultrasonic assisted bonding method for heterogeneous microstructures using self-balanced zig *Lab Chip* AQ7

[22] Maszara W P, Goetz G, Caviglia A and McKitterick J B 1988 Bonding of silicon wafers for silicon-on-insulator *J. Appl. Phys.* **64** 4943–50

[23] Mair D A, Rolandi M, Snauko M, Noroski R, Svec F and Fréchet J M J 2007 Room-temperature bonding for plastic high-pressure microfluidic chips *Anal. Chem.* **79** 5097–102

[24] Wan A M D, Sadri A and Young E W K 2015 Liquid phase solvent bonding of plastic microfluidic devices assisted by retention grooves *Lab Chip* **15** 3785–92

[25] Eddings M A, Johnson M A and Gale B K 2008 Determining the optimal PDMS–PDMS bonding technique for microfluidic devices *J. Micromech. Microeng.* **18** 067001

[26] Bhattacharya S, Datta A, Berg J M and Gangopadhyay S 2005 Studies on surface wettability of poly(dimethyl) siloxane (PDMS) and glass under oxygen-plasma treatment and correlation with bond strength *J. Microelectromech. Syst.* **14** 590–7

[27] Anderson T L 2005 *Fracture Mechanics: Fundamentals and Applications* 3rd edn (London: Taylor and Francis)

SUPPLEMENTARY INFORMATION

Laser ablated micropillar energy directors for ultrasonic welding of microfluidic systems

Carl Esben Poulsen[a], Kasper Kistrup[a], Nis Korsgaard Andersen[a], Rafael Taboryski[a], Mikkel Fougt Hansen[a] and Anders Wolff[a]*

[a] Department of Micro- and Nanotechnology, Technical University of Denmark, DTU Nanotech, Building 345 East, DK-2800 Kongens Lyngby, Denmark

S1. Bonding strength assessment by razor-blade test

Welding strength was assessed using the razor-blade test based on fracture propagation developed by Maszara *et al.* [22], and employed by Matteucci *et al.* [13], which uses the equation $\gamma = 3\mathrm{H}^2h^3E/(16L^4)$. Here, γ [J/m^2] is the surface energy required for fracturing the welding, creating new surfaces, H is the deflection height, h is the foil thickness, L is the equilibrium crack length and E is Young's modulus which for COC 5013S-04 is 3.2 GPa (suppliers datasheet), see Fig. S1 for annotations. H was the blade thickness (250 µm) minus the ultrasonic welding gap [19]. The welding gap was measured by scanning electron microscopy (SEM) to be 15.3 µm and 14.1 µm for conventional and CLP-EDs, respectively. It is important to note that in this context, the surface energy, γ, includes irreversible bond breakages, and must not be confused with surface tension. In this test, shear effects of the foil are neglected which is reasonable when $L > 3h/2$ as is the case in the presented data [22]. The razor blade test was repeated on ten devices for each ED type. Cross-sectional SEM images similar to the those presented in Figs. 5g,h were used for determining the bonding gap height.

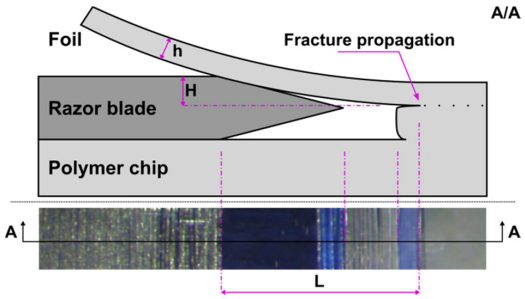

Fig. S1 A/A: Schematic cross-section of the razor blade test for determination of bonding strength (not to scale). Bottom inset: image of experiment with cross-section A/A highlighted.

S2. Bonding strength data

Table S1. Bonding strength data comparing the two types of energy directors. For all samples, blade thickness is 250 µm, *h* is 167 µm, Young's modulus is 3.2 GPa, and the Poisson ratio is 0.37. *H* is 235 µm and 236 µm for the conventional- and micropillar EDs, respectively.

Conventional ED			CLP-ED		
Sample#	*L* [mm]	Surface energy [J/m^2]	Sample#	*L* [mm]	Surface energy [J/m^2]
1	1.17	95	1	1.13	111
2	1.26	71	2	1.13	111
3	1.06	142	3	1.02	165
4	1.04	155	4	1.05	151
5	1.13	109	5	1.14	107
6	1.18	93	6	1.16	99
7	1.34	55	7	1.17	95
8	1.23	19	8	1.08	130
9	1.15	101	9	1.08	130
10	1.16	99	10	1.11	120
Avg	1.17	100	Avg	1.11	122
SD	0.09	30	SD	0.05	23
CV%	7.67	30	CV%	4.43	19

S3. Bonding strength estimated from device burst pressure

The bonding strength in terms of surface energy, γ [J/m^2], can be estimated from the minimum pressure causing the device to fail. This is done by assuming that the applied pressure results in tensile stress normal to the surface, while taking into account the geometry and flexibility of the device [27]. For a circular chamber (for example, an inlet), we solve the equation describing the minimum tensile stress required to cause an infinite sized object harvesting a penny shaped crack to fail [27]. This leads to the equation $\gamma = P_{\max}^2 2(1-\nu^2)a/(\pi E)$, where $P_{\max}$ is the minimum failing pressure, ν is the poisson ratio, a is the radius of the chamber, and E is Young's modulus. Similarly, for a rectangular channel, we solve the equation for a rectangular void, leading to the equation $\gamma = P_{\max}^2 \pi a/(2E)$. Here $2a$ is the smallest dimension of the channel.

Table S2. Bonding strength values calculated from literature data on channel dimensions and burst pressure.

Reference	Bonding type	Material	Shape	$2a$ [mm]	ν	E [MPa]	$P_{\max}$ [bar]	γ [J/m^2]
Eddings *et al.* (2008)[25]	Oxygen plasma	PDMS to PDMS	Circular	5.0	0.5	2.5	3.0	43.0
Bhattacharya *et al.* (2005)[26]	Oxygen plasma	PDMS to PDMS	Circular	3.0	0.5	2.5	4.0	45.8
Eddings *et al.* (2008)[25]	Uncured PDMS as adhesive	PDMS to PDMS	Circular	5.0	0.5	2.5	6.9	227
Mair *et al.* (2007)[23]	Solvent, cyclohexane	Topas 8007	Rectangular	0.082	0.37	3200	173	6.16

S4. Particle formation

Particle formation is often presumed to be a problem in connection with UW. To quantify whether particles were formed during the vibrations of ultrasonic welding, devices featuring a circular ⌀=6 mm, 300 µm deep chamber were fabricated and bonded using either conventional EDs or CLP-EDs.

Quantification was done by bright field imaging the chamber using a Zeiss Axio Imager.M2 microscope with 10× magnification yielding a pixel width of 0.645 µm. To eliminate background dust and/or mould voids, particle counting was performed pre and post welding.

Testing revealed that UW using either type of EDs in our laboratory did not cause any detectable particle formation. Details are given in Table S3. However, we noted that samples, which had been discarded due to the occurrence of skating (i.e., lateral movement of the ED during welding), were the only ones containing particles (on the order of 10 particles/device). The fact that skating generates particles is not surprising when considering that the two polymer surfaces are scrubbing while under high pressure and 20 kHz vibrations.

Table S3. Particle and void count of welded foil before and after ultrasonic welding. As can be seen, the observed number of voids and particles are *fewer* after welding, suggesting little or no particle formation during ultrasonic welding.

	Particles+voids
Unbonded foil	7.5±3.4
Foil bonded using conventional EDs	7.0±2.4
Foil bonded using micropillar EDs	2.5±0.5

S5. Supplementary video

The video shows the ultrasonic welding process, described in the main section, played back in real time. First, the chip part is placed in the fixture. Then the protective film of the foil is removed and it is placed on top of the chip part. Finally, the ultrasonic welding machine is engaged and the bonded chip removed from the fixture. The chip being welded is the droplet PCR chip presented in [7].

S6. References

References used in this supplementary information are numbered according to the bibliography of the main text:

[13] Matteucci M, Christiansen T L, Tanzi S, Ostergaard P F, Larsen S T and Taboryski R 2013 Fabrication and characterization of injection molded multi level nano and microfluidic systems *Microelectron. Eng.* **111** 294–8.

[19] Kistrup K, Poulsen C E, Østergaard P F, Haugshøj K B, Taboryski R, Wolff A and Hansen M F 2014 Fabrication and modelling of injection moulded all-polymer capillary microvalves for passive microfluidic control *J. Micromechanics Microengineering* **24** 125007.

[22] Maszara W P, Goetz G, Caviglia A and McKitterick J B 1988 Bonding of silicon wafers for silicon-on-insulator *J. Appl. Phys.* **64** 4943–50.

[23] Mair D a., Rolandi M, Snauko M, Noroski R, Svec F and Fréchet J M J 2007 Room-temperature bonding for plastic high-pressure microfluidic chips *Anal. Chem.* **79** 5097–102.

[25] Eddings M a, Johnson M a and Gale B K 2008 Determining the optimal PDMS–PDMS bonding technique for microfluidic devices *J. Micromechanics Microengineering* **18** 067001.

[26] Bhattacharya S, Datta A, Berg J M and Gangopadhyay S 2005 Studies on surface wettability of poly(dimethyl) siloxane (PDMS) and glass under oxygen-plasma treatment and correlation with bond strength *J. Microelectromechanical Syst.* **14** 590–7.

[27] Anderson T L 2005 *Fracture Mechanics: Fundamentals and Applications, Third Edition* (Taylor & Francis)

This is page 96:
For typesetting reasons, it has intentionally been left completely blank.

7

Paper 4: Droplet based liquid-liquid extraction

Using the energy directors developed and described in paper 3, I embarked on designing, fabricating and testing our first injection moulded, ultrasonic welded, droplet generation chip[a]. To separate the work of developing the biology of ddPCR in injection moulded chips from the development of the chip production, it was decided that the first application of the droplet generation chip should be that of demonstrating droplet based liquid-liquid extraction.

As described in the introduction of this paper (page 100-101), liquid-liquid extraction is the transport of a chemical specie by crossing the interface from one liquid phase to another. When the net transport between the two phases equals out and the system is in an equilibrium state, valuable information may be extracted from the ratio of concentrations in the two phases. Specifically, the *partition coefficient* (P) is defined as the ratio between the concentrations of the solute in an octan-1-ol phase and an aqueous phase:[194,195]

$$P = \frac{[X_{octanol}]}{[X_{aqueous}]}.$$

For a compound which has ionized forms in the equilibrium state of the system, a generalised version of P may be formulated; The *distribution coefficient* (D):

$$D = \frac{[X^0_{octanol}] + \left[X^{charge}_{octanol}\right]}{\left[X^0_{aqueous}\right] + \left[X^{charge}_{aqueous}\right]}. \tag{7.1}$$

Though simple in definition and concept, the distribution coefficient and it's dependence on pH (protonation and deprotonation of the specie) is a key indicator for the

[a] The ddPCR chip of Paper 2 had droplets made off-chip in a commercial device, see Section 5.1.1.2 on page 66

behaviour in a multiphase system such as the interaction with a cellular membrane. Membrane-crossing capability of a chemical specie is an important pharmacokinetic property for the performance of for example orally administered drugs.

As elaborated in the paper, I developed a disposable microfluidic device for rapidly determining the distribution coefficient by using aqueous droplets in octanol for increasing the surface area. The developed device and system also held several other advantages when comparing to the conventional (and standard[196]) experimental methodology for measuring distribution coefficients. These are listed in Table 4 on page 104.

The driving force for separating droplets from the oil phase was gravity, and due to the low difference in in density of the two liquids (resulting in a low net gravitational force) and the relatively high stokes drag from the high viscosity of octanol, a long residence time was required. To achieve a large residence time while limiting the droplets to flow in a single monolayer, it was necessary to make the "separation chamber" large in the droplet monolayer plane (large $l \times w$), but shallow in the height. See Figure 1 on page 101.

The final dimensions of the system were based on analytical estimates which were also supported by numerical calculations. The entirety of the analysis is presented in the supporting information of the paper on page 107. Further, the validity of numerical model was supported by experimental observations. As shown in the supporting information of the paper on page 110, the model agrees nicely with the observations.

7.1 Remarks

7.1.1 Annealing

An important difference between this study and the work conducted in paper 2 is the types of oil used; This study used octanol whereas paper 2 used flourinated oil. Octanol was observed to cause a high amount of stress cracking in the COC of the polymer devices, probably because it penetrated the polymer, as a somewhat weak hydrocarbon solvent. Flourinated oil, on the other hand, did not act as a solvent on the polymers. As shown in the supplementary material (page 114), the stress cracking was detrimental to the integrity of the assembled device. This chemical interaction between the device (COC) and the solvent (octanol) is inevitable without the addition of a barrier layer, and to keep the fabrication protocol simple and high throughput, I developed a polymer annealing method; Inspired by steel or glass annealing, the polymer was cycled from room temperature to 125 °C (10 °C below the glass transition temperature, T_g) over a period of 2 hours. The images presented on page 114 compares octanol exposure with and without annealing, and show that even after 2 weeks of exposure, no stress cracking is observed in the annealed device. For reference, without annealing, stress-cracking was observed within minutes. To further study the origin of the polymer stress, 3 types of annealing comparisons were made: No annealing, pre-welding and post welding. This

experiment showed that the stress contribution from ultrasonic welding is significant, but minor compared to the stress present from the injection moulding.

I attempted to study the removal of residual stress quantitatively by observing stress induced birefringence using crossed polarisers. However, the stress-optic coefficient[b] of COC is only -2 to -27$\times 10^{-12}$/Pa (suppliers data sheet). For comparison, the stress-optic coefficient is 4.8×10^{-9}/Pa[197], 3 orders of magnitude larger.

7.1.2 Droplet volume polydispersity

As seen in Table 2 on page 103, standard error of the arithmetic mean of droplet diameters and the average coefficient of variation of droplet diameters suggest that the droplets produced are polydisperse. This is no issue for the developed droplet liquid-liquid extraction system, since the purpose of the droplets is to increase the surface area of the interface for improved mass exchange. However, as will be addressed in the following chapter (page 115), the state-of-the-art mathematical tools for conducting droplet based limiting dilution assays break down when the droplet population becomes polydisperse in volume.

7.1.3 External stay

The work of this paper was conducted as part of an external stay: The chip design, development and testing was conducted at DTU Nanotech. The actual data for the paper was conducted at the laboratory of the deMello group, Institute of Chemical and Bioengineering, Department of Chemistry and Applied Biosciences, ETH Zürich, Zürich, Switzerland, in the months of August to October 2014. The advantages of using commercially relevant, high-throughput fabrication methods proved very useful: I simply brought a suitcase of $\sim$ 100 finished devices.

I was fortunate to receive funding to partially cover my expenses for dual rent and travelling by the following funds:

- Otto Mønsteds Fond 5,979.00 DKK
- Oticon Fonden 10,000 DKK
- Augustinus Fonden 8,500 DKK

[b] Also known as the photoelastic coefficient, which linearly scales the observed birefringence.

analytical chemistry

Article

pubs.acs.org/ac

A Microfluidic Platform for the Rapid Determination of Distribution Coefficients by Gravity-Assisted Droplet-Based Liquid−Liquid Extraction

Carl Esben Poulsen,[†] Robert C. R. Wootton,[‡] Anders Wolff,[†] Andrew J. deMello,[‡] and Katherine S. Elvira*[,‡]

[†]Department of Micro- and Nanotechnology, Technical University of Denmark, Kgs. Lyngby, Denmark

[‡]Institute of Chemical and Bioengineering, Department of Chemistry and Applied Biosciences, ETH Zurich, Zurich, Switzerland

Supporting Information

ABSTRACT: The determination of pharmacokinetic properties of drugs, such as the distribution coefficient (D) is a crucial measurement in pharmaceutical research. Surprisingly, the conventional (gold standard) technique used for D measurements, the shake-flask method, is antiquated and unsuitable for the testing of valuable and scarce drug candidates. Herein, we present a simple microfluidic platform for the determination of distribution coefficients using droplet-based liquid−liquid extraction. For simplicity, this platform makes use of gravity to enable phase separation for analysis and is 48 times faster and uses 99% less reagents than performing an equivalent measurement using the shake-flask method. Furthermore, the D measurements achieved in our platform are in good agreement with literature values measured using traditional shake-flask techniques. Since D is affected by volume ratios, we use the apparent acid dissociation constant, pK', as a proxy for intersystem comparison. Our platform determines a pK' value of 7.24 ± 0.15, compared to 7.25 ± 0.58 for the shake-flask method in our hands and 7.21 for the shake-flask method in the literature. Devices are fabricated using injection molding, the batchwise fabrication time is <2 min per device (at a cost of $1 U.S. per device), and the interdevice reproducibility is high.

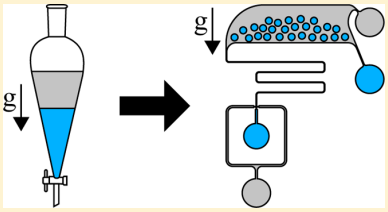

The pharmacokinetic properties of drugs are key indicators of how a drug will perform in the human body. The objective behind the study of these properties is to allow prediction of the viability of a drug prior to its administration to human subjects so that the cost and high attrition rates associated with drug discovery can be mitigated. One of the most commonly used metrics to determine pharmacokinetic properties is the distribution coefficient (D), which is an important indicator of the interaction between a compound and cellular membranes and, hence, allows the prediction of the extent of absorption of orally administered drugs.

The standard experimental methodology for measuring distribution coefficients is the shake-flask method, where the distribution of a drug between a hydrophilic (aqueous) phase and a hydrophobic phase (normally octanol) is measured through use of a separating funnel or centrifuge.[1] The advantages associated with this method are historical and based on the experimental simplicity and availability of the required equipment in normal laboratory settings. However, such measurements take a long time, since the phases must be pre-equilibrated with the opposite phase over the course of 24 h,[1] and large volumes are required, which is problematic when assaying valuable drug samples.[2] Furthermore, D is known to be sensitive to contaminants.[1]

The adoption of microfluidic technologies provides interesting alternatives to the shake-flask method. Microfluidic platforms specialize in the manipulation of fluids on the microscale, with key advantages related to reduced sample sizes, enhanced assay speed, and increased control over physical and chemical characteristics associated with the system under study.[3] However, microfluidic platforms have not become *de rigueur* for distribution coefficient measurements because of factors related to the material used for fabrication, phase control, and overall system complexity. For example, microfluidic platforms presented in the literature have been fabricated in materials that scale poorly or are too expensive for commercial-scale production, such as polydimethylsiloxane (PDMS),[4−7] glass,[8−10] silicon,[11,12] and polymers (such as thiolene,[13] SIFEL,[13] or NOA81[14]) or require surface modification[5] prior to use. Both these characteristics make commercial application of such platforms unfeasible. Furthermore, many microfluidic platforms have used the co-flow of oil and water phases through a device,[4,11,13] which requires complicated structures for phase separation and stabilization (such as the use of porous fluoropolymer membranes[2,11]), or relies on surface modification of wetting characteristics to stabilize the co-flowing phases.[5,8,13]

An alternative microfluidic method for liquid−liquid extraction makes use of droplets, which maximize the available surface area for the partitioning of compounds between the

Received: March 19, 2015
Accepted: May 18, 2015

DOI: 10.1021/acs.analchem.5b01061
Anal. Chem. XXXX, XXX, XXX−XXX

immiscible phases. These systems have the advantage of allowing easy removal of artifacts, since each droplet defines a single measurement and, hence, contaminants are easily identified. Droplet-based microfluidic systems are in fact closely related to the shake-flask method, where phase agitation causes emulsification prior to phase separation by allowing the mixture to re-equilibrate using gravity. However, microfluidic droplet-based systems normally use surfactants to stabilize droplets[15] and, hence, require complicated techniques to drive de-emulsification for phase separation, such as the use of strong electric fields,[12] or require complicated detection methods to perform in-droplet measurements, such as laser-induced fluorescence.[9]

It is clear that microfluidic platforms have the potential to revolutionize the measurement of distribution coefficients, especially for high-value drugs, and to ensure that these measurements are user-independent and considerably faster than conventional methods. However, for microfluidic platforms to achieve this goal, they must be easy to use, inexpensive to produce commercially, of simple design, disposable, and able to provide a clear advantage over the shake-flask technique. The use of microfluidic technologies in commercial applications is an enduring goal in the field, but very few microfluidic platforms are commercially viable, specifically because of factors such as the material used for fabrication and ease of use. Herein, we present a droplet-based microfluidic platform for the determination of distribution coefficients using gravity to separate the phases for analysis. The platform is fabricated using injection molding and can be easily integrated into a production line. The devices are low-cost and, hence, disposable, which we demonstrate through the analysis of data gathered using over 30 devices. The material used for device fabrication is compatible with the solvent systems used for distribution coefficient measurements, and we show that our microfluidic platform performs in a superior manner to the shake-flask method, specifically where cost, reagent volume, and experimental time are paramount.

MATERIALS AND METHODS

Design of the Microfluidic Platform. The microfluidic platform was designed to maximize the interaction between the aqueous and oil phases and ensures optimal mass transfer through the use of aqueous-in-oil droplets. After creation at a flow focusing geometry, droplets enter the separation chamber (Figure 1, Video S1 in the Supporting Information (SI)). Extended droplet residence times in this chamber allow the droplets to travel a significant portion of the chamber width (w) relative to the continuous phase due to gravity (further details of these calculations can be found in section S1 in the Supporting Information), hence allowing the removal of aqueous droplets from the continuous oil phase for further analysis of the oil phase. In other words, gravitational forces allow aqueous droplets to settle at the bottom of the separation chamber and hence exit at the lower, aqueous, outlet. This allows the droplet-free oil phase to be collected from the upper outlet and used for absorption measurements.

As described in detail in section S1 in the Supporting Information, if gravity is to enable an aqueous droplet suspended in octanol to migrate at least the entire width of the separation chamber, relative to the continuous phase, the following inequality must be fulfilled:

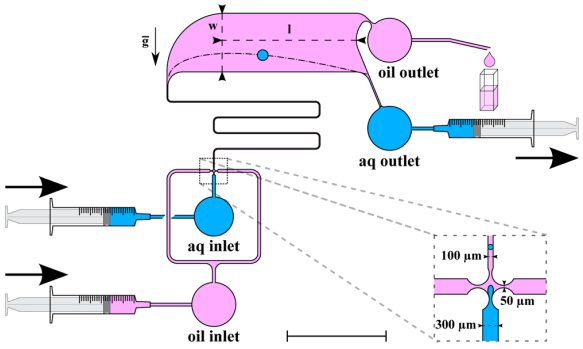

Figure 1. Scale drawing of the microfluidic platform used for droplet-based liquid−liquid extraction (the syringes and the cuvette at the oil outlet are not to scale). Droplets are formed at a flow focusing geometry and then inserted into a large separation chamber where gravity ($\vec{g}$) enables separation of the two phases. Blue denotes the aqueous (aq) phase, and pink denotes the oil phase. The width (w) of the separation chamber is 6 mm, its length (l) is 13.7 mm, and the channel height is 100 μm throughout. The width of the channels connecting both outlets to the separation chamber is 150 μm. The oil phase was collected in a cuvette at the oil outlet, and absorbance measurements were performed as detailed in the liquid−liquid extraction section. The scale bar in the main figure is 10 mm, and the enlarged area shows the dimensions of the flow focusing geometry used for droplet generation. Single-headed arrows denote the directions of flow from the syringe pumps and of gravity. The images of syringes and the cuvette are taken from Wikimedia.org and are used under a creative commons license.

$$\frac{\tilde{d}^2\tilde{h}\tilde{l}}{\tilde{Q}_{tot}} \geq 18N_{St} \quad (1)$$

where $\tilde{d}$ is the dimensionless droplet diameter, $\tilde{h}$ the dimensionless height of the separation chamber, $\tilde{l}$ the dimensionless chamber length, $\tilde{Q}_{tot}$ the dimensionless total flow rate, and N_{St} the Stokes number (the ratio of viscous to gravitational forces). Therefore, in the microfluidic platform used herein, where h = 100 μm, w = 6 mm, l = 13.7 mm, and $d \leq h$, the total flow rate should be kept smaller than 20.8 μL/min. It is important to note that this value defines the maximum flow rate, since smaller droplets will have a lower terminal velocity and will hence require a longer residence time in the separation chamber to allow for a channel width migration. Furthermore, the Bond number (Bo) is $\leq$ 0.0031, confirming that surface tension forces dominate in our platform and, hence, droplets are round (for details of the interfacial tension measurements used to determine the Bo, see section S3 in the SI).

Chip Fabrication. *Micromilling.* A structured mold insert for injection molding was designed in Autodesk Inventor Professional 2012, converted to G-code in CimatronE10, and fabricated in 2017 aluminum alloy (MetalCentret, Denmark) by micromilling (NTI CADcenter A/S, Denmark). Energy directors for ultrasonic welding[16] were defined using a 60° helical engraving tool (No. 7025, DIXI polytool, Herstad +Piper, Denmark) producing 50-μm-high prism-shaped energy directors.

Injection Molding. The aluminum mold insert and a matching countermold with 12 ISO Luer-fittings[17] were installed in a Victory 80/45 Tech injection molder (Engel, Austria). The polymer used for injection molding was COC

DOI: 10.1021/acs.analchem.5b01061
Anal. Chem. XXXX, XXX, XXX−XXX

(Grade 5013L-10, TOPAS Advanced Polymers, Germany) with a glass transition temperature (T_g) of 135 °C. The injection temperature of the polymer was 270 °C, and the mold and demolding temperatures were kept stable at 120 °C.

Ultrasonic Welding. To seal the microfluidic device, a 152 μm thick COC sheet (Grade 5013S-04, TOPAS Advanced Polymers, Germany) was bonded to the injection molded piece using a Telsonic-USP4700 ultrasonic welder (Telsonic, Herstad +Piper, Denmark). The welding was conducted using 45 J at 90% amplitude and 20 kHz, with a trigger force on the piece of 600 N in the normal direction.

Annealing. To avoid solvent-induced cracking, internal stress from the isothermal injection molding and ultrasonic welding was removed by annealing. The entire batch of chips (200 pieces) was loaded into an oven, which was cycled from room temperature to 125 °C and back to room temperature over a period of 2 h. A comparison of solvent-induced stress cracking in annealed and nonannealed chips due to octanol exposure is shown in section S5 in the SI.

Overall, including handling, the total turn-around time per chip was 40 s for injection molding, 20 s for ultrasonic welding, and 36 s for annealing, which amounts to a fabrication time of less than 2 min per device.

Liquid–Liquid Extraction. Standards for determining quinine extinction coefficients were prepared by dissolving quinine hydrochloride dihydrate (≥99.0%, Sigma-Aldrich, Switzerland) either in 1× DPBS (Dulbecco's phosphate-buffered saline, pH 7.4, Life Technologies, Switzerland) or in octan-1-ol (≥99.0%, Alfa Aesar, Germany) with 3% (w/w) ABIL EM90 (cetyl dimethicone copolyol, Rose Chemicals, U.K.). The DPBS and octanol used in the preparation of the standards were stored with 5% octanol and DPBS, respectively, to ensure mutual saturation of the two phases.

Samples for "bulk" analyses were prepared in glass vials with aqueous to octanol (aqueous/octanol) volume ratios of 2:1, 1:1, 1:2, 1:4, 1:8, 1:16, 1:32, and 1:10, the latter of which creates a bulk sample with a volume ratio similar to the flow rate ratio in the droplet-based experiments. The total volume for each sample was 4 mL, and all eight concentrations were prepared in triplicate, for a total of 24 samples. All aqueous and octanol volumes were calculated from mass measurements and density to ensure consistency. At the start of each experiment, the aqueous solution contained 1 mM quinine hydrochloride dihydrate.

Droplet-based liquid–liquid extraction was conducted on the microfluidic platform described above using three Aladdin syringe pumps (AL-1000, WPI-Europe, U.K.) mounted with 500 μL Hamilton gas-tight syringes (VWR, Denmark): two for controlling the inlet flow rates and one for controlling the aqueous outlet flow rate. Assuming the system is operated under a stable flow for 30–90 min per experiment, the oil outlet flow rate was assumed to satisfy the continuity equation

$$0 = Q_{aq,in} + Q_{oil,in} + Q_{aq,out} + Q_{oil,out}$$

where the subscripts "aq" and "oil" denote aqueous and oil phases, respectively, and the subscripts "in" and "out" denote the direction of flow as into and out of the microfluidic device, respectively. The aqueous outlet flow rate ($Q_{aq,out}$) was set to 3.5 μL/min, and this ensures that no droplets exit from the oil outlet, that the flow at the oil outlet is stable, and that enough oil can be collected to finish the experiment within 30 min. During the experiment, the microfluidic device was mounted such that the width of the separation chamber was parallel to the gravitational force (see $\vec{g}$ in Figure 1). The absorbance of the oil phase was measured by collecting a set volume of oil from the oil outlet and performing off-line measurements at 340 nm on a BioPhotometer Plus system (Eppendorf, Switzerland) using UVette cuvettes (Eppendorf, Switzerland). For the measurement of absorbance values in the range of 0.05 to 1.00, both the 10 mm and the 2 mm path lengths of the cuvettes were used. Quinine concentrations determined from absorbance measurements using the Beer–Lambert law were used to calculate D (see the SI for further information). The parameters used for on-chip liquid–liquid extraction are summarized in Table 1.

Table 1. Parameters for On-Chip Liquid–Liquid Extraction[a]

	(+)	(x)
$Q_{aq,in}$ (μL/min)	0.5	1.0
$Q_{oil,in}$ (μL/min)	5.0	5.0
$Q_{aq,out}$ (μL/min)	3.5	3.5
$r_Q = Q_{oil,in}/Q_{aq,in}$	10	5
Quinine concentration (μM)	100, 250, 500, 750, 1000	
Number of experiments	3	3
Total number of devices	15	15

[a]The red plus sign symbol (+) and the blue cross symbol (×) denote datasets of unique r_Q and will be used for identification in Figures 3 and 4.

On-chip droplet imaging was performed using a Manta G046B ASG camera (Allied Vision, Denmark) mounted on a (1–4)× adjustable zoom lens. Images were subsequently analyzed using a custom-made MATLAB algorithm incorporating circle detection by circular Hough transform to determine droplet size.

RESULTS AND DISCUSSION

Characterization of the Microfluidic Platform. The performance of the microfluidic platform over a range of aqueous and oil flow rates is illustrated in Figure 2, in terms of droplet size statistics. During initial device characterization, it

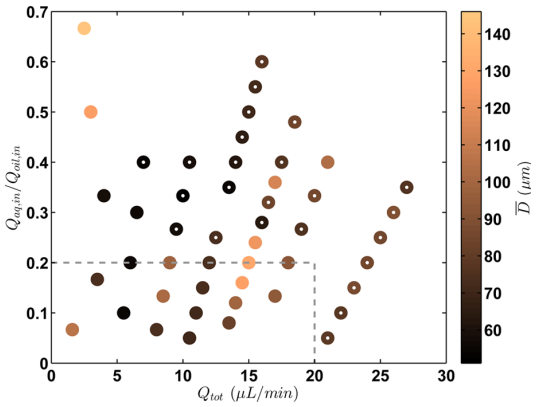

Figure 2. Characterization of droplet formation on the microfluidic device. Average droplet diameter (color map) versus total flow rate (Q_{tot}) and versus the flow rate ratio ($Q_{aq,in}/Q_{oil,in}$). Data points with a white dot represent system conditions where the droplet residence time is too low to allow phase separation, calculated using eq S2 in the SI. The section highlighted by the dashed rectangle denotes the parameter space where flow rate combinations allow efficient droplet guidance. Note that the separation chamber has a height of 100 μm, and, hence, droplets with a larger diameter are nonspherical.

DOI: 10.1021/acs.analchem.5b01061
Anal. Chem. XXXX, XXX, XXX–XXX

was found that configurations of $Q_{aq,in}/Q_{oil,in} > 0.2$ produced too many droplets for efficient droplet migration and hence separation of the phases at the device outlets. Since droplets at these flow rates do not leave the chamber quickly enough, the high droplet density effectively constricts the chamber dimensions, causing new droplets to have higher flow rates and thus lower residence times. This phenomenon is related to hydraulic damming and, practically, means that droplets agglomerate at the aqueous outlet, causing new droplets to exit via the oil outlet. The box in Figure 2 highlights the maximum flow rate ($Q_{tot} = Q_{aq,in} + Q_{oil,in} = 20$ μL/min) and inlet flow rate ratio ($Q_{aq,in}/Q_{oil,in} = 0.2$) at which droplets can be separated from the oil flow at the maximum droplet diameter ($d = h$). This is the region in which $\tilde{s}_w \leq \tilde{w}$ and the boundaries of the box depend on the droplet size because smaller droplets have a lower terminal velocity (further details can be found in section S1 in the SI). Figure 2 clearly shows the robustness of the microfluidic platform in terms of the variety of flow rate combinations at which stable droplet production is possible.

The interdevice droplet production reproducibility was measured in triplicate under the experimental conditions described in Table 1. The statistical analysis of these data is summarized in Table 2. It is evident that the produced droplets

Table 2. Droplet Size Statistics for On-Chip Liquid−Liquid Extraction Experiments[a]

$Q_{aq,in}$ (μL/min)	$Q_{oil,in}$ (μL/min)	$\overline{CV_D}$[b] (%)	$\bar{\bar{d}}$[c] (μm)	$SEM_{\bar{d}}$[d] (μm)
1.0	5.0	34.1 ± 9.3	70.9	19.7
0.5	5.0	33.7 ± 6.8	66.2	9.55

[a]The statistical analysis is based on droplet images acquired in the experiments described in Table 1, and each image contained a minimum of 50 droplets (on average, there were 384 droplets per image). Each set of flow rate conditions was analyzed in 15 individual experiments on 15 different microfluidic platforms. [b]$\overline{CV_D}$ is the average coecient of variation of droplet diameters. [c]$\bar{\bar{d}}$ is the grand mean of droplet diameters is defined as the arithmetic mean of the arithmetic mean. [d]$SEM_{\bar{d}}$ is the standard error of the arithmetic mean of droplet diameters.

have a high polydispersity ($\overline{CV_D} \approx 34\% \pm 8.1\%$) but that average droplet diameters are conserved across different microfluidic devices ($SEM_{\bar{d}} \approx 15$ μm). As shown in Figure 1, the flow-focusing geometry used for droplet creation has rounded edges, which explains the high polydispersity when compared to other microfluidic platforms where the droplet formation geometry has sharp corners. These rounded edges are caused by a limitation of the milling process which, unlike lithographic methods, defines geometries by material removal using milling tools of finite diameters (200 μm). In addition, micromilling introduces surface roughness, which may also introduce variations during droplet breakoff and formation.

Liquid−Liquid Extraction. To verify that on-chip liquid−liquid extraction was not limited by diffusion at low droplet residence times, extractions were conducted with aqueous quinine concentrations of 100 μM, 250 μM, 500 μM, 750 μM, and 1 mM, at aqueous flow rates of 1 μL/min and 0.5 μL/min and with a constant oil flow rate of 5 μL/min throughout. The distribution of quinine between the aqueous and oil phases is described by the relationship between the inbound aqueous mass flow rate ($I_{aq,in}$) and the outbound oil mass flow rate ($I_{oil,out}$), as shown in Figure 3, where $I = cQ$ and c is the

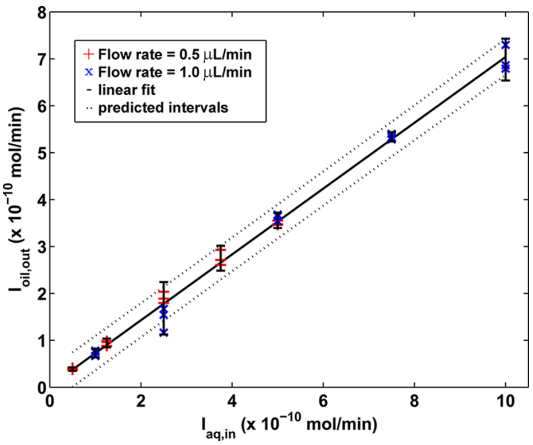

Figure 3. Outbound versus inbound molar flow rates for on-chip liquid−liquid extraction. The inbound molar flow rate is varied by adjusting the aqueous flow rate and hence the aqueous quinine concentration. The concentration of quinine was calculated using extinction coefficient data shown in Figure S3 in the SI. Error bars show two standard deviations from the mean. Prediction intervals were calculated using the MATLAB package *polyconf* and illustrate the upper and lower bounds in which 95% of future data points will fall.

concentration. Since the outbound mass flow rate is observed to scale linearly with the inbound mass flow rate, the system is at equilibrium when the phases are separated for analysis. If the residence time of the droplets in the separation chamber was insufficient to allow for mass transfer equilibrium, variations in the inbound mass flow rate introduced by varying the flow rate (and hence the residence time of the droplets) or the aqueous quinine concentration would result in a nonlinear relationship between $I_{oil,out}$ and $I_{aq,in}$. The two total flow rates used in this study of 5.5 and 6.0 μL/min cause average residence times of 129 and 118 s, respectively. The fastest droplets shown in Video S1 in the SI have a residence time of 68 s. Our average residence times are at least 1 order of magnitude more than what was needed to achieve a steady state in diffusion studies of fluorophores in larger droplets (equilibrium was reached in less than 8 s).[7,18]

In order to assess the performance of liquid−liquid extraction on the droplet microfluidic platform compared to standard methodologies, the distribution coefficients of quinine from bulk overnight experiments and on-chip liquid−liquid extractions are compared in Figure 4. For bulk experiments, this figure shows the distribution coefficients determined at the volume ratios stated in the Materials and Methods section. Equation 2 was used to calculate the apparent acid dissociation constant, pK',[19] which is unique to the system (pH and buffer) and, unlike the distribution coefficient, is independent of the volume ratio.

$$D = \frac{V_{aq}}{V_{oil}}(10^{pK_a - pK' - 1}) \quad (2)$$

Here, V is volume and pK_a is the true acid dissociation constant. Table 3 summarizes the experimental values of pK' both from bulk and on-chip droplet based liquid−liquid extraction experiments, and from the literature. The pK_a value used to calculate pK' from eq 2 was 8.505, which defines the average of two literature values: 8.58[20] and 8.43.[21]

DOI: 10.1021/acs.analchem.5b01061
Anal. Chem. XXXX, XXX, XXX−XXX

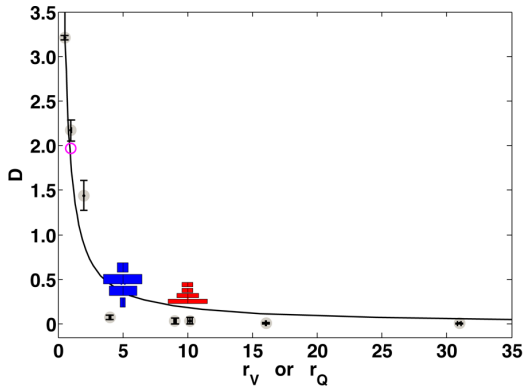

Figure 4. Distribution coefficients, D, both from bulk experiments (depicted by gray circles with black error bars representing the standard deviation) plotted versus volume ratio, $r_V = V_{oil}/V_{aq}$, and from on-chip liquid–liquid extraction experiments at aqueous flow rates of 0.5 μL/min (red violin plot) and 1.0 μL/min (blue violin plot) plotted versus the volume flow rate ratio, $r_Q = Q_{oil,in}/Q_{aq,in}$. The concentration of quinine was calculated using extinction coefficient data shown in Figure S3 in the SI. The distribution of data points from on-chip experiments are illustrated as violin plots to highlight the large amount of measurements gathered for each data point when using a microfluidic platform (each violin plot incorporates data gathered from 15 separate experiments as detailed in Table 1). The solid line represents the least squares fit of eq 2 for the data from bulk experiments, $D = (10^{pK_a - pK' - 1}) \times (1/r_V) = 10^{0.25} \times (1/r_V)$. The open pink circle represents literature data.[20]

As is evident from the data presented in Table 3, there is good agreement between the pK' values measured in bulk and on-chip experiments, and these values are also in good agreement with the literature. Table 4 shows how other parameters such as cost and reagent consumption compare between microfluidic and traditional methodologies. In terms of cost efficiency (reagent consumption and time) and sensitivity to user interference, the microfluidic platform greatly outperforms traditional methodologies. Furthermore, it is possible to perform continuous measurements using the microfluidic platform, such as in-line absorbance measurements, and during one continuous experiment in the microfluidic platform, the variation of combinations of $Q_{aq,in}$ and $Q_{oil,in}$ allows for the concurrent acquisition of multiparameter data (e.g., r_Q, D).

CONCLUSIONS

The microfluidic devices presented herein are fabricated using injection molding, ultrasonic welding, and annealing, which are all processes currently used in commercial manufacturing, with a time per device of <2 min. We demonstrate the reliability of the devices by performing experiments on 30 different devices, with distribution coefficient data gathered on these platforms showing close agreement with literature values and low statistical variation under a variety of flow conditions and concentrations. To enable the use of this platform in nonspecialist laboratory settings, the device design is simple, and gravity is used to enable phase separation. Finally, we assess the parameters associated with this microfluidic platform, in comparison to the shake-flask method. We show that our microfluidic platform is 48 times faster and uses 99% less reagents than the shake-flask method. In addition, user sensitivity and contamination, which are sources of error for conventional techniques, are negligible in our platform. As future work, the system will be integrated with online absorption detection to allow extraction of data from individual droplets to enhance analytical efficiency.

Table 4. Comparison of Parameters Associated with Bulk and On-Chip Methodologies for Liquid–Liquid Extraction

	bulk	on-chip
experiment time	>24 h	30 min
reagent volume	>20 mL	300 μL
cost of reagents	>25 US dollars	0.37 US dollars
cost of microfluidic device	N/A[a]	1 US dollars
sensitivity to user interference	high	low
repeatability	good	good
continuous measurements	not possible	possible
phase space sweep	not possible	possible

[a]N/A = not applicable.

ASSOCIATED CONTENT

Supporting Information

A mathematical description and a two-dimensional numerical (COMSOL) model of the effect gravity has on droplets in the separation chamber, experimental data to verify our model, absorbance data at different quinine concentrations and equations used to calculate the extinction coefficient of quinine, interfacial tension measurements of our octanol/DPBS/Abil EM90 system required to calculate the Bond number, derivations of the equations used for calculating D from quinine concentrations, and data to show the effect that annealing has on ultrasonically welded devices; a video of gravity-assisted droplet-based liquid–liquid extraction. The Supporting Information is available free of charge on the ACS Publications website at DOI: 10.1021/acs.analchem.5b01061.

AUTHOR INFORMATION

Corresponding Author

*E-mail: katherine.elvira@chem.ethz.ch.

Notes

The authors declare no competing financial interest.

Table 3. Comparison of Experimental Data Gathered from Bulk and Microfluidic Experiments with Literature Values[a]

	r_V or r_Q	D	pK'
Data from bulk experiments, (●)	1/2 to 32/1	Fig. 4	7.25 ± 0.58
Data from on-chip experiments, (+) and (×)	5.0/1.0 and 5.0/0.5	Fig. 4	7.24 ± 0.15
Data from literature,[20] (○)	1	1.97	7.21

[a]The apparent acid dissociation constant, pK', was calculated from volume or flow rate ratios, r_V or r_Q, using D at pH 7.4, a pK_a value of 8.505,[20,21] and eq 2. The markers (gray circle, red plus sign (+), blue cross symbol (×), and pink open circle (○) used in the table refer to Figure 4. Error estimations in the pK' values refer to the standard deviation. Values for D, as measured from bulk and microfluidic experiments in this table, refer to the data in Figure 4, because D is dependent on the volume ratios (unlike pK', which, therefore, is a better standard for intersystem comparison).

DOI: 10.1021/acs.analchem.5b01061
Anal. Chem. XXXX, XXX, XXX–XXX

■ ACKNOWLEDGMENTS

This work was partially funded by The Danish Council for Independent Research (grant number 09066477). Carl Esben Poulsen would like to thank The Oticon Foundation, The Otto Mønsted Foundation, and The Augustinus Foundation for funding.

■ REFERENCES

(1) *OECD Guidelines for the Testing of Chemicals: Partition Coefficient (n-octanol/water): Shake Flask Method*; Organisation for Economic Co-operation and Development: Paris, 1995.
(2) Alimuddin, M.; Grant, D.; Bulloch, D.; Lee, N.; Peacock, M.; Dahl, R. *J. Med. Chem.* **2008**, *51*, 5140−5142.
(3) Elvira, K. S.; Casadevall i Solvas, X.; Wootton, R. C. R.; deMello, A. J. *Nat. Chem.* **2013**, *5*, 905−915.
(4) Soares, R.; Novo, P.; Azevedo, A.; Fernandes, P.; Aires-Barros, M. R.; Chu, V.; Conde, J. P. *Lab Chip* **2014**, *14*, 4284−4294.
(5) Xiao, H.; Liang, D.; Liu, G.; Guo, M.; Xing, W.; Cheng, J. *Lab Chip* **2006**, *6*, 1067−1072.
(6) Marine, N. A.; Klein, S. A.; Posner, J. D. *Anal. Chem.* **2009**, *81*, 1471−1476.
(7) Mary, P.; Studer, V.; Tabeling, P. *Anal. Chem.* **2008**, *80*, 2680−2687.
(8) Miyaguchi, H.; Tokeshi, M.; Kikutani, Y.; Hibara, A.; Inoue, H.; Kitamori, T. *J. Chromatogr. A* **2006**, *1129*, 105−110.
(9) Kumemura, M.; Korenaga, T. *Anal. Chim. Acta* **2006**, *558*, 75−79.
(10) Chen, H.; Fang, Q.; Yin, X.-F.; Fang, Z.-L. *Lab Chip* **2005**, *5*, 719−725.
(11) Kralj, J. G.; Sahoo, H. R.; Jensen, K. F. *Lab Chip* **2007**, *7*, 256−263.
(12) Kralj, J. G.; Schmidt, M. A.; Jensen, K. F. *Lab Chip* **2005**, *5*, 531−535.
(13) Goyal, S.; Desai, A. V.; Lewis, R. W.; Ranganathan, D. R.; Li, H.; Zeng, D.; Reichert, D. E.; Kenis, P. J. *Sens. Actuators, B* **2014**, *190*, 634−644.
(14) Wagli, P.; Chang, Y.; Homsy, A.; Hvozdara, L.; Herzig, H. P.; de Rooij, N. F. *Anal. Chem.* **2013**, *85*, 7558−7565.
(15) Baret, J.-C. *Lab Chip* **2012**, *12*, 422−433.
(16) Kistrup, K.; Poulsen, C. E.; Østergaard, P. F.; Haugshøj, K. B.; Taboryski, R.; Wolff, A.; Hansen, M. F. J. *J. Micromech. Microeng.* **2014**, *24*, 125007.
(17) Andresen, K. Ø.; Hansen, M.; Matschuk, M.; Jepsen, S. T.; Sørensen, H. S.; Utko, P.; Selmeczi, D.; Hansen, T. S.; Larsen, N. B.; Rozlosnik, N.; Taboryski, R. J. *J. Micromech. Microeng.* **2010**, *20*, 055010.
(18) Yu, J.; Chin, L.; Chen, Y.; Zhang, G.; Lo, G. J. In *MicroTAS 2010*, Groningen, The Netherlands, Oct. 3−7, 2010; pp 1079−1081.
(19) Clarke, F. H. *J. Pharm. Sci.* **1984**, *73*, 226−230.
(20) Warhurst, D. C.; Craig, J. C.; Adagu, I. S.; Meyer, D. J.; Lee, S. Y. *Malar. J.* **2003**, *2*, 26.
(21) Schulman, S. G.; Threatte, R. M.; Capomacchia, A. C.; Paul, W. L. *J. Pharm. Sci.* **1974**, *63*, 876−880.

DOI: 10.1021/acs.analchem.5b01061
Anal. Chem. XXXX, XXX, XXX−XXX

A Microfluidic Platform for the Rapid Determination of Distribution Coefficients by Gravity-Assisted Droplet-Based Liquid-Liquid Extraction

Carl Esben Poulsen,[†] Robert C. R. Wootton,[‡] Anders Wolff,[†] Andrew J. deMello[‡] and Katherine S. Elvira[‡]*

[†]*Department of Micro- and Nanotechnology, Technical University of Denmark, Kgs. Lyngby, Denmark*

[‡]*Institute of Chemical and Bioengineering, Department of Chemistry and Applied Biosciences, ETH Zurich, Zurich, Switzerland.*

*katherine.elvira@chem.ethz.ch

This Supporting Information contains five sections. In the first section we present both a mathematical description and a two-dimensional numerical (COMSOL) model of the effect gravity has on droplets in the separation chamber. We also present experimental data to verify our model. The second section contains absorbance data at different quinine concentrations used to calculate the extinction coefficient of our system. The third section includes interfacial tension measurements of the octanol/DPBS/Abil EM90 system required to calculate the Bond number. The fourth section presents the equations used for calculating the distribution coefficients from quinine concentrations, and the final section presents data to show the effect that annealing has on ultrasonically welded devices.

S1 The effect of gravity on droplets in the separation chamber

Theory. The effect of gravity on the position of droplets in the separation chamber can be understood by assuming that a hard, spherical droplet with density ρ_d (subscript d denotes dispersed phase) suspended in a continuous phase of density ρ_c (subscript c denotes continuous phase) in a gravity field is subjected to three forces: gravity, F_g, buoyancy, F_b, and a viscous drag force, F_d, caused by the surrounding fluid. Unlike the drag force, the buoyancy and gravity forces are independent of the droplet speed, and the droplet will quickly reach an equilibrium state and terminal velocity, $\vec{U}$:

$$\begin{aligned} 0 &= \vec{F_g} + \vec{F_b} + \vec{F_d} \\ 0 &= -\left(\rho_d - \rho_c\right) d^3 \frac{\pi}{6} g\hat{z} - 3\pi\eta_c d\vec{U} \end{aligned} \tag{S1}$$

Here d is the droplet diameter, g is the gravitational constant, $\hat{z}$ is the normal vector that is antiparallel to gravity and η_c is the viscosity of the continuous phase. In dimensionless quantities, Equation S1 may be solved for the dimensionless terminal velocity $\tilde{\vec{u}}$:

$$\begin{aligned} \tilde{\vec{u}} &= -\frac{\left(\rho_d - \rho_c\right) L_0^2 g}{\eta_c V_0} \frac{\tilde{d}^2}{18}\hat{z} \\ \tilde{\vec{u}} &= -\frac{1}{N_{\mathrm{St}}} \frac{\tilde{d}^2}{18}\hat{z} \end{aligned}$$

where L_0 is the characteristic length, $\tilde{d}$ is the dimensionless droplet diameter, V_0 is the characteristic volume and N_{St} is the Stokes number (the ratio of viscous to gravitational forces). Assuming that all droplet manipulation by gravity is conducted in the separation chamber, the distance travelled by the droplet relative to the surrounding fluid, $\vec{s}$, can be calculated through knowledge of the residence time, τ:

$$\begin{aligned} \tau &= \frac{V_{chamber}}{Q_{tot}} \\ \vec{s} &= \tau\vec{U} \\ \tilde{\vec{s}} &= -\frac{\tilde{d}^2 \tilde{V}_{chamber}}{\tilde{Q}_{tot}} \frac{1}{N_{\mathrm{St}}} \frac{1}{18}\hat{z} \end{aligned}$$

Here $V_{chamber}$ is the volume of the separation chamber and Q_{tot} is the total flow rate. The distance travelled relative to the surrounding fluid is proportional to all chamber dimensions. Since the objective of the microfluidic platform is to move the droplets relative to the surrounding fluid, the w (the width of the separation chamber) component of $\tilde{\vec{s}}$ must be calculated with the chamber tilted at angle θ (Figure S1),

$$\frac{\tilde{s}_w}{\tilde{w}} = \frac{\tilde{d}^2 \tilde{V}_{chamber}}{\tilde{w}\tilde{Q}_{tot}} \frac{1}{N_{\mathrm{St}}} \frac{1}{18} cos(\theta) \tag{S2}$$

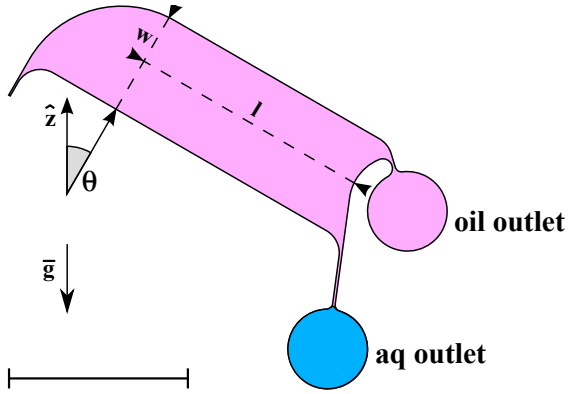

Figure S1: Schematic representation of the separation chamber of the microfluidic platform. $\overline{g}$ is the gravitational constant, θ denotes the tilt angle relative to gravity and $\hat{z}$ is the normal vector that is antiparallel to gravity. The scale bar is 10 mm.

In order for the droplet to cross enough streamlines to exit through the lower (aqueous) exit, it is necessary to design the experiment such that $\tilde{s}_w/\tilde{w} \geq 1$. For the water-in-octanol system this inequality simplifies to:

$$\frac{\tilde{d}^2 \tilde{V}_{chamber}}{\tilde{w}\tilde{Q}_{tot}} cos(\theta) \geq 18 N_{\mathrm{St}} \tag{S3}$$

As illustrated in Figure 2, since the final chip dimensions of the separation chamber are $w = 6$ mm, $l = 13.7$ mm and $h = 100$ µm, the total flow rate should be kept below 20.8 µL/min (since $d \leq h$). Since the terminal velocity depends on the droplet size, for smaller droplets, the maximum total flow rate will be lower. Effects such as droplet-droplet interactions and droplet-wall interactions have been neglected in these calculations. We note that for all droplet diameters ($d \leq h = 100$ µm), the Bond number of the described water-in-octanol system is $Bo \leq 0.0031$ (calculated using the interfacial tension measurements shown in Section S3). This indicates that surface tension forces are always much larger than gravitational forces, and that the assumption that droplets are spherical is reasonable.

Numerical analysis. Prior to fabrication of the first generation of microfluidic devices, the theoretical analysis was refined using a finite element simulation conducted in COMSOL Multiphysics 4.3a (COMSOL, Denmark). The 'Laminar Flow' and 'Particle Tracing for Fluid Flow' packages were used to simulate fluid-particle interactions (convection) as well as gravity and Stokes drag. The two-dimensional model did not include particle-particle or particle-fluid interactions since its purpose was to estimate whether the proposed device design was applicable at all to experimental scenarios. Accordingly, particles were removed from

the simulation when any boundary (wall or outlet) was reached (*i.e.* no droplet stacking is included in the model). COMSOL model predictions and experimental data are compared in Figure S2. To emphasise gravity-induced migration, droplets were released equidistant across the chamber inlet and streamlines coinciding with droplet release points are highlighted. Since droplet trajectories and streamlines have common starting points at the inlet, droplets that are deflected from their original streamlines show the effect of gravity.

Droplet migration. The droplet migration paths of two experimental configurations with high (169 %) and low (20.2 %) values of the theoretical migration ratio ($\tilde{s}_w/\tilde{w}$, Equation S2) are plotted in Figure S2. This Figure shows two distinct droplet migration regimes and presents both experimental and simulation data in each case. Figure S2a shows a droplet sedimentation-dominated regime that occurs under experimental conditions of low flow rates and large droplet volumes. In this case, the COMSOL simulation, which does not consider droplet-droplet and droplet-liquid interactions, suggests that droplets sediment and slide along the bottom wall of the separation chamber and hence exit the chamber only through the lower outlet. However, from the experimental data, it can be seen that as more droplets are introduced, the sedimented droplets constrict the chamber and effectively redirect the flow, causing incoming droplets to move faster and hence migrate less. The system has entered a *quasi* steady state where droplets migrate to a droplet cluster which is directly connected to the aqueous outlet.

Figure S2b shows a droplet convection-dominated regime that occurs under experimental conditions of high flow rates and small droplet volumes. In this case, the COMSOL simulation and experimental data both show that droplets (blue trajectories) mainly migrate due to convection, are not extracted completely from the oil stream (they mostly flow with the streamlines) and therefore exit the chamber through both outlets. Figure S2d shows that seven streamlines and three droplet trajectories exit through the oil (upper) outlet. This suggests that the droplets have crossed four (or 20 %) of the 20 plotted streamlines, which correlates well with the $\tilde{s}_w/\tilde{w}$ value of 20.2 % predicted by the analytical model.

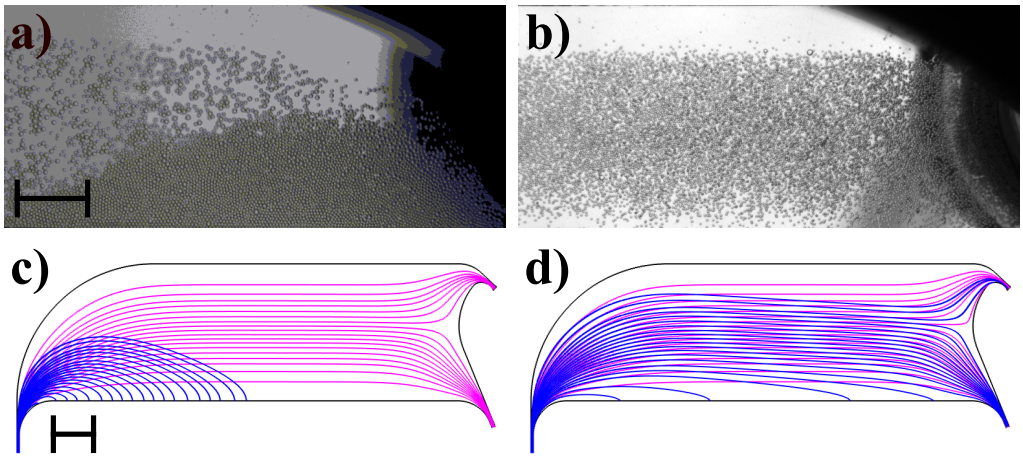

Figure S2: Droplet migration in the separation chamber as observed experimentally and as predicted by the COMSOL model. **a)** Experimental conditions for the droplet sedimentation-dominated regime: $Q_{oil,in} = 5.0$ µL/min, $Q_{aq,in} = 0.5$ µL/min and $Q_{aq,out} = 3.5$ µL/min (58.3 % of Q_{tot}), $\overline{d} = 75.0$ µm, $\tilde{s}_w/\tilde{w} = 169$ % and $\tau = 2$ minutes. **b)** Experimental conditions for the droplet convection-dominated regime: $Q_{oil,in} = 12.5$ µL/min, $Q_{aq,in} = 2.5$ µL/min, $Q_{aq,out} = 9.0$ µL/min (60 % of Q_{tot}), $\overline{d} = 42.9$ µm, $\tilde{s}_w/\tilde{w} = 20.2$ % and $\tau = 1.83$ minutes. **c)** and **d)** are the COMSOL simulations corresponding to **a)** and **b)** respectively. Each simulation shows 20 particle trajectories (blue lines) on 20 equidistant stream lines (pink lines), both with origin at the separation chamber inlet. The scale bars are 2 mm and apply to both photos and both COMSOL simulations.

S2 Quinine standards

Standards for the determination of quinine extinction coefficients at 340 nm where prepared both in 1x DPBS at pH 7.4 and in octan-1-ol with 3 % (w/w) ABIL EM90. The DPBS and octanol used for the preparation of the standards were stored with 5 % octanol and DPBS respectively to ensure mutual saturation of the two phases. Standards comparing absorbance and quinine concentrations for extinction coefficient calculations are shown in Figure S3.

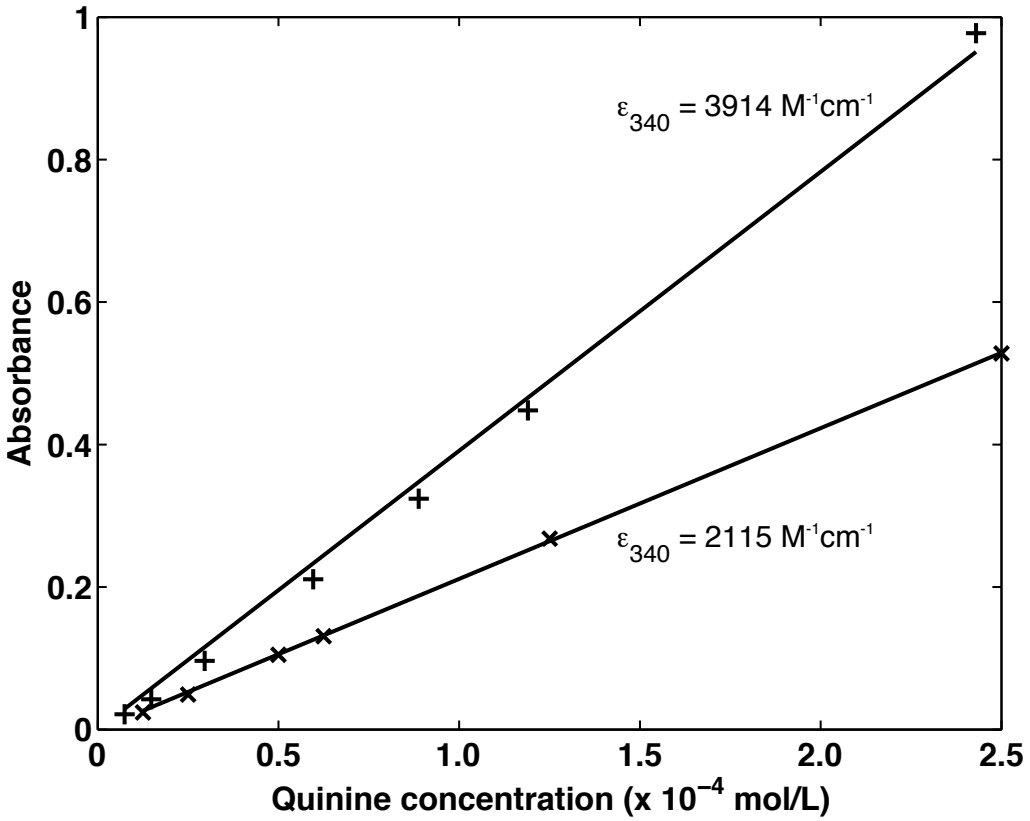

Figure S3: Standards used for calculating extinction coefficients. Vertical crosses, +, denote absorbance data gathered at different quinine concentrations in octanol with 3 % (w/w) Abil EM90 saturated with 1x DPBS. The value for the extinction coefficient, $\epsilon_{340,oil}$, is 3914 ± 437 $M^{-1}cm^{-1}$. Diagonal crosses, X, denote absorbance data gathered at different quinine concentrations in 1x DPBS saturated with octanol with 3 % (w/w) Abil EM90. The value for the extinction coefficient, $\epsilon_{340,aq}$, is 2115 ± 91.8 $M^{-1}cm^{-1}$.

S3 Interfacial tension measurements

The interfacial tension of the octanol/surfactant/DPBS system was measured using a Krüss DSA10 droplet shape analyser (Krüss, Germany) in pendant drop mode. A 500 µm diameter needle was submerged into a cuvette filled with the oil phase (Phase 2 as shown in Table S1), and 3 µL of the aqueous phase (Phase 1) was carefully dispensed into the cuvette to form a droplet of suitable pendant shape. For the aqueous phase, both MilliQ water and DPBS were used. Additional measurements were conducted to determine whether mutual saturation of the two phases influenced the surface tension measurements. All measurements were performed in triplicate and are listed in Table S1. As is evident from this data, the addition of 3 % (w/w) Abil EM90 reduces the surface tension by 30 % on average, while presaturation of the phases and the use of DPBS or MilliQ water do not have a large influence on the interfacial tension.

Table S1: Interfacial tension data from pendant drop measurements. All entries are from triplicate measurements. [a]Octanol with 3 % (w/w) Abil EM90 as used in the droplet-based liquid-liquid extraction experiments presented in the paper.

Phase 1	Phase 2	Presaturation	Interfacial tension (mN/m)
MilliQ	octanol	No	7.75 ± 0.18
MilliQ	octanol	Yes	8.02 ± 0.05
MilliQ	octanol + 3 % Abil EM90[a]	No	5.41 ± 0.08
MilliQ	octanol + 3 % Abil EM90[a]	Yes	5.46 ± 0.30
DPBS	octanol	No	7.66 ± 0.02
DPBS	octanol	Yes	7.70 ± 0.03
DPBS	octanol + 3 % Abil EM90[a]	No	5.38 ± 0.08
DPBS	octanol + 3 % Abil EM90[a]	Yes	5.47 ± 0.05

S4 Calculating D from experimental data

To calculate D from the experimental bulk data, we use the definition of D and the quinine mass balance. Concentrations are described using the format $\left[q_{phase,i/f}\right]$, where q_{phase} denotes the phase (oil or aqueous) where the concentration of quinine is measured and subscripts i or f denote *initial* or *final* concentrations respectively. V_{oil} and V_{aq} represent the volumes of the two phases.

$$D = \frac{[q_{oil,f}]}{[q_{aq,f}]}$$
$$[q_{oil,i}]\,V_{oil} + [q_{aq,i}]\,V_{aq} = [q_{oil,f}]\,V_{oil} + [q_{aq,f}]\,V_{aq}$$

Using the fact that $[q_{oil,i}] = 0$ and $[q_{aq,f}] = [q_{oil,f}]\,/D$, the following expression is obtained:

$$D = \frac{V_{aq}\,[q_{oil,f}]}{[q_{aq,i}]\,V_{aq} - [q_{oil,f}]\,V_{oil}} \tag{S4}$$

Equation S4 was derived from a volumetric mass balance for the bulk experimental data. For the droplet-based liquid-liquid extraction method presented in this paper, a mass balance based on volumetric flow rates is required, and identical derivations lead to:

$$D = \frac{Q_{aq,in}\,[q_{oil,f}]}{[q_{aq,i}]\,Q_{aq,in} - [q_{oil,f}]\,Q_{oil,in}} \tag{S5}$$

S5 Annealing of ultrasonically welded devices

Injection moulding and ultrasonic welding introduce residual stress in the microfluidic devices which, if they are not annealed, may result in chemically-induced stress cracking when exposed to solvents. Figure S4 shows this effect for devices like those used in this paper. An unannealed chip is imaged after 24 hours of octanol exposure and shows a significant amount of cracking. Conversely, a device annealed post-welding shows no signs of cracking after 2 weeks of octanol exposure. As an intermediate case, a device annealed prior to welding shows some signs of cracking after 24 hours of octanol exposure. This confirms that both injection moulding and ultrasonic welding introduce some residual stress in the polymer devices.

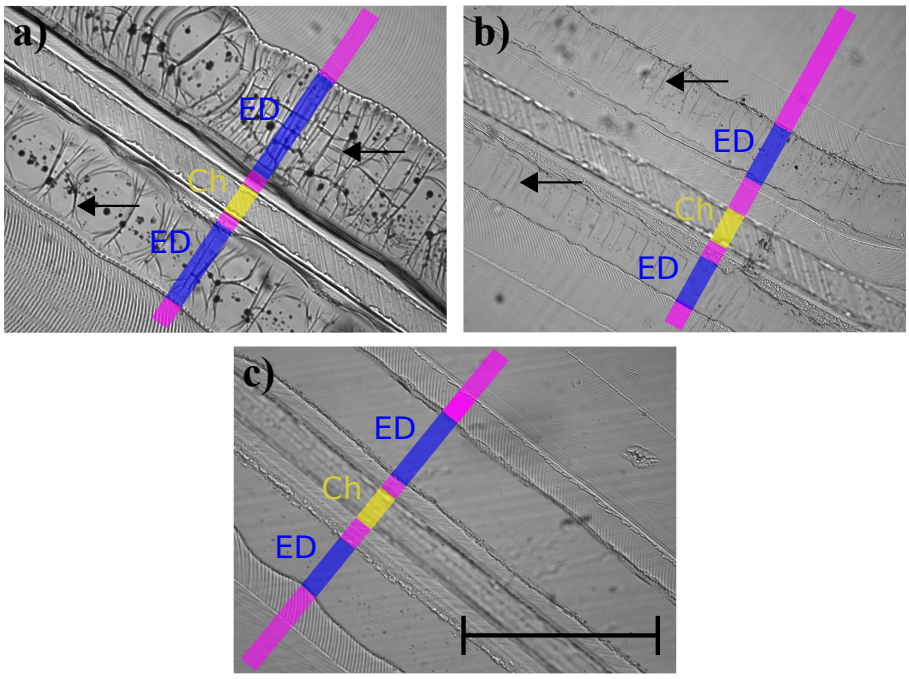

Figure S4: Chemically-induced stress cracking of injection moulded and ultrasonically welded microfluidic devices due to exposure to octanol. **a)** An unannealed device after 24 hours of octanol exposure shows significant cracking. **b)** A microfluidic device annealed prior to welding shows some cracking after 24 hours of octanol exposure. **c)** A microfluidic device annealed post-welding shows no signs of cracking even after 2 weeks of octanol exposure. Arrows denote cracks, **ED** denotes melted energy directors, **Ch** highlights microfluidic channels and magenta areas show locations where there is a small gap between the top and bottom plates of the device, which is a side-effect of using energy directors (Kistrup *et al.*, *J. Micromech. Microeng.*, **2014**, *24*, 125007). The scale bar is 1 mm in all cases.

This material is available free of charge via the Internet at `http://pubs.acs.org/`.

8

Paper 5: Optimized protocols for droplet-based single-hit limiting-dilution assays

8.1 List of mathematical symbols

Symbol	Meaning	Usage
k	Number of targets in a reaction vessel	Eq. (8.5)
μ	Expected value of k	Eq. (8.6)
$P_k(\mu)$	Probability of k targets in reaction vessel	Eq. (8.5)
V	Volume of reaction vessel	Eq. (8.6)
$\vec{V}$	Vector containing value(s) of V	Sec. 8.6.1
$\overline{V}$	Average of values contained in $\vec{V}$	Sec. 8.6.1
c^*	True value of target concentration	Eq. (8.6)
N	Number of vessels (droplets)	Sec. 8.5.1
N_0	Number of vessels void of target	Sec. 8.5.1
N_1	Number of vessels containing target	Sec. 8.5.1
$\vec{b}$	Vector containing value(s) of N_0 and N_1	Sec. 8.6.1
$\overline{b}$	Average of values contained in $\vec{b}$	Sec. 8.6.1
$\hat{c}$	State-of-the-art estimator	Sec. 8.6.1
$\hat{c}_{\mathrm{bc}}$	Bias-corrected estimator	Sec. 8.6.2
$\hat{c}_{\mathrm{ml}}$	Maximum likelihood estimator	Sec. 8.6.4
$E(\cdot)$	Expected value	Box 8.1
$\mathcal{O}(\cdot)$	Limiting behaviour of remaining terms	Eq. (8.10)
$\sim N(\cdot)$	Property is normally distributed	Eq. (8.26)

8.2 Motivation

When entering a new field of study, it is generally safe to assume that the established methods and protocols are optimised to reduce labour and expenses, while resulting in the clearest possible answers. However, if the reason for the choice of method is purely historical, it's never pointless to enter the "engine room". One might learn something.

This is exactly how the work of Paper 5 begun: After conducting a thorough literature study, it became clear that all studies on digital droplet microfluidics employed the assumptions and prerequisite that their droplets were monodisperse (all droplet volumes were identical)[71,72,75,90,198,199]. Using too polydisperse droplets had severe consequences on the accuracy and precision of their estimators[71,72,75,90,198], and so ddPCR has mostly seen progress in chip manufacturing for making uniform and plentiful droplets[47].

Before I continue, allow me to explain a few terms frequently used in this chapter:

Box 8.1: Estimators

In quantitative science, the purpose of experiments is often to *estimate* an underlying value, the *true* value, (x^*) of a stochastic quantity X. The *estimator*, $\hat{x}\left(\vec{y}\right)$, is the mathematical equation used for converting measurement points, $\vec{y} = (y_1, \ldots, y_N)$, into an estimate, $\hat{x}$. The mathematical equation of an estimator is derived from the equations describing the probability of $X = x$, $P(x|\theta)$, with θ representing one or several parameters. The probability distribution is in turn obtained from a theory/model of how the stochastic numbers are distributed and are influenced by changes in the parameters.
In many cases, the data points are of the same data type as the estimate, and the the estimator may be a simple average $\hat{x}\left(\vec{x}\right) = \overline{x}$. Using maximum likelihood estimation, one may show that this works because many observations are independent and identically normal distributed. The estimators of this section is however more complicated, since these estimate a target concentration from the binary read out of droplets, given the droplet volumes.
An estimator may be chosen based on its performance metrics;

- Is the estimator accurate or is it biased? - In words: Will bigger data sets result in an estimate closer to the true value? Is $\lim_{N\to\infty} \frac{E(\hat{x})-x^*}{x^*} = 0$? N being number of data points, and $E\left(\cdot\right)$ being the *expected* value of the $\hat{x}$, the value of the parameter weighted against its probability $E\left(x\right) = \int_{-\infty}^{\infty} xP(x|\theta)dx$ or $E\left(x\right) = \sum_{n=1}^{N} x_n P(x_n|\theta)$ for discrete values.
- How does precision of the estimator depend on experimental parameters, θ, and the number of data points N?

8.2.1 State-of-the-art

As introduced in Section 5.1.2.5 on page 72, the state-of-the-art estimator for ddPCR is based on the assumption that the targets enter the droplets via a *Poisson* process (e.i. (1) the targets do in no way influence each other) and (2), the probability of a target entering a droplet i constant in time, given the constant concentration) and that the droplet size distribution is monodisperse[82]. When the targets enter the droplets in a *Poisson* process, the probability of a droplet of volume V to contain k droplets, given the loading concentration c^* is *Poisson* distributed:

$$P_k(\mu) = \frac{\mu^k}{k!} e^{-\mu} \tag{8.1}$$

where $\mu = c^* V$ is expected value of the occupancy ($\mu = \langle k \rangle$). Using this, the probability of obtaining a positive droplet ($k > 0$) is calculated by subtracting $P_0(\mu)$ from 1,

$$P_+(\mu) = \sum_{k=1}^{\infty} \frac{\mu^k}{k!} e^{-\mu} = 1 - P_0(\mu) = 1 - e^{-\mu}, \tag{8.2}$$

and by assuming that the percentage of positive droplets (N_1/N) approaches the probability of obtaining a positive droplet when the sample size increases,

$$\begin{aligned} \lim_{N \to \infty} \frac{N_1(\mu)}{N} &= P_+(\mu) \\ &= 1 - e^{-\mu}, \end{aligned} \tag{8.3}$$

we may solve for, μ:

$$\hat{\mu} = -\ln\left(1 - \frac{N_1}{N}\right). \tag{8.4}$$

The template concentration can be estimated from the fraction of positive droplets from $\hat{c} = \hat{\mu}/\overline{V}$, resulting in the state-of-the-art estimator of Equation (8.7). Specifically, the estimator is applied by using the average volume,$\overline{V}$, and so $\hat{c}(\overline{V}, N_1/N) = -\frac{1}{\overline{V}} \ln(1 - \frac{N_1}{N})$. This is elaborated in the paper, Equation (8.8).

8.2.2 Violation of assumptions

With the high inter- and intra chip polydispersity observed in Paper 4, it was clear that if the state-of-the-art methods of ddPCR were to be transferred to the presented

polymer platform, the assumption of a monodisperse droplet population would be violated[71,72,75,90,198,199] (See motivation section, previous page). With the above equations in mind, a few questions arose: (1) How does polydispersity in droplet volume influence the estimator? (2) Is the only option to make major improvements in the droplet forming department? (3) Is it possible to couple the individual volumes with the amplification outcome to perhaps include more information in the calculations? (Or in other words) Presumably, the two quantities, $\overline{V}$ and N_1/N carries less information about c^* than the N values of V and the N values of $N_{0/1}$ if combined properly.

To substantiate my concern let me repeat that the probability of a droplet containing a target is dependent on its volume $P_+\left(V, c^*\right) = 1 - e^{-Vc^*}$, see Equation (8.2). Observing a small droplet to be "negative" may therefore not be a consequence of a low target concentration (the number we wish to estimate), but merely a consequence its small volume. Likewise, a large, "positive" droplet may not necessarily prove that c^* is high. See Figure 8.1 further explanation and annotation of parameters.

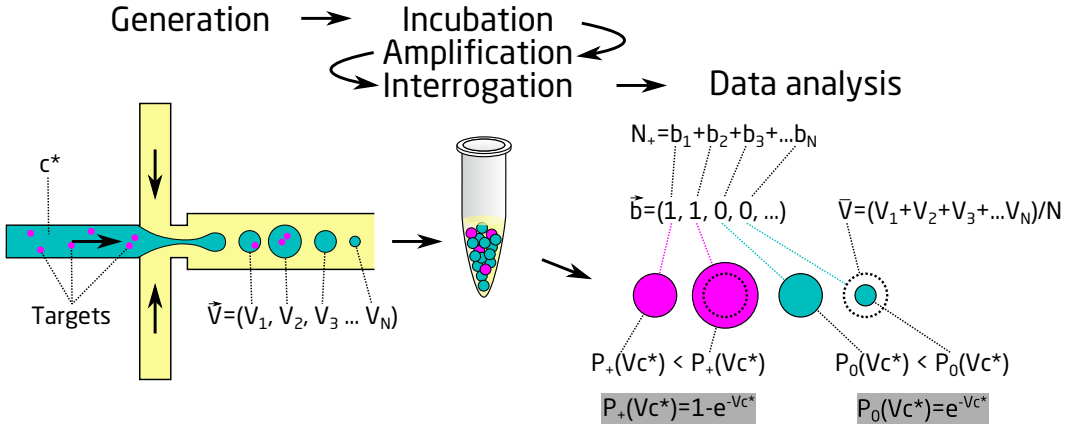

Figure 8.1: Droplet analysis from droplet volumes, $\vec{V} = (V_1, V_2, \ldots, V_N)$, and binary results, $\vec{b} = (b_1, b_2, \ldots, b_N)$. Note that different droplet volumes result in different probabilities for capturing a target. The $\vec{b}$ notation is elaborated in Section 8.6.1 on page 124.

To get an estimate of how polydispersity would influence the estimate and verify if my concern was unwarranted, I decided to leave out as many experimental contributors of noise and error as possible, and used the cleanest lab possible: the computer. A *Monte Carlo* simulation was constructed to generate synthetic droplet data from a given concentration, c^*, and droplet volume distribution by using the binomial distribution[a] with $P_+\left(V_n, c^*\right)$ probability of marking the droplet as "positive". If the reader is sceptical towards synthetic data, I may point out that the only thing this program does is using the fact/prerequisite/assumption that the cells enter the droplets in a *Poisson* process, coining small weighted coins with heads and tails of weights $P_+\left(V_n, c^*\right)$ and $P_0\left(V_n, c^*\right)$, followed by flipping said coins to determine if the droplet in question (the data point we are generating) is positive or negative). The computer model is described in depth in Figure 8.4 on page 129. Since I designed the experiment, the estimated value $\hat{c}$ could be compared to the value used to generate the data, c^*, by calculating the bias.

[a] Coin toss: Yes/no.

After confirming that the model worked for monodisperse droplet volume populations, polydispersity was introduced in the volumes. This numerical result showed a linear, negative correlation between bias and the variance (given as the coefficient of variation, CV, squared), see Figure 8.2. This correlation is derived analytically in the paper, see Section 8.6.1.1 on page 125 and 8.8.1 on page 133 (supplementary section).

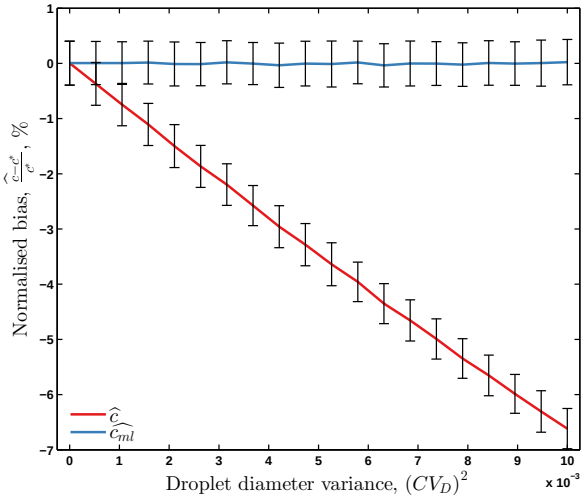

Figure 8.2: Bias of estimators from *Monte Carlo* experiments. Each entry on the plot (marked with error bars, representing standard deviation) represents the average of 1.000 experiments each of which is comprised of 100.000 droplets. Droplet diameters are normal distributed as $\sim N\left(D_0, CV_D \cdot D_0\right)$, where CV_D is the coefficient of variation of diameter. To minimise variation $c^* = V_0\left(D_0\right)/1.6$ (proved in Section 8.8.2 on page 134). Note that the highest value of droplet diameter variance, $CV_D^2 = 10^{-4}$ corresponds to a coefficient of variation of 10%, a reasonable value considering that other studies have reported $1\% < CV_D < 15\%$[96,200–205]. Note also that $CV_D = 10$ is ~ 3 times less than what was observed in Paper 4.

Also plotted in Figure 8.2 is the bias of the *Maximum Likelihood Estimator* (MLE), $\hat{c}_{\mathrm{ml}}$, the main result of this paper. This estimator is described in detail in Section 8.6.4 on page 128 and 8.9 on page 139, but in brief: $\hat{c}_{\mathrm{ml}}(\vec{b}, \vec{V})$ is the most likely "value of c^*" to have produced the observed data.

8.3 Remarks

A few other considerations were made, which were not included in the paper:

1. We show in Section 8.8.2, Figure 8.7 on page 138, that to minimise the variance for set number of droplet, N, $\mu = 1.6$. However, if the the sample material is limited in volume, and the entirety of the sample material is "droplyfied" ($V_{tot} = N \cdot V$), then it can be shown that the variance is minimised by $\mu \to 0$. This is not surprising, since we are then interrogating the sample atom-by-atom.
2. As mentioned in the papers introduction, $\mu \ll 1$, increases the risk of $N_0 = N$, a useless result. Likewise, $\mu \gg 1$, increases the risk of $N_1 = N$, which is equally useless. One may show that the probability of obtaining a *useful* result ($N_0 < N < N_1$) is maximised by $\mu = ln\,(2)$. However, as shown in Figure 8.3, the risk of producing unusable data falls off exponentially with N (contrary to the variance).

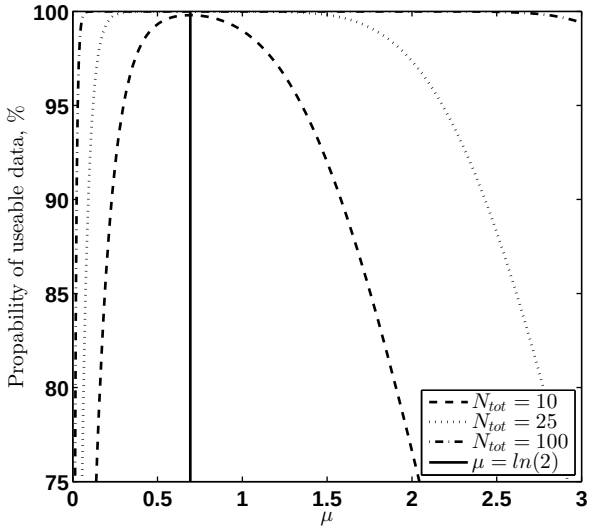

Figure 8.3: Probability of obtaining useable data ($N_0 < N < N_1$) plotted versus μ for several values of N. $\mu = ln\,(2)$ is highlighted by the vertical line.

8.3.1 Experimental verification

To some, the *Monte Carlo* simulations and the analytic results presented in this chapter are sufficient for proving the superiority of our new estimator, while others may disagree. We originally intended to submit the paper in its current theoretical form, we have, however, recently decided to include experimental data, and I have therefore started the work on a droplet-based isothermal amplification system for quantifying *Salmonella* spp. As presented on Figure 9.3 on page 148, the LAMP reaction has been confirmed to not be inhibited by the presence of octanol. In Chapter 9, I will present the microfluidic device and the current experimental progress.

For this reason, this paper is not yet published. Unlike the other papers of this thesis which has been edited by the editors staff, this allows the usage of direct referencing to the Supplementary Information, e.g. "(see Supplementary Note Section 8.9.3 on page 141)".

8.3.2 Contribution

The following too-be submitted paper is authored in collaboration with Associate Professor Henrik Flyvbjerg, group leader of Stochastic Systems and Signals at DTU Nanotech. My contribution consists of conceiving the idea for the studying the consequences of deviating of the established assumptions, programming and conducting the *Monte Carlo* simulations, deriving the maximum likelihood estimator and studying its properties numerically, proposing and studying (numerically) the usefulness of $\hat{c}_{\mathrm{ml}}$ for experimental planning for quantification of unknown concentrations (real samples, Section 8.6.6 on page 130), participated in analytical derivations, made first paper draft, and producing all figures.

Optimized protocols for droplet-based single-hit limiting-dilution assays

Carl Esben Poulsen[a], Anders Wolff[a] and Henrik Flyvbjerg[*a]

8.4 Abstract

We demonstrate huge inefficiency in current protocols for target quantification in single-hit *limiting dilution assays (LDA)*, such as *droplet digital polymerase chain reaction (ddPCR)* for nucleic acid quantification. In most ddPCR experiments, a simple change in protocol removes bias and reduces the variance of estimates by a factor 30 or more. Consequently, our protocols need 30 times fewer droplets to yield accurate results of equal precision. As one of our protocols applies to droplets with any size distribution, it also enables use of bulk droplet production methods. Lastly, if a prior estimate of the target concentration exists, a polydisperse droplet-size distribution is optimal, as we show. We give its parameters as functions of the prior estimate.

8.5 Introduction

8.5.1 State-of-the-art

Limiting dilution assays (LDA) for concentration determination of, e.g., bacteria in food products is a robust and well established method[206]. In a LDA, a set of reaction vessels is prepared, and the amplification reactions that determine the presence or absence ("hit" or "miss") of targets in each vessel, are executed in parallel. One assumes that the medium to be analyzed is "well stirred" in the sense that targets are randomly and independently distributed in it. Then targets enter a reaction vessel in a Poisson process when such a vessel is filled. Consequently, the number k of targets in a reaction vessel is Poisson distributed,

$$P_k(\mu) = \frac{\mu^k}{k!} e^{-\mu} \ . \tag{8.5}$$

Here μ is the expected value of k and is given by the concentration, c^*, of targets and the volume, V, of the reaction vessel,

$$\mu = \langle k \rangle = c^* V \ . \tag{8.6}$$

[a] *Technical University of Denmark, Department of Micro- and Nanotechnology, Ørsteds Plads, Building 345E, DK-2800 Kgs. Lyngby, Denmark*
[*] *E-mail: henrik.flyvbjerg@nanotech.dtu.dk*

Given N vessels of identical volumes V, it then follows that the number of vessels, N_0, observed to contain no targets is binomially distributed on $\{0, 1, 2, \ldots, N\}$ with expected value $NP_0(\mu)$. Thus N_0/N has expected value e^{-c^*V}, and c^* is consequently estimated by

$$\hat{c} = -\frac{1}{V} \ln\left(\frac{N_0}{N}\right) \quad . \tag{8.7}$$

With the emergence of advanced microfabrication techniques and microfluidics, several well-chip-based solutions capable of quantifying nucleic acid have been commercialised[b] These proprietary chips distribute a sample over several thousand separate on-chip reaction chambers, thermo-cycle it for PCR, and read out a fluorescence signal to evaluate N_0.

Alternatively, compartmentalisation of the sample can be achieved by emulsifying the sample into water-in-oil droplets[34]. Emulsification has several advantages over compartmentalisation in chambers, including higher density of reaction vessels[47], adjustable vessel (=droplet) volume, reduced dead-volume, alternative interrogation methods, such as flow-cytometry[207], and the possibility to manipulate the droplet population as a bulk liquid (pipetting, in-tube thermo-cycling, etc.)[47,58,208,209].

Droplet digital PCR (ddPCR) is an example of a single-hit LDA conducted in water-in-oil droplets. It has been used to accurately quantify DNA[4,47,58,68–79], e.g. to quantify rare alleles in high wild-type background[57,58], and to quantify RNA using reverse transcriptase PCR (RT-PCR)[84–87] and real-time RT-PCR[93,96].

8.5.2 Shortcomings

Although the ddPCR technology is useful and has been commercialised[b], two shortcomings have been recognised experimentally: (i) ddPCR tends to underestimate c^* when $\mu \sim 1$[71,72,75,90,198], and (ii) droplets must be of identical size and stable[199].

It is common practice to reduce the degree of underestimation by arranging that $\mu \ll 1$[58]. In consequence, $P_0 \approx 1$, so one needs a large number of droplets, N, to measure anything—in the order of millions for low c^*[47]. At lower N, one is likely to find $N_0 = N$ and hence $c = 0$. At fixed N, one navigates between Scylla and Charybdis: If one reduces bias by reducing μ, one increases stochastic errors on c in Equation (8.7); see below.

Uniformity of droplet size is improved by using high precision lithography for chip fabrication, custom synthesized surfactants, and pressure pumps instead of syringe pumps[210]. Thus, most ddPCR studies have achieved standard deviations, σ_D, of

[b] Well-chip-based: The Biomark® HD from Fluidigm Corporation, the OpenArray RealTime PCR System from Life Technologies and the Constellation Digital PCR from Formulatrix.
Droplet bassed: The QX100/QX200 ddPCR System from Bio-Rad Laboratories and the RainDrop Digital PCR system from RainDance Technologies.
See Table 1.2 on page 18 for comparison of specifications.

droplet diameters of $1\% - 15\%$ of the average droplet diameter, $\bar{D}$[96,200–205]. These droplet distribution are considered monodisperse for lack of alternatives, but they are Gaussian[200,205,211], and this causes estimation bias towards underestimation.

Pinheiro *et al.* (2012)[72] observed that this bias is independent of the sample concentration, and suggested that in the limit $N \to \infty$ the bias may be explained partly by inter-experiment dispersion in droplet volume.

8.5.3 Solutions

We prove here that this is the case, indeed, and deal with it as follows.

(1) We examine how dispersion in droplet size affects mean and variance of the estimator $\hat{c}$ in Equation (8.7);

(2) we present $\hat{c}_{\mathrm{bc}}$, a bias-corrected version of $\hat{c}$, which, contrary to $\hat{c}$, allows for experimental designs that minimise bias *and* variance simultaneously;

(3) we explain how to calibrate a LDR-device that produced droplets with Gaussian size-distribution. Calibration is a simple alternative to measuring individual droplet sizes or their variance, if such measurements are not an option.

(4) we present $\hat{c}_{\mathrm{ml}}$, the *Maximum Likelihood Estimator (MLE)*, which applies to *any* distribution of droplet-sizes, is unbiased, and, for given droplet distribution, has the smallest variance possible for an unbiased estimator. This allows *any* distribution of droplet-sizes to be used in ddPCR, which is important, because

(5) we show that when an estimate already exists for the true concentration, c^*, then a *polydisperse* distribution minimizes the variance of $\hat{c}_{\mathrm{ml}}$.

(6) Droplet-size distributions are typically Gaussian, so we provide the parameters of the Gaussian distribution that minimizes the variance of $\hat{c}_{\mathrm{ml}}$, as functions of the prior estimate.

8.6 Estimators for droplet-based LDA

8.6.1 State-of-the-art estimator $\hat{\mathbf{c}}$

Consider N droplets with volumes $(V_1, V_2, \ldots, V_N) = \vec{V}$. Let $(b_1, b_2, \ldots, b_N) = \vec{b}$ be binary variables, with $b_n = 1$ denoting a hit in the nth volume, and $b_n = 0$ denoting no hit there. Then the average volume is $\overline{V} = (\sum_{n=1}^{N} V_n)/N$, while the average number

of hits is $\bar{b} = (\sum_{n=1}^{N} b_n)/N$. The average number of misses[c] is $N_0/N = 1 - \bar{b}$. With this notation, the state-of-the-art estimator for droplet based LDA, such as ddPCR, reads

$$\hat{c}(\overline{V}, \bar{b}) = -\frac{1}{\overline{V}} \ln(1 - \bar{b}) \ . \tag{8.8}$$

It replaces V in Equation (8.7) with $\overline{V}$, and this is why $\hat{c}$ is a biased estimator for polydisperse reaction volumes: rewriting Equation (8.8) as

$$e^{-\hat{c}\overline{V}} = 1 - \bar{b} \tag{8.9}$$

reveals that this estimator says: *For given $\overline{V}$ and $\bar{b}$, chose the concentration $\hat{c}$ that makes the probability $e^{-\hat{c}\overline{V}}$ of a miss in the volume $\overline{V}$ equal to the observed frequency of misses, $1 - \bar{b}$.* Non-identity of volumes do not affect this relationship, since only $\overline{V}$ occurs in it, and this is wrong, because the probability of a miss in a given volume depends non-linearly on the volume, so a good estimator for c^* must depend also on the variance of volumes in an experiment and possibly on higher central moments of the distribution of volumes.

8.6.1.1 Bias of $\hat{c}$

The bias of $\hat{c}$ in units of c^* is (see Supplementary Note Section 8.8.1 on page 133)

$$\frac{E(\hat{c}) - c^*}{c^*} = -\frac{1}{2}\frac{c^* \mathrm{Var}(V)}{E(V)} + \mathcal{O}(N^{-1/2}) \ . \tag{8.10}$$

Here $E(\cdot)$ denotes expected value.

The order-of-magnitude estimates given here for left-out terms hold for a Gaussian distribution of droplet volumes, while the left-out terms are small also for approximately Gaussian distributions; they just do not vanish in the limit $N \to \infty$ (see Supplementary Note Section 8.8.1 on page 133).

The dominant, explicitly given term in Equation (8.10), shows that the bias of $\hat{c}$ is negative, independent of N, and can be reduced only by reducing the target concentration, c^*, and/or by reducing the variance $\mathrm{Var}(V)$ of droplet volumes. Both of these approaches to bias-reduction are currently considered prerequisite for ddPCR[58].

8.6.2 Bias-corrected estimator $\hat{c}_{\mathrm{bc}}$

For any set of volumes, $V_1, V_2, \ldots, V_N$, we know that the probability of a miss in the nth volume is $e^{-c^* V_n}$, and hence that the expected frequency of misses in this set is

$$\frac{1}{N}\sum_{n=1}^{N} e^{-c^* V_n} = \overline{e^{-c^* V}} \tag{8.11}$$

[c] We will use the terms "no-hit" and "miss" interchangeably.

where the right-hand side is a shorthand notation for the left-hand side. It is consequently logical to *chose the concentration* $\hat{c}_{\mathrm{bc}}$ *that makes the expected frequency of misses,* $\overline{e^{-\hat{c}_{\mathrm{bc}}V}}$*, equal to the observed frequency of misses,* $1-\overline{b}$*,*

$$\overline{e^{-\hat{c}_{\mathrm{bc}}V}} = 1-\overline{b}\ . \tag{8.12}$$

Equation (8.12) requires that we know $\vec{V}$, while Equation (8.8) only demands that we know $\overline{V}$. Also, Equation (8.12) gives $\hat{c}_{\mathrm{bc}}(\vec{V},\overline{b})$ implicitly, while Equation (8.8) gives $\hat{c}$ explicitly. However, for given $\vec{V}$ and $\overline{b}$, Equation (8.12) is easily solved for $\hat{c}_{\mathrm{bc}}$ numerically; the explicit expression for $\hat{c}$ is a good initial guess for $\hat{c}_{\mathrm{bc}}$. Moreover, for a Gaussian distribution of droplet volumes,

$$\overline{e^{-\hat{c}_{\mathrm{bc}}V}} = e^{-\hat{c}_{\mathrm{bc}}\overline{V}+\hat{c}_{\mathrm{bc}}^2\overline{(V-\overline{V})^2}/2} \tag{8.13}$$

up to terms of order $N^{-1/2}$; this follows from the cumulant expansion of the left-hand side.

For large N, this identity is actually a good approximation for most distributions of droplet volumes, Gaussian or not, as long as the relative variance, $\overline{(V-\overline{V})^2}/\overline{V}^2$ is small and the distribution does not have fat tails. Using this in Equation (8.12) and using $\hat{c}$ as a short-hand notation for the right-hand side of Equation (8.8), Equation (8.12) reads

$$\hat{c} = \hat{c}_{\mathrm{bc}} - \hat{c}_{\mathrm{bc}}^2\frac{\overline{(V-\overline{V})^2}}{2\overline{V}}\ . \tag{8.14}$$

Solving for $\hat{c}_{\mathrm{bc}}$, we find

$$\begin{aligned}
&\hat{c}_{\mathrm{bc}}(\,\overline{V},\overline{(V-\overline{V})^2},\overline{b}\,) \\
&\qquad = \frac{\overline{V}}{\overline{(V-\overline{V})^2}}\left[1-\left(1-2\frac{\overline{(V-\overline{V})^2}}{\overline{V}}\hat{c}\right)^{1/2}\right] &(8.15)\\
&\qquad \approx \hat{c}\left(1+\frac{\overline{(V-\overline{V})^2}}{2\overline{V}}\,\hat{c}\right)\ , &(8.16)
\end{aligned}$$

where the last approximation is good if the relative variance $\overline{(V-\overline{V})^2}/\overline{V}^2$ is small, since $\hat{c}\overline{V}$ at most is of order one in practise.

8.6.2.1 Bias of $\hat{\mathbf{c}}_{\mathrm{bc}}$

A calculation (see Supplementary Note Section 8.8.3 on page 138) similar to Equation (8.10) gives the bias of $\hat{c}_{\mathrm{bc}}$):

$$\frac{E(\hat{c}_{\mathrm{bc}})-c^*}{c^*} = -\frac{1}{2}\left(\frac{c^*\mathrm{Var}(V)}{E(V)}\right)^2+\mathcal{O}(N^{-1})\ . \tag{8.17}$$

Comparing Equations (8.10) and (8.17), we see that the bias of $\hat{c}_{\mathrm{bc}}$ is a factor $c^*\mathrm{Var}(V)/E(V)$ smaller than the bias of $\hat{c}$. This is typically a factor 1/30 or less.

Figure 8.4 on page 129, top panel, compares the performance of the two estimators on synthetic data and demonstrates that $\hat{c}_{\mathrm{bc}}$ has much less bias than $\hat{c}$, while their variances look identical.

8.6.3 Bias removed by calibration

Equations (8.15) and (8.16) both give $\hat{c}_{\mathrm{bc}}$ explicitly and do not require knowledge of $\vec{V}$. Knowing $\overline{V}$ and $\overline{(V-\overline{V})^2}$ is sufficient. Consequently, a device that produces polydisperse droplets with reproducible statistics may be calibrated. If measuring $\vec{V}$ is not an option, calibration may be the second-best way to remove bias.

8.6.3.1 How to calibrate.

Specifically, if $\overline{V}$ and $\overline{(V-\overline{V})^2}$ are independent of the concentration of targets in the droplets, they characterize of the droplet-producing device. Then $\overline{(V-\overline{V})^2}$ can be measured by measuring $\bar{b}$ (and $\overline{V}$ if unknown) for a set of unknown volumes $\vec{V}$ for a sample of known concentration. That done, $\overline{(V-\overline{V})^2}$ is determined by solving Equations (8.8) and (8.14) for $\overline{(V-\overline{V})^2}$. In the result,

$$\overline{(V-\overline{V})^2} = \frac{2(\hat{c}_{\mathrm{bc}}\overline{V} + \ln(1-\bar{b}))}{\hat{c}^2} \ , \tag{8.18}$$

the known concentration is inserted in $\hat{c}$'s place. This experimental determination of $\overline{(V-\overline{V})^2}$ for a given device should be repeated for several known target-concentrations. That will result in correspondingly different values for $\bar{b}$, while each determination of $\overline{(V-\overline{V})^2}$ should result in the same value up to experimental errors, since $\overline{(V-\overline{V})^2}$ is a property of the droplet-producing device/setup.

8.6.3.2 Calibration errors due to finite statistics are typically less than 1%.

A device that produces droplets with Gaussian distributed volumes with standard deviation $\sigma(V)$, will reproduce $\overline{V}$ with standard deviation $\sigma(\overline{V}) = \sigma(V)/\sqrt{N}$ and reproduce $\overline{(V-\overline{V})^2}$ with standard deviation $\sigma\left(\overline{(V-\overline{V})^2}\right) = \sqrt{2}\sigma^2(V)/\sqrt{N}$. Consequently, even if the Gaussian scatter $\sigma(V)$ of individual droplet volumes is a substantial fraction of their mean volume, $\overline{V}$ and $\overline{(V-\overline{V})^2}$ are reproduced with less than 1% scatter in measurements using $N \geq 10,000$ droplets. Thus, if one cannot simply measure $\vec{V}$, calibration is desirable in view of the improvement that $\hat{c}_{\mathrm{bc}}$ represents compared to $\hat{c}$.

8.6.4 Maximum likelihood estimator $\hat{c}_{\mathrm{ml}}$

For a non-Gaussian distribution of droplet volumes, both results for $\hat{c}_{\mathrm{bc}}$ in Equations (8.15) and (8.16) are approximate. They can be improved systematically by keeping higher cumulants in the exponent on the right-hand side of Equation (8.13). The results are useful only if we can determine those higher cumulants, e.g. via calibration experiments. If we can measure $\vec{V}$ while we measure $\vec{b}$, we know all moments, of course. But in this case we can just solve Equation (8.12), or, even more attractive, use maximum likelihood estimation.

It is well established that in the limit $N \to \infty$ the so-called *maximum likelihood estimator* gives estimates that are Gaussian distributed about the true value, here c^*, with the smallest variance possible for an unbiased estimator. Deviations from this ideal behaviour are of order $1/N$, i.e., negligible for the values of N that we consider.

Given $\vec{V}$ and $\vec{b}$, the maximum likelihood estimator $\hat{c}_{\mathrm{ml}}(\vec{V}, \vec{b})$ for c^* is implicitly given as the solution to

$$\overline{V} = \overline{\left(\frac{bV}{1 - e^{-\hat{c}_{\mathrm{ml}} V}} \right)} \tag{8.19}$$

(see Supplementary Note Section 8.9.1 on page 139). Its variance is identical to the variance of $\hat{c}$ and $\hat{c}_{\mathrm{bc}}$; see below. The performances of $\hat{c}_{\mathrm{ml}}$ and $\hat{c}$ are compared in Figure 8.4, bottom panel.

MLE works and is the optimal estimator for any given distribution of droplet volumes. It concequently permits droplet production methods previously inapplicable for ddPCR, such as Couette shear mixing[212]. Also, it is no longer a problem if two droplets merge prior to signal read-out, because merges do not change the likelihood function. Typically, $\geq 5\%$ of the droplets merge during thermo-cycling, and this data must be discarded when $\hat{c}$ is used[47].

8.6.5 Variances of $\hat{c}$, $\hat{c}_{\mathrm{bc}}$, and $\hat{c}_{\mathrm{ml}}$

The estimators $\hat{c}$ and $\hat{c}_{\mathrm{bc}}$ have the same variance (see Supplementary Note Section 8.8.2 on page 134),

$$\mathrm{Var}\left(\hat{c}_{\mathrm{bc}}\right) = \mathrm{Var}\left(\hat{c}\right) = \frac{1}{N \int_0^\infty p_V(\cdot) \frac{V^2}{e^{c^* V} - 1} dV} \approx \frac{1}{N} \frac{\overline{e^{-c^* V}} - \overline{e^{-2c^* V}}}{\overline{V}^2 \left(\overline{e^{-c^* V}}\right)^2} \ . \tag{8.20}$$

For a nearly monodisperse distribution $p(V)$ centered on V_0,

$$\mathrm{Var}\left(\hat{c}_{\mathrm{bc}}\right) = \mathrm{Var}\left(\hat{c}\right) = \frac{e^{c^* V_0} - 1}{N V_0^2} \ . \tag{8.21}$$

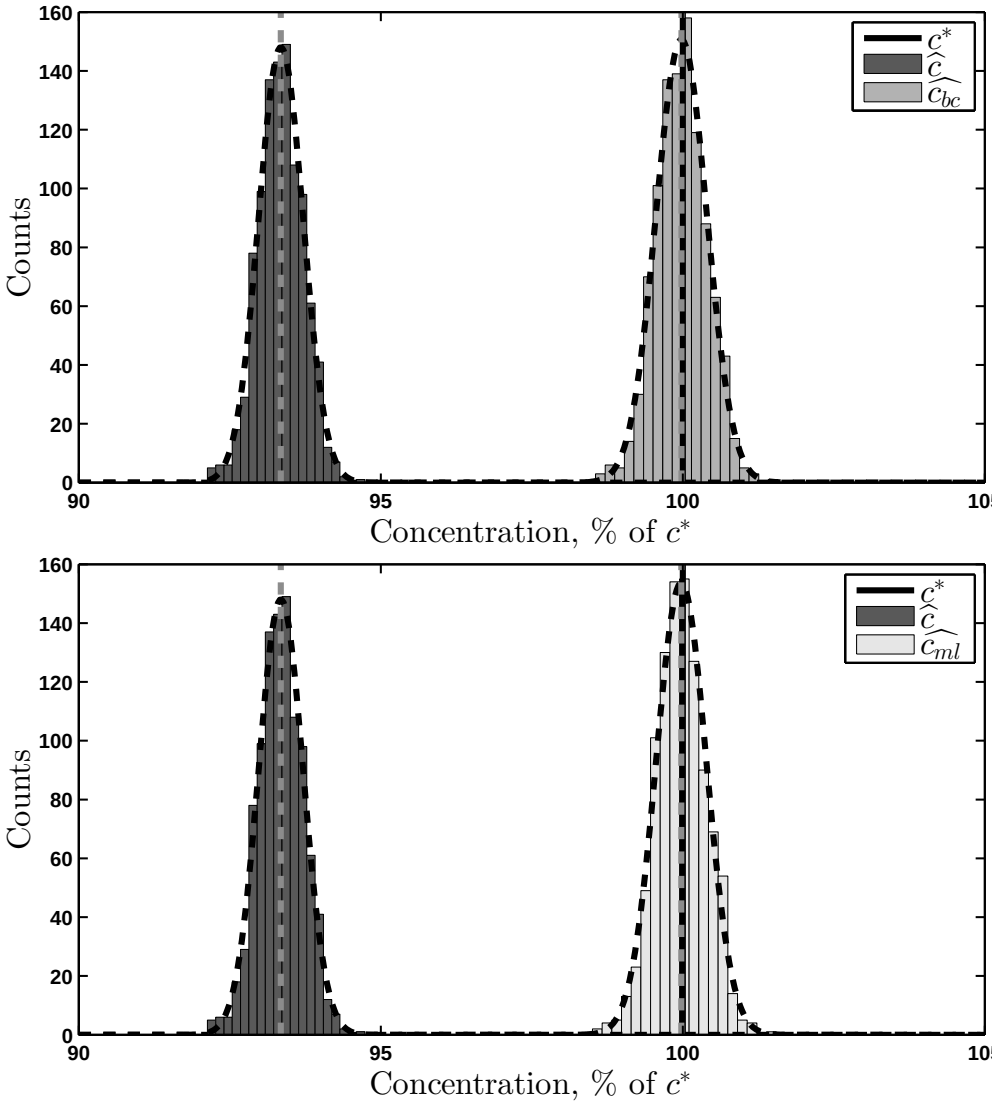

Figure 8.4: Histograms of estimates $\hat{c}$, $\hat{c}_{\mathrm{bc}}$, and $\hat{c}_{\mathrm{ml}}$ from 1000 simulated experiments, each using 100,000 droplets. Droplet volumes were chosen at random from a Gaussian distribution of droplet diameters D with mean D_0 and 10% scatter σ_D/D_0. Droplet volumes were spherical, $V(D) = \pi D^3/6$, and consequently nearly Gaussian distributed. D_0 was chosen such that $c^*V(D_0) = 1.6$, since that maximizes estimator precision (see Figure 8.7) . Thus, c^* can be any concentration; droplet volumes are adjusted accordingly, as in real experimental planning. $\vec{b}$ was generated by choosing $b_n = 0$ with Poisson probability $P_0(c^*V_n)$ and $b_n = 1$ with probability $1 - P_0(c^*V_n)$, repeated independently for all values of n from 1 to 100,000. (top) Histograms of estimates $\hat{c}$ and $\hat{c}_{\mathrm{bc}}$ Vertical lines represent c^* (at 100%) and mean values for $\hat{c}$ and $\hat{c}_{\mathrm{bc}}$ found by averaging their values from the 1000 experiments. The biases of the estimators in equations (8.8) , (8.12), (8.15), (8.16), and (8.19) were, -6.648, -0.015, 0.730, -0.312, and -0.007% of c^*, respectively. (bottom) Histograms of $\hat{c}$ and $\hat{c}_{\mathrm{ml}}$ (normalised to c^*).Vertical lines represent c^* and mean values for $\hat{c}$ and $\hat{c}_{\mathrm{ml}}$ found by averaging their values from the 1000 simulated experiments.

Likewise, the variance of $\hat{c}_{\mathrm{ml}}$ is (see Supplementary Note Section 8.9.3 on page 141)

$$\mathrm{Var}(\hat{c}_{\mathrm{ml}}|\vec{V}) = \frac{1}{N}\left[\overline{\left(\frac{V^2}{e^{c^*V}-1}\right)}\right]^{-1}, \tag{8.22}$$

and may be estimated by

$$\widehat{\mathrm{Var}}(\hat{c}_{\mathrm{ml}}) = \frac{1}{N}\left[\overline{\left(\frac{V^2}{e^{\hat{c}_{\mathrm{ml}}V}-1}\right)}\right]^{-1}. \tag{8.23}$$

8.6.6 Experimental design for polydisperse droplet LDA

For a given number of droplets, N, and concentration, c^*, this variance is minimal for volume

$$V_0 = 1.6/c^* \ . \tag{8.24}$$

So if a reliable à priori estimate of c^* exists, further estimation may be optimized for precision by choosing droplets satisfying Equation (8.24). Bias, however, is minimal in Equation (8.10) for c^*V_0 minimal, given the relative variance $\mathrm{Var}(V)/V_0^2$ is fixed. Thus with $\hat{c}$ one must choose between large bias and large variance if N is fixed. The only way to reduce both bias and variance for $\hat{c}$ is by making c^*V_0 small and N large, as noted in the literature. The same considerations apply to $\hat{c}_{\mathrm{bc}}$, but this is a moot point: because of its much smaller bias, we have negligible bias even with $c^*V_0 = 1.6$.

As mentioned previously, $\mathrm{Var}\left(\hat{c}_{\mathrm{ml}}\right)$ is minimised when $c^*V_0 = 1.6$, and an LDA should therefore be designed accordingly. However, in a real LDA experiment, the objective is to estimate an unknown c^*, and the planning of the experiment must hence be based on prior knowledge/estimates of c^*. If the prior estimate, c_{prior}, is Gaussian distributed around c^* with standard deviation $\sigma_{c_{\mathrm{prior}}}$, and the experiment is designed such that $V_0 = 1.6/c_{\mathrm{prior}}$, it is desired that the variance, $\mathrm{Var}\left(\hat{c}_{\mathrm{ml}}\right)$, of results from independent identical experiments is minimized. We calculate the average variance by integrating Equation (8.22) over the probability distribution p_{prior} of c_{prior}.

$$\overline{\mathrm{Var}\left(\hat{c}_{\mathrm{ml}}\right)_{p_V(\cdot),p_{\mathrm{prior}}}} = \int_0^\infty p_{\mathrm{prior}}(c_{\mathrm{prior}})\mathrm{Var}\left(\hat{c}_{\mathrm{ml}}\right) dc_{\mathrm{prior}} \tag{8.25}$$

$$p_{\mathrm{prior}} \sim N\left(c^*, \sigma_{c_{\mathrm{prior}}}\right), \tag{8.26}$$

Equation (8.25) is plotted in Figure 8.5 where the minimum average variance for a given $\sigma_{c_{\mathrm{prior}}}/c^*$ is highlighted in magenta.

As seen, when $\sigma_{c_{\mathrm{prior}}}/c^* \geq 25.25\%$, droplet volume dispersion becomes feasible, since the average variance is not longer minimised by employing a monodisperse droplet volume population.

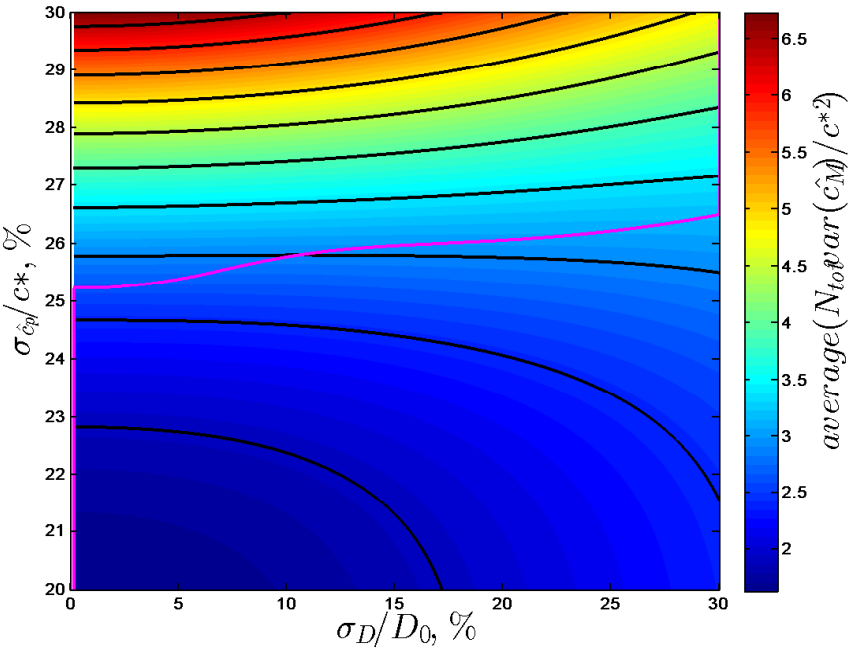

Figure 8.5: Average variance of $\hat{c}_{\mathrm{ml}}$ for LDAs designed such that $V_0 = 1.6/c_{\mathrm{prior}}$, where the prior estimate, c_{prior}, has probability distribution $p_{\mathrm{prior}} \sim N\left(c^*, \sigma_{c_{\mathrm{prior}}}\right)$. The minimum average variance for a given $\sigma_{c_{\mathrm{prior}}}/c^*$ is highlighted in magenta. Contour levels are denoted by tick marks on the colour bar.

8.7 Conclusion

If one can measure the volumes of individual droplets while recording whether they contain hits or misses, then maximum likelihood estimation with $\hat{c}_{\mathrm{ml}}$ in Equation (8.19) is the very best way to estimate c^*. No other unbiased estimater determines c^* with smaller error bar from given data $(\vec{V}, \vec{b})$.

If one can measure only the sample mean and variance, $\overline{V}$ and $\overline{(V-\overline{V})^2}$, for the samle of N droplets for which one measures $\vec{b}$, then $\hat{c}_{\mathrm{bc}}(\overline{V}, \overline{(V-\overline{V})^2}, \overline{b})$ in Equation (8.15) is the best way to estimate c^*, provided that the distribution of droplet volumes is either Gaussian, close to Gaussian, or narrow.

If one cannot measure both the sample mean and the sample variance, but one's droplet-producing device produces samples with constant statistics, then calibration experiments can determine $\overline{(V-\overline{V})^2}$ and test the assumption of constant statistics in the process. The same calibration experiments can determine $\overline{V}$ as well, if it also cannot be measured. This should open up for a poor-man's LDA with simpler devices, since only $\vec{b}$ needs to be measured.

For those stuck with the former state-of-the-art estimator, $\hat{c}$, we have proven theoreti-

cally what was previously conjectured based on experiments: $\hat{c}$ is negatively biased; its bias is independent of the number of droplets N in a sample; this bias can be reduced only by reducing the concentration, c^*, or the variance $\mathrm{Var}(V)$ of droplet volumes, or both, but this reduces precision for given sample size.

Supplementary Note: Calculations

8.8 State-of-the-art estimator, $\hat{c}$

8.8.1 The bias of $\hat{c}$

The bias of $\hat{c}$ is the amount by which its expected value, $E(\hat{c})$, differs from the true value, c^*. We calculate this bias here.

Let $E(\hat{c}|\vec{V})$ denote the expected value of $\hat{c}$ for given fixed $\vec{V}$. That is, $E(\hat{c}|\vec{V})$ results from statistical averaging over all possible outcomes for $\vec{b}$, keeping $\vec{V}$ fixed. When doing that, we use that $b_1, b_2, \ldots, b_N$ are independent stochastic variables. They are not identically distributed, however, when referring to different droplet volumes: the probability that $b_n = 0$ is $\exp(-c^*V_n)$, and the probability that $b_n = 1$ is $1-\exp(-c^*V_n)$. Consequently, e.g.,

$$E(b_n|V_n) = 1 - e^{-c^*V_n} \tag{8.27}$$

and

$$\mathrm{Var}(b_n|V_n) = e^{-c^*V_n}\left(1 - e^{-c^*V_n}\right) \tag{8.28}$$

depend on n.

The estimator $\hat{c}$ depends on $\vec{b}$ only through $\overline{b}$, however, and being an average value, $\overline{b}$'s variance is small.

$$\mathrm{Var}(\overline{b}|\vec{V}) = \frac{1}{N^2}\sum_{n=1}^{N}\mathrm{Var}(b_n|V_n) = \frac{1}{N}\overline{\mathrm{Var}(b|V)} \tag{8.29}$$

shows *how* small $\overline{b} - E(\overline{b}|\vec{V})$ is: Its expected value is zero by construction, and its standard deviation is $\mathcal{O}(N^{-1/2})$. We consequently Taylor-expand $\hat{c}(\overline{V}, \overline{b})$ in powers of this small quantity,

$$\begin{aligned}
\hat{c}(\overline{V}, \overline{b}) &= -\frac{1}{\overline{V}}\left[\ln\left(1 - E(\overline{b}|\vec{V})\right) + \ln\left(1 - \frac{\overline{b} - E(\overline{b}|\vec{V})}{1 - E(\overline{b}|\vec{V})}\right)\right] \\
&= -\frac{1}{\overline{V}}\left[\ln\left(1 - E(\overline{b}|\vec{V})\right) - \frac{\overline{b} - E(\overline{b}|\vec{V})}{1 - E(\overline{b}|\vec{V})}\right. \\
&\quad \left. - \frac{1}{2}\left(\frac{\overline{b} - E(\overline{b}|\vec{V})}{1 - E(\overline{b}|\vec{V})}\right)^2 + \ldots\right] .
\end{aligned} \tag{8.30}$$

Taking the expected value on both sides of this identity, we find

$$E(\hat{c}|\overline{V}) = -\frac{1}{\overline{V}}\left[\ln\left(1 - E(\overline{b}|\vec{V})\right) - \frac{\overline{\mathrm{Var}(b|V)}}{2N(1 - E(\overline{b}|\vec{V}))^2} + \ldots\right] . \tag{8.31}$$

We assume that N always is so large that terms of order $1/N$ safely can be ignored with no discernible loss of accuracy nor precision. Since typical values for N are 10^4–10^6, this is a very safe assumption[47,58,75,86]. Thus we have

$$E(\hat{c}|\overline{V}) = -\frac{1}{\overline{V}} \ln\left(1 - E(\bar{b}|\vec{V})\right) = -\frac{1}{\overline{V}} \ln\left(\overline{e^{-c^*V}}\right) \quad , \tag{8.32}$$

where we have used that

$$E(\bar{b}|\vec{V}) = \frac{1}{N}\sum_{N=1}^{N} E(b_n|\vec{V}) = \frac{1}{N}\sum_{N=1}^{N}\left(1 - e^{-c^*V_n}\right) = 1 - \overline{e^{-c^*V}} \quad . \tag{8.33}$$

The sample mean values $\overline{V}$ and $\overline{e^{-c^*V}}$ in Equation (8.32) fluctuate about their expected values by terms of order $N^{-1/2}$. Thus, neglecting terms of order N^{-1}, we have

$$E(\hat{c}) = -\frac{1}{E(V)} \ln\left(E(e^{-c^*V})\right) \quad . \tag{8.34}$$

For a Gaussian distribution of droplet volumes,

$$E(e^{-c^*V}) = e^{-c^*E(V) + c^{*2}\mathrm{Var}(V)/2} \quad . \tag{8.35}$$

This is an exact identity. For distributions that are approximately Gaussian or narrow or both, in the sense that the variance is small and higher cumulants approximately negligible, this Equation is a good approximation. The criterion is that one can treat as negligible all higher cumulants than the second (the variance) in the cumulant expansion of $E(e^{-c^*V})$.

Equation (8.35) inserted into Equation (8.34) then gives

$$E(\hat{c}) = c^* - c^{*2}\frac{\mathrm{Var}(V)}{2E(V)} \quad . \tag{8.36}$$

We conclude that the relative bias of $\hat{c}$ is

$$\frac{E(\hat{c}) - c^*}{c^*} = -c^*\frac{\mathrm{Var}(V)}{2E(V)} \tag{8.37}$$

for a Gaussian distribution of droplet volumes. For a non-Gaussian droplet distribution, higher cumulants should be included in the derivation above, unless the distribution is very narrow.

8.8.2 Variance of $\hat{c}$

$$\mathrm{Var}(\hat{c}) = E((\hat{c}(\overline{V}, \bar{b}) - E(\hat{c}))^2) \quad . \tag{8.38}$$

Here

$$\hat{c}(\overline{V},\bar{b}) - E(\hat{c}) = \hat{c}(\overline{V},\bar{b}) - E(\hat{c}|\overline{V}) + E(\hat{c}|\overline{V}) - E(\hat{c}) \ , \tag{8.39}$$

where $\hat{c}(\overline{V},\bar{b}) - E(\hat{c}|\overline{V})$ has zero covariance with $E(\hat{c}|\overline{V}) - E(\hat{c})$, because the first difference fluctuates with $\vec{b}$ with vanishing expected value, while the second difference is independent of $\vec{b}$. Thus

$$\begin{aligned} \mathrm{Var}(\hat{c}) &= E((\hat{c}(\overline{V},\bar{b}) - E(\hat{c}|\overline{V}))^2) + E((E(\hat{c}|\overline{V}) - E(\hat{c}))^2) \\ &= E(\mathrm{Var}(\hat{c}|\overline{V})) + \mathrm{Var}(E(\hat{c}|\overline{V})) \ , \end{aligned} \tag{8.40}$$

Equations (8.30) and (8.32) combined give that, to lowest non-vanishing order,

$$\hat{c}(\overline{V},\bar{b}) - E(\hat{c}|\vec{V}) = \frac{1}{\overline{V}} \frac{\bar{b} - E(\bar{b}|\vec{V})}{1 - E(\bar{b}|\vec{V})} \ , \tag{8.41}$$

and hence

$$\begin{aligned} \mathrm{Var}(\hat{c}|\vec{V}) &= \frac{1}{\overline{V}^2} \frac{\mathrm{Var}(\bar{b}|\vec{V})}{(1 - E(\bar{b}|\vec{V}))^2} \\ &= \frac{1}{N} \frac{1}{\overline{V}^2} \frac{\overline{\mathrm{Var}(b|V)}}{(1 - E(\bar{b}|\vec{V}))^2} \\ &= \frac{1}{N} \frac{\overline{(1 - e^{-c^*V})\, e^{-c^*V}}}{\overline{V}^2 \left(\overline{e^{-c^*V}}\right)^2} \\ &= \frac{1}{N} \frac{\overline{e^{-c^*V}} - \overline{e^{-2c^*V}}}{\overline{V}^2 \left(\overline{e^{-c^*V}}\right)^2} \ . \end{aligned} \tag{8.20 revisited}$$

This result is already of order N^{-1}, while the difference between $\overline{V}$ and $E(\overline{V}) = E(V)$ is of order $N^{-1/2}$. Thus, to leading order in powers of $N^{-1/2}$, we can replace $\overline{V}$ with $E(V)$ in Equation (8.20), when we take the expected value of both sides of this Equation. By the same argument, we replace $\overline{e^{-c^*V}}$ with $E(\overline{e^{-c^*V}}) = E(e^{-c^*V})$ and $\overline{e^{-2c^*V}}$ with $E(e^{-2c^*V})$.

$$E(\mathrm{Var}(\hat{c}|\vec{V})) = \frac{1}{N} \frac{E(e^{-c^*V}) - E(e^{-2c^*V})}{E(V)^2 E(e^{-c^*V})^2} \ . \tag{8.42}$$

For a Gaussian distribution of droplet volumes, this results simplifies to

$$E(\mathrm{Var}(\hat{c}|\vec{V})) = \frac{1}{N} \frac{e^{c^*E(V) - c^{*2}\mathrm{Var}(V)/2} - e^{c^{*2}\mathrm{Var}(V)}}{E(V)^2} \ . \tag{8.43}$$

To calculate $\mathrm{Var}\,(\hat{c})$ for an LDA experiment employing droplets with a size distribution, $p(V)$, which is narrow, but not necessarily Gaussian, we must evaluate and scale Equation (8.20) according to probability of the volume in question:

$$\mathrm{Var}\left(\hat{c}\right)_{p_V(\cdot),c^*} = \int_0^\infty p_V\left(\cdot\right)\mathrm{Var}(\hat{c}|V,c^*)dV$$

Replacing $\frac{1}{f} = \mathrm{Var}(\hat{c}|V,c^*)$ and using the identity[d] $\frac{1}{f} = \int_0^\infty e^{-\alpha f}d\alpha$, we get

$$\begin{aligned}\mathrm{Var}\left(\hat{c}\right)_{p_V(\cdot),c^*} &= \int_0^\infty\int_0^\infty p_V\left(\cdot\right)e^{-\alpha f}dVd\alpha \\ &= \int_0^\infty e^{\ln\left(\int_0^\infty p_V(\cdot)e^{-\alpha f}dV\right)}d\alpha\end{aligned}$$

If $p_V\left(\cdot\right)$ is a narrow distribution,

$$\begin{aligned}\mathrm{Var}\left(\hat{c}\right)_{p_V(\cdot),c^*} &\approx \int_0^\infty e^{-\alpha\int_0^\infty p_V(\cdot)fdV}d\alpha \\ &= \frac{1}{\int_0^\infty p_V\left(\cdot\right)fdV} \\ &= \frac{1}{\int_0^\infty p_V\left(\cdot\right)\frac{1}{\frac{1}{N}\frac{e^{-c^*V}-e^{-2c^*V}}{V^2\left(e^{-c^*V}\right)^2}}dV} \\ &= \frac{1}{N\int_0^\infty p_V\left(\cdot\right)\frac{V^2e^{-c^*V}}{1-e^{-c^*V}}dV}. \\ &= \frac{1}{N\int_0^\infty p_V\left(\cdot\right)\frac{V^2}{e^{c^*V}-1}dV}. \qquad \text{(8.20 revisited)}\end{aligned}$$

Assuming the droplet diameter population is Gaussian distributed[200,205,211], described by $p_D\left(\cdot\right) \sim N\left(D_0,\sigma_D\right)$, we get a droplet volume distribution described by

$$p_V\left(\cdot\right) = \left(\frac{2}{p\pi V^2}\right)^2\frac{1}{\sqrt{2\pi}\sigma_D}e^{-\frac{\left(\left(\frac{6V}{\pi}\right)^{\frac{1}{3}}-D_0\right)^2}{2\sigma_D^2}}$$

Figure 8.6 illustrates $\mathrm{Var}\left(\hat{c}\right)_{p_V(\cdot),c^*}$ plotted versus V_0 and σ_D/D_0.

[d] From a table of integrals[213], we have $\int e^{ax}\,dx = \frac{1}{a}e^{ax}$. So $\int_0^\infty e^{-f\alpha}\,d\alpha = \left[\frac{1}{-f}e^{-f\alpha}\right]_0^\infty = \frac{1}{f}$.

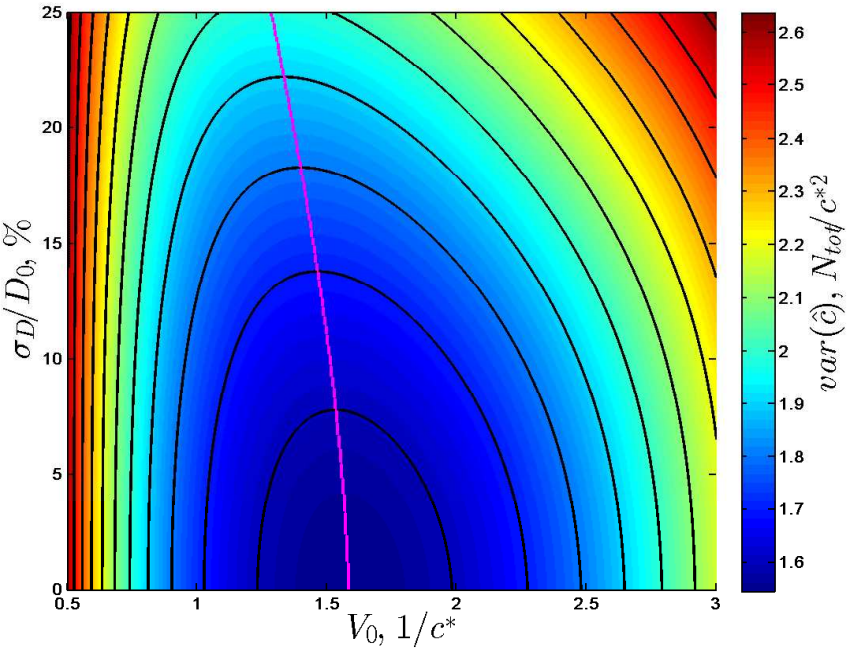

Figure 8.6: Variance of droplet population with diameter size distribution $p_D(\cdot) \sim N(D_0, \sigma_D)$ plotted versus V_0 and σ_D/D_0. Contour levels are denoted by tick marks on the colour bar.

For a truly monodisperse droplet population, Equation (8.20) simplifies and may be minimised by solving $\frac{\partial \mathrm{Var}(\hat{c})_{V,c^*}}{\partial V} = 0$ in which case $V_0 c^* = 1.59$, see Figure 8.7. This conclusion may also be obtained by minimising the variance of a Bernoulli trial (which is exactly what a monodisperse droplet LDA is)[214].

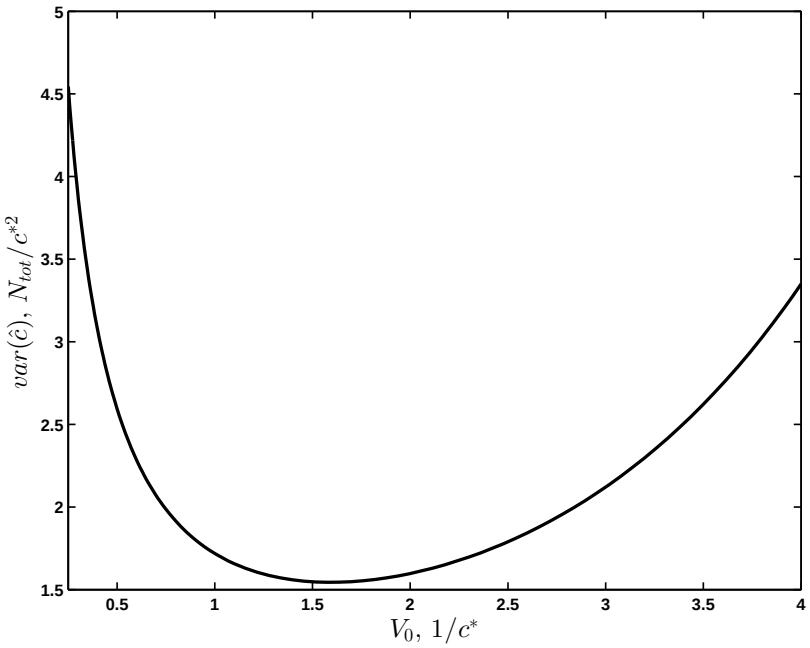

Figure 8.7: Variance of a monodisperse droplet population, $\mathrm{Var}\left(\hat{c}\right)_{V,c^*}$, plotted versus V_0.

8.8.3 Bias corrected estimator, $\hat{c}_{\mathrm{bc}}$

The expected value of $\hat{c}_{\mathrm{bc}}$ is calculated from Equation (8.16). For brevity, $\alpha = \frac{\overline{(V-\overline{V})^2}}{2\overline{V}}$.

$$\begin{aligned} E\left(\hat{c}_{\mathrm{bc}}\right) &= \hat{c}\left(1+\alpha\hat{c}\right) \\ &= E\left(\hat{c}\right) + \alpha E\left(\hat{c}^2\right) \\ &= c^* - \alpha c^{*2} + \alpha\left(\mathrm{Var}\left(\hat{c}\right) + E\left(\hat{c}\right)^2\right) \\ &= c^* + \alpha\mathrm{Var}\left(\hat{c}\right) + \alpha^2 c^{*3}\left(\alpha c^* - 2\right) \\ &\approx c^* - 2\alpha^2 c^{*3} \end{aligned}$$

This is used for calculating the variance of $\hat{c}_{\mathrm{bc}}$:

$$\begin{aligned} \mathrm{Var}\left(\hat{c}_{\mathrm{bc}}\right) &= E\left(\hat{c}_{\mathrm{bc}}^2\right) - \langle\hat{c}_{\mathrm{bc}}\rangle^2 \\ &= E\left(\left(\hat{c}+\alpha\hat{c}\right)^2\right) - \left(c^* - 2\alpha c^{*3}\right)^2 \\ &\approx E\left(\hat{c}^2\right) + \alpha^2 c^{*4} + 2\alpha c^{*3} - \left(c^* - 2\alpha c^{*3}\right)^2 \\ &\approx \mathrm{Var}\left(\hat{c}\right) \qquad \text{(8.20 revisited)} \end{aligned}$$

8.9 Maximum likelihood estimation MLE

Maximum likelihood estimation (MLE) is usually introduced as follows: Given an experiment that measures a stochastic quantity X, and given a theory that for every possible outcome $X = x$ of a measurement gives its probability $P(x|\theta)$, with θ one or several parameters of the theory. Then the joint probability of outcome $(x_1, x_2, \ldots, x_N)$ of N independent measurements done with unchanged conditions, and hence with identical distribution $P(\cdot|\theta)$, is

$$\mathcal{P}(\vec{x}\,|\theta) = \prod_{n=1}^{N} P(x_n|\theta) \tag{8.44}$$

where $\vec{x} = (x_1, \ldots, x_N)$. Given the experimental outcomes $\vec{x}$, MLE of θ is done in two steps: First, define the likelihood of θ, given $\vec{x}$, as

$$\mathcal{L}(\theta|\vec{x}\,) = \mathcal{P}(\vec{x}\,|\theta) \ . \tag{8.45}$$

Second, find the value of θ that maximizes $\mathcal{L}(\theta|\vec{x}\,)$ for the given set of outcomes $\vec{x}$. This value of θ, call it $\hat{\theta}_{\mathrm{ml}}(\vec{x}\,)$, is the *maximum-likelihood estimate* of θ, given $\vec{x}$.

This textbook-version of MLE generalizes to an experiment that measures a stochastic quantity X, and a theory that gives the probability $P(x|\theta, \vartheta)$ for every possible outcome $X = x$ of a measurement, with θ one or several parameters of the theory, and ϑ yet another parameter of the theory, which describes an experimental condition that can differ between different measurements, which θ cannot. While θ denotes the parameter(s) that we wish to estimate from a series of N independent measurements with outcomes $\vec{x}$, $\vec{\vartheta} = (\vartheta_1, \vartheta_2, \ldots, \vartheta_N)$ is known and describes the N experimental conditions under which the N entries in $\vec{x}$ were obtained. Each component in $\vec{\vartheta}$ can be the result of a random process taking place in the experiment, and we may have measured a pair (x, ϑ) in each repetition of the experiment—(x_n, ϑ_n) in the nth repetition—but for our present purpose we need not know a theory that gives $P(x, \vartheta|\theta)$. The theory that gives $P(x|\theta, \vartheta)$ is fully sufficient, because its joint probability for $\vec{x}$ is

$$\mathcal{P}(\vec{x}\,|\theta, \vec{\vartheta}) = \prod_{n=1}^{N} P(x_n|\theta, \vartheta_n) \tag{8.46}$$

from which we form the *likelihood*

$$\mathcal{L}(\theta|\vec{x}, \vec{\vartheta}) = \mathcal{P}(\vec{x}\,|\theta, \vec{\vartheta}) \tag{8.47}$$

and determine our maximum-likelihood estimate $\hat{\theta}_{\mathrm{ml}}(\vec{x}, \vec{\vartheta})$. Note that the likelihood is called so in order to emphasize that it is *not* a probability.

8.9.1 The maximum-likelihod estimator $\hat{c}_{\mathrm{ml}}(\vec{b}, \vec{V})$

In our case, the experiment is the interrogation of a droplet volume, V, and the outcome is either a “hit" or a “miss": there are or aren’t any targets in the droplet. Such an

experiment is called a *Bernoulli trial* in statistics and the outcomes “success" and “failure." We record the outcome in a binary variable b, with $b = 1$ denoting “hit” = “success" = “targets present," and $b = 0$ denoting “miss" = “failure" = “targets absent." Thus, our b corresponds the outcome x in the general formulation above.. We also record the volume V. It corresponds to the parameter ϑ above.

At concentration c, Poisson statistics gives that the probability of a miss/hit is

$$P(b = 0|c, V) = e^{-cV} \tag{8.48}$$
$$P(b = 1|c, V) = 1 - e^{-cV} \ , \tag{8.49}$$

i.e.,

$$P(b|c, V) = (1 - b)e^{-cV} + b(1 - e^{-cV}) \ , \tag{8.50}$$

and hence Equations (8.27) and (8.28) with c substituted for c^*. Consequently,

$$\mathcal{L}(c|\vec{b}, \vec{V}) = \mathcal{P}(\vec{b}\,|c, \vec{V}) = \prod_{n=1}^{N} P(b_n|c, \vec{V}_n) \ , \tag{8.51}$$

which is maximal at $c = \hat{c}_{\mathrm{ml}}(\vec{b}, \vec{V})$, where $\hat{c}_{\mathrm{ml}}(\vec{b}, \vec{V})$ is implicitly given by the following stationarity condition for $\ln \mathcal{L}(c|\vec{b}, \vec{V})$ with respect to variation in c with fixed $\vec{b}, \vec{V}$,

$$\overline{V} = \overline{\left(\frac{bV}{1 - e^{-\hat{c}_{\mathrm{ml}} V}} \right)} \ . \tag{8.52}$$

This equation is our main result.

Note that for a monodisperse distribution of volumes, all V_n are equal in this equation, and it consequently reads

$$1 - e^{-\hat{c}_{\mathrm{ml}} V} = \overline{b} \ . \tag{8.53}$$

This is Equation (8.8) with $\overline{V} = V$. The power of MLE is that it applies to any distribution of volumes, and that it is both accurate (= unbiased) and *efficient* in the limit $N \to \infty$, where by “efficient" is meant that no other unbiased estimator is more precise.

We now find the accuracy and precision explicitly for our particular maximum-likelihood estimator.

8.9.2 Accuracy of $\hat{c}_{\mathrm{ml}}(\vec{b}, \vec{V})$

Let c^* denote the true value of the concentration that we estimate. The *bias* of $\hat{c}_{\mathrm{ml}}$ is then defined as $E(\hat{c}_{\mathrm{ml}}) - c^*$. To evaluate this bias, we introduce

$$\delta\hat{c}_{\mathrm{ml}} = \hat{c}_{\mathrm{ml}} - c^* \tag{8.54}$$

because it is a small quantity for N large. We Taylor-expand Equation (8.52) in $\delta\hat{c}_{\mathrm{ml}}$. This gives

$$\overline{V} = \overline{\left(\frac{bV}{1-e^{-c^*V}}\right)} - \delta\hat{c}_{\mathrm{ml}}\overline{\left(\frac{bV^2e^{-c^*V}}{(1-e^{-c^*V})^2}\right)} + \mathcal{O}\left((\delta\hat{c}_{\mathrm{ml}})^2\right) \tag{8.55}$$

and hence

$$\delta\hat{c}_{\mathrm{ml}} = \frac{\overline{\left(\frac{bV}{1-e^{-c^*V}}\right)} - \overline{V}}{\overline{\left(\frac{bV^2e^{-c^*V}}{(1-e^{-c^*V})^2}\right)}} + \mathcal{O}\left((\delta\hat{c}_{\mathrm{ml}})^2\right) \quad . \tag{8.56}$$

Writing

$$b = E(b|V) + \Delta b = 1 - e^{-c^*V} + \Delta b \ , \tag{8.57}$$

$$\delta\hat{c}_{\mathrm{ml}} = \frac{\overline{\left(\frac{\Delta bV}{1-e^{-c^*V}}\right)}}{\overline{\left(\frac{V^2e^{-c^*V}}{1-e^{-c^*V}}\right)}} - \frac{\overline{\left(\frac{\Delta bV}{1-e^{-c^*V}}\right)}\ \overline{\left(\frac{\Delta bV^2e^{-c^*V}}{(1-e^{-c^*V})^2}\right)}}{\overline{\left(\frac{V^2e^{-c^*V}}{1-e^{-c^*V}}\right)}^2} + \mathcal{O}\left((\delta\hat{c}_{\mathrm{ml}})^2\right) \quad , \tag{8.58}$$

from which follows, using $E(\Delta b|V) = 0$ and Equation (8.28), that the bias of $\hat{c}_{\mathrm{ml}}$ is

$$E(\delta\hat{c}_{\mathrm{ml}}|\vec{V}) = \frac{1}{N}\frac{\overline{\left(\frac{V^3}{(e^{c^*V}-1)^2}\right)}}{\overline{\left(\frac{V^2}{e^{c^*V}-1}\right)}^2} + \mathcal{O}\left(E((\delta\hat{c}_{\mathrm{ml}})^2|\vec{V})\right) \quad , \tag{8.59}$$

where $E((\delta\hat{c}_{\mathrm{ml}})^2|\vec{V}) = \mathrm{Var}(\hat{c}_{\mathrm{ml}}|\vec{V})$ also is of order N^{-1}, as we shall see in the next subsection. Thus $\hat{c}_{\mathrm{ml}}$ is biased only to order N^{-1}. This result justifies the Taylor approximation which lead to it, i.e., the derivation is self-consistently correct, for N large.

8.9.3 Precision of $\hat{c}_{\mathrm{ml}}(\vec{b}, \vec{V})$

We keep only the leading-order term in Equation (8.58) and find

$$\begin{aligned}\mathrm{Var}(\hat{c}_{\mathrm{ml}}|\vec{V}) = E\left((\delta\hat{c}_{\mathrm{ml}})^2|\vec{V}\right) &= \frac{1}{N}\frac{\overline{\left(\frac{V^2\mathrm{Var}(b|V)}{(1-e^{-c^*V})^2}\right)}}{\overline{\left(\frac{V^2}{e^{c^*V}-1}\right)}^2} \\ &= \frac{1}{N}\left[\overline{\left(\frac{V^2}{e^{c^*V}-1}\right)}\right]^{-1} + \mathcal{O}(N^{-2}).\end{aligned} \tag{8.22 revisited}$$

Thus, once we have determined $\hat{c}_{\mathrm{ml}}$ from a given set of data $(\vec{b}, \vec{V})$, we have also an estimate for the variance of our estimate that is good to leading order in N^{-1} in the estimate

$$\widehat{\mathrm{Var}}(\hat{c}_{\mathrm{ml}}) = \frac{1}{N}\left[\overline{\left(\frac{V^2}{e^{\hat{c}_{\mathrm{ml}}V}-1}\right)}\right]^{-1} \quad . \tag{8.23 revisited}$$

The square-root of this variance is our estimate for the *standard deviation* of the Gaussian distribution centered on c^* which values of $\hat{c}_{\mathrm{ml}}$ are known to scatter with if we repeat our measurement and produce new and independent data sets $(\vec{b}, \vec{V})$ under the same experimental conditions, and thus get new and independent estimates $\hat{c}_{\mathrm{ml}}(\vec{b}, \vec{V})$.

Calculating $\hat{c}_{\mathrm{ml}}$ from data

Being implicit in $\hat{c}_{\mathrm{ml}}$, Equation (8.19) must be solved numerically for a data set (given as $\vec{V}$ and $\vec{b}$). In practice, this is done by fitting $\hat{c}_{\mathrm{ml}}$ until the error of Equation (8.19),

$$error = \left| 1 - \frac{1}{\overline{V}} \overline{\left(\frac{bV}{1 - e^{-\hat{c}_{\mathrm{ml}} V}} \right)} \right|, \tag{8.60}$$

is sufficiently small. As starting guess for $\hat{c}_{\mathrm{ml}}$ one may use $\hat{c}_{\vec{V},\vec{b}}$ calculated using Equation (8.8). Below is a routine for estimating $\hat{c}$ and $\hat{c}_{\mathrm{ml}}$ using MATLAB. For error minimisation, the function `fminsearch` is used, however, any steepest descend based optimisation routine is applicable.

```
function [c,c_mle]=MLE_algorithm(V_vec,b_vec)
V_bar=mean(V_vec);
c=-1/V_bar*log(1-mean(b_vec));
error_fun = @(c_fit) ...
    abs(1-1/V_bar*mean(b_vec.*V_vec./(1-exp(-c_fit*V_vec))));
c_mle=fminsearch(error_fun,c);
end
```

Typically, the error (Equation (8.60)) is on the order of $10^{-6} - 10^{-7}$ after 12 iterations, which on a modern laptop takes ~ 16 ms for 10.000 droplets.

9

Recapitulation and future perspectives

The work presented in this PhD thesis has made improvements to multiple aspects of fabricating and conducting droplet (or multiphase) microfluidics:

- Design phase: Numerical prediction of the capillary burst pressure of a multiphase system.
- Fabrication: Two new types of energy directors for ultrasonic welding of microfluidic systems have been presented:
  1. Tongue-and-groove energy directors.
  2. Laser ablated micropillar energy directors.
- Annealing of polymer devices for use with hydrocarbon oils, enabling the application octanol multiphase systems.
- Experimental design and data analysis: Optimised estimators for single-hit limiting-dilution assays.

The technologies have been demonstrated in multiple injection moulded, ultrasonic welded microfluidic devices:

- Device with large area, shallow chamber (1.8 cm^2 × 150 μm) for storing, thermocycling and imaging of droplets for ddPCR.
- High aspect ratio device, welded by using micro pillar energy directors.
- Device with droplet forming junction and large area, shallow chamber (>0.82 cm^2 × 100 μm) for conducting droplet-based liquid-liquid extraction.

Further, a range of concurrent activities have been undertaken:

- TransForm-technologies, a to-be spin-out of this PhD project has been initiated, and 725.000 DKK has been raised and spent on maturation of the mould microstructuring technology, incorporating and testing the technology in a commercial setting, formulating a business plan and composing patent applications. See Appendix A on page A1.
- Three patent applications have been submitted to the European Patent Office:
  1. Replication tool and method of providing a replication tool.
  2. Micro-scale energy directors for ultrasonic welding.

3. Method of producing an item with enhanced wetting properties by fast replication and replication tool used in the method.

The project description (Box 1.1 on page 19) can therefore be considered as fulfilled, however, as mentioned in Section 8.3.1 on page 120, it is desired to support the *Monte Carlo* simulations and the analytical results presented with experimental observations.

It is difficult to determine if the gravity assisted droplet packing method employed in this project is applicable in a commercial setting, but the current version of the device (described below), employs fewer proprietary components (only the device itself), and is more flexible in terms of interrogation (we used a fluorescence microscope, but any imaging with high enough resolution and fluorescence capabilities is applicable) than the existing commercial solutions presented in Section 1.3.2.

This leads me to the future perspectives / work-in-progress section of this project:

9.1 Future of project: LAMP in droplets

An alternative to the PCR reaction is desired since the thermo-cycling is highly time-consuming and requires careful calibration and precise temperature control, and bubbles were a big problem during thermo-cycling, see Section 5.2. The loop-mediated isothermal amplification (LAMP) for detection of *Salmonella* spp. in food samples presented by the BioLabChip group, Sun *et al.* (2015)[189], was chosen as a starting point for the experiment. The mechanism behind LAMP is described in Box 9.1 on page 146. The generated droplet LAMP data will be used to compare the experimental performances of the estimators presented in Paper 5 on page 115.

9.1.1 Design and mode-of-action

At the time of writing, a new microfluidic chip for producing, incubating and imaging droplets for LAMP has been fabricated and confirmed to work (with regards to droplet production) as intended. The droplet junction is based on the design developed for the liquid-liquid extraction devices presented previously. Two symmetrical isolated microfluidic systems were incorporated in each device for the purpose of comparing experiments in the same fluorescence image. For the final device, a single chamber is sufficient, but there are still uncertainties concerning biological compatibility, efficiency of the reaction, efficiency of the staining, and general uncertainty of the detection it is always useful to have a side-by-side comparison of a 100% or a 0% positive sample. The on-chip droplet production is particular important in this matter, since it reduces the risk of cross contamination. To achieve on-chip sample loading and droplet formation, a new design was incorporated, which relied on two oil lines with one harvesting a loading port for the sample. The droplet LAMP chip is illustrated in Figure 9.1. Loading of the sample is done by pipetting, and the sample loading procedure is illustrated in Figure 9.2.

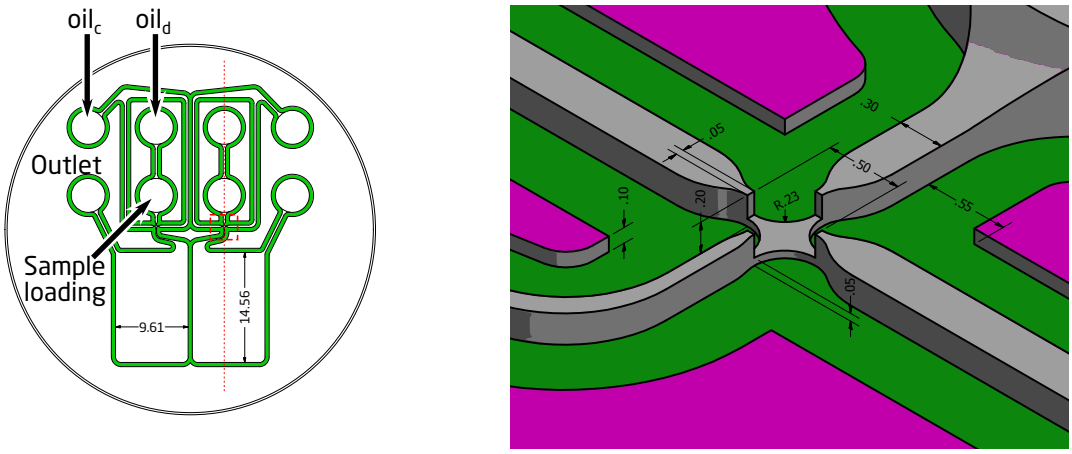

Figure 9.1: Scheme of the droplet chip for conducting droplet LAMP. Green areas denote protruding channel walls. Units are in mm, left-hand drawing is scaled 1:1. oil$_c$ is the the oil inlet for the continuous phase, and oil$_d$ denotes the oil inlet for driving the disperse phase (sample) during droplet formation. During droplet formation, the device is held upright to enable gravity to guide the droplets to the bottom of the chamber. Vertical line indicates cross section of Figure 9.2. (right) Zoom in on the insert for injection moulding at the droplet forming junction.

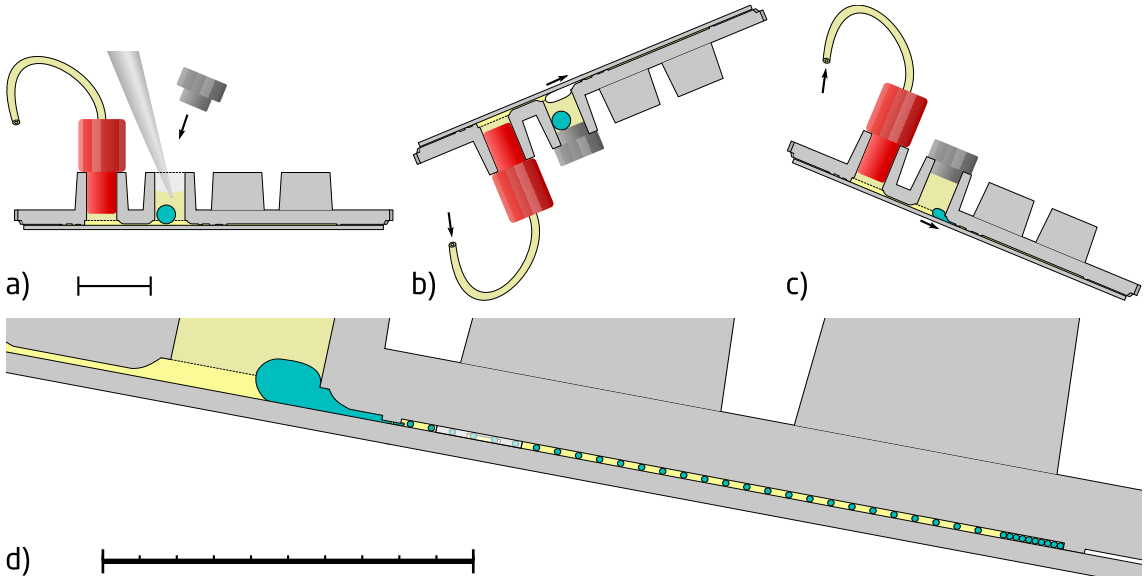

Figure 9.2: Cross section of sample loading procedure. Note that the device has been primed with oil. Scale bars are 10 mm. (a) Sample (blue) is loaded into the sample port of Figure 9.1 where after a disposable plug is inserted. Some air will most likely be caught, and (b) the device is inverted. Since the aqueous phase is heavier than the oil phase (octanol), it will sink, contrary to the gaseous phase (white) which floats. The oil phase of the sample channel (oil$_d$) in Figure 9.1) is engaged, and the gas is driven into the chamber. (c) After all bubbles have been removed, the device is inverted again and tilted forward to drive the aqueous sample into the constriction of the droplet forming junction. (d) Close up of the droplet junction.

Box 9.1: Loop-mediated isothermal amplification (LAMP)

LAMP is a fairly recent invention for amplifying DNA under isothermal conditions (60-65 °C) by strand displacement[215]. A *Bst* DNA polymerase and four primers recognising a total of six sequences in the target is used for continuously synthesising complimentary DNA while displacing the previous strand, resulting in the release of single stranded DNA which in turn acts as a template strand. An additional pair of "loop primers" may be added for further accelerating the reaction (not included below), reducing amplification time from ~ 60 down to ~ 30 minutes[216]. The steps of LAMP are illutstrated below. "F#" and "B#" stands for forward ($5' \rightarrow 3'$) detection sequences of the primary and complimentary strand, respectively. FIB and BIP stands for forward and backward inner primer, respectively. Subscript "c"$_c$ annotates complimentary sequences. Broken arrows denote continued amplification into bigger products. The final products are cauliflower-like and are polydisperse in size[216].

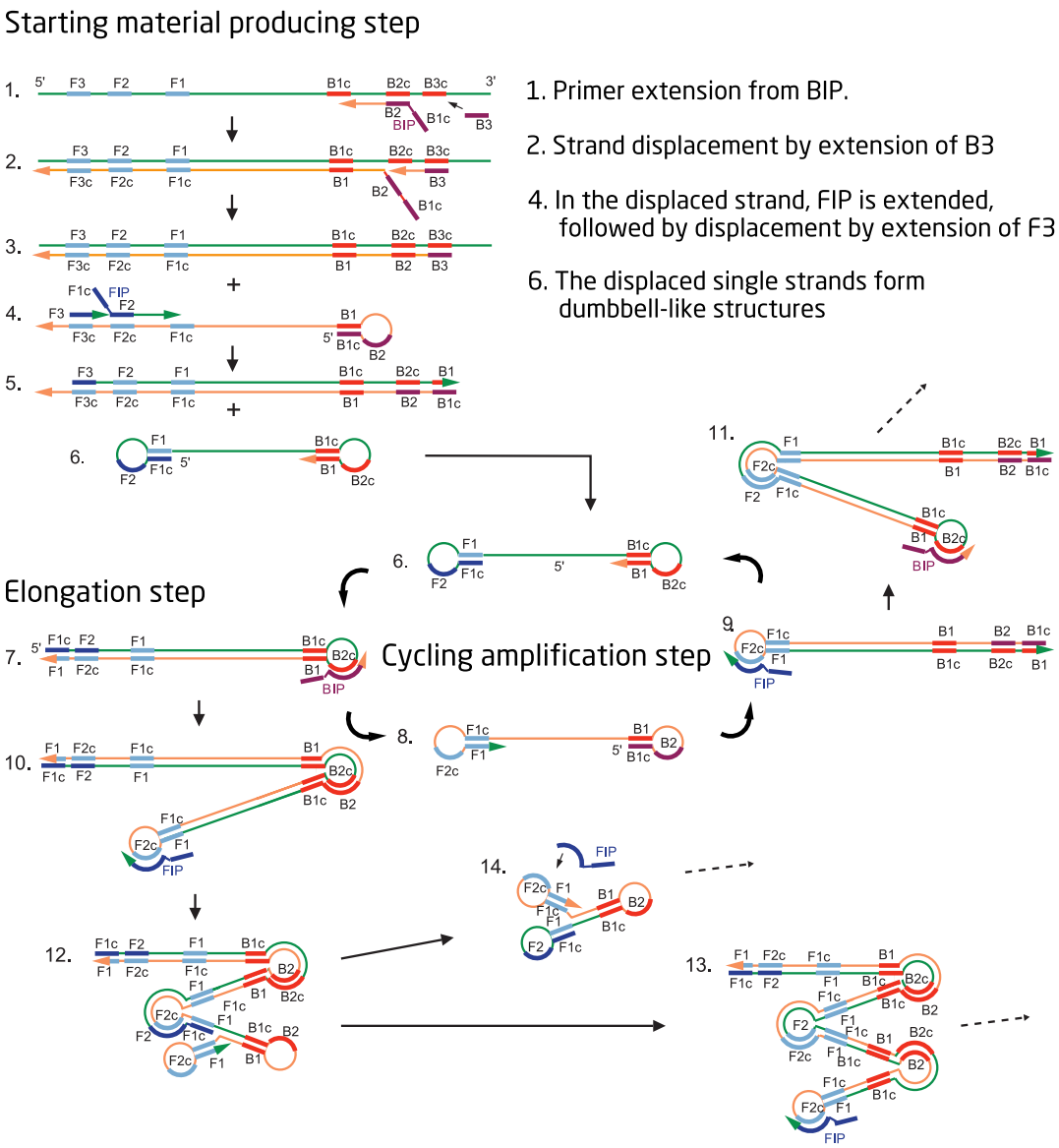

Figure is adapted and modified from Nagamine *et al.* (2002)[216].

9.1.2 Experimental progress

The original intention was to apply the LAMP protocol for detection *Salmonella* spp. demonstrated by Sun *et al.* (2015)[189] which used DNA staining for detection of amplification. Importantly, Sun *et al.* (2015)[189] showed that some DNA staining dyes (5 μM) inhibited the amplification whereas others did not. In the study, the two least inhibiting dyes were found to be SYTO-62 and SYTO-82, and these dyes were therefore chosen as candidates for the present droplet LAMP experiment. Obviously, the concern of dye-LAMP compatibility was only one critical pre-requisite to a successful experiment amongst many:

- Chip polymer - octanol compatibility
  - Achieved by annealing the COC chips post ultrasonic welding, see pages 102 and 114.
- The droplets formed must be stable during amplification at 65 °C for atleast one hour.
  - Interestingly, the 2% of Pico-Surf® 1 in FC40 (Dolomite) used as the continuous phase in Paper 2 was stable enough to be thermo-cycled with PCR reagents, but stability was very poor when using LAMP reagents. Droplets imaged before and after thermal incubation is illustrated in Figure 9.5. To investigate if the droplet stability could be regained by increasing the surfactant concentration, experiments were repeated using the stock surfactant concentration of 5%, unfortunately without no significant effect (images not shown). This cemented the decision to work towards an octanol based system.
- LAMP reaction - octanol compatibility
  - Verified by conducting in-tube LAMP with octanol added in 1:1 ratio; 10 μL of mastermix (see reference[189]) was mixed with 10 μL of octanol (with 3% (w/w) ABIL EM90 surfactant, cetyl dimethicone copolyol, Rose Chemicals, U.K.) in a PCR tube. As seen in Figure 9.3, the amplification was not inhibited, and we decided to pursue droplet microfluidics based on octanol as the continuous phase.
- Dye - octanol compatibility
  - The distribution coefficient (or partition coefficient for uncharged dyes, Equation 7.1 on page 97) must not be too high, or the dye will primarily occupy the oil phase, masking the fluorescent signal of the droplets.[a]
    Unfortunately, from experiments[b] we found that the SYTO-62 dye had serious compatibility issues with the octanol phase. As shown in Figure 9.4, the fluorescence signal (imaging) was completely inverted from the dye entering

[a] Preferably, the system is operated in an equilibrium with regards to the mass-transport of the dye; Remember: all droplets have dye, but only some have DNA, and there is therefore no reason to attempt to maintain a gradient of dye. On the contrary, the task of maintaining an out-of-equilibrium system with different dye concentrations in different droplets requires the addition of "helper" molecules such as BSA, which (my hypothesis) sticks to the dye or occupy the interface of the droplet[217].

[b] This is the major reason why no experimental results are included in the draft of Paper 5, and completion of the experimentation has been postponed to after the submission of this thesis

the oil phase.
Because the LAMP reaction is highly sensitive to the choice of dye[189], a new approach will be attempted[c] where pyrophosphate released from the polymerase reaction is detected instead of the DNA. This is done by adding calcein and manganese ions: (1) Prior to reaction, the calcein is quenched by coordinating to the manganes ions. (2) After reaction, the manganese ions form insoluble salts with the pyrophosphate and precipitates. (3) The calcein is then free to coordinate to the magnesium ions in the solutions and is thereby dequenched[218].

- Sensitivity/discrimination: "Positive" must be distinguishable from "negative" samples (droplets).
  - This fundamental objective was verified by loading pre-amplified samples into droplets, skipping potential issues with oil-LAMP compatibility or thermal stability of the droplet. The dual chamber-design of the microfluidic layout (Figure 9.1) was particularly useful for verifying this since a positive and a negative sample could be analysed on the simultaneously on the same image, eliminating factors such as lamp intensity. Figure 9.5 shows two samples converted into droplets pre- and post-heating. Ignoring the merged droplets, it is evident that the two samples can be discriminated.
  - Preliminary experiments using SYTO-82 showed that positive samples could not be discriminated from no-template samples using our current equipment, and this dye was abandoned (data not shown).

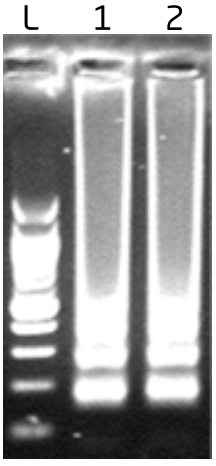

Figure 9.3: Agarose gel electrophoresis of LAMP products confirming that the LAMP reaction was not inhibited by the presence of octanol. L represents DNA ladder, and $1 + 2$ represents positive samples. This experiment was kindly conducted by Than Linh Quyen, Division of Food Microbiology, National Food Institute (DTU-Food), Technical University of Denmark, Mørkhøj Bygade 19, DK-2860 Søborg, Denmark.

[c] At the time of writing, we have only just received the chemicals.

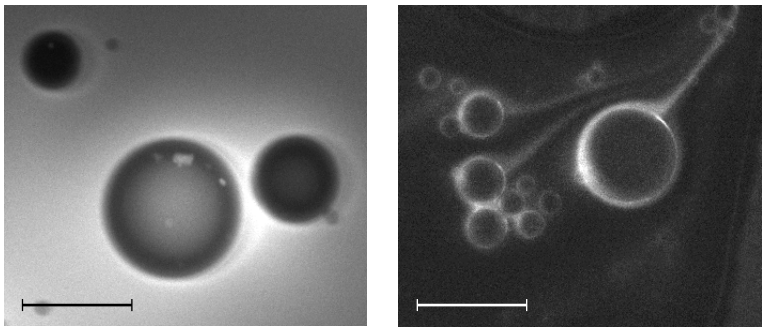

Figure 9.4: Examples of incompatible oil/dye (5 µM SYTO-62) combinations resulting in the dye migrating to the oil phase. Imaging is done using a LaVision BioAnalyzer 4F/4S Scanner (LaVision Biotech Germany) fitted with a Cy5 filter cube. Scale bars are 500 µm. Both oils have 3% (w/w) ABIL EM90 surfactant. (left) Octanol. Imaged 10 minutes after generation using 50 ms of exposure. Note that the oil is more fluorescent than the droplets. This suggest at high distribution coefficient and/or reduced quenching of the dye in the oil. (right) Mineral oil (CAS# 8042-47-5, Sigma-Aldrich). Droplets are imaged 1 hour after generation using 50 ms of exposure. The "trails" of dye is from the droplets moving due to gravity during incubation.

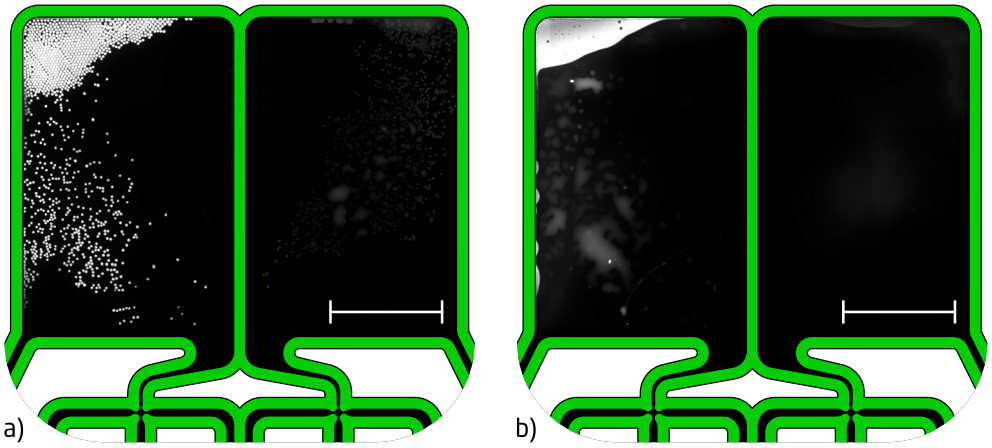

Figure 9.5: Fluorescence image of droplets loaded with pre-amplified LAMP reaction mix. Each device is imaged in a single image for intensity comparison of negative and positive droplets which (to avoid saturation) means that negative droplets are hard to see in the printet version of this thesis. The continuous phase is 2% of Pico-Surf® 1 in FC40 (Dolomite). The CAD design of the chip (Figure 9.1) has been superimposed, and the figure is scaled 1:3. Scale bars are 5.0 mm. Imaging is done using a LaVision BioAnalyzer 4F/4S Scanner (LaVision Biotech Germany) fitted with a Cy5 filter cube using 100 ms of exposure. (left chamber) "Positive" LAMP sample with template DNA. (right chamber) "Negative" LAMP sample without template DNA. (a) Pre thermal-incubation. (b) Post thermal-incubation.

Bibliography

[1] Carl Esben Poulsen, Kasper Kistrup, Nis Andersen, Rafael Taboryski, Mikkel Hansen, and Anders Wolff. "Laser ablated micropillar energy directors for ultrasonic welding of microfluidic systems". In: *Journal of Micromechanics and Microengineering* Accepted: (2016).

[2] Carl Esben Poulsen, Robert C. R. Wootton, Anders Wolff, Andrew J. DeMello, and Katherine S. Elvira. "A Microfluidic Platform for the Rapid Determination of Distribution Coefficients by Gravity-Assisted Droplet-Based Liquid–Liquid Extraction". In: *Analytical Chemistry* 87.12 (2015), pp. 6265–6270. DOI: 10.1021/acs.analchem.5b01061.

[3] Kasper Kistrup, Carl Esben Poulsen, Peter Friis Østergaard, Kenneth Brian Haugshøj, Rafael Taboryski, Anders Wolff, and Mikkel Fougt Hansen. "Fabrication and modelling of injection moulded all-polymer capillary microvalves for passive microfluidic control". In: *Journal of Micromechanics and Microengineering* 24.12 (2014), p. 125007. DOI: 10.1088/0960-1317/24/12/125007.

[4] Kasper Kistrup, Carl Esben Poulsen, Mikkel Hansen, and Anders Wolff. "Ultrasonic welding for fast bonding of self-aligned structures in lab-on-a-chip systems". In: *Lab Chip* 15 (2015), pp. 1998–2001. DOI: 10.1039/C5LC00174A.

[5] Carl Esben Poulsen, Kasper Kistrup, Nis Korsgaard Andersen, Flemming Larsen, Rafael Taboryski, and Anders Wolff. *Replication Tool and Method of Providing a Replication Tool*. 2015.

[6] Carl Esben Poulsen, Kasper Kistrup, Nis Korsgaard Andersen, Rafael Taboryski, and Anders Wolff. *Micropillar Energy directors for ultrasonic welding*. 2014.

[7] Carl Esben Poulsen, Kasper Kistrup, Nis Korsgaard Andersen, Rafael Taboryski, and Anders Wolff. *Method of Producing an Item with Enhanced Wetting Properties by Fast Replication and Replication Tool Used in the Method*. 2014.

[8] Carl Esben Poulsen, Kasper Kistrup, Nis Korsgaard Andersen, Rafael J Taboryski, Mikkel Fougt Hansen, and Anders Wolff. "TransForm: Injection moulded 3D superhydrophobic surfaces". In: *Abstract Book - DTU Sustain Conference 2014*. Kgs. Lyngby: Technical University of Denmark, 2014.

[9] Carl Esben Poulsen, Dang Duong Bang, Martin Dufva, and Anders Wolff. "An injection moulded microfluidic chip for polymerase chain reaction (PCR) thermo-cycling and imaging of droplets to detect food-borne pathogens Campylobacter spp". In: *15th International Conference on Biomedical Engineering*. 2014.

[10] Kasper Kistrup, Carl Esben Poulsen, Nis Korsgaard Andersen, Rafael J Taboryski, Anders Wolff, and Mikkel Fougt Hansen. "Ultrasonic welding for bonding of microfluidic chip systems". In: *20th International Conference on Commercializing Micro- and Nanotechnology*. Kraków, Poland, 2015.

[11] Tran Quang Hung, Yi Sun, Carl Esben Poulsen, Quyen Than Linh, Wai Hoe Chin, Bang Dang Duong, and Anders Wolff. "Miniaturization of a micro-optics array for highly sensitive and parallel detection on injection moulded lab-on-a-chip". In: *Lab Chip* (2015). DOI: 10.1039/C5LC00176E.

[12] Tran Quang Hung, Yi Sun, Carl Esben Poulsen, Wai Hoe Chin, Anders Wolff, and Dang Duong Bang. "Injection Moulded Micro-Optics Arrays for Quantification of Surface Bound Fluorescent Molecules in Air and Aqueous Media". In: *Proceedings Microtas 2015* (2015).

[13] A. Manz, N. Graber, and H.M. Widmer. "Miniaturized total chemical analysis systems: A novel concept for chemical sensing". In: *Sensors and Actuators B: Chemical* 1.1-6 (1990), pp. 244–248. DOI: 10.1016/0925-4005(90)80209-I.

[14] U S Department of Health, Human Services, and Others. *Recommendations: Clinical Laboratory Improvement Amendments of 1988 (CLIA) Waiver Applications for Manufacturers of In Vitro Diagnostic Devices*. 2008.

[15] Curtis D. Chin, Vincent Linder, and Samuel K. Sia. "Commercialization of microfluidic point-of-care diagnostic devices". In: *Lab on a Chip* 12.12 (2012), p. 2118. DOI: 10.1039/c2lc21204h.

[16] Aaron M. Streets and Yanyi Huang. "Chip in a lab: Microfluidics for next generation life science research". In: *Biomicrofluidics* 7.1 (2013), p. 011302. DOI: 10.1063/1.4789751.

[17] Holger Becker. "Mind the gap!" In: *Lab on a chip* 10.3 (2010), pp. 271–273. DOI: 10.1039/b925993g.

[18] Andrew McWilliams. *Microfluidics: Technologies and Global Markets*. Tech. rep. BCC Research, 2013, p. 130.

[19] Curtis D Chin et al. "Microfluidics-based diagnostics of infectious diseases in the developing world." In: *Nature medicine* 17.8 (2011), pp. 1015–1019. DOI: 10.1038/nm.2408.

[20] Simone Tanzi, Marco Matteucci, Thomas Lehrmann Christiansen, Søren Friis, Mette Thylstrup Christensen, Joergen Garnaes, Sandra Wilson, Jonatan Kutchinsky, and Rafael Taboryski. "Ion channel recordings on an injection-molded polymer chip." In: *Lab on a chip* (2013). DOI: 10.1039/c3lc50760b.

[21] Christian D. Ahrberg, Bojan Robert Ilic, Andreas Manz, and Pavel Neuzil. "Handheld Real-Time PCR Device". In: *Lab Chip* (2015). DOI: 10.1039/C5LC01415H.

[22] Jong Wook Hong and Stephen R Quake. "Integrated nanoliter systems." In: *Nature biotechnology* 21.10 (2003), pp. 1179–1183. DOI: 10.1038/nbt871.

[23] Carlos Duarte, Eric Salm, Brian Dorvel, Bobby Reddy, and Rashid Bashir. "On-chip parallel detection of foodborne pathogens using loop-mediated isothermal amplification." In: *Biomedical microdevices* 15.5 (2013), pp. 821–30. DOI: 10.1007/s10544-013-9769-5.

[24] Amelia L Markey, Stephan Mohr, and Philip J R Day. "High-throughput droplet PCR". In: *Methods (San Diego, Calif.)* 50.4 (2010), pp. 277–81. DOI: 10.1016/j.ymeth.2010.01.030.

[25] Eric K. Sackmann, Anna L. Fulton, and David J. Beebe. "The present and future role of microfluidics in biomedical research." In: *Nature* 507.7491 (2014), pp. 181–9. DOI: 10.1038/nature13118.

[26] Masumi Yamada, Megumi Nakashima, and Minoru Seki. "Pinched flow fractionation: Continuous size separation of particles utilizing a laminar flow profile in a pinched microchannel". In: *Analytical Chemistry* 76.18 (2004), pp. 5465–5471. DOI: 10.1021/ac049863r.

[27] Ali Fallah-Araghi, Jean-Christophe Baret, Michael Ryckelynck, and Andrew D Griffiths. "A completely in vitro ultrahigh-throughput droplet-based microfluidic screening system for protein engineering and directed evolution". In: *Lab on a chip* 12.5 (2012), pp. 882–91. DOI: 10.1039/c2lc21035e.

[28] Lotien Richard Huang. "Continuous Particle Separation Through Deterministic Lateral Displacement". In: *Science* 304.5673 (2004), pp. 987–990. DOI: 10.1126/science.1094567.

[29] Abraham D Stroock. “Chaotic Mixer for Microchannels”. In: *Science* 295.5555 (2002), pp. 647–651. DOI: 10.1126/science.1066238.

[30] Noo Li Jeon, Harihara Baskaran, Stephan K W Dertinger, George M Whitesides, Livingston Van De Water, and Mehmet Toner. “Neutrophil chemotaxis in linear and complex gradients of interleukin-8 formed in a microfabricated device”. In: *Nature Biotechnology* 20.8 (2002), pp. 826–830. DOI: 10.1038/nbt712.

[31] Henrik Bruus. “Diffusion”. In: *Theoretical Microfluidics*. 1st. Chippenham, UK: Oxford University Press, 2008. Chap. 5, p. 91.

[32] Andres W. Martinez, Scott T. Phillips, Manish J. Butte, and George M. Whitesides. “Patterned Paper as a Platform for Inexpensive, Low-Volume, Portable Bioassays”. In: *Angewandte Chemie International Edition* 46.8 (2007), pp. 1318–1320. DOI: 10.1002/anie.200603817.

[33] Emanuel Carrilho, Andres W Martinez, and George M Whitesides. “Understanding Wax Printing: A Simple Micropatterning Process for Paper-Based Microfluidics”. In: *Analytical Chemistry* 81.16 (2009), pp. 7091–7095. DOI: 10.1021/ac901071p.

[34] Todd Thorsen, Richard W. Roberts, Frances H. Arnold, and Stephen R. Quake. “Dynamic Pattern Formation in a Vesicle-Generating Microfluidic Device”. In: *Physical Review Letters* 86.18 (2001), pp. 4163–4166. DOI: 10.1103/PhysRevLett.86.4163.

[35] Jean-Christophe Baret. “Surfactants in droplet-based microfluidics”. In: *Lab on a chip* 12.3 (2012), pp. 422–33. DOI: 10.1039/c1lc20582j.

[36] Aaron P. Debon, Robert C. R. Wootton, and Katherine S. Elvira. “Droplet confinement and leakage: Causes, underlying effects, and amelioration strategies”. In: *Biomicrofluidics* 9.2 (2015), p. 024119. DOI: 10.1063/1.4917343.

[37] David J. Collins, Adrian Neild, Andrew DeMello, Ai-Qun Liu, and Ye Ai. “The Poisson distribution and beyond: methods for microfluidic droplet production and single cell encapsulation”. In: *Lab Chip* 15.17 (2015), pp. 3439–3459. DOI: 10.1039/C5LC00614G.

[38] Zhuang Zhi Chong, Say Hwa Tan, Alfonso M. Gañán-Calvo, Shu Beng Tor, Ngiap Hiang Loh, and Nam-Trung Nguyen. “Active droplet generation in microfluidics”. In: *Lab Chip* 16.1 (2016), pp. 35–58. DOI: 10.1039/C5LC01012H.

[39] Darren R. Link, Erwan Grasland-Mongrain, Agnes Duri, Flavie Sarrazin, Zhengdong Cheng, Galder Cristobal, Manuel Marquez, and David A. Weitz. “Electric Control of Droplets in Microfluidic Devices”. In: *Angewandte Chemie International Edition* 45.16 (2006), pp. 2556–2560. DOI: 10.1002/anie.200503540.

[40] Jean-Christophe Baret et al. “Fluorescence-activated droplet sorting (FADS): efficient microfluidic cell sorting based on enzymatic activity”. In: *Lab on a chip* 9.13 (2009), pp. 1850–8. DOI: 10.1039/b902504a.

[41] Staffan L Sjostrom, Yunpeng Bai, Mingtao Huang, Zihe Liu, Jens Nielsen, Haakan N Joensson, and Helene Andersson Svahn. “High-throughput screening for industrial enzyme production hosts by droplet microfluidics”. In: *Lab on a chip* (2013). DOI: 10.1039/c3lc51202a.

[42] Muhsincan Sesen, Tuncay Alan, and Adrian Neild. “Microfluidic on-demand droplet merging using surface acoustic waves”. In: *Lab on a Chip* (2014). DOI: 10.1039/c4lc00456f.

[43] Helen Song, Joshua D. Tice, and Rustem F. Ismagilov. “A Microfluidic System for Controlling Reaction Networks in Time”. In: *Angewandte Chemie International Edition* 42.7 (2003), pp. 768–772. DOI: 10.1002/anie.200390203.

[44] Ansgar Huebner, Dan Bratton, Graeme Whyte, Min Yang, Andrew J Demello, Chris Abell, and Florian Hollfelder. “Static microdroplet arrays: a microfluidic device for

droplet trapping, incubation and release for enzymatic and cell-based assays". In: *Lab on a chip* 9.5 (2009), pp. 692–8. DOI: 10.1039/b813709a.

[45] Yunpeng Bai, Ximin He, Dingsheng Liu, Santoshkumar N Patil, Dan Bratton, Ansgar Huebner, Florian Hollfelder, Chris Abell, and Wilhelm T S Huck. "A double droplet trap system for studying mass transport across a droplet-droplet interface". In: *Lab on a chip* 10.10 (2010), pp. 1281–5. DOI: 10.1039/b925133b.

[46] Philip Huw King, Gareth Jones, Hywel Morgan, Maurits R. R. de Planque, and Klaus-Peter Zauner. "Interdroplet bilayer arrays in millifluidic droplet traps from 3D-printed moulds". In: *Lab Chip* 14.4 (2014), pp. 722–729. DOI: 10.1039/C3LC51072G.

[47] Andrew C Hatch, Jeffrey S Fisher, Armando R Tovar, Albert T Hsieh, Robert Lin, Stephen L Pentoney, David L Yang, and Abraham P Lee. "1-Million droplet array with wide-field fluorescence imaging for digital PCR". In: *Lab on a Chip* 11.22 (2011), p. 3838. DOI: 10.1039/c1lc20561g.

[48] Xavier Casadevall i Solvas, Monpichar Srisa-Art, Andrew J DeMello, and Joshua B Edel. "Mapping of fluidic mixing in microdroplets with 1 micros time resolution using fluorescence lifetime imaging". In: *Analytical chemistry* 82.9 (2010), pp. 3950–6. DOI: 10.1021/ac100055g.

[49] Mohammad Ali Khorshidi, Prem Kumar Periyannan Rajeswari, Carolina Wählby, Haakan N Joensson, and Helene Andersson Svahn. "Automated analysis of dynamic behavior of single cells in picoliter droplets". In: *Lab on a chip* 14.5 (2014), pp. 931–7. DOI: 10.1039/c3lc51136g.

[50] Helen Song, Delai L Chen, and Rustem F Ismagilov. "Reactions in droplets in microfluidic channels". In: *Angewandte Chemie (International ed. in English)* 45.44 (2006), pp. 7336–56. DOI: 10.1002/anie.200601554.

[51] Delai L. Chen, Cory J. Gerdts, and Rustem F. Ismagilov. "Using Microfluidics to Observe the Effect of Mixing on Nucleation of Protein Crystals". In: *Journal of the American Chemical Society* 127.27 (2005), pp. 9672–9673. DOI: 10.1021/ja052279v.

[52] Cory J. Gerdts, David E. Sharoyan, and Rustem F. Ismagilov. "A Synthetic Reaction Network: Chemical Amplification Using Nonequilibrium Autocatalytic Reactions Coupled in Time". In: *Journal of the American Chemical Society* 126.20 (2004), pp. 6327–6331. DOI: 10.1021/ja0316891.

[53] Lucas Frenz, Kerstin Blank, Eric Brouzes, and Andrew D Griffiths. "Reliable microfluidic on-chip incubation of droplets in delay-lines". In: *Lab on a chip* 9.10 (2009), pp. 1344–8. DOI: 10.1039/b816049j.

[54] Ying Zhu and Qun Fang. "Analytical detection techniques for droplet microfluidics—A review". In: *Analytica Chimica Acta* 787 (2013), pp. 24–35. DOI: 10.1016/j.aca.2013.04.064.

[55] L. Spencer Roach, Helen Song, and Rustem F. Ismagilov. "Controlling Nonspecific Protein Adsorption in a Plug-Based Microfluidic System by Controlling Interfacial Chemistry Using Fluorous-Phase Surfactants". In: *Analytical Chemistry* 77.3 (2005), pp. 785–796. DOI: 10.1021/ac049061w.

[56] James Q Boedicker, Liang Li, Timothy R Kline, and Rustem F Ismagilov. "Detecting bacteria and determining their susceptibility to antibiotics by stochastic confinement in nanoliter droplets using plug-based microfluidics". In: *Lab on a Chip* 8.8 (2008), p. 1265. DOI: 10.1039/b804911d.

[57] Benjamin J Hindson et al. "High-throughput droplet digital PCR system for absolute quantitation of DNA copy number". In: *Analytical chemistry* 83.22 (2011), pp. 8604–10. DOI: 10.1021/ac202028g.

[58] Deniz Pekin et al. “Quantitative and sensitive detection of rare mutations using droplet-based microfluidics”. In: *Lab on a chip* 11.13 (2011), pp. 2156–66. DOI: 10.1039/c1lc20128j.

[59] Richard Williams, Sergio G Peisajovich, Oliver J Miller, Shlomo Magdassi, Dan S Tawfik, and Andrew D Griffiths. “Amplification of complex gene libraries by emulsion PCR”. In: 3.7 (2006), pp. 545–550. DOI: 10.1038/NMETH896.

[60] Wadim L Matochko, Simon Ng, Mohammad R Jafari, Joseph Romaniuk, Sindy K Y Tang, and Ratmir Derda. “Uniform amplification of phage display libraries in monodisperse emulsions”. In: *Methods (San Diego, Calif.)* 58.1 (2012), pp. 18–27. DOI: 10.1016/j.ymeth.2012.07.012.

[61] Shigeyoshi Matsumura, Faith M Coldren, Annick Marin, Ali Fallah-araghi, and Andrew D Griffiths. “WHY IS THE MINIMUM UNIT OF LIFE A CELL ? : BUILDING AN “ RNA WORLD ” MODEL PROTOCELL USING DROPLET-BASED MICROFLUIDICS”. In: (2012), pp. 166–168.

[62] Mingyan He, J. Scott Edgar, Gavin D M Jeffries, Robert M. Lorenz, J. Patrick Shelby, and Daniel T. Chiu. “Selective Encapsulation of Single Cells and Subcellular Organelles into Picoliter- and Femtoliter-Volume Droplets”. In: *Analytical Chemistry* 77.6 (2005), pp. 1539–1544. DOI: 10.1021/ac0480850.

[63] Brian Buder, Michael Alexander, Rahul Krishnan, David W Chapman, and Jonathan RT Lakey. “Encapsulated Islet Transplantation: Strategies and Clinical Trials”. In: *Immune Network* 13.6 (2013), p. 235. DOI: 10.4110/in.2013.13.6.235.

[64] Alison M Skelley, Oktay Kirak, Heikyung Suh, Rudolf Jaenisch, and Joel Voldman. “Microfluidic control of cell pairing and fusion”. In: *Nature Methods* 6.2 (2009), pp. 147–152. DOI: 10.1038/nmeth.1290.

[65] G F Christopher and S L Anna. “Microfluidic methods for generating continuous droplet streams”. In: *Journal of Physics D: Applied Physics* 40.19 (2007), R319–R336. DOI: 10.1088/0022-3727/40/19/R01.

[66] Rémi Dangla, S Cagri Kayi, and Charles N Baroud. “Droplet microfluidics driven by gradients of confinement”. In: *Proceedings of the National Academy of Sciences of the United States of America* 110.3 (2013), pp. 853–8. DOI: 10.1073/pnas.1209186110.

[67] Carl Taswell. “Limiting dilution assays for the determination of immunocompetent cell frequencies. I. Data analysis”. In: *The Journal of Immunology* 4 (1981), pp. 1614–1619.

[68] Christopher M Hindson, John R Chevillet, Hilary A Briggs, Emily N Gallichotte, Ingrid K Ruf, Benjamin J Hindson, Robert L Vessella, and Muneesh Tewari. “Absolute quantification by droplet digital PCR versus analog real-time PCR”. In: *Nature methods* 10.10 (2013), pp. 1003–5. DOI: 10.1038/nmeth.2633.

[69] Dany Morisset, Dejan Štebih, Mojca Milavec, Kristina Gruden, and Jana Žel. “Quantitative Analysis of Food and Feed Samples with Droplet Digital PCR”. In: *PLoS ONE* 8.5 (2013), e62583. DOI: 10.1371/journal.pone.0062583.

[70] Matthew C Strain, Steven M Lada, Tiffany Luong, Steffney E Rought, Sara Gianella, Valeri H Terry, Celsa A Spina, Christopher H Woelk, and Douglas D Richman. “Highly precise measurement of HIV DNA by droplet digital PCR.” In: *PloS one* 8.4 (2013), e55943. DOI: 10.1371/journal.pone.0055943.

[71] Lianhua Dong, Ying Meng, Jing Wang, and Yingying Liu. “Evaluation of droplet digital PCR for characterizing plasmid reference material used for quantifying ammonia oxidizers and denitrifiers.” In: *Analytical and bioanalytical chemistry* 406.6 (2014), pp. 1701–12. DOI: 10.1007/s00216-013-7546-1.

[72] Leonardo B Pinheiro, Victoria a Coleman, Christopher M Hindson, Jan Herrmann, Benjamin J Hindson, Somanath Bhat, and Kerry R Emslie. "Evaluation of a droplet digital polymerase chain reaction format for DNA copy number quantification." In: *Analytical chemistry* 84.2 (2012), pp. 1003–11. DOI: 10.1021/ac202578x.

[73] Friedrich Schuler et al. "Digital Droplet PCR on Disk". In: *Lab Chip* (2015). DOI: 10.1039/C5LC01068C.

[74] Yolanda Schaerli, Robert C Wootton, Tom Robinson, Viktor Stein, Christopher Dunsby, Mark a a Neil, Paul M W French, Andrew J Demello, Chris Abell, and Florian Hollfelder. "Continuous-flow polymerase chain reaction of single-copy DNA in microfluidic microdroplets". In: *Analytical chemistry* 81.1 (2009), pp. 302–6. DOI: 10.1021/ac802038c.

[75] Margaret Macris Kiss, Lori Ortoleva-Donnelly, N. Reginald Beer, Jason Warner, Christopher G. Bailey, Bill W. Colston, Jonathon M. Rothberg, Darren R. Link, and John H. Leamon. "High-throughput quantitative polymerase chain reaction in picoliter droplets". In: *Analytical chemistry* 80.23 (2008), pp. 8975–81.

[76] Hanyoup Kim, Siarhei Vishniakou, and Gregory W Faris. "Petri dish PCR: laser-heated reactions in nanoliter droplet arrays". In: *Lab on a chip* 9.9 (2009), pp. 1230–5. DOI: 10.1039/b817288a.

[77] Alexandra S. Whale, Jim F. Huggett, Simon Cowen, Valerie Speirs, Jacqui Shaw, Stephen Ellison, Carole A. Foy, and Daniel J. Scott. "Comparison of microfluidic digital PCR and conventional quantitative PCR for measuring copy number variation". In: *Nucleic Acids Research* 40.11 (2012), e82–e82. DOI: 10.1093/nar/gks203.

[78] Zhi Zhu, Wenhua Zhang, Xuefei Leng, Mingxia Zhang, Zhichao Guan, Jiangquan Lu, and Chaoyong James Yang. "Highly sensitive and quantitative detection of rare pathogens through agarose droplet microfluidic emulsion PCR at the single-cell level". In: *Lab on a chip* 12.20 (2012), pp. 3907–13. DOI: 10.1039/c2lc40461c.

[79] Qun Zhong, Smiti Bhattacharya, Steven Kotsopoulos, Jeff Olson, Valérie Taly, Andrew D Griffiths, Darren R Link, and Jonathan W Larson. "Multiplex digital PCR: breaking the one target per color barrier of quantitative PCR". In: *Lab on a chip* 11.13 (2011), pp. 2167–74. DOI: 10.1039/c1lc20126c.

[80] Yi Zhang, Vasudev Bailey, Christopher M Puleo, Hariharan Easwaran, Elizabeth Griffiths, James G Herman, Stephen B Baylin, and Tza-Huei Wang. "DNA methylation analysis on a droplet-in-oil PCR array". In: *Lab on a chip* 9.8 (2009), pp. 1059–64. DOI: 10.1039/b821780g.

[81] Friedrich Schuler, Frank Schwemmer, Martin Trotter, Simon Wadle, Roland Zengerle, Felix von Stetten, and Nils Paust. "Centrifugal step emulsification applied for absolute quantification of nucleic acids by digital droplet RPA". In: *Lab Chip* 15.13 (2015), pp. 2759–2766. DOI: 10.1039/C5LC00291E.

[82] Linas Mazutis et al. "Droplet-based microfluidic systems for high-throughput single DNA molecule isothermal amplification and analysis". In: *Analytical chemistry* 81.12 (2009), pp. 4813–21. DOI: 10.1021/ac900403z.

[83] Sissel Juul et al. "Droplet microfluidics platform for highly sensitive and quantitative detection of malaria-causing Plasmodium parasites based on enzyme activity measurement". In: *ACS nano* 6.12 (2012), pp. 10676–83. DOI: 10.1021/nn3038594.

[84] Tushar D Rane, Helena C Zec, Chris Puleo, Abraham P Lee, and Tza-Huei Wang. "Droplet microfluidics for amplification-free genetic detection of single cells". In: *Lab on a chip* 12.18 (2012), pp. 3341–7. DOI: 10.1039/c2lc40537g.

[85] Yunxia Zhang, Ying Zhu, Bo Yao, and Qun Fang. "Nanolitre droplet array for real time reverse transcription polymerase chain reaction". In: *Lab on a chip* 11.8 (2011), pp. 1545–9. DOI: 10.1039/c0lc00502a.

[86] Huifa Zhang, Gareth Jenkins, Yuan Zou, Zhi Zhu, and Chaoyong James Yang. "Massively parallel single-molecule and single-cell emulsion reverse transcription polymerase chain reaction using agarose droplet microfluidics". In: *Analytical chemistry* 84.8 (2012), pp. 3599–606. DOI: 10.1021/ac2033084.

[87] Tushar D. Rane, Liben Chen, Helena Claire Zec, and Jeff Tza-Huei Wang. "Microfluidic Continuous Flow Digital Loop-Mediated Isothermal Amplification (LAMP)". In: *Lab Chip* (2014). DOI: 10.1039/C4LC01158A.

[88] Yen-Heng Lin, Chun-Hong Lee, and Gwo-Bin Lee. "Droplet Formation Utilizing Controllable Moving-Wall Structures for Double-Emulsion Applications". In: *Journal of Microelectromechanical Systems* 17.3 (2008), pp. 573–581. DOI: 10.1109/JMEMS.2008.924273.

[89] Hao Hu et al. "Mutation screening in 86 known X-linked mental retardation genes by droplet-based multiplex PCR and massive parallel sequencing". In: *The HUGO journal* 3.1-4 (2009), pp. 41–9. DOI: 10.1007/s11568-010-9137-y.

[90] G Jenkins, H Zhang, Y Zou, X Leng, W Zhang, and C Yang. "AGAROSE DROPLET MICROFLUIDICS FOR HIGHLY PARALLEL SINGLE MOLECULE EMULSION RT-PCR". In: *rsc.org* (2011), pp. 945–947.

[91] Yong Zeng, Richard Novak, Joe Shuga, Martyn T Smith, and Richard a Mathies. "High-performance single cell genetic analysis using microfluidic emulsion generator arrays". In: *Analytical chemistry* 82.8 (2010), pp. 3183–90. DOI: 10.1021/ac902683t.

[92] Shaun W Lim and Adam R Abate. "Ultrahigh-throughput sorting of microfluidic drops with flow cytometry." In: *Lab on a chip* 13.23 (2013), pp. 4563–72. DOI: 10.1039/c3lc50736j.

[93] NR Beer and EK Wheeler. "On-chip single-copy real-time reverse-transcription PCR in isolated picoliter droplets". In: *Analytical chemistry* 80.6 (2008), pp. 1854–8. DOI: 10.1021/ac800048k.

[94] S. Mohr, Y.-H. Zhang, A. Macaskill, P. J. R. Day, R. W. Barber, N. J. Goddard, D. R. Emerson, and P. R. Fielden. "Numerical and experimental study of a droplet-based PCR chip". In: *Microfluidics and Nanofluidics* 3.5 (2007), pp. 611–621. DOI: 10.1007/s10404-007-0153-8.

[95] Feng Shen, Wenbin Du, Elena K Davydova, Mikhail A Karymov, Janmajay Pandey, and Rustem F Ismagilov. "Nanoliter Multiplex PCR Arrays on a SlipChip". In: *Analytical Chemistry* 82.11 (2010), pp. 4606–4612. DOI: 10.1021/ac1007249.

[96] N Reginald Beer, Benjamin J Hindson, Elizabeth K Wheeler, Sara B Hall, Klint A Rose, Ian M Kennedy, and Bill W Colston. "On-chip, real-time, single-copy polymerase chain reaction in picoliter droplets." In: *Analytical chemistry* 79.22 (2007), pp. 8471–5. DOI: 10.1021/ac701809w.

[97] James D Watson. *Recombinant DNA: genes and genomes: a short course*. Macmillan, 2007.

[98] Madprime. *File:PCR.svg*. 2007. URL: https://commons.wikimedia.org/wiki/File:PCR.svg (visited on 03/24/2016).

[99] Liat Rosenfeld, Tiras Lin, Ratmir Derda, and Sindy K Y Tang. "Review and analysis of performance metrics of droplet microfluidics systems". In: *Microfluidics and Nanofluidics* 16.5 (2014), pp. 921–939. DOI: 10.1007/s10404-013-1310-x.

[100] Todd Thorsen. "Microfluidic Large-Scale Integration". In: *Science* 298.5593 (2002), pp. 580–584. DOI: 10.1126/science.1076996.

[101] Elizabeth a Ottesen, Jong Wook Hong, Stephen R Quake, and Jared R Leadbetter. "Microfluidic digital PCR enables multigene analysis of individual environmental bacteria." In: *Science (New York, N.Y.)* 314.5804 (2006), pp. 1464–1467. DOI: 10.1126/science.1131370.

[102] Fiona M F Lun, Rossa W K Chiu, K. C. Allen Chan, T. Yeung Leung, T. Kin Lau, and Y. M. Dennis Lo. "Microfluidics Digital PCR Reveals a Higher than Expected Fraction of Fetal DNA in Maternal Plasma". In: *Clinical Chemistry* 54.10 (2008), pp. 1664–1672. DOI: 10.1373/clinchem.2008.111385.

[103] Savaş Tay, Jacob J. Hughey, Timothy K. Lee, Tomasz Lipniacki, Stephen R. Quake, and Markus W Covert. "Single-cell NF-κB dynamics reveal digital activation and analogue information processing". In: *Nature* 466.7303 (2010), pp. 267–271. DOI: 10.1038/nature09145.

[104] Life-Technologies. *Product Bulletin: OpenArray technology*. DOI: https://www.thermofisher.com/dk/en/home/life-science/pcr/real-time-pcr/real-time-openarray/open-array-technology.html. (Visited on 02/18/2016).

[105] Jessica Melin and Stephen R Quake. "Microfluidic large-scale integration: the evolution of design rules for biological automation." In: *Annual review of biophysics and biomolecular structure* 36 (2007), pp. 213–231. DOI: 10.1146/annurev.biophys.36.040306.132646.

[106] Fluidigm. *BiomarkHD System Brochure*. URL: https://www.fluidigm.com/products/biomark-hd-system (visited on 02/18/2016).

[107] Formulatrix. *Constellation User's Guide*. 2016. URL: http://www.formulatrix.com/downloads/docs/constellation/constellation-users-guide.pdf (visited on 02/24/2016).

[108] BIO-RAD. *QX200™ Droplet Digital™ PCR System Brochure*. 2015. URL: http://www.bio-rad.com/webroot/web/pdf/lsr/literature/Bulletin{_}6311.pdf (visited on 02/17/2016).

[109] Kenji Takahashi, Irene K. Yan, Chaeyoung Kim, Jungsu Kim, and Tushar Patel. "Analysis of Extracellular RNA by Digital PCR". In: *Frontiers in Oncology* 4.June (2014), pp. 2–7. DOI: 10.3389/fonc.2014.00129.

[110] Nejc Rački, Dany Morisset, Ion Gutierrez-Aguirre, and Maja Ravnikar. "One-step RT-droplet digital PCR: a breakthrough in the quantification of waterborne RNA viruses". In: *Analytical and Bioanalytical Chemistry* 406.3 (2014), pp. 661–667. DOI: 10.1007/s00216-013-7476-y.

[111] Monya Baker. "Digital PCR hits its stride". In: *Nature Methods* 9.6 (2012), pp. 541–544. DOI: 10.1038/nmeth.2027.

[112] Fluidigm. *Fluidigm System for Rapid, Reliable, and Cost Effective SNP Genotyping*. 2016. URL: https://www.fluidigm.com/binaries/content/documents/fluidigm/marketing/fluidigm-system-for-rapid-reliable-and-cost-effective-genotyping/fluidigm-system-for-rapid-reliable-and-cost-effective-genotyping/fluidigm:file (visited on 02/25/2016).

[113] Thermo Fisher Scientific. *QuantStudio™ 12K Flex Real-Time PCR System - Brochure*. URL: https://tools.thermofisher.com/content/sfs/brochures/cms{_}098456.pdf (visited on 02/25/2016).

[114] Ben Butkus. *Leveraging Microfluidics Experience, Formulatrix Set to Launch First Digital PCR System*. 2014. URL: https://www.genomeweb.com/pcrsample-prep/leveraging-microfluidics-experience-formulatrix-set-launch-first-digital-pcr-sys (visited on 02/25/2016).

[115] Bio-Rad. *QX200™ Droplet Digital™ PCR System Consumables*. URL: http://www.bio-rad.com/en-us/product/qx200-droplet-digital-pcr-system (visited on 02/25/2016).

[116] Andrew C. Hatch, Tathagata Ray, Kelly Lintecum, and Cody Youngbull. "Continuous flow real-time PCR device using multi-channel fluorescence excitation and detection". In: *Lab on a Chip* (2014). DOI: 10.1039/c3lc51236c.

[117] Bio-Rad. *BIO-RAD QX100™ DROPLET READER AND QUANTASOFT™ GUIDE*. 2012. URL: http://sydney.edu.au/medicine/bosch/facilities/molecular-biology/nucleic-acid/287-11137-C{_}BRQL{_}DR{_}Manual.pdf (visited on 03/08/2016).

[118] H.T.G. van Lintel, F.C.M. van De Pol, and S. Bouwstra. "A piezoelectric micropump based on micromachining of silicon". In: *Sensors and Actuators* 15.2 (1988), pp. 153–167. DOI: 10.1016/0250-6874(88)87005-7.

[119] D. Jed. Harrison, Andreas. Manz, Zhonghui. Fan, Hans. Luedi, and H. Michael. Widmer. "Capillary electrophoresis and sample injection systems integrated on a planar glass chip". In: *Analytical Chemistry* 64.20 (1992), pp. 1926–1932. DOI: 10.1021/ac00041a030.

[120] Dong Qin, Younan Xia, and George M. Whitesides. "Rapid prototyping of complex structures with feature sizes larger than 20 µm". In: *Advanced Materials* 8.11 (1996), pp. 917–919. DOI: 10.1002/adma.19960081110.

[121] J. Cooper McDonald and George M. Whitesides. "Poly(dimethylsiloxane) as a material for fabricating microfluidic devices". In: *Accounts of Chemical Research* 35.July (2002), pp. 491–499. DOI: 10.1021/ar010110q.

[122] George M Whitesides. "The origins and the future of microfluidics". In: *Nature* 442.7101 (2006), pp. 368–73. DOI: 10.1038/nature05058.

[123] Rajendrani Mukhopadhyay. "When PDMS isn't the best". In: *Analytical chemistry* 79.9 (2007), pp. 3248–3253.

[124] Pere Roca-Cusachs, Félix Rico, Elena Martínez, Jordi Toset, Ramon Farré, and Daniel Navajas. "Stability of microfabricated high aspect ratio structures in poly(dimethylsiloxane)". In: *Langmuir* 21.4 (2005), pp. 5542–5548. DOI: 10.1021/la046931w.

[125] S R Quake. "From Micro- to Nanofabrication with Soft Materials". In: *Science* 290.5496 (2000), pp. 1536–1540. DOI: 10.1126/science.290.5496.1536.

[126] M A Unger. "Monolithic Microfabricated Valves and Pumps by Multilayer Soft Lithography". In: *Science* 288.5463 (2000), pp. 113–116. DOI: 10.1126/science.288.5463.113.

[127] Jianping Fu, Yang-kao Wang, Michael T Yang, Ravi A Desai, Xiang Yu, Zhijun Liu, and Christopher S Chen. "Mechanical regulation of cell function with geometrically modulated elastomeric substrates". In: *Nature Methods* 7.9 (2010), pp. 733–736. DOI: 10.1038/nmeth.1487.

[128] Dongeun Huh, Benjamin D Matthews, Akiko Mammoto, Martín Montoya-Zavala, Hong Yuan Hsin, and Donald E Ingber. "Reconstituting Organ-Level Lung Functions on a Chip". In: *Science* 328.5986 (2010), pp. 1662–1668. DOI: 10.1126/science.1188302.

[129] David C. Duffy, J. Cooper McDonald, Olivier J A Schueller, and George M. Whitesides. "Rapid Prototyping of Microfluidic Systems in Poly(dimethylsiloxane)". In: *Analytical Chemistry* 70.23 (1998), pp. 4974–4984. DOI: 10.1021/ac980656z.

[130] Mark A Eddings, Michael A Johnson, and Bruce K Gale. *Determining the optimal PDMS–PDMS bonding technique for microfluidic devices*. 2008. DOI: 10.1088/0960-1317/18/6/067001.

[131] Shantanu Bhattacharya, Arindom Datta, Jordan M. Berg, and Shubhra Gangopadhyay. "Studies on surface wettability of poly(dimethyl) siloxane (PDMS) and glass under oxygen-plasma treatment and correlation with bond strength". In: *Journal of Microelectromechanical Systems* 14.3 (2005), pp. 590–597. DOI: 10.1109/JMEMS.2005.844746.

[132] Jinwen Zhou, Amanda Vera Ellis, and Nicolas Hans Voelcker. "Recent developments in PDMS surface modification for microfluidic devices". In: *ELECTROPHORESIS* 31.1 (2010), pp. 2–16. DOI: 10.1002/elps.200900475.

[133] T. C. Merkel, V. I. Bondar, K. Nagai, B. D. Freeman, and I. Pinnau. "Gas sorption, diffusion, and permeation in poly(dimethylsiloxane)". In: *Journal of Polymer Science Part B: Polymer Physics* 38.3 (2000), pp. 415–434. DOI: 10.1002/(SICI)1099-0488(20000201)38:3<415::AID-POLB8>3.0.CO;2-Z.

[134] Qiangyuan Zhu et al. "Digital PCR on an integrated self-priming compartmentalization chip". In: *Lab Chip* 14.6 (2014), pp. 1176–1185. DOI: 10.1039/C3LC51327K.

[135] Linas Mazutis, John Gilbert, W Lloyd Ung, David A Weitz, Andrew D Griffiths, and John A Heyman. "Single-cell analysis and sorting using droplet-based microfluidics". In: *Nature Protocols* 8.5 (2013), pp. 870–891. DOI: 10.1038/nprot.2013.046.

[136] Yonggang Y. Huang, Weixing Zhou, K. J. Hsia, Etienne Menard, Jang Ung Park, John a. Rogers, and Andrew G. Alleyne. "Stamp collapse in soft lithography". In: *Langmuir* 21.8 (2005), pp. 8058–8068. DOI: 10.1021/la0502185.

[137] Erwin Berthier, Edmond W. K. Young, and David Beebe. *Engineers are from PDMS-land, Biologists are from Polystyrenia*. 2012. DOI: 10.1039/c2lc20982a.

[138] Kathryn Futrega, Jianshi Yu, Jace W. Jones, Maureen A. Kane, William B Lott, Kerry Atkinson, and Michael Robert Doran. "Polydimethylsiloxane (PDMS) modulates CD38 expression, absorbs retinoic acid and may perturb retinoid signalling". In: *Lab Chip* (2016). DOI: 10.1039/C6LC00269B.

[139] David T. Eddington, John P. Puccinelli, and David J. Beebe. "Thermal aging and reduced hydrophobic recovery of polydimethylsiloxane". In: *Sensors and Actuators B: Chemical* 114.1 (2006), pp. 170–172. DOI: 10.1016/j.snb.2005.04.037.

[140] Dhananjay Bodas and Chantal Khan-Malek. "Formation of more stable hydrophilic surfaces of PDMS by plasma and chemical treatments". In: *Microelectronic Engineering* 83.4-9 (2006), pp. 1277–1279. DOI: 10.1016/j.mee.2006.01.195.

[141] Holger Becker. "It's the economy..." In: *Lab on a chip* 9.19 (2009), pp. 2759–62. DOI: 10.1039/b916505n.

[142] Andrew Kamholz. "Proliferation of microfluidics in literature and intellectual property". In: *Lab on a Chip* 4.2 (2004), 16N. DOI: 10.1039/b400810n.

[143] Swathi Murthy et al. "Fabrication of Nanostructures by Roll-to-Roll Extrusion Coating". In: *Advanced Engineering Materials* (2015). DOI: 10.1002/adem.201500347.

[144] John M. Stormonth-Darling and Nikolaj Gadegaard. "Injection Moulding Difficult Nanopatterns with Hybrid Polymer Inlays". In: *Macromolecular Materials and Engineering* 297.11 (2012), pp. 1075–1080. DOI: 10.1002/mame.201100397.

[145] Brendan Rockey. *Injection moulding scheme*. 2010. URL: https://commons.wikimedia.org/wiki/File:Principe{_}moulage{_}injection{_}polymere.svg (visited on 03/10/2016).

[146] Usama M. Attia, Silvia Marson, and Jeffrey R. Alcock. "Micro-injection moulding of polymer microfluidic devices". In: *Microfluidics and Nanofluidics* 7.1 (2009), pp. 1–28. DOI: 10.1007/s10404-009-0421-x.

[147] Michael J. Troughton. "Ultrasonic Welding". In: *Handbook of Plastics Joining - A Practical Guide*. 2nd ed. Boston: William Andrew Publishing, 2009. Chap. 2, pp. 15–35. ISBN: 9780815515814. DOI: 10.1016/B978-0-8155-1581-4.50004-4.

[148] Chia-Wen Tsao and Don L. DeVoe. "Bonding of thermoplastic polymer microfluidics". In: *Microfluidics and Nanofluidics* 6.1 (2008), pp. 1–16. DOI: 10.1007/s10404-008-0361-x.

[149] Yi Luo, Zongbo Zhang, Xiaodong Wang, and Yingsong Zheng. "Ultrasonic bonding for thermoplastic microfluidic devices without energy director". In: *Microelectronic Engineering* 87.11 (2010), pp. 2429–2436. DOI: 10.1016/j.mee.2010.04.020.

[150] Branson Ultrasonics. "Part Design for Ultrasonic Welding". In: *Technical Information PW-3*. Vol. 1. Emerson Industrial Automation, 1975.

[151] Henrik Bruus. "Governing equations". In: *Theoretical Microfluidics*. 1st. Chippenham, UK: Oxford University Press, 2008. Chap. 2, p. 19.

[152] Henrik Bruus. "Basic flow solutions". In: *Theoretical Microfluidics*. 1st. Chippenham, UK: Oxford University Press, 2008. Chap. 3, p. 37.

[153] Henrik Bruus. "Capillary effects". In: *Theoretical Microfluidics*. 1st. Chippenham, UK: Oxford University Press, 2008. Chap. 7, p. 123.

[154] P Atkins. *Atkins' physical chemistry*. 2006.

[155] Wikipedia. *Contact angle*. URL: https://upload.wikimedia.org/wikipedia/commons/e/e4/Contact{_}angle.svg (visited on 07/16/2015).

[156] Joost W van Honschoten, Nataliya Brunets, and Niels R Tas. "Capillarity at the nanoscale". In: *Chemical Society Reviews* 39.3 (2010), p. 1096. DOI: 10.1039/b909101g.

[157] Patrick Tabeling. *Introduction to microfluidics*. Oxford University Press, 2010.

[158] John W. M. Bush. *MIT Lecture Notes on Surface Tension*. 2004. URL: http://web.mit.edu/1.63/www/Lec-notes/Surfacetension/Lecture5.pdf (visited on 08/28/2015).

[159] ALFONSO M. GAÑÁN-CALVO. "Jetting–dripping transition of a liquid jet in a lower viscosity co-flowing immiscible liquid: the minimum flow rate in flow focusing". In: *Journal of Fluid Mechanics* 553.-1 (2006), p. 75. DOI: 10.1017/S0022112006009013.

[160] A S Utada, L.-Y. Chu, A. Fernandez-Nieves, D. R. Link, C. Holtze, and D. A. Weitz. "Dripping, Jetting, Drops, and Wetting: The Magic of Microfluidics". In: *MRS Bulletin* 32.09 (2007), pp. 702–708. DOI: 10.1557/mrs2007.145.

[161] Andrew Utada, Alberto Fernandez-Nieves, Howard Stone, and David Weitz. "Dripping to Jetting Transitions in Coflowing Liquid Streams". In: *Physical Review Letters* 99.9 (2007), p. 094502. DOI: 10.1103/PhysRevLett.99.094502.

[162] Pierre Guillot, Annie Colin, Andrew Utada, and Armand Ajdari. "Stability of a Jet in Confined Pressure-Driven Biphasic Flows at Low Reynolds Numbers". In: *Physical Review Letters* 99.10 (2007), pp. 1–4. DOI: 10.1103/PhysRevLett.99.104502.

[163] Carsten Cramer, Peter Fischer, and Erich J. Windhab. "Drop formation in a co-flowing ambient fluid". In: *Chemical Engineering Science* 59.15 (2004), pp. 3045–3058. DOI: 10.1016/j.ces.2004.04.006.

[164] Mads Jakob Jensen. "Numerical simulations of interface dynamics in microfluidics". PhD-thesis. Technical University of Denmark, 2005.

[165] Hsuan-Chung Wu, Huey-Jiuan Lin, and Weng-Sing Hwang. "A numerical study of the effect of operating parameters on drop formation in a squeeze mode inkjet device". In:

Modelling and Simulation in Materials Science and Engineering 13.1 (2005), pp. 17–34. DOI: 10.1088/0965-0393/13/1/002.

[166] DuPont. "Assembly Techniques - Category II Welding, Adhesive Bonding". In: *General Design Principles*. Chap. 10.

[167] Yi Sun, Jonas Høgberg, Thanner Christine, Laouenan Florian, Lisandro G Monsalve, Sonia Rodriguez, Cuong Cao, Anders Wolff, Jesus M Ruano-Lopez, and Dang Duong Bang. "Pre-storage of gelified reagents in a lab-on-a-foil system for rapid nucleic acid analysis". In: *Lab on a chip* (2013). DOI: 10.1039/c2lc41386h.

[168] J Parkhill et al. "The genome sequence of the food-borne pathogen Campylobacter jejuni reveals hypervariable sequences". In: *Nature* 403.6770 (2000), pp. 665–8. DOI: 10.1038/35001088.

[169] T R Tofteberg and E Andreassen. "Multiscale Simulation of Injection Molding of Parts with Low Aspect Ratio Microfeatures". In: *International Polymer Processing* 25.1 (2010), pp. 63–74. DOI: 10.3139/217.2318.

[170] Young Ho Kim, Inchul Yang, Young-Seuk Bae, and Sang-Ryoul Park. "Performance evaluation of thermal cyclers for PCR in a rapid cycling condition". In: *BioTechniques* 44.4 (2008), 495–6, 498, 500 passim. DOI: 10.2144/000112705.

[171] Ina Vandenbroucke, Herwig Van Marck, Peter Verhasselt, Kim Thys, Wendy Mostmans, Stéphanie Dumont, Veerle Van Eygen, Katrien Coen, Marianne Tuefferd, and Jeroen Aerssens. "Minor variant detection in amplicons using 454 massive parallel pyrosequencing: experiences and considerations for successful applications." In: *BioTechniques* 51.3 (2011), pp. 167–77. DOI: 10.2144/000113733.

[172] Elena Miotto, Elena Saccenti, Laura Lupini, Elisa Callegari, Massimo Negrini, and Manuela Ferracin. "Quantification of Circulating miRNAs by Droplet Digital PCR: Comparison of EvaGreen- and TaqMan-Based Chemistries". In: *Cancer Epidemiology Biomarkers & Prevention* 23.12 (2014), pp. 2638–2642. DOI: 10.1158/1055-9965.EPI-14-0503.

[173] Yann Karlen, Alan McNair, Sébastien Perseguers, Christian Mazza, and Nicolas Mermod. "Statistical significance of quantitative PCR". In: *BMC bioinformatics* 8 (2007), p. 131. DOI: 10.1186/1471-2105-8-131.

[174] Linas Mazutis, Jean-Christophe Baret, Patrick Treacy, Yousr Skhiri, Ali Fallah Araghi, Michael Ryckelynck, Valérie Taly, and Andrew D Griffiths. "Multi-step microfluidic droplet processing: kinetic analysis of an in vitro translated enzyme". In: *Lab on a chip* 9.20 (2009), pp. 2902–8. DOI: 10.1039/b907753g.

[175] Jenifer Clausell-Tormos et al. "Droplet-based microfluidic platforms for the encapsulation and screening of Mammalian cells and multicellular organisms". In: *Chemistry & biology* 15.5 (2008), pp. 427–37. DOI: 10.1016/j.chembiol.2008.04.004.

[176] Kevin A Heyries, Carolina Tropini, Michael Vaninsberghe, Callum Doolin, Oleh I Petriv, Anupam Singhal, Kaston Leung, Curtis B Hughesman, and Carl L Hansen. "Megapixel digital PCR". In: *Nature methods* 8.8 (2011), pp. 649–51. DOI: 10.1038/nmeth.1640.

[177] Fangyuan Chen, Yihong Zhan, Tao Geng, Hongzhen Lian, Peisheng Xu, and Chang Lu. "Chemical transfection of cells in picoliter aqueous droplets in fluorocarbon oil". In: *Analytical chemistry* 83.22 (2011), pp. 8816–20. DOI: 10.1021/ac2022794.

[178] Jung-uk Shim, Rohan T Ranasinghe, Clive A Smith, Shehu M Ibrahim, Florian Hollfelder, Wilhelm T S Huck, David Klenerman, and Chris Abell. "Ultrarapid generation of femtoliter microfluidic droplets for single-molecule-counting immunoassays". In: *ACS nano* 7.7 (2013), pp. 5955–64. DOI: 10.1021/nn401661d.

[179] Jean-Christophe Baret, Felix Kleinschmidt, Abdeslam El Harrak, and Andrew D Griffiths. "Kinetic aspects of emulsion stabilization by surfactants: a microfluidic analysis". In: *Langmuir : the ACS journal of surfaces and colloids* 25.11 (2009), pp. 6088–93. DOI: 10.1021/la9000472.

[180] Manhee Lee, Jesse W Collins, Donald M Aubrecht, Ralph a Sperling, Laura Solomon, Jong-Wook Ha, Gi-Ra Yi, David a Weitz, and Vinothan N Manoharan. "Synchronized reinjection and coalescence of droplets in microfluidics". In: *Lab on a chip* 1 (2013). DOI: 10.1039/c3lc51214b.

[181] Haakan N Joensson, Mathias Uhlén, and Helene Andersson Svahn. "Droplet size based separation by deterministic lateral displacement-separating droplets by cell–induced shrinking". In: *Lab on a chip* 11.7 (2011), pp. 1305–10. DOI: 10.1039/c0lc00688b.

[182] Christian H J Schmitz, Amy C Rowat, Sarah Köster, and David A Weitz. "Dropspots: a picoliter array in a microfluidic device". In: *Lab on a chip* 9.1 (2009), pp. 44–9. DOI: 10.1039/b809670h.

[183] Zhenning Cao, Fangyuan Chen, Ning Bao, Huacheng He, Peisheng Xu, Saikat Jana, Sunghwan Jung, Hongzhen Lian, and Chang Lu. "Droplet sorting based on the number of encapsulated particles using a solenoid valve". In: *Lab on a chip* 13.1 (2013), pp. 171–8. DOI: 10.1039/c2lc40950j.

[184] M'Hamed Ali Hamza, Guy Serratrice, Marie Jose Stebe, and Jean-Jacques Delpuech. "Solute-solvent interactions in perfluorocarbon solutions of oxygen. An NMR study". In: *Journal of the American Chemical Society* 103.13 (1981), pp. 3733–3738. DOI: 10.1021/ja00403a020.

[185] Wenming Wu, Kyung-Tae Kang, and Nae Yoon Lee. "Bubble-free on-chip continuous-flow polymerase chain reaction: concept and application". In: *The Analyst* 136 (2011), pp. 2287–2293. DOI: 10.1039/c0an01034k.

[186] G M F Wallace and P H Brown. "Horse rug lung: toxic pneumonitis due to fluorocarbon inhalation." In: *Occupational and environmental medicine* 62.6 (2005), pp. 414–6. DOI: 10.1136/oem.2004.015784.

[187] C J Johnston, J N Finkelstein, P Mercer, N Corson, R Gelein, and G Oberdörster. "Pulmonary effects induced by ultrafine PTFE particles." In: *Toxicology and applied pharmacology* 168.3 (2000), pp. 208–15. DOI: 10.1006/taap.2000.9037.

[188] Masakatsu Sakata, Hisashi Kazama, Akemi Miki, Akiko Yoshida, Masanobu Haga, and Masahiko Morita. "Acute toxicity of fluorocarbon-22: Toxic symptoms, lethal concentration, and its fate in rabbit and mouse". In: *Toxicology and Applied Pharmacology* 59.1 (1981), pp. 64–70. DOI: 10.1016/0041-008X(81)90453-1.

[189] Yi Sun, Than Linh Quyen, Tran Quang Hung, Wai Hoe Chin, Anders Wolff, and Dang Duong Bang. "A lab-on-a-chip system with integrated sample preparation and loop-mediated isothermal amplification for rapid and quantitative detection of Salmonella spp. in food samples". In: *Lab Chip* 15.8 (2015), pp. 1898–1904. DOI: 10.1039/C4LC01459F.

[190] Stephan Brüning, Gerald Jenke, Keming Du, and Arnold Gillner. "High Precision Laser Processing of Steel Surfaces with Sub-ns-lasers". In: *Physics Procedia* 56.0 (2014), pp. 919–926. DOI: 10.1016/j.phpro.2014.08.111.

[191] LPKF LaserWelding. *Plastic Joining : Process Comparison How Laser Plastic Welding Stacks Up to the Competition*. 2011. URL: http://www.laserplasticwelding.com/process{_}comparison{_}laser{_}plastic{_}welding{_}versus{_}the{_}competition.pdf (visited on 03/03/2016).

[192] Miranda Marcus. *Aesthetic Assembly - The Art to Attractive Bonding*. 2016. URL: http://www.dukane.com/us/WP{_}AestheticAssembly.htm (visited on 03/03/2016).

[193] Mike Johnston. *Choosing the Right Welding Process*. 2005. URL: http://www.mddionline.com/article/choosing-right-welding-process (visited on 03/03/2016).

[194] Alex Avdeef. "pH-metric log P. II: Refinement of partition coefficients and lonization constants of multiprotic substances". In: *Journal of pharmaceutical sciences* 82.2 (1993), pp. 183–190. DOI: 10.1002/jps.260082021.

[195] A Berthod and S Carda-Broch. "Determination of liquid–liquid partition coefficients by separation methods". In: *Journal of Chromatography A* 1037.1-2 (2004), pp. 3–14. DOI: 10.1016/j.chroma.2004.01.001.

[196] OECD. *OECD Guidelines for the Testing of Chemicals*. 1994. URL: http://scholar.google.com/scholar?hl=en{\&}btnG=Search{\&}q=intitle:OECD+GUIDELINES+FOR+THE+TESTING+OF+CHEMICALS{\#}0 (visited on 09/02/2014).

[197] D. C. Venerus, S.-H. Zhu, and H. C. Ottinger. "Stress and birefringence measurements during the uniaxial elongation of polystyrene melts". In: *Journal of Rheology* 43.3 (1999), p. 795. DOI: 10.1122/1.551004.

[198] BIO-RAD. *Digital PCR*. URL: http://www.bio-rad.com/en-dk/applications-technologies/digital-pcr (visited on 01/27/2014).

[199] Valérie Taly, Deniz Pekin, Abdel El Abed, and Pierre Laurent-Puig. "Detecting biomarkers with microdroplet technology". In: *Trends in molecular medicine* 18.7 (2012), pp. 405–16. DOI: 10.1016/j.molmed.2012.05.001.

[200] PB Umbanhowar, V Prasad, and DA Weitz. "Monodisperse emulsion generation via drop break off in a coflowing stream". In: *Langmuir* 4 (2000), pp. 347–351.

[201] Craig Priest, Stephan Herminghaus, and Ralf Seemann. "Generation of monodisperse gel emulsions in a microfluidic device". In: *Applied Physics Letters* 88.2 (2006), p. 024106. DOI: 10.1063/1.2164393.

[202] Isao Kobayashi, Sayumi Hirose, Takanori Katoh, Yanping Zhang, Kunihiko Uemura, and Mitsutoshi Nakajima. "High-aspect-ratio through-hole array microfabricated in a PMMA plate for monodisperse emulsion production". In: *Microsystem Technologies* 14.9-11 (2008), pp. 1349–1357. DOI: 10.1007/s00542-007-0526-7.

[203] Venkatachalam Chokkalingam, Stephan Herminghaus, and Ralf Seemann. "Self-synchronizing pairwise production of monodisperse droplets by microfluidic step emulsification". In: *Applied Physics Letters* 93.25 (2008), p. 254101. DOI: 10.1063/1.3050461.

[204] Keng-Shiang Huang, Ming-Kai Liu, Chun-Han Wu, Yu-Tang Yen, and Yu-Cheng Lin. "Calcium alginate microcapsule generation on a microfluidic system fabricated using the optical disk process". In: *Journal of Micromechanics and Microengineering* 17.8 (2007), pp. 1428–1434. DOI: 10.1088/0960-1317/17/8/003.

[205] A Huebner, M Srisa-Art, D Holt, C Abell, F Hollfelder, Andrew J DeMello, and J B Edel. "Quantitative detection of protein expression in single cells using droplet microfluidics". In: *Chemical communications (Cambridge, England)* 2.12 (2007), pp. 1218–20. DOI: 10.1039/b618570c.

[206] Churchill Eisenhart and PW Wilson. "Statistical methods and control in bacteriology". In: *Bacteriological Reviews* 68 (1943).

[207] Ashleigh B Theberge, Fabienne Courtois, Yolanda Schaerli, Martin Fischlechner, Chris Abell, Florian Hollfelder, and Wilhelm T S Huck. "Microdroplets in microflu-

idics: an evolving platform for discoveries in chemistry and biology". In: *Angewandte Chemie* 49.34 (2010), pp. 5846–68. DOI: 10.1002/anie.200906653.

[208] Andrew C Hatch, Jeffrey S Fisher, Stephen L Pentoney, David L Yang, and Abraham P Lee. "Tunable 3D droplet self-assembly for ultra-high-density digital micro-reactor arrays." In: *Lab on a chip* 11.15 (2011), pp. 2509–17. DOI: 10.1039/c0lc00553c.

[209] Andrew D Griffiths and Dan S Tawfik. "Miniaturising the laboratory in emulsion droplets". In: *Trends in biotechnology* 24.9 (2006), pp. 395–402. DOI: 10.1016/j.tibtech.2006.06.009.

[210] Zida Li, Sze Yi Mak, Alban Sauret, and Ho Cheung Shum. "Syringe-pump-induced fluctuation in all-aqueous microfluidic system implications for flow rate accuracy." In: *Lab on a chip* 14.4 (2014), pp. 744–9. DOI: 10.1039/c3lc51176f.

[211] Shengqing Xu, Zhihong Nie, Minseok Seo, Patrick Lewis, Eugenia Kumacheva, Howard a. Stone, Piotr Garstecki, Douglas B. Weibel, Irina Gitlin, and George M. Whitesides. "Generation of Monodisperse Particles by Using Microfluidics: Control over Size, Shape, and Composition". In: *Angewandte Chemie* 117.5 (2005), pp. 734–738. DOI: 10.1002/ange.200462226.

[212] T. G. Mason and J. Bibette. "Shear Rupturing of Droplets in Complex Fluids". In: *Langmuir* 13.17 (1997), pp. 4600–4613. DOI: 10.1021/la9700580.

[213] B. E. Shapiro. *Table of Integrals*. 2004. URL: http://integral-table.com/ (visited on 03/18/2016).

[214] Suzanne Weaver, Simant Dube, Alain Mir, Jian Qin, Gang Sun, Ramesh Ramakrishnan, Robert C Jones, and Kenneth J Livak. "Taking qPCR to a higher level: Analysis of CNV reveals the power of high throughput qPCR to enhance quantitative resolution". In: *Methods* 50.4 (2010), pp. 271–6. DOI: 10.1016/j.ymeth.2010.01.003.

[215] T Notomi. "Loop-mediated isothermal amplification of DNA". In: *Nucleic Acids Research* 28.12 (2000), 63e–63. DOI: 10.1093/nar/28.12.e63.

[216] K. Nagamine, T. Hase, and T. Notomi. "Accelerated reaction by loop-mediated isothermal amplification using loop primers". In: *Molecular and Cellular Probes* 16.3 (2002), pp. 223–229. DOI: 10.1006/mcpr.2002.0415.

[217] Fabienne Courtois, Luis F Olguin, Graeme Whyte, Ashleigh B Theberge, Wilhelm T S Huck, Florian Hollfelder, and Chris Abell. "Controlling the retention of small molecules in emulsion microdroplets for use in cell-based assays". In: *Analytical chemistry* 81.8 (2009), pp. 3008–16. DOI: 10.1021/ac802658n.

[218] Norihiro Tomita, Yasuyoshi Mori, Hidetoshi Kanda, and Tsugunori Notomi. "Loop-mediated isothermal amplification (LAMP) of gene sequences and simple visual detection of products." In: *Nature protocols* 3.5 (2008), pp. 877–82. DOI: 10.1038/nprot.2008.57.

A

TransForm-Technologies

To pursue the oppotunity of turning the mould structuring method presented in Paper 3 into a company, two rounds of spin out funding was raised:

- 475,000 DKK from DTU PoC
- 250,000 DKK from Copenhagen Spin Outs

The funding was spent on investigating the commercial feasibility of the micro structuring technology for producing energy directors for ultrasonic welding (Chapter C on page C1) and superhydrophobic polymer pieces (Chapter D on page D1). This was done in collaboration with external commercial partners under a non-disclosure agreement and cannot be disclosed in this thesis. However, I would like to include a section of the business plan[a] to summarise the different business models which may be combined to generate revenue:

TransForm business model

With the technology and know-how owned by TransForm, there are a number of alternatives for developing the business and addressing the market. The list of products that could be offered include:

- Consultancy: High-value consultancy specialised in micro component fabrication, structural NES implementation, and ultrasonic welding.
- Tool shop: A tool shop service includes laser patterning of injection molding tools aimed at plastic component manufacturers and tool makers.
- Licensing: Providing royalty-based TransForm technology licenses to major plastic component producers
- Components: Produce and sell high-value plastic components with specific functionality based on the TransForm surfaces as sub-supplier to system providers.

In Table A.1, the four Business Model alternatives are assessed in terms of capital requirements for establishing the business, scalability of the business, the market potential of the business and ease of market entry. In general, the most optimal business

[a] The business plan was prepared in collaboration with business developer Torsten Freltoft, FrelTec.

Table A.1: Overview of the four Business Models.

Business model	**Capital Requirements**	**Scalability**	**Market potential**	**Ease of market access**
1. Consultancy	Low	Low	$100 thousands	Easy
2. Tool shop	Low/Medium	Low	$100 thousands	Medium
3. Licensing	Low	High	$10 million	Difficult
4. Components	High	Medium	$10 million	Difficult

would be one requiring low capital investments, high scalability, large market potential and easy market access.

As an early start-up, Business Model 4: Components is not very feasible due to the high capital requirements. At the same time, the only model with high scalability is Business Model 3: Licensing, although the initial market access here is considered quite difficult. The reason for the difficult market access for the licensing model is that the technology is new and largely unknown.

However, a strategy to gain access to the licensing market would be to combine Business Model 1, 2 and 3 by offering focused consultancy and tool shop services to potential licensees. As the technology becomes more and more established, the consultancy business would decrease, while tool shop services potentially could be scaled based on e.g. a franchise model. In any case, the plastic component producer using the technology in his molding tools would pay a royalty per component molded to TransForm.

Partnership: Before this strategy can be initiated, the technology would need to reach Proof of Market, i.e. that at least one application of the technology has been successfully implemented in a real product.

Commercialisation Road Map & short term action plan

In order to fully evaluate the potential for the TransForm technology, a number of technological questions have to be addressed. These questions relate to features like chemical and physical durability of the functional surfaces produced and how these features e.g. depend on the choice of polymer. Further, in order to implement the first commercial application, quite some work needs to be done. As has already been initiated, this work should be conducted in close collaboration with potential customers for the technology. Amongst the most promising candidates are the hearing aid industry.

It is unlikely that external investors are willing to fund the Feasibility phase. At the same time, revenue generation in this phase is expected to be non-existent or very modest. However, due to the significant interest shown by industrial collaboration partners, the first commercial implementation may not require many resources to accomplish.

The two TransForm entrepreneurs are both completing their PhD degrees during the summer of 2016 and will be able to continue the feasibility process at some level during this process. It is thus recommended to apply for additional Proof of Concept funding for a 3-4-month period in the fall of 2016 with the specific goal of securing the first commercial implementation while at the same time attracting seed funding for the continued commercialization process (Phase 2). The phases of the commercialization road map for TransForm-Technologies are illustrated in Figure A.1.

The goal would then be to close the seed financing as well as an IP licensing agreement with DTU by the end of 2016.

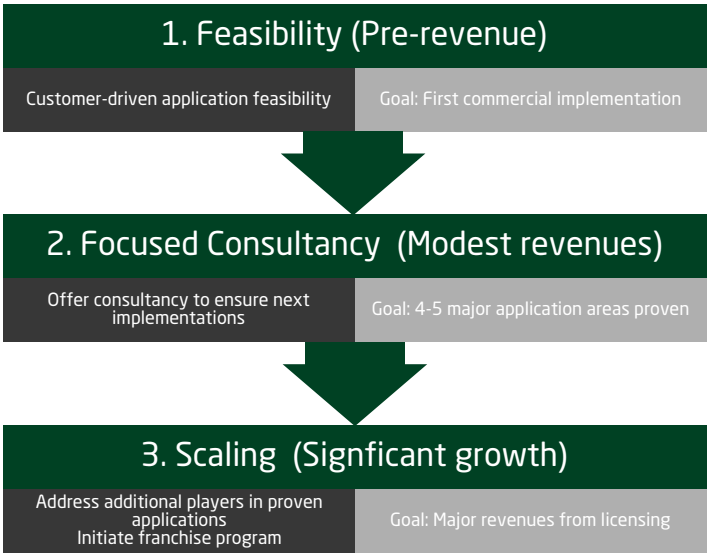

Figure A.1: Proposed commercialization road map for TransForm-Technologies. This figure was originally produced by Torsten Freltoft, Freltec, and Birgit O'Sullivan, O'Sullivan Consulting.

This is page A4:
For typesetting reasons, it has intentionally been left completely blank.

B

Patent application 1: Microstructured tool

Prior to publishing the mould structuring method presented in Paper 3, three patent applications were submitted to the European Patent Office (EPO):

1. Replication tool and method of providing a replication tool.
2. Micro-scale energy directors for ultrasonic welding.
3. Method of producing an item with enhanced wetting properties by fast replication and replication tool used in the method.

Remarks

This patent application describes the method of introducing the microphase explosions in the tool, and the characteristics of the tool. To summarise: What separates our method from other laser ablation methods is that multiple microphase explosions happen simultaneously, and this parallelisation makes our method faster than conventional direct-writing. The microphase explosions happen randomly, which means that the formed craters lateral position is random (contrary to direct-writing). To prove that our method is operating with random crater formation, I (after a fruitful discussion with Henrik Flyvbjerg of DTU Nanotech) showed that the lateral spacing between randomly placed (uniform probability distribution) events was exponentially distributed. This is described in Section B.1.2 and in Drawing 10.

This method patent application is cited in (device) patent applications 2 and 3.

The content, points, argumentation and figures of patent application one through three were drafted by me, and the text was written into ”patent language” by patent attorney Oliver Kuhn from Guardian IP, Kgs. Lyngby.

B.1 Replication tool and method of providing a replication tool

The present invention relates in one aspect to a replication tool and in a further aspect to a method of providing the replication tool. In a yet further aspect, the present invention relates to a method of producing a part by replication, using the replication tool.

B.1.1 Background of the invention

Producing items at industrial scales often involves replicating such items by replication techniques involving the transfer of a shape from a master tool to a mouldable material. Examples for such replication techniques include e.g. moulding techniques for producing large numbers of discrete items, or roll-to-roll techniques for high volume processing of material into continuous webs. The tools used for replication techniques have to have highly wear resistant and precise tool surfaces, and are therefore costly to produce. In return, the high volume production allows for a very low unit price of the produced items.

While such items can be produced at low cost, high value may be added by adapting these items for innovative uses. Such innovative uses typically involve or even inevitably require a functionalization of the surface One kind of functionalization involves providing the surface of the replicated items or produced materials with a particular finish, for example a microscale texture roughening.

However, known technologies for adding a microscale roughening typically involve expensive additional processing of the item after the replication step, thereby adding to the cost of the item, which in some cases is prohibitive to the commercial exploitation of such innovative improvements.

Therefore, there is a need for improved techniques for the cost-effective fabrication of replicated items with functionalized surfaces, more particular for the cost-effective production of replicated items with a microscale roughened surface. Furthermore, there is a need for suitable tooling for use in the fabrication of replicated items with microscale roughened surfaces. Furthermore, there is a need for a fast and reliable process for providing such suitable tooling.

B.1.2 Summary of the invention

A first aspect of the invention relates to a method of providing a replication tool, the method comprising providing a forming tool having a tool surface adapted to define a general shape of a part to be formed; modifying at least portions of the tool surface by a pulsed laser treatment to obtain a microscale structured master surface with a lateral master pattern and a vertical master profile; wherein the pulsed laser treatment is adapted to generate microscale phase explosions on the tool surface, thereby forming the microscale structured master surface as a lateral arrangement of microscale crater-shaped depressions. The crater-shaped depressions obtained by the microscale phase explosions are irregular in shape and

polydisperse, i.e. varying in size with a spread about a most prominent size. The size may e.g. be characterized by the area covered by the depression as seen in a vertical projection on a lateral plane.

The microscale structuring of the tool surface is provided by the localized application of laser pulses directly to selected portions of the tool surface. This post-treatment of the tool surface by means of localized laser treatment has the advantage that the replication tool with the shape defining tool surface may be designed and produced using existing techniques and equipment for tool making, thereby contributing to a relatively simple and cost effective implementation of the surface modification in an existing fabrication process.

At the targeted portion of the tool surface, the localized pulsed laser treatment is adapted to melt and evaporate material at the tool surface to generate microscale phase explosions, thereby producing a randomised surface structure of polydisperse microscale features. The microscale surface features are depressions, which are typically crater shaped with steeply sloped side walls. The process of provoking microscale phase explosions by locally applying laser energy to the tool surface so as to form the crater-shaped depressions is stochastic in nature, wherein upon appropriate exposure the microscale surface features are densely packed and may even partially overlap, thereby forming a microscale lateral pattern with a microscale porous appearance. The localized application of laser power may be scanning a laser spot along a predetermined scanning path at a pre-determined scan speed over the tool surface. The path may follow a single scan along the path over the tool surface, a repetitive scanning along the same linear path, or a combination of both. The path is adapted to cover the selected portions of the tool surface. The path may e.g. be straight, curved, meandering, segmented or a combination thereof and some sections of the path may overlap other sections of the path in order to achieve an even exposure of the selected portions of the tool surface with laser energy.

The pulsed laser radiation has to be of a wave length and pulse characteristics that is absorbed by the tool surface in order to be able to locally melt and evaporate material from the tool surface so as to produce microscale phase explosions creating the crater-shaped depressions. For example, the laser radiation may be from a picosecond-laser source with a wavelength in the near infrared, such as 1064 nm, but other wavelength ranges, e.g. in the visible part of the electromagnetic spectrum, and pulse characteristics that are suitable for locally heating the tool surface to generate microscale phase-explosions may be conceived, too. The finish of the targeted portions of the tool surface is controlled by adapting the exposure of these tool surface portions with the pulsed laser radiation. The exposure of the tool surface is controllable e.g. by adjusting the laser power/spot intensity and/or by varying the scan speed, wherein exposure of a given surface portion increases with increasing laser power, but decreases with increasing scan speed. The finish of the targeted portions of the tool in turn determines the finish of the replicated part in the corresponding regions on the surface of the part via the replication process. Furthermore, multiple exposures of the same surface portions, e.g. by repetitive and/or overlapping scanning of the laser spot over these surface portions, results in an exposure that is increased correspondingly.

As mentioned above, the formation of crater-shaped microscale features by the microscale phase explosions of the laser-based modification process according to the present invention is random in nature and may best be described as a *Poisson*-process where the microscale phase explosions occur in a stochastic manner. The stochastic nature of the structure formation is best seen in the resulting surface structure, where a spatial distribution of the microscale

structures over the surface follows a *Poisson* distribution function.

As a further consequence of the stochastic nature of the laser-modification process, a surprisingly evenly distributed random appearance is observed. The porous appearance best resembles a roughness, rather than a periodic patterning, as would be the case e.g. in prior art techniques of sequential ablation of individual features using so-called femtosecond lasers with a pulse-length of 1ps or below. Instead, the surface finish according to the present invention is formed by stochastically distributed polydisperse microscale features (crater-shaped depressions) with no apparent trace of individual lines or stitching effects, despite the exposure by scanning along a path and/or along repetitive path segments. The surprising uniformity of the randomized micro-structuring makes this technique particularly well suited for preparing a tool with a microscale structured master surface adapted for replicating items with a microscale roughened surface finish applied to a larger surface area. In addition thereto, the present technique is considerably faster than any sequential writing technique where nano and microscale features are formed one by one, and therefore allows for modifying relatively large tool surface areas in an efficient manner.

Preferably, the lateral pattern of the microscale structured master surface has an area density of microscale master features of at least $5000/\text{mm}^2$. Thereby, a reasonably densely packed lateral distribution of microscale features on the master surface is achieved.

Further preferably, the lateral pattern of the microscale structured master surface has an area density of microscale master features of at least $8000/\text{mm}^2$, or even of at least $10000/\text{mm}^2$. Thereby, an even more densely packed lateral distribution of microscale features on the master surface is achieved.

It should be noted, however, that an upper limit for the area density resulting from the microscale of the surface structuring exists, which is discussed in detail further below.

An important advantage of the laser-based tool-modification technique according to the invention is that it facilitates the commercially viable implementation of microscale roughened surfaces for innovative uses. One innovative use of microscale roughening of the surface of replicated items includes the formation of ultrasonic welding flanges with integrated energy directors. The ultrasonic welding flanges are shaped as regions covered with densely packed polydisperse microscale cone-like projections. As disclosed in a parallel application by the same inventors, when using such micro-textured flanges, ultrasonic welding seams with astonishing precision and surprising bonding strength can be obtained. Another innovative use of a microscale surface roughening on replicated items is the enhancement of wetting properties, such as rendering a surface of a hydrophobic material superhydrophobic, or enhancing a hydrophilic surface so it becomes superhydrophilic. As also disclosed in a parallel application by the same inventors, this can be achieved in the same step as the shaping/forming of the replicated item by using a laser modified replication tool.

As mentioned above, the laser treatment of the tool surface results in a porous surface appearance produced by a randomised lateral arrangement of, preferably densely packed, microscale depressions, which are typically shaped as relatively deep, steep-walled craters with a more or less pointed bottom. The sloped sidewalls facilitate an easy demoulding of a replicated item in the step of releasing the item from the tool surface.

Since the method is useful for the production of items by a fast replication process, it allows

for a low-cost and/or mass production of the items. A replication process may be considered fast, for example, if the replication period from contacting the tool surface with the molten replication material to releasing the formed part is short, such as well below ten minutes, such as less than five minutes, such as less than 3 minutes, such as less than one minute, such as less than 30 seconds, or even less than 10 seconds. In particular, the suggested thermally controlled replication process using a thermoplastic replication material can be performed fast as compared to for example replication processes using thermosetting replication materials, or chemically setting replication materials. However, the method is also useful for the production of items with a microscale surface texturing thereon by other replication techniques, such as the mentioned slower methods using thermosetting or chemically setting replication materials, or for replication techniques like compression moulding and hot embossing.

The term microscale refers to dimensions of about 1 μm to 1000 μm that are generally measured in microns (micrometres), typically in the range of about 1 μm to 100 μm. Accordingly, the term nanoscale refers to dimensions of about 1 nm to 1000 nm that are generally measured in nanometres, typically in the range of about 1 nm to 100 nm.

The microscale structure of the master surface and, accordingly, the microscale texture of the replica surface have a three-dimensional topography of microscale elements arranged next to each other and may be decomposed in a lateral pattern and a vertical profile. The term ”lateral pattern” refers to the arrangement in lateral directions of the (3D) microscale elements making up the microscale structure/texture, as seen in vertical projection on to a lateral plane. The term ”vertical profile” refers to the variation of the location of the surface in a direction perpendicular to the lateral directions.

When a surface structuring/texturing is applied to an object having a general shape, such as a tool surface or an item, the surface structuring/texturing can be seen as a vertical variation of the surface, which is added to the general shape of the tool surface/item. Accordingly, on an object with a microscale structured/textured surface, an average surface that flattens out any vertical variations of the surface by averaging on a lateral scale larger than that of the microscale structuring/texturing essentially follows the general shape of the object. The general shape of the object is thus defined independent of any nano- or microscale surface roughness / finish / structuring. At a given point on the surface of the object, lateral directions are parallel / tangential to a surface defining the general shape of the object on a scale larger than the scale of the lateral pattern. Accordingly, the vertical direction at a given point on the surface of the object is the surface normal to the general shape in that point. In each given point, the vertical direction is perpendicular to the corresponding lateral directions.

The general shape of the replicated part is defined by the general shape of the tool surface. The replication process is for accurately replicating the general shape of the part as defined by the tool surface. The surface of the replicated part is functionalised by applying a surface finish with a microscale texture at least on selected regions of the surface of the part. For example, the particular functionalization may be to make a flange portion of the replicated part susceptible to concentrate ultrasonic energy so as to act as a distributed energy director when forming an ultrasonic joint with a cooperating flange portion of a counterpart. To concentrate the ultrasonic energy applied across the interface between the first and second flange portions, the area of contact is reduced to point contacts where the tops of the protrusions meet the surface of the counterpart when the first flange portion is brought in contact with the cooperating second flange portion.

An important advantage of the present method is that the laser treatment of the tool surface is only limited by the requirement of an optical access to the surface to be modified. Consequently, a microscale structured master surface may be applied to virtually any surface topology, including very narrow and deep trenches or holes, as long as a laser beam can be guided to the tool surface to be modified. This allows for an improved freedom for designing the parts to be replicated. Furthermore, at the choice of the designer, the microscale protrusions of the replicated item may be distributed over the entire surface of the replicated parts or only to selected regions thereof. Also, the exposed portion may be arbitrarily shaped as seen in the lateral direction, e.g. the exposed portion may easily be adapted to cover larger surfaces. The microscale features may even be arranged on curved and/or oblique surfaces following a more complex general shape of the replicated part, thereby adding to the abovementioned improved freedom of design.

According to some embodiments, the method comprises the steps of (a) providing a replication tool having a tool surface adapted to define a general shape of the first part, wherein the tool surface comprises a microscale structured master surface obtained by localized pulsed laser treatment of the tool surface to generate microscale phase explosions, said microscale structured master surface having a lateral master pattern and a vertical master profile; (b) contacting the tool surface with a replication material in the melt phase, wherein the tool surface is maintained at a process temperature below a melt temperature of the replication material, thereby (c) cooling the replication material to a stabilized shape with a microscale textured replica surface, wherein the lateral master pattern defines a corresponding lateral replica pattern of the microscale textured replica surface and wherein the amplitude of a vertical profile of the microscale textured replica surface is in the microscale, and (d) releasing the shaped item from the tool surface.

A replication process, where the tool surface is maintained at a more or less constant temperature below the melt temperature throughout the production process is sometimes referred to as an "isothermal" type process. Isothermal processes may be performed at high throughput. As also mentioned above, the truthfulness of the replication of the vertical profile of the microscale master structure is uncritical as long as the peak-to-peak amplitude of the vertical profile of the microtexture on the replica surface is sufficient, and further preferably the lateral pattern is faithfully transferred.

Alternatively, e.g. in a so-called variothermal injection moulding process, the microscale structured master surface is prior to contact with the replication material heated to an injection temperature above the melting temperature of the replication material, but immediately upon injection of the replication material rapidly cooled to a temperature below the melting temperature of the replication material, at which the first part is finally released from the mould.

Further according to some embodiments the replication process is one of injection moulding, hot embossing, compression moulding, and extrusion coating.

Further according to one embodiment of the method, the microscale textured replica surface has a peak-to-peak amplitude of at least 0.1 μm, or at least 0.3 μm, or at least 0.5 μm, or at least 1 μm and up to 5 μm, or up to 10 μm, or even up to 30 μm. Note that the part/item may be made entirely from replication material with a shape defined by the tool surface, or the replication material may be applied to/carried by a substrate material, e.g. in an additive moulding step or a coating step.

Further according to one embodiment of the method, the replication process used for producing the part is injection moulding. Injection moulding is a cyclic replication process with a fast cycle time, i.e. using this embodiment a large number of separate items with a microscale textured replica surface may be produced at high throughput. The inner surface of the injection mould is the tool surface defining the general shape of the part. At least portions of the tool surface have a finish with a microscale structuring generated by localised treatment with a pulsed laser source. The thermoplastic replication material is heated to above the melt transition temperature and in the melt phase injected into the closed mould, which is kept at a temperature between the glass transition temperature and the melt transition temperature of the replication material. When the molten replication material contacts the cooled tool surface it solidifies, whereby it is shaped and textured, before the item is released from the mould.

In another particularly advantageous embodiment of the method, the replication process is extrusion coating. Extrusion coating is a process for rolltoroll processing, i.e. using this embodiment the part may be produced in a continuous process as a layered web with a microscale textured replica surface. To that end, a substrate web may be passed between a nib roll and a cooling roll, in a conventional manner, wherein the rotary surface of the cooling roll is the tool surface defining the general shape of the item. The tool surface has a finish with a microscale structuring generated by treatment with a pulsed laser source. A thermoplastic replication material is heated to above the melting temperature and in the melt phase supplied between the substrate web and the cooling roll, which is kept at a temperature below the melting temperature of the replication material. When the molten replication material contacts the cooled tool surface it solidifies, whereby it is shaped and textured, before the item is released from the replication tool.

Further according to one embodiment of the method for producing a part with microscale energy directors on flange portions thereof, a replication period from contacting the tool surface with the molten replication material to releasing the shaped item is less than 3 minutes, such as less than one minute, such as less than 30 seconds, or even less than 10 seconds. Typically, in an injection moulding process, the replication time may be less than one minute, i.e. a few tens of seconds, such as about 30 seconds. Typically, an extrusion coating process is even faster with replication times of less than 10 seconds.

In a further aspect, a method for producing a part with microscale energy directors on flange portions thereof comprises preparing a replication tool using the abovementioned method, and repeatedly performing the method of producing an item with a microscale textured replica surface by a replication process according to any one of the abovementioned embodiments. Large numbers of items exhibiting enhanced hydrophobicity or superhydrophobicity may thus be produced cheaply.

According to a further aspect, the invention relates to a part with a microscale textured replica surface produced by replication according to any of the abovementioned methods.

A further aspect of the invention relates to a replication tool for producing a part with a microscale textured replica surface by replication, the replication tool comprising a tool surface defining a general shape of the part, the tool surface comprising at least on portions thereof a microscale structured master surface having a lateral master pattern and a vertical master profile, wherein said microscale structured master surface has been provided by localized pulsed laser treatment adapted to generate microscale phase explosions.

Preferably, the vertical master profile has a peak-to-peak amplitude of at least 0.5 μm

Preferably, the lateral master pattern has an area density of microscale master features of at least 5000/mm^2.

The replication tool for the replication process in question, e.g. a mould for injection moulding or a roller for extrusion coating, has a tool surface defining the general shape of the part to be formed and may be provided in a conventional manner and using conventional tooling materials as known in the art, such as tool steel or 2017 aluminium. The microscale surface structuring is applied as a post treatment of the tool surface by means of a pulsed laser directly scanned over the tool surface. A suitable pulsed laser may be, but is not limited to, an industrial picosecondlaser operating in the near infrared, such as at 1064 nm. The exposure of the surface to the pulsed laser radiation is adapted to generate microscale phase explosions. This includes localised melting of tool material on the tool surface, evaporating molten tool material, and ejecting molten and evaporated material in microscale eruptions from the melt surface, thereby forming a densely packed arrangement of microscale crater shaped depressions. The localized pulsed laser treatment is adapted to produce a micro porous structure, wherein the micro porous structure is formed by a densely packed, randomly distributed arrangement of crater shaped microscale depressions with outwardly sloped side walls. The obtained microscale structured master surface has a lateral master pattern and a vertical master profile as described above. The occurrence of the microscale phase explosions on the surface under the laser processing according to the invention is stochastic (random and uncorrelated) and may be described by a *Poisson* process. The microscale crater shaped depressions resulting from that process are randomly distributed over the processed surface. By randomly distributed it is understood that the lateral location of the of the microscale features as they occur in the lateral master pattern on the tool surface is a random (and accordingly the replicated microscale features produced from that master), wherein the occurrence of observed spacing between adjacent microscale features follows a distribution function that is exponentially decaying for increasing distances. Since the post treatment applied here does not require the precise micro milling of a specific predetermined shape of the master structure, such as a regular array of micro cones, the post treatment may be applied using cheaper equipment. Furthermore, this post treatment adapted to generate a microscale porous surface from microscale phase explosions is faster to apply than e.g. micro milling of microscale features. Furthermore, as also mentioned above, the microscale phase explosions generate microscale crater shaped depressions with sloped sidewalls that are well suited for fast replication processes, such as injection moulding and extrusion coating. Amongst others, the crater shape with sloped sidewalls facilitates easy releasing of the shaped items from the tool surface at the end of the moulding process (demoulding).

Further according to one embodiment of the replication tool, the tool surface is made of a metal, such as aluminium or steel. The tool surface has to be suited for the fast replication processes for which the method is intended. The tool surface comprising the microscale master structure can be directly produced on a mould surface for contacting the replication material and/or on an inlay attached to the inside of a mould. It is understood that the tool surface may be broken up in subsurface that form part of the mould as is customary in tool design for fast replication processes, such as injection moulding or extrusion coating. Examples of commonly used metals that are also suitable for the present invention include, but are not limited to, aluminium alloys of the types 2017, 1050 or 5754, or tool steel, such as ”Sandvik Corona C60”, Orvar2343 or similar.

Further according to one embodiment of the replication tool, the microscale structured master surface is a lateral arrangement of polydisperse microscale master features. The term polydisperse refers to microscale features having varying transverse dimensions as seen in a vertical projection. Typically, the polydisperse dimensions are characterized by a statistical distribution having a centre value and a spread. The transverse dimensions may be specified as transverse linear dimensions characteristic of the lumen defined by the crater shaped depression. Given the irregular nature of a polydisperse arrangement, transverse dimensions can also be defined in combination by specifying an area covered by the crater shaped depression. An equivalent linear dimension characterizing a given crater shaped depression may then be defined as the diameter of a circle with the same area. The microscale master features on the master surface are preferably densely packed, with neighbouring crater shaped depressions only being separated from each other by a ridge having a width that is comparable to or preferably less than the transverse linear dimension characterizing the crater shaped depression.

Further according to some embodiments of the replication tool the microscale master features are crater shaped depressions. Typically the crater shaped depressions appear more or less circular as seen in a vertical projection. Furthermore, the crater shape implies an outwardly sloped side wall providing a positive release angle facilitates demoulding of the shaped item.

Further according to one embodiment of the replication tool, the vertical profile of the microscale structured master surface has a peak-to-peak amplitude of at least 0.3 μm, or at least 0.5 μm or at least 1 μm and below 30 μm, below 20 μm, or preferably below 10 μm.

Further according to one embodiment of the replication tool, the lateral pattern of the microscale structured master surface has an area density of microscale master features of at least 5000/mm^2, at least 8000/mm^2, or at least 10000/mm^2. Thereby, the replication tool is particularly useful for producing parts comprising a microscale textured surface with a reasonably densely packed lateral distribution of microscale features.

It should be noted, however, that the process according to the present invention will not exceed an inherent upper limit for the area density of the microscale lateral structuring. Such an inherent limit is due to the fact that the microscale features produced by the microscale phase explosions according to the present invention require a minimum footprint in order to be resolved. While the present invention produces polydisperse features with a distribution that may include submicron elements, their average (most prominent) lateral dimensions are in the microscale. Increasing the area density of the microscale features results in an increasing probability for the occurrence of overlap between adjacent microscale features. Above a critical overlap, the microscale features are overlapping to such an extent that they appear merged and effectively have a much larger lateral extension than a targeted feature size of individual, unmerged microscale features. As a consequence, above a critical area density such merged features increasingly dominate the actual feature size produced on the replication tool.

In a characterization of the microscale surface structure of the master surface, e.g. by commonly known image analysis techniques applied to micrographs thereof, the merged features are then counted as a single feature with a larger lateral dimension or foot print. This effect is best seen in a graph showing the area density of microscale features, e.g. counted in a given surface portion by means of image analysis, as a function of the laser energy exposure applied to that surface portion. By way of example, such a graph is shown in Fig.19. The data

shown has been obtained by an analysis of the microscale structuring applied to more than 70 replication tool blanks (tool grade aluminium as specified elsewhere in this application) using the method according to the invention. The ordinate shows the exposure dose expressed in terms of the number of repetitions divided by the scan speed; the coordinate shows the area density of holes detected by an image analysis performed on micrographs of the processed surface; and the marker size indicates the size of the detected feature determined by the same image analysis algorithm. In an initial regime at low exposure, the individual microscale features are resolved and all have essentially the same size. The initial regime covers a low density regime up to about 5000/mm^2 where the distribution of the microscale features may be considered as sparse. In an intermediate exposure regime above about 5000/mm^2, the microscale features may be considered as more and more densely packed, reaching a critical density of about 12000/mm^2, where overlap of adjacent microscale features begins to become significant. The critical density is the maximum achievable density for a given system, which in the example of Fig.19 is about 12000/mm^2. Other material systems and laser processing setups may have a different maximum achievable area density, such as about 100000/mm^2, or about 50000/mm^2, or 20000/mm^2, or about 15000/mm^2. An inherent limit to the maximum achievable area density is given by the requirement of microscale dimensions of the lateral structuring as achieved by the present invention. Increasing the exposure beyond the critical value then only results in merging of the microscale features and in a deterioration of the desired patterning. In the example of Fig.19, a significant decrease of the area density of microscale features to below 5000/mm^2, accompanied by a corresponding increase of the average feature size is observed. When the microscale structure of the replication tool master surface is transferred onto a replicated item to form a microscale surface texture for the enhancement of a wetting behaviour, a sparse distribution of microscale features may prove insufficient to provide a significant wetting behaviour enhancement – if any at all. In a preferred exposure regime around the maximum achievable area density of about 100000/mm^2, or about 50000/mm^2, or 20000/mm^2, or about 15000/mm^2, or about 12000/mm^2, the microscale features are adequately dimensioned in their lateral extend, yet are packed sufficiently dense so as to achieve a significant wetting behaviour enhancement. An adequate range may be determined by an exposure experiment as outlined in Fig.19, wherein preferably the area density is at least 60%, at least 70%, at least 80%, or at least 90% of the maximum achievable area density of microscale features. Above a critical exposure, in the regime where merging becomes more and more dominant, the wetting behaviour enhancement of the replicated item also deteriorates more and more.

Further according to one embodiment of the replication tool, the microscale master features have an aspect ratio of a vertical dimension to a lateral dimension of at least 1:2, or about 1:1, wherein the vertical dimension is the peak-to-peak amplitude and the lateral dimension is the square root of the average footprint area per microscale master feature, which for a given microscale structured surface area is calculated as the inverse of the area density of microscale master features per area, i.e. the area of the given surface in lateral projection divided by the count of microscale features in that area.

B.2 Brief description of the drawings

Preferred embodiments of the invention will be described in more detail in connection with the appended drawings, which show in

FIG. 1ac SEM micrographs of a microscale structured master surface at different magnifications,
FIG. 2ac SEM micrographs of a microscale textured replica surface at different magnifications,
FIG. 3 a SEM micrograph of another microscale structured master surface,
FIG. 4 a SEM micrograph of the microscale textured surface of an injection moulded item (polypropylene) using an isotherm process,
FIG. 5 a SEM micrograph of the microscale textured surface of an injection moulded item (polypropylene) using a variotherm process,
FIG. 6 schematically, the surface modification of a tool surface by pulsed laser treatment to generate microscale phase explosions,
FIG. 7 schematically, an injection moulding process according to one embodiment of the invention,
FIG. 8 schematically, an extrusion coating process according to a further embodiment of the invention,
FIG. 9 a graph plotting hole density on a number of microscale structured master surfaces against the exposure in terms of repetitions divided by scan speed used during the pulsed laser treatment of the respective tool surfaces;
FIG. 10 a graph analysing the random distribution of microscale features over the exposed region for an ensemble of 76 samples;
FIGS.11–14 four graphs plotting hole size and hole density on a microscale structured master surface for different parameter settings of the pulsed laser treatment of the tool surface, and in
FIGS.15–18 four graphs plotting hole density on a number of microscale structured master surfaces against the scan speed used during the pulsed laser treatment of the respective tool surfaces;
Figs. 19ad SEM micrographs of
(a) cone like protrusions in an Al2017 mould at a 30° view angle,
(b) cone like protrusions in an Al2017 mould at a 0° view angle,
(c) replication of the Al2017 mould in cyclic olefin copolymer, and
(d) an Orvar2343 steel surface modified using the presented technology as seen at an 0° view angle;
Figs. 20ad SEM micrographs of
(a,c) a laser modified mould on indicated length scales,
(b,d) the corresponding injection moulded piece seen at 30° tilt,

B.3 Detailed description of preferred embodiments

B.3.0.1 Replication Tool

Examples of suitable materials are materials commonly used as inlays or mould materials in e.g. injection moulding or extrusion coating processes. These materials of the tool surface suited to be modified by pulsed laser treatment to generate microscale phase explosions include Aluminium alloys, such as so-called 1050 aluminium, 5754 aluminium, or 2017 aluminium, as well as tool steel, such as Sandvik corona C60 and Orvar2343.

Figs.1ac show micrographs taken by scanning electron microscopy (SEM) of an aluminium tool surface, more particular a tool surface made of 2017 aluminium, which has been modified by pulsed laser treatment using a picosecond laser with a maximum power output of 50 W operating at a pulse frequency of 200 kHz and at a wavelength of 1064 nm. The surface was scanned repetitively at a given power setting in per cent of the maximum power output and with a given speed. The laser beam was incident on the tool surface in a vertical direction, wherein the laser was slightly defocused by shifting the focal point by 1,3 mm in a vertical direction with respect to the tool surface to be modified. While the apparent spot size was about 50 µm on the surface, a line scan of the laser produced a modified trace width of about 10 µm ± 5 µm. A broader trace as the one shown in Fig.1a and 1b was obtained by a meander line scan with adjacent legs of the meander shifted in a direction perpendicular to the scanning direction. Thereby an arbitrary area can be covered by a microscale surface structure. As best seen in Fig. 1a, the laser treatment results in an ablation of some of the tool surface material. The parameters of the pulsed laser treatment are, however, adjusted such that the bottom of the trace exhibits a lateral arrangement of polydisperse microscale master features, see e.g. Fig.1b. The microscale master features obtained by this pulsed laser treatment are crater shaped depressions. The crater shaped depressions at the bottom of the trace are a consequence of the localized pulsed laser treatment generating microscale phase explosions.

Fig. 3 shows a SEM micrograph of tool surface made of tool steel, more particular Sandvik corona C60 tool steel, which has been modified by pulsed laser treatment using the same picosecond laser with a maximum power output of 50 W operating at a pulse frequency of 200 kHz and at a wavelength of 1064 nm. Again, the surface was scanned repetitively at a given power setting in per cent of the maximum power output and with a given speed. The laser beam was incident on the tool surface in a vertical direction, wherein the laser was slightly defocused. Also here, the localized pulsed laser treatment generates microscale phase explosions resulting in a lateral arrangement of polydisperse microscale master features, wherein the microscale master features are crater shaped depressions.

B.3.0.2 Replicated Item

Figs. 2ac show an example of a microscale textured replica surface on a mould insert for injection moulding, as observed in a scanning electron microscope at different magnifications, wherein the width of the image corresponds to 1.2 mm in Fig.2a, 0.23 mm in Fig.2b, and 0.03 mm in Fig.2c. The mould insert for injection moulding was designed and fabricated in 2017 aluminium alloy (MetalCentret, Denmark) by micro milling using conventional techniques to provide a tool surface defining the general shape of the part to be fabricated. To create the microscale structured master surface on the tool surface, a 1064 nm, 200kHz, 50 W (max power) picosecond laser (FUEGO, Time Bandwidth) mounted in a microSTRUCT vario (3DMicromac AG) was used to generate microscale phase explosions on the tool surface, thereby producing a densely packed lateral arrangement of microscale crater shaped depressions. The area intended for structuring was irradiated by the laser in parallel lines separated by 20 µm. In the example shown in Figs.2ac, this pattern was repeated 20 times, and the laser power was set to 25% of the max power. Focus was offset by +1.3 mm above the surface. The microscale structured master surface produced in this example consisted of 10 lines (200 µm wide) and was 305.5 mm long. The part with the microscale textured replica surface thereon was replicated from this replication tool with the microscale structured master surface on its

tool surface using a Victory 80/45 Tech injection moulder (Engel, Schwertberg, Austria). The polymer substrate used for injection moulding was cyclic olefin copolymer (COC) TOPAS grade 5013L10 (TOPAS Advanced Polymers, Düsseldorf, Germany) with a glass transition temperature (Tg) of 135 C. Injection temperature of the polymer was 270 C and the mould temperature was kept stable at 120 C. The injection moulding was performed in isothermal mode. The resulting microscale surface texturing is depicted in Figs.2ac. The microscale textured replica surface on this first part is adapted to act as microscale energy directors for forming an ultrasonic welding joint with a cooperating second part.

Further examples for the microscale textured replica surface on replicated parts are given in Figs.4 and 5. To produce these replica surfaces, the laser structured aluminium insert was installed in a Victory 80/45 Tech injection moulder (Engel). The polymer substrate used for injection moulding polypropylene HD120MO (Borealis) with a Heat Deflection Temperature (0.45 N/mm^2) of 88 °C. Injection temperature of the polymer was 255 °C with an injection pressure of 1200 bar. Both variotherm and isotherm injection moulding processes were tested.

Parameters specific for isotherm injection moulding:

- Temperature of microscale structured aluminium insert face = 80 °C. (constant)
- Temperature of "backside" mould = 60 °C. (constant)

Parameters specific for variotherm injection moulding:

- Temperature of structured aluminium insert face = 120 °C. (injection)
- Temperature of "backside" mould = 100 °C. (injection)
- Active cooling was applied immediately after polymer injection for the duration of the holding time (60 seconds) followed by and additional cooling time (60 seconds). This resulted in a final mould temperature of 40 to 50 degrees.

The respective surfaces have been characterised with respect to the shape of the microscale features on the microscale textured surface of the replicated item, see Fig.4 and Fig.5. The isothermal process results in a surface texture with rounded tops, see Fig.4, and the variothermal process results in a surface texture with a hairy appearance ("pulled polypropylene"), see Fig.5. Both surfaces faithfully replicate the lateral pattern of the master, but only provide a low fidelity replication of the vertical profile of the master. Nevertheless, both processes result in a fast replication of parts with microscale energy directors on flange portions thereof. The isothermal process is preferable for high throughput or high volume production, because the isothermal moulding process is not time limited by any process step(s) involving temperature adjustments of mould and/or mould inserts, whereas the variotherm moulding process is partially time limited by one or more process step(s) involving temperature adjustments of mould and/or mould inserts.

B.3.0.3 Replication Process

Fig.7 shows schematically an injection moulding process for producing a replicated part 4. The process uses a mould having mould parts 1a and 6, wherein mould part 6 has an insert

1b. Tool surfaces 2a, 2b, 7 define a general shape of the replicated item 4. Tool surfaces 2a, 2b are provided with microscale structured master surfaces 3a, 3b, 3c, 3d, which are replicated on the item 4 as microscale textures 5a, 5b, 5c, 5d respectively.

Fig. 8 shows schematically an extrusion coating process for coating a substrate web S, with a coating 14. The process uses a roll 11, 11a with a tool surface 12, 12a defining a general shape of the coating. The tool surface comprises microscale structured master surfaces 13, 13a, which are replicated as microscale surface texture 15 on the coating 14. A microscale structured master surface 13 may be applied directly to the tool surface 12 of the roll 11 and/or a microscale structured master surface 13a may be applied to the tool surface 12a of a replication tool insert 11a for attachment to the roll 11.

Localized Pulsed Laser Treatment Generating Microscale Phase Explosions Fig.6 shows schematically the configuration of the setup for localized pulsed laser treatment of a tool surface 2 on a replication tool 1 to generate a microscale structured master surface 3 by scanning a pulsed laser beam 99 over the tool surface.

B.4 Example

The example illustrates different ways of identifying suitable laser processing parameters for modifying a given tool surface to obtain a microscale structured master surface.

Aluminium 2017 (available from "Metalcenteret" Glostrup, Denmark) was surface structured using a 1064 nm, 200kHz, 50 W picosecond laser (FUEGO, Time Bandwidth) mounted in a microSTRUCT vario (3DMicromac AG). To perform the surface structuring, the area intended for structuring was irradiated by the laser in parallel lines separated by 20 μm. Every second layer was perpendicular to the previous, and so one set of perpendicular planes of lines is referred to as one "cross repetition". The laser power was set to 25% and 10 repetitions was conducted with focus offset +1.3 mm above the surface.

As illustrated in 1118, the average dimension and standard deviation of the hole sizes may be adjusted by varying parameters such as laser power in percent of maximum power output, scanning speed, number of cross repetitions and z offset of the focus plane. To identify the optimal parameter settings for achieving a desired hole size population and hole density in the alloy in question, one may map the parameter space of the laser settings. When replicated in polymer, the hole size population and hole density will determine the surface structure and roughness and hence the final wetting properties of the polymer piece. In the example below, the parameter space was for the

- Laser power in percent of the maximum power of 50 W: from 10 to 100 (both included), in increments of 5;
- Scan Speed in mm/s: from 150 to 1950 (both included), in increments of 100; and from 600 to 4200 (both included), in increments of 200;
- Number of cross repetitions: from 3 to 39 (both included), in increments of 2;

It may be noted that similar surface characteristics may be achieved using different parameter combinations. However, to minimise time consumption for the laser process, the parameter

coordinate with the highest (scan speed / cross repetition) value, and hence lowest process time, is preferred.

A recommended method to reduce the number of parameters and experiments is by locking parameter pairs in a fixed ratio, such as keeping (laser power / scan speed) constant, see Fig.11 and Fig.12, where the numerical value of the ratio of (laser power (in percent of the max power of 50 W) divided by the scan speed (in mm/s) is kept constant at 25E5 (= 0.00025) or 50E5 (= 0.0005) and allows for identification of the desired modification characteristics: both figures show peaks in hole density X. Likewise, the numerical value of the ratio of the number of repetitions divided by the scan speed (in mm/s) can be kept constant, see Fig.13 and Fig.14, where this ratio is kept constant at 1E2 (= 0.01) or 2E2 (= 0.02) and allows for identifying desired modification characteristics. As can be seen in Fig. 14, the high intensity (slow speed) results in few but large holes, whereas Fig. 13 shows that for the numerical value of the ratio of repetitions over scan speed (in mm/s) equal to 0.01 a more densely packed and uniform hole formation is achieved.

Figs.1518 show four graphs plotting hole density against the scan speed used during the pulsed laser treatment of the respective tool surfaces. At speeds $\leq$ 1250 mm/s, the hole density is consistent regardless of other parameters than speed, and it is concluded that writing speed is the main determining factor in this regime. At speeds $\geq$ 1250 mm/s, the hole density varies with the number of cross repetitions. This is true, even when the product (power X repetitions) is kept constant, (see Fig. 16). Marker size represents cross repetitions in Fig.15 and (cross repetitions X power) in Fig.16. Regardless of the parameter settings used to achieve a desired hole density, the coefficient of variance (CV) of hole size is observed to be stable in the regime where (speed $\geq$ 1250 mm/s), see Fig.17, and accordingly for the standard deviation (STD), see Fig.18. Marker size represents hole size CV in Fig.17 and hole size STD in Fig.18. Similarly, the laser focus parameter space may be mapped to identify applicable laser settings.

B.5 Example: Microscale Crater Shaped Depressions

Referring to Figs.1920 in the following, an example is given for forming crater shaped depressions in mould materials, and their subsequent replication.

Figures 19a and 19b show scanning electron microscopy (SEM) images of the microscale cratershaped depressions written in an Al2017 mould. It is noteworthy that although the laser scanning is conducted in bundles of parallel lines, the formed cratershaped depressions are stochastically formed within the laser ablated area without any apparent traces of the propagation path or any indications for stitching effects. This may be ascribed to the fact that the microphase explosions causing the cratershaped depressions are caused by a combination of metal impurities (alloy) picking up the energy, the pulsing nature of the laser beam and nonuniformity of the laser fluence distribution. The cratershaped depressions have a typical depth and spacing of 10 µm and 10 µm, respectively. On average, the area with the cratershaped depressions is about 47 µm lower than the untreated plane of the tool. Note that the cratershaped depressions are locally convex depressions in the mould that hence facilitate easy demoulding during replication. Fig. 19c shows a SEM image of a COC replica of the mould. The replicated structures are observed to have rounded tops due to imperfect filling during replication. Operating at conditions yielding higher fidelity replication may result in more difficult demoulding, due to stronger adhesion between the mould and its replica. Fig. 19d shows tool steel Orvar2343 ablated to produce cratershaped depressions similar to those demonstrated in Al2017.

Figures 20a and 20b show SEM images of cratershaped depressions in the Al2017 mould for fabrication of a high aspect ratio microfluidic system. The images clearly show the feasibility of writing cratershaped depressions structures at the bottom of deep trenches in the mould. Note that the separation and joining of bundles of laser lines do not alter the pattern and formation of cratershaped depressions. Thus, cratershaped depressions can be formed in any pattern or geometry. Corresponding SEM images of the injection moulded COC replica (Figs. 20c, 20d) clearly show that micropillar structures (cone like projections) are well reproduced on the top of the high aspect ratio wall.

The laser processing method has further been demonstrated to work in high endurance tool steel used for making high performance injection moulding tools. Furthermore, the method of the invention supports a modification rate of 200 seconds/cm2 and post processing capabilities on full three-dimensional mould surface shapes, as long as these are optically accessible.

A statistical analysis shows that the process for producing microstructures by microscale phase explosions with the method according to the invention is indeed random. The statistical analysis shows that the one-dimensional spacings between holes are exponentially distributed, proving that the process is indeed a *Poisson* process, i.e. the holes are formed randomly and uncorrelated. The xaxis spacings are found by sorting the x coordinates of the center of mass of the microstructures by size, and calculating the increment. The y spacings may be determined in the same manner, and since the sum of two independent identical distributed exponential distributions is also an exponential distribution, we may add the populations of x and y spacings. Plotting the histogram of the spacings reveals that they are indeed exponentially distributed for the samples, proving that the presented process is a random.

Fig.10 shows such histogram plot obtained from an ensemble average of 76 samples (Sample average). An average exponential probability distribution (Average exp PDF) and errorbars representing standard deviation of the samples in the ensemble have been added. Individual probability density functions have also been fitted to the histogram data for the individual samples. These are marked in the background (Sample exp PDF).

The exponential probability density function is given as $f(x;\lambda) = \lambda e^{-\lambda x}$ (support is $x \geq 0$). Typical values for the rate parameter, λ, is 0.16±0.04 (with maximum and minimum of 0.22 and 0.06, respectively), which is reasonable, since the expected value of $x = 1/\lambda = 6.774 \pm 2.36$ µm (with maximum and minimum of 15.57 µm and 4.475 µm, respectively).

B.6 Claims

1. Method of providing a replication tool, the method comprising
   - providing a forming tool having a tool surface adapted to define a general shape of a part to be formed;
   - modifying at least portions of the tool surface by a pulsed laser treatment to obtain a microscale structured master surface with a lateral master pattern and a vertical master profile; wherein
   - the pulsed laser treatment is adapted to randomly generate microscale phase explosions on the tool surface, thereby forming the microscale structured master surface as a lateral arrangement of randomly distributed microscale cratershaped depressions.
2. Method according to claim 1, wherein random generation of the microscale phase explosions is a stochastic *Poisson* process.
3. Method according to any of the preceding claims, wherein the occurrence of spacings between the randomly distributed microscale cratershaped depressions projected on one dimension x follows an exponentially decaying distribution function $f(x;\lambda) = \lambda e^{-\lambda x}$.
4. Method according to any of the preceding claims, wherein the lateral pattern of the microscale structured master surface has an area density of microscale cratershaped depressions of at least 5000/mm^2, at least 8000/mm^2, or at least 10000/mm^2.
5. Method according to any of the preceding claims, wherein the forming tool is a forming tool adapted for use in a replication process, wherein the replication process is one of injection moulding, hot embossing, compression moulding, and extrusion coating.
6. Replication tool for producing a part with a microscale textured replica surface by replication, the replication tool comprising a tool surface defining a general shape of the part, the tool surface comprising a microscale structured master surface having a lateral master pattern and a vertical master profile, wherein said microscale structured master surface has been provided by localized pulsed laser treatment adapted to randomly generate microscale phase explosions.
7. Replication tool according to claim 6, wherein random generation of the microscale phase explosions is a stochastic *Poisson* process.
8. Replication tool according to claim 6 or claim 7, wherein the occurrence of spacings between the randomly distributed microscale cratershaped depressions projected on one dimension x follows an exponentially decaying distribution function $f(x;\lambda) = \lambda e^{-\lambda x}$.
9. Replication tool according to any one of claims 68, wherein the replication tool is adapted for use in a replication process, wherein the replication process is one of injec-

tion moulding, hot embossing, compression moulding, and extrusion coating.

10. Replication tool according to any one of claims 69, wherein the microscale structured master surface is a lateral arrangement of polydisperse microscale master features.
11. Replication tool according to any one of claims 610, wherein the microscale master features are cratershaped depressions.
12. Replication tool according to any one of claims 611, wherein the vertical master profile has a peak-to-peak amplitude of at least 0.3 µm, or at least 0.5 µm, or at least 0.8 µm, or at least 1 µm, or at least 2 µm.
13. Replication tool according to any one of claims 612, wherein the vertical master profile has a peak-to-peak amplitude of up to 5 µm, or up to 10 µm, or up to 20 µm, or even up to 30 µm.
14. Replication tool according to any one of claims 613, wherein the lateral master pattern has an area density of microscale master features of at least 5000/mm^2, or at least 8000/mm^2, or at least 10000/mm^2.
15. Replication tool according to any one of claims 614, wherein the microscale master features have an aspect ratio of a vertical dimension to a lateral dimension of at least 1:2, or about 1:1, wherein the vertical dimension is the peak-to-peak amplitude and the lateral dimension is the square root of the average footprint area per microscale master feature.

B.7 Abstract

The invention relates to a replication tool for producing a part with a microscale textured replica surface. The replication tool comprises a tool surface defining a general shape of the item. The tool surface comprises a microscale structured master surface having a lateral master pattern and a vertical master profile. The microscale structured master surface has been provided by localized pulsed laser treatment to generate microscale phase explosions. A method for producing a part with microscale energy directors on flange portions thereof uses the replication tool to form an item with a general shape as defined by the tool surface. The formed item comprises a microscale textured replica surface with a lateral arrangement of polydisperse microscale protrusions. The microscale protrusions may be provided on a flange portion of a first part and are configured to act as energy directors when forming an ultrasonic joint with a cooperating flange portion of a second part.

1/9

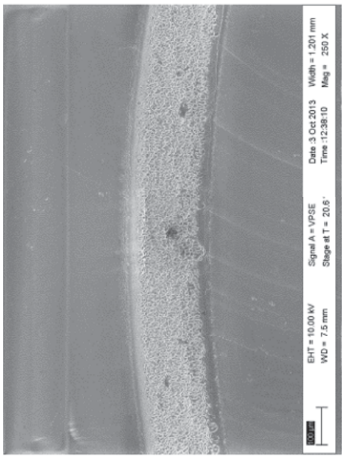

Fig. 2a

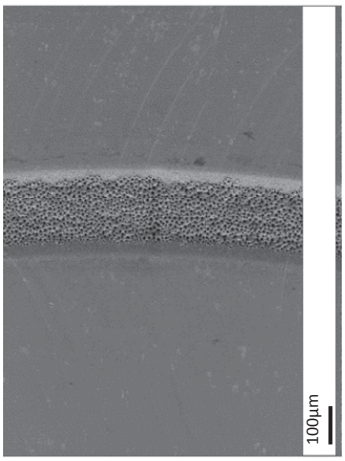

Fig. 1a

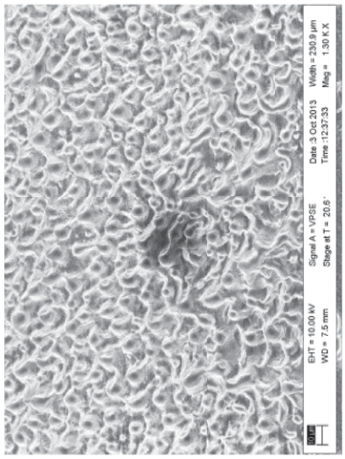

Fig. 2b

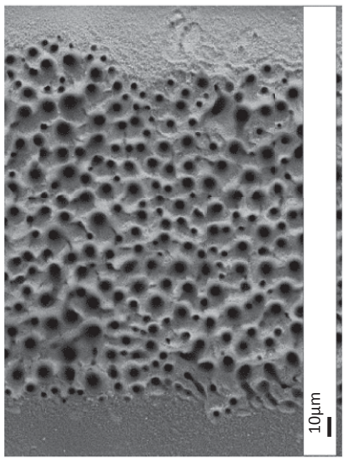

Fig. 1b

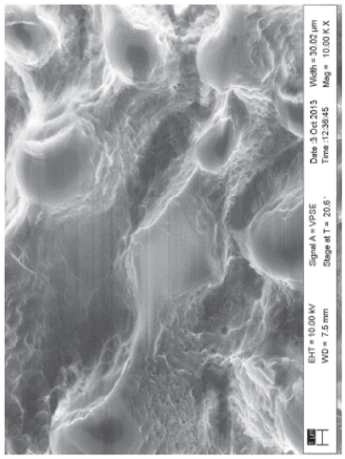

Fig. 2c

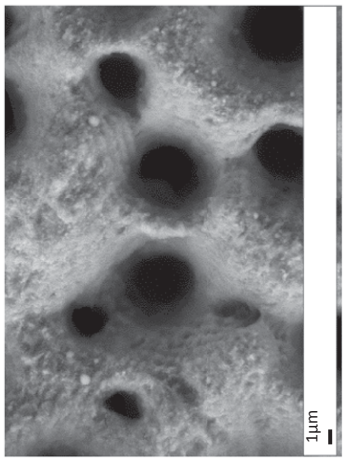

Fig. 1c

2/9

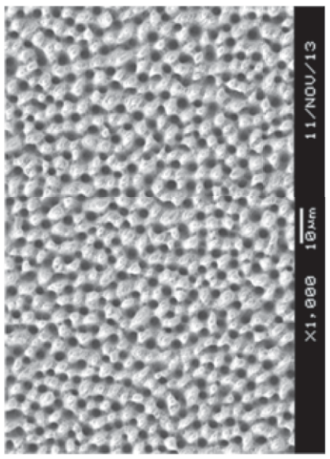

Fig. 3

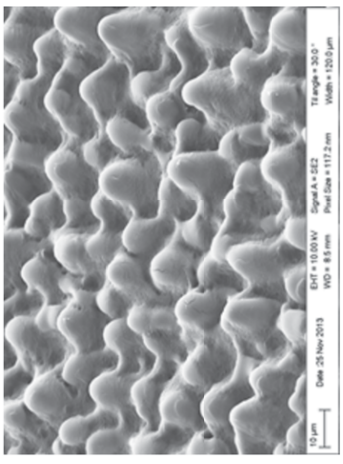

Fig. 4

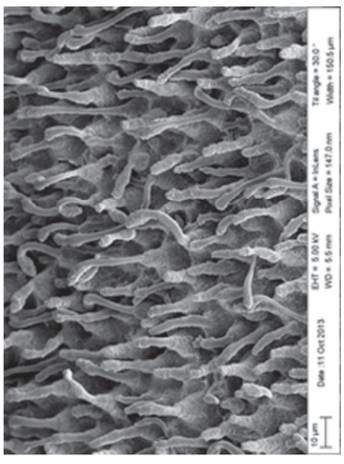

Fig. 5

3/9

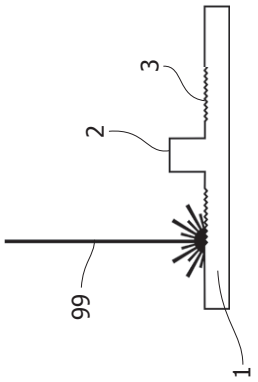

Fig. 6

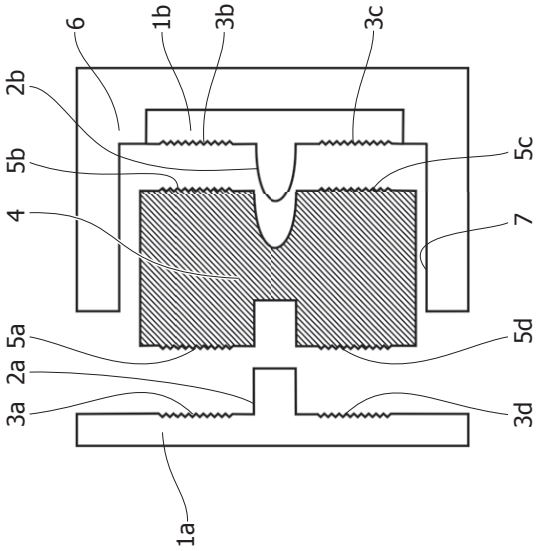

Fig. 7

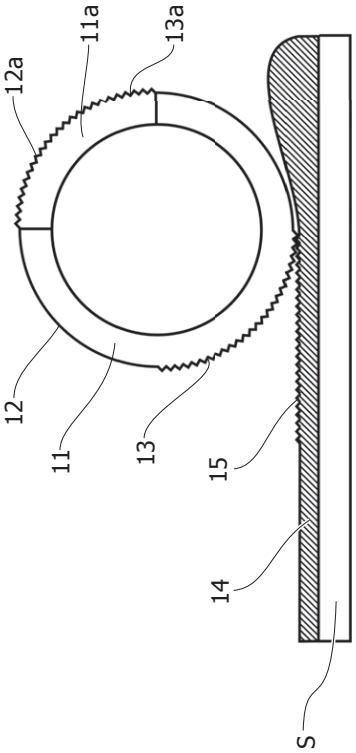

Fig. 8

4/9

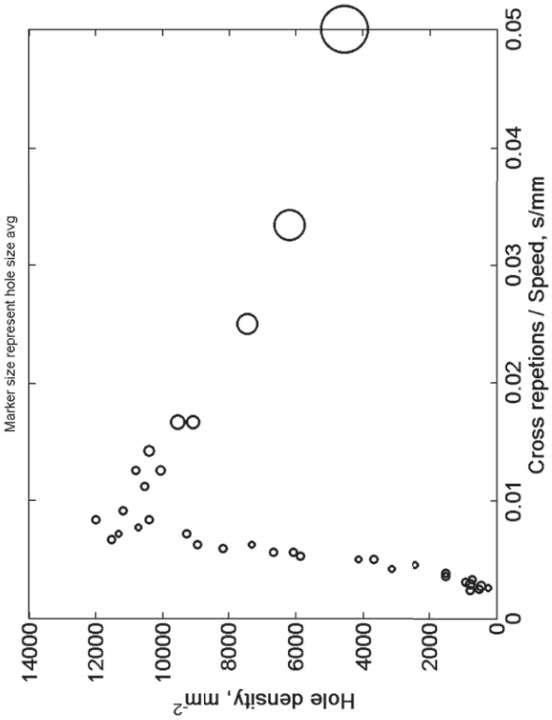

Fig. 9

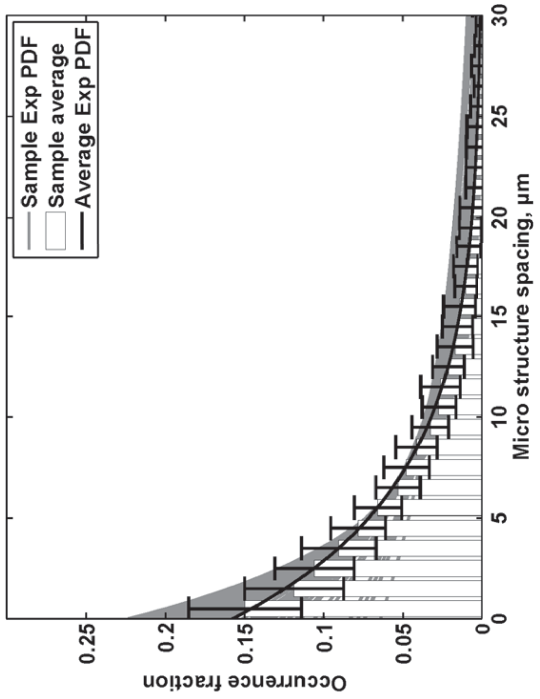

Fig. 10

5/9

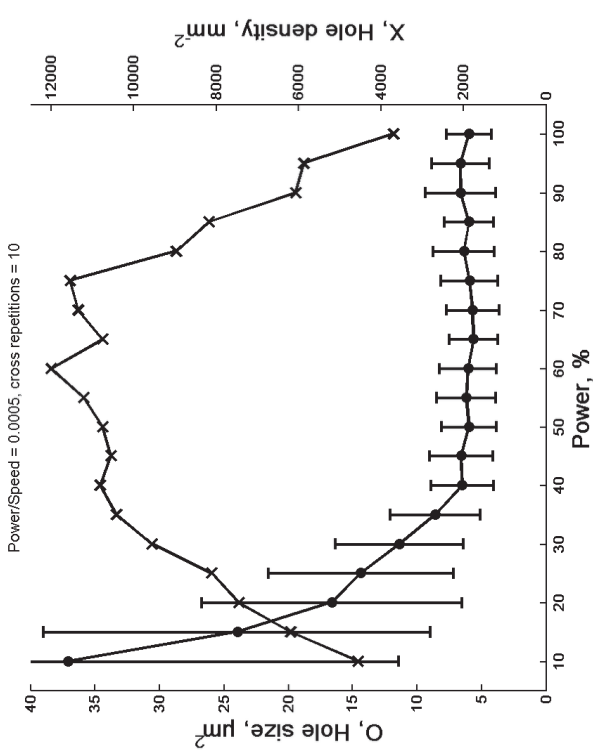

Fig. 11

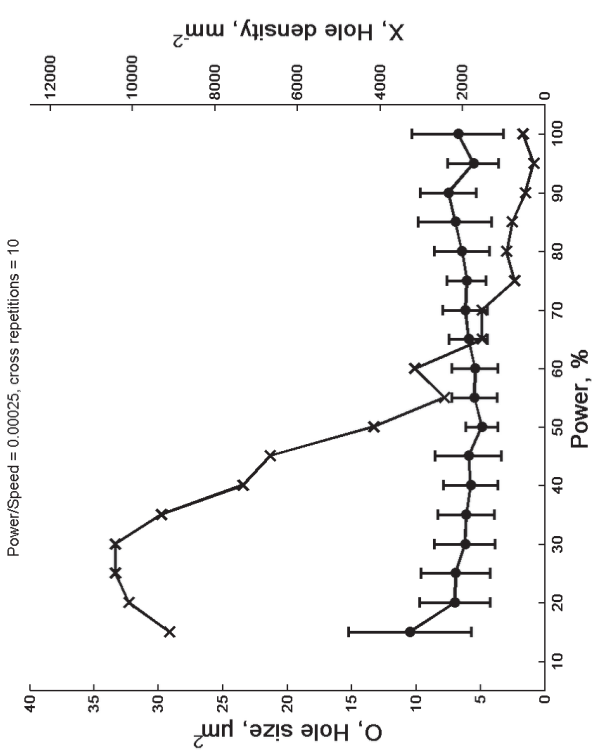

Fig. 12

6/9

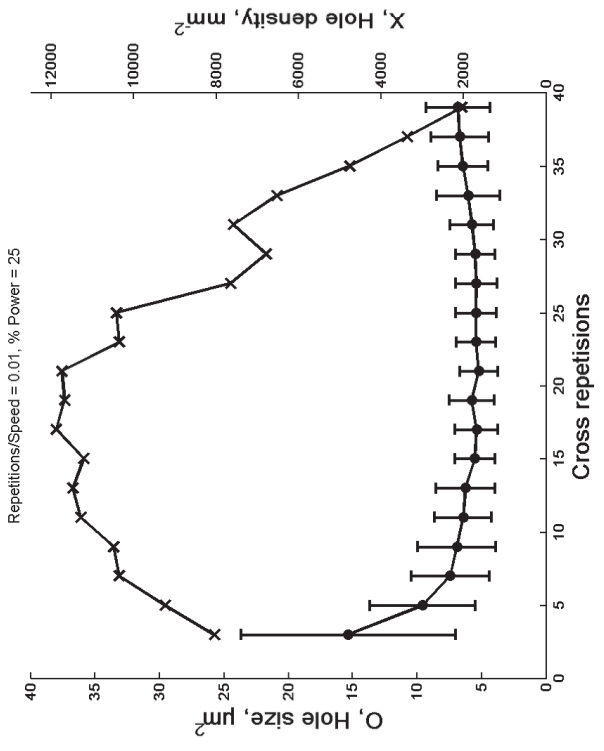

Fig. 13

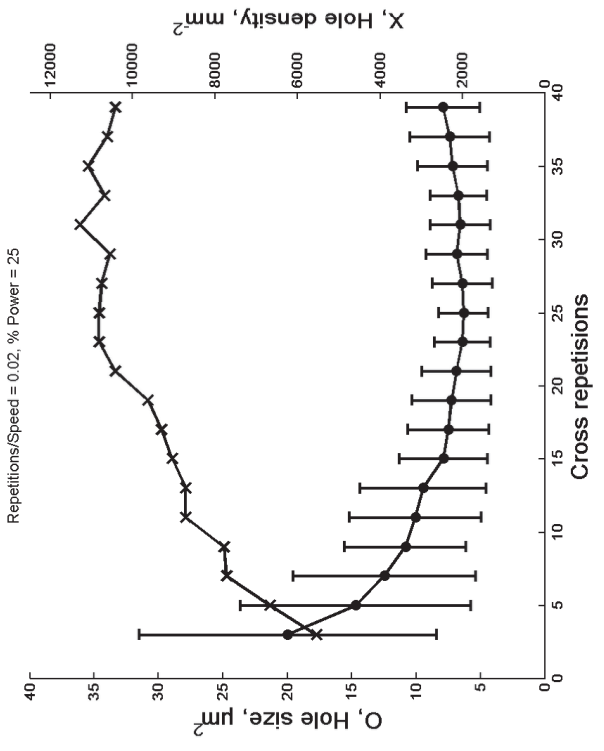

Fig. 14

7/9

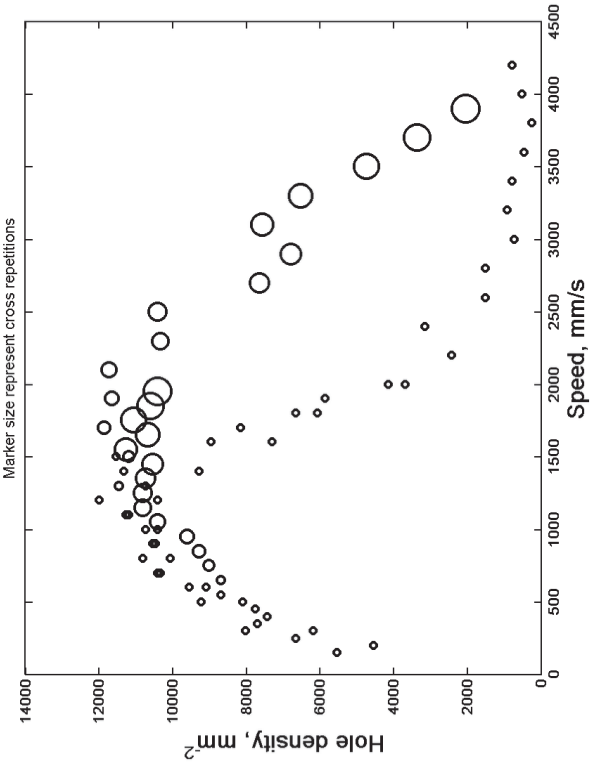

Fig. 15

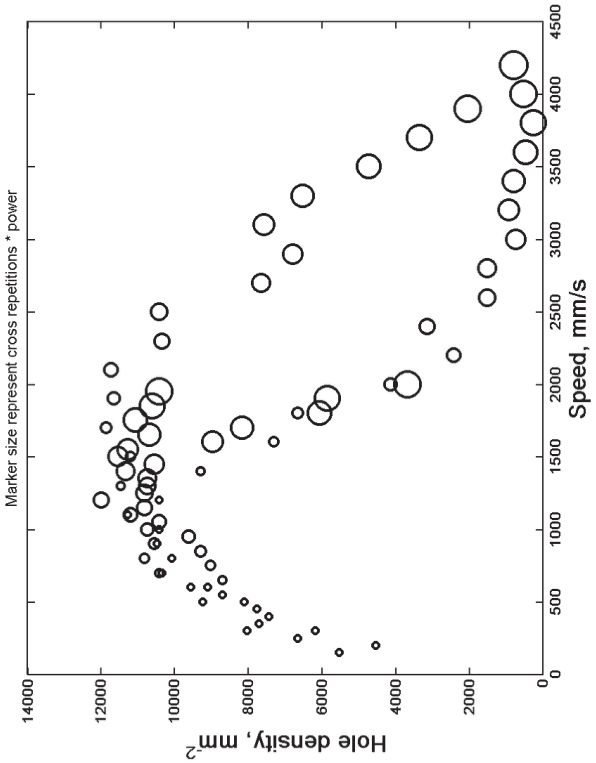

Fig. 16

8/9

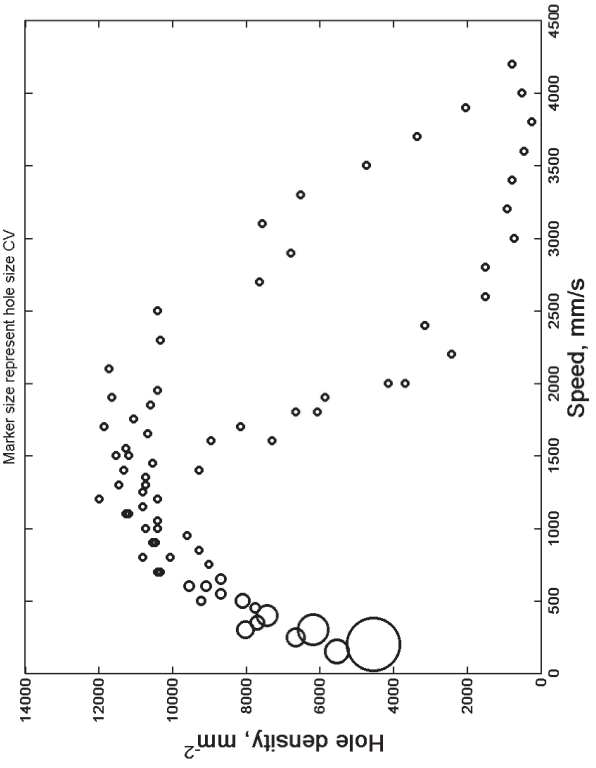

Fig. 17

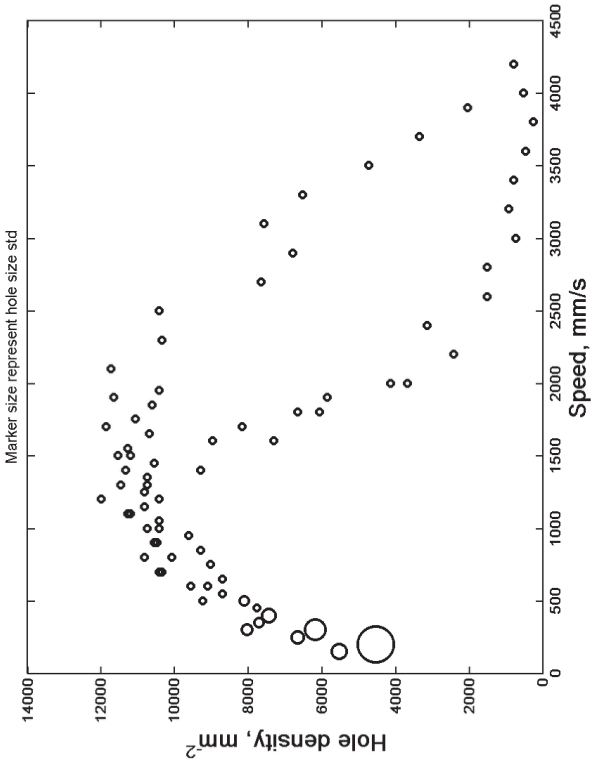

Fig. 18

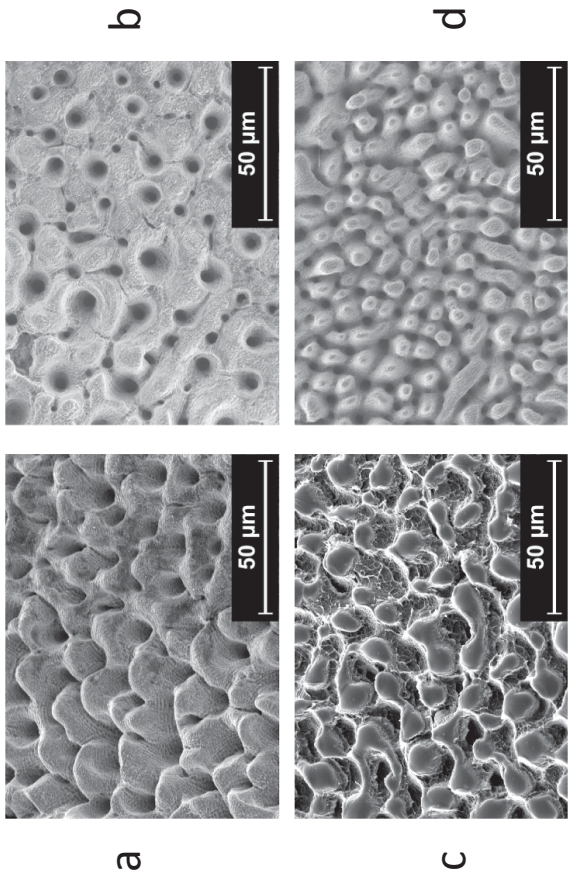

Fig. 19

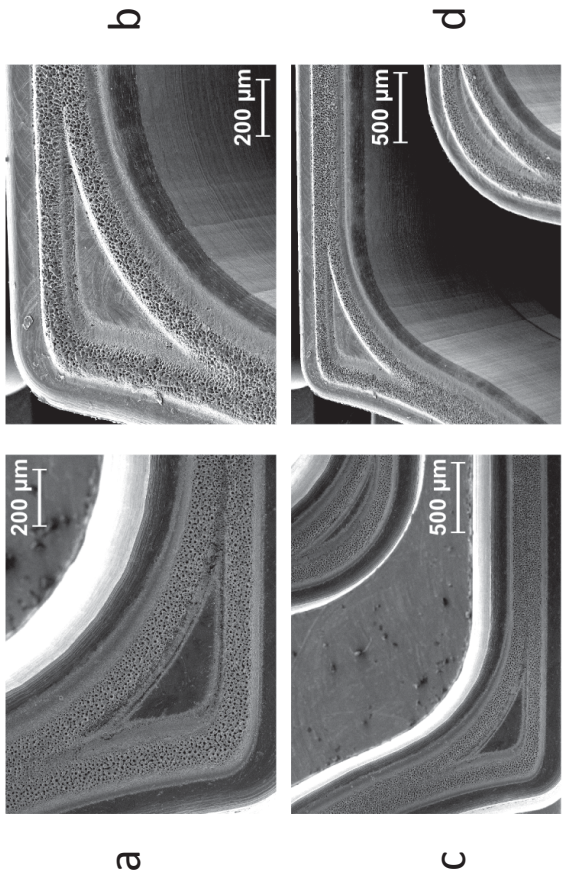

Fig. 20

C

Patent application 2: Micropillar energydirectors

Remarks

This patent application describes a device produced by using Patent application 1 where the microstructures are used as energy directors as was done in Paper 3.

As with the other patent applications, the content, points, argumentation and figures were drafted by me, and the text was written into ”patent language” by patent attorney Oliver Kuhn from Guardian IP, Kgs. Lyngby.

C.1 Micro-scale energy directors for ultrasonic welding

The present invention relates in one aspect to a replication tool and a method of providing the replication tool. In a further aspect, the present invention relates to a method of producing a part by replication, the part having a flange portion for use in the formation of an ultrasonic welding joint. In yet a further aspect, the invention relates to a method of joining two parts by ultrasonic welding.

C.1.1 Background of the invention

Ultrasonic welding is a technique for joining thermoplastics parts by applying high-frequency ultrasonic acoustic vibrations across the joint surfaces while pressing the parts together. The acoustic vibrations are absorbed by the thermoplastic material, which melts locally, thereby forming a welded seam. In a typical ultrasonic welding process, at least one of the flanges of the joint comprises pointed or knife edge type protrusions, so-called energy directors that concentrate the ultrasonic energy to the location where the weld is to be formed. Energy directors commonly known from industrial processes have several disadvantages, in particular when high precision welds with high weld strength are to be formed. Examples of such applications, where high precision to form a fluid tight weld seam is essential, are microfluidic chips, such as used for medical diagnosis or environmental testing. In such applications, often a base chip with a system of microfluidic channels and components is formed e.g. as a replicated part in an injection moulding, compression moulding or hot embossing process. The base chip is then covered by a counter-part, which may equally comprise microfluidic channels and components, but may as well be a simple lid. The two parts are joined to form a fluid tight seal. Such joints may be formed e.g. by gluing, thermal bonding, or vapour bonding, but attempts have also been made to use ultrasonic bonding for joining such parts. In particular, ultrasonic bonding may overcome some of the challenges encountered with other bonding techniques, e.g. when packaging hazardous materials or sensitive reagents, where the other bonding techniques, due to the process parameters involved, are outright incompatible with the product. However, the uncontrolled deformation of the energy directors during the ultrasonic welding process typically results in the occurrence of so-called flashes that may penetrate into the microfluidic channels, or may lead to uncontrolled cross-sectional dimensions of the microfluidic channels and components.

Therefore, there is a need for a reliable and cost-effective process for forming an ultrasonic joint overcoming at least some of the above-mentioned disadvantages, or at least to provide an alternative to known methods. Furthermore, there is a need for suitable tooling for use in the above method of forming an ultrasonic joint. Furthermore, there is a need for a process for providing such suitable tooling.

C.1.2 Summary of the invention

A first aspect of the invention relates to a method of providing a replication tool, the method comprising providing a forming tool having a tool surface adapted to define a general shape of a part to be formed; modifying at least portions of the tool surface by a pulsed laser treatment to obtain a microscale structured master surface with a lateral master pattern and a vertical master profile; wherein the pulsed laser treatment is adapted to generate microscale phase explosions on the tool surface, thereby forming the microscale structured master surface as a lateral arrangement of microscale crater-shaped depressions. The crater-shaped depressions obtained by the microscale phase explosions are irregular in shape and polydisperse, i.e. varying in size with a spread about a most prominent size. The size may e.g. be characterized by the area covered by the depression as seen in a vertical projection on a lateral plane.

The microscale structuring of the tool surface is provided by the localized application of

laser pulses directly to selected portions of the tool surface. This post-treatment of the tool surface by means of localized laser treatment has the advantage that the replication tool with the shape defining tool surface may be designed and produced using existing techniques and equipment for tool making, thereby contributing to a relatively simple and cost effective implementation of the surface modification in an existing fabrication process.

At the targeted portion of the tool surface, the localized pulsed laser treatment is adapted to melt and evaporate material at the tool surface to generate microscale phase explosions, thereby producing a randomised surface structure of polydisperse microscale features. The microscale surface features are depressions, which are typically crater shaped with steeply sloped side walls. The process of provoking microscale phase explosions by locally applying laser energy to the tool surface so as to form the crater-shaped depressions is stochastic in nature, wherein upon appropriate exposure the microscale surface features are densely packed and may even partially overlap, thereby forming a microscale lateral pattern with a microscale porous appearance. The localized application of laser power may be scanning a laser spot along a predetermined scanning path at a pre-determined scan speed over the tool surface. The path may follow a single scan along the path over the tool surface, a repetitive scanning along the same linear path, or a combination of both. The path is adapted to cover the selected portions of the tool surface. The path may e.g. be straight, curved, meandering, segmented or a combination thereof and some sections of the path may overlap other sections of the path in order to achieve an even exposure of the selected portions of the tool surface with laser energy.

The pulsed laser radiation has to be of a wave length and pulse characteristics that is absorbed by the tool surface in order to be able to locally melt and evaporate material from the tool surface so as to produce microscale phase explosions creating the crater-shaped depressions. For example, the laser radiation may be from a picosecond-laser source with a wavelength in the near infrared, such as 1064 nm, but other wavelength ranges, e.g. in the visible part of the electromagnetic spectrum, and pulse characteristics that are suitable for locally heating the tool surface to generate microscale phase-explosions may be conceived, too. The finish of the targeted portions of the tool surface is controlled by adapting the exposure of these tool surface portions with the pulsed laser radiation. The exposure of the tool surface is controllable e.g. by adjusting the laser power/spot intensity and/or by varying the scan speed, wherein exposure of a given surface portion increases with increasing laser power, but decreases with increasing scan speed. The finish of the targeted portions of the tool in turn determines the finish of the replicated part in the corresponding regions on the surface of the part via the replication process. Furthermore, multiple exposures of the same surface portions, e.g. by repetitive and/or overlapping scanning of the laser spot over these surface portions, results in an exposure that is increased correspondingly.

Preferably, the lateral pattern of the microscale structured master surface has an area density of microscale master features of at least $5000/mm^2$. Thereby, a reasonably densely packed lateral distribution of microscale features on the master surface is achieved, thereby allowing for producing parts with a replicated microscale surface texture that is useful for forming high precision, fluid tight ultrasonic joints with improved bond strength.

Further preferably, the lateral pattern of the microscale structured master surface has an area density of microscale master features of at least $8000/mm^2$, or even of at least $10000/mm^2$. Thereby, a densely packed lateral distribution of microscale features on the master surface is achieved, thereby allowing for forming high precision, fluid tight ultrasonic joints with

particularly improved bond strength. It should be noted that an upper limit for the area density resulting from the microscale of the surface structuring exists, which is discussed in detail further below.

A further aspect of the invention relates to a method of producing a first part having a flange portion for use in the formation of an ultrasonic welding joint with a cooperating second part, the method comprising the steps of

> providing a replication tool with a microscale structured master surface by a method according to the above-mentioned embodiment; and
> using the replication tool to form the first part by the replication process, wherein the formed first part has the general shape as defined by the tool surface, and wherein the formed first part comprises a microscale textured replica surface with a lateral arrangement of microscale cone-like protrusions on at least the flange portion of the first part.

Preferably, the lateral pattern of the microscale textured replica surface has an area density of microscale cone-like protrusions of at least $5000/mm^2$. As mentioned above, this allows for forming high precision, fluid tight ultrasonic joints with improved bond strength.

Further preferably, the lateral pattern of the microscale textured replica surface has an area density of microscale cone-like protrusions of at least $8000/mm^2$, or even of at least $10000/mm^2$. As also mentioned above, this allows for forming high precision, fluid tight ultrasonic joints with particularly improved bond strength. An upper limit for the area density resulting from the microscale of the cone-like protrusions forming the surface texture exists, which is discussed in detail further below.

The method is useful for forming the first part from a replication material replicating the microscale structured master surface onto the first part to form a surface region with a lateral arrangement of polydisperse microscale energy directors shaped as polydisperse microscale protrusions on the first part. A lateral replica pattern is defined by the lateral master pattern, and a vertical replica profile has finite peak-to-peak amplitude to form a three-dimensional texture. Since the lateral replica pattern is defined by the lateral master pattern, it is equally irregular as seen in a projection onto a lateral plane, and the microscale protrusions are polydisperse. The method is for producing the first part by a fast replication process using the replication tool, such as required by a commercially viable production of the item in large numbers.

As mentioned above, the laser treatment of the tool surface results in a porous surface appearance produced by a randomised lateral arrangement of, preferably densely packed, microscale depressions, which are typically shaped as relatively deep, steep-walled craters with a more or less pointed bottom. The sloped sidewalls facilitate an easy de-moulding of the replicated item in the step of releasing the item from the tool surface.

Since the method is useful for the production of first parts by a fast replication process, it allows for a low-cost and/or mass production of the first part with a first flange portion that is prepared for ultrasonic bonding with a cooperating second flange portion on a second part by providing the first flange portion with microscale energy directors. A replication process may be considered fast, for example, if the replication period from contacting the tool surface

with the molten replication material to releasing the formed part is short, such as well below ten minutes, such as less than five minutes, such as less than 3 minutes, such as less than one minute, such as less than 30 seconds, or even less than 10 seconds. In particular, the suggested thermally controlled replication process using a thermoplastic replication material can be performed fast as compared to for example replication processes using thermosetting replication materials, or chemically setting replication materials. However, the method is also useful for the production of first parts having a flange portion with microscale energy directors thereon by other replication techniques, such as the mentioned slower methods using thermosetting or chemically setting replication materials, or for replication techniques like compression moulding and hot embossing.

The term microscale refers to dimensions of about 1 μm to 1000 μm that are generally measured in microns (micrometres), typically in the range of about 1 μm to 100 μm. Accordingly, the term nanoscale refers to dimensions of about 1 nm to 1000 nm that are generally measured in nanometres, typically in the range of about 1 nm to 100 nm.

The microscale structure of the master surface and, accordingly, the microscale texture of the replica surface have a three-dimensional topography of microscale elements arranged next to each other and may be decomposed in a lateral pattern and a vertical profile. The term “lateral pattern” refers to the arrangement in lateral directions of the (3D) microscale elements making up the microscale structure/texture, as seen in vertical projection on to a lateral plane. The term ”vertical profile” refers to the variation of the location of the surface in a direction perpendicular to the lateral directions.

When a surface structuring/texturing is applied to an object having a general shape, such as a tool surface or an item, the surface structuring/texturing can be seen as a vertical variation of the surface, which is added to the general shape of the tool surface/item. Accordingly, on an object with a microscale structured/textured surface, an average surface that flattens out any vertical variations of the surface by averaging on a lateral scale larger than that of the microscale structuring/texturing essentially follows the general shape of the object. The general shape of the object is thus defined independent of any nano- or microscale surface roughness / finish / structuring. At a given point on the surface of the object, lateral directions are parallel / tangential to a surface defining the general shape of the object on a scale larger than the scale of the lateral pattern. Accordingly, the vertical direction at a given point on the surface of the object is the surface normal to the general shape in that point. In each given point, the vertical direction is perpendicular to the corresponding lateral directions.

The general shape of the replicated part is defined by the general shape of the tool surface. The replication process is for accurately replicating the general shape of the part as defined by the tool surface. The surface of the replicated part is functionalised by applying a surface finish with a microscale texture at least on selected regions of the surface of the part. The particular functionalization is to make a flange portion of the replicated part susceptible to concentrate ultrasonic energy so as to act as a distributed energy director when forming an ultrasonic joint with a cooperating flange portion of a counterpart. To concentrate the ultrasonic energy applied across the interface between the first and second flange portions, the area of contact is reduced to point contacts where the tops of the protrusions meet the surface of the counterpart when the first flange portion is brought in contact with the cooperating second flange portion.

The protrusions are sacrificial; Upon formation of the joint, the protrusions are flattened out by the ultrasonic energy dissipated and the pressure applied. The material of the energy directors spreads in lateral directions, but is easily absorbed on the spot also on a microscale, due to the lateral interspaces between the protrusions. Thereby, the quality and precision of the ultrasonic joint is improved, and the formation of undesirable ”flashes”, i.e. the spreading of material into regions adjacent to the ultrasonic joint, is avoided.

An important advantage of the present method is that the laser treatment of the tool surface is only limited by the requirement of an optical access to the surface to be modified. Consequently, a microscale structured master surface may be applied to virtually any surface topology, including very narrow and deep trenches or holes, as long as a laser beam can be guided to the tool surface to be modified. This allows for an improved freedom for designing the ultrasonic joint and accordingly for designing the replicated parts to be assembled. Furthermore, at the choice of the designer, the microscale protrusions may be distributed over the entire flange portion of the replicated parts or only to selected regions thereof. Also, the flange portion may be arbitrarily shaped as seen in the lateral direction, e.g. the flange portion may easily be adapted to cover larger surfaces. The microscale energy directors may even be arranged on curved and/or oblique surfaces following a more complex general shape of the replicated part, thereby adding to the above-mentioned improved freedom of design.

According to some embodiments, the method comprises the steps of (a) providing a replication tool having a tool surface adapted to define a general shape of the first part, wherein the tool surface comprises a microscale structured master surface obtained by localized pulsed laser treatment of the tool surface to generate microscale phase explosions, said microscale structured master surface having a lateral master pattern and a vertical master profile; (b) contacting the tool surface with a replication material in the melt phase, wherein the tool surface is maintained at a process temperature below a melt temperature of the replication material, thereby (c) cooling the replication material to a stabilized shape with a microscale textured replica surface, wherein the lateral master pattern defines a corresponding lateral replica pattern of the microscale textured replica surface and wherein the amplitude of a vertical profile of the microscale textured replica surface is in the microscale, and (d) releasing the shaped item from the tool surface.

A replication process, where the tool surface is maintained at a more or less constant temperature below the melt temperature throughout the production process is sometimes referred to as an ”isothermal” type process. Isothermal processes may be performed at high throughput. As also mentioned above, the truthfulness of the replication of the vertical profile of the microscale master structure is uncritical as long as the peak-to-peak amplitude of the vertical profile of the micro-texture on the replica surface is sufficient, and further preferably the lateral pattern is faithfully transferred.

Alternatively, e.g. in a so-called variothermal injection moulding process, the microscale structured master surface is prior to contact with the replication material heated to an injection temperature above the melting temperature of the replication material, but immediately upon injection of the replication material rapidly cooled to a temperature below the melting temperature of the replication material, at which the first part is finally released from the mould.

Further according to some embodiment the replication process is one of injection moulding, hot embossing, compression moulding, and extrusion coating.

Further according to one embodiment of the method, the microscale textured replica surface has a peak-to-peak amplitude of at least 0.5 μm, or at least 1 μm and up to 5 μm, or up to 10 μm, or even up to 30 μm. A minimum vertical profile required to form a 3D textured surface suited for forming point contacts between cooperating first and second flange portions. To achieve a concentration of the ultrasonic energy to point contacts, the exact 3D-shape of each of the microscale features on the tool surface and their exact arrangement with respect to each other is not critical. Also, the exact details of the individual microscale elements and of their arrangement making up the micro-texture on the surface of the replicated item are uncritical for achieving a concentration effect by the microscale energy directors. The fast replication process thus yields proper items as long as the general shape is faithfully obtained reliably, the microscale lateral pattern is reliably reproduced in each reproduction process, and the peak-to-peak amplitude of the vertical profile of the replica surface is adapted to provide point contacts between the tops of the protrusions on the first part and the cooperating flange portion of the second part. Reduced amplitude gives less "flashes", but requires corresponding precision in the flatness/fit of the cooperating first and second flange portions. Relatively small amplitudes of the vertical profile of the texture of the replica surface may already achieve a sufficient concentration of ultrasonic energy into point contacts, such as amplitudes of at least 100 nm, alternatively at least 200 nm, alternatively at least 500 nm, and preferably in the microscale, such as 1 μm - 100 μm, such as 1 μm - 30 μm, preferably in the range 1 μm - 10 μm. For ensuring a good production yield it is therefore sufficient to control the lateral scale of the texture which is well controlled by the lateral scale of the pattern of the master surface – and ensuring that the amplitude of the profile of the texture on the replica surface exceeds the local flatness of the cooperating flange surface so as to reliably form distributed point contacts between the top of the protrusions and the surface of the counterpart. A further important insight therefore relates to the nature of the fast replication process. Here, it is exploited that the lateral pattern of the microscale master structure on the tool surface is inherently reproduced with high fidelity on the replicated item. The fidelity of replication of the vertical profile on the other hand tends to be affected by standard parameters of processes for fast replication in thermoplastic materials, such as tool temperature, replication period, and temperature and/or pressure of the thermoplastic replication material in the melt phase. This is owing to the ability of the thermoplastic replication material to fill the depressions of the relatively deep steep-walled master structure before solidifying, which may be controlled by these parameters. Thereby, the fidelity of replication may be controlled. For example, fidelity of microstructure replication may be reduced by reducing the temperature at which the tool surface is maintained. When the replication material contacts the tool surface at the lower the melt is cooled more rapidly, thereby increasing the viscosity of the melt and impeding the filling of the microscale depressions/crevices/craters/pores of the master structure on the tool surface by the melt before it solidifies. A reduced fidelity is reflected by a reduced amplitude of the replicated profile as compared to the master profile: the replication is more shallow than the master. The fidelity of replication of the vertical profile may thus be characterised e.g. by comparing the peak-to-peak amplitudes of the vertical profiles of the replicated microscale texture and the microscale master structure to each other, wherein for a low fidelity replication the amplitude of the replicated profile as compared to the master profile is lower than for a higher fidelity replication. Typically, the low-fidelity replicated microscale textures exhibit a rounded top. Since the energy concentration is uncritical as to the exact shape and arrangement of the individual microscale features, another advantage of the method is that it facilitates a relatively simple and cost effective implementation of the surface functionalization in an existing fabrication process by merely modifying the tool surface of a replication tool in a post-treatment step.

Further according to one embodiment of the method, the lateral pattern of the microscale textured replica surface has an area density of microscale cone-like protrusions of at least $5000/mm^2$, at least $8000/mm^2$, or at least $10000/mm^2$. Preferably, the protrusions are densely packed to provide a good mechanical strength of the joint. Furthermore, a densely packed lateral arrangement of the protrusions also ensures good fluid sealing properties of the ultrasonic joint, e.g. when forming hermetically sealed chambers or channels.

Note that the part may be made entirely from replication material with a shape defined by the tool surface, or the replication material may be applied to/carried by a substrate material, e.g. in an additive moulding step or a coating step.

Further according to one embodiment of the method, the replication process used for producing the part is injection moulding. Injection moulding is a cyclic replication process with a fast cycle time, i.e. using this embodiment a large number of separate items with a microscale textured replica surface may be produced at high throughput. The inner surface of the injection mould is the tool surface defining the general shape of the part. At least portions of the tool surface have a finish with a microscale structuring generated by localised treatment with a pulsed laser source. The thermoplastic replication material is heated to above the melt transition temperature and in the melt phase injected into the closed mould, which is kept at a temperature between the glass transition temperature and the melt transition temperature of the replication material. When the molten replication material contacts the cooled tool surface it solidifies, whereby it is shaped and textured, before the item is released from the mould.

A surprising insight is that the replica surface produced in a fast injection moulding process using the replication tool presented herein exhibits a microscale textured replica surface which is well suited for forming a reliable ultrasonic welding joint also if the vertical profile of the microscale texture on the replica surface is a low fidelity replication of the corresponding profile of the microscale structure on the master surface. Precise and strong ultrasonic welding joints may be reliably obtained as long as the lateral pattern is faithfully transferred and the peak-to-peak amplitude of the vertical profile of the micro-texture on the replica surface is in the microscale, or at least has an amplitude that is sufficient for forming point contacts that are distributed over the respective flange portions. Thereby, a robust low-cost mass-production process for parts is achieved, which are suited for being joined to other parts by ultrasonic welding, and even form a fluid tight seal.

In another particularly advantageous embodiment of the method, the replication process is extrusion coating. Extrusion coating is a process for roll-to-roll processing, i.e. using this embodiment the part may be produced in a continuous process as a layered web with a microscale textured replica surface. To that end, a substrate web may be passed between a nib roll and a cooling roll, in a conventional manner, wherein the rotary surface of the cooling roll is the tool surface defining the general shape of the item. The tool surface has a finish with a microscale structuring generated by treatment with a pulsed laser source. A thermoplastic replication material is heated to above the melting temperature and in the melt phase supplied between the substrate web and the cooling roll, which is kept at a temperature below the melting temperature of the replication material. When the molten replication material contacts the cooled tool surface it solidifies, whereby it is shaped and textured, before the item is released from the replication tool.

Further according to one embodiment of the method for producing a part with microscale

energy directors on flange portions thereof, a replication period from contacting the tool surface with the molten replication material to releasing the shaped item is less than 3 minutes, such as less than one minute, such as less than 30 seconds, or even less than 10 seconds. Typically, in an injection moulding process, the replication time may be less than one minute, i.e. a few tens of seconds, such as about 30 seconds. Typically, an extrusion coating process is even faster with replication times of less than 10 seconds.

Further according to one embodiment of the method for producing a part with microscale energy directors on flange portions thereof, the vertical replica profile predominantly has rounded tops with a radius of curvature in the microscale. As described above, the replication process may be controlled to influence the fidelity of replication to provide a vertical replica profile that predominantly has rounded tops with a radius of curvature in the microscale. A low fidelity replication may be achieved in a fast replication process with short replication periods. A process goal/constraint of a faithful replication of the vertical profile of the master structure, on the other hand may entail long settling or curing times incompatible with a fast replication process.

Advantageously, the radius of curvature of the rounded tops is of the same order as the lateral distance between adjacent structures/features of the lateral pattern, such as predominantly above 1 μm, above 5 μm, or even above 10 μm, and predominantly less than 300 μm, less than 100 μm or even less than 50 μm. Further advantageously, the vertical amplitude of the replica profile is about equal or less than the lateral distance between adjacent microscale features.

In a further aspect, a method for producing a part with microscale energy directors on flange portions thereof comprises preparing a replication tool using the above-mentioned method, and repeatedly performing the method of producing an item with a microscale textured replica surface by a replication process according to any one of the above-mentioned embodiments. Large numbers of items exhibiting enhanced hydrophobicity or super-hydrophobicity may thus be produced cheaply.

According to a further aspect, the invention relates to a part with a microscale textured replica surface produced by replication according to any of the above-mentioned methods.

According to a further aspect, a method of joining a first part and a second part by ultrasonic welding, comprises the steps of

> producing the first part with microscale energy directors in the form of microscale cone-like protrusions on a flange portion thereof by the method according to any one of the above-mentioned embodiments;
> producing a second part having a cooperating flange portion;
> bringing the microscale cone-like protrusions on the flange portion of the first part in contact with the cooperating flange portion of the second part; and
> applying ultrasonic energy and pressure, thereby flattening out the cone-like protrusions, to form an ultrasonic welding joint between the first and second parts.

The ultrasonic energy is applied across the flange portions while applying a compression force pressing the two cooperating flanges together. In contrast to energy directors commonly used for forming ultrasonic joints, the invention provides areas of microscale energy directors

distributed over flange portions where the work pieces are to be welded together. According to the present invention, a master of the micro-scale energy directors is produced by at least partially covering corresponding flange portions of the work piece negative in a forming tool with a micro-scale roughening, and subsequently replicating the microscale roughening into the flange portions of the work pieces in a forming step. It has turned out that the above described pulsed laser treatment of the tool surface gives an adequate microscale roughening that may be replicated onto the part to form micro-scale energy directors. In particular, by tuning the laser treatment to generate "microscale phase explosions" when applied to tool surfaces, such as forming steel surfaces or aluminium tool surfaces/inserts), a proper scale of the depressions is obtained. By using laser processing of the tool surface a welding joint portion may even be defined on the forming tool in a post processing process, e.g. on an existing forming tool, independent of the process of preparing the forming tool / tool surface. By applying the micro-scale roughening to the tool, the welding joint portion may be produced in the same replicating step as the part itself. The master surface has a microscale structuring with a lateral master patterning and a vertical master profile. Accordingly, the replicated part has a microscale texture with lateral replica patterning and a vertical replica profile.

Further according to some embodiments of the method of joining first and second parts, at least one of the first part and the second part is made of a thermoplastics material.

Further according to some embodiments of the method, the first part comprises a flexible web carrying the microscale textured replica surface with a lateral arrangement of microscale cone-like protrusions on at least a flange portion thereof. For example, such embodiments may be useful for assemblies comprising a functionalized flexible web integrated therein, or for packaging purposes, or when using the flexible web as a cover for a closed container in food packaging, in medical packaging, in analytic devices, or similar applications.

A further aspect of the invention relates to a replication tool for producing a part with a microscale textured replica surface by replication, the replication tool comprising a tool surface defining a general shape of the part, the tool surface comprising at least on portions thereof a microscale structured master surface having a lateral master pattern and a vertical master profile, wherein said microscale structured master surface has been provided by localized pulsed laser treatment adapted to generate microscale phase explosions. Preferably, the vertical master profile has a peak-to-peak amplitude of at least 0.5 μm, and the lateral master pattern has an area density of microscale master features of at least $5000/\text{mm}^2$.

The replication tool for the replication process in question, e.g. a mould for injection moulding or a roller for extrusion coating, has a tool surface defining the general shape of the part to be formed and may be provided in a conventional manner and using conventional tooling materials as known in the art, such as tool steel or 2017 aluminium. The microscale surface structuring is applied as a post treatment of the tool surface by means of a pulsed laser directly scanned over the tool surface. A suitable pulsed laser may be, but is not limited to, an industrial picosecond-laser operating in the near infrared, such as at 1064 nm. The exposure of the surface to the pulsed laser radiation is adapted to generate microscale phase explosions. This includes localised melting of tool material on the tool surface, evaporating molten tool material, and ejecting molten and evaporated material in microscale eruptions from the melt surface, thereby forming a densely packed arrangement of microscale crater-shaped depressions. The localized pulsed laser treatment is adapted to produce a micro-porous structure, wherein the micro-porous structure is formed by a densely packed

arrangement of crater-shaped microscale depressions with outwardly sloped side walls. The obtained microscale structured master surface has a lateral master pattern and a vertical master profile as described above. Since the post-treatment applied here does not require the precise micro-milling of a specific pre-determined shape of the master structure, such as a regular array of micro-cones, the post-treatment may be applied using cheaper equipment. Furthermore, this post-treatment adapted to generate a microscale porous surface from microscale phase explosions is faster to apply than e.g. micro-milling of microscale features. Furthermore, as also mentioned above, the microscale phase explosions generate microscale crater-shaped depressions with sloped sidewalls that are well suited for fast replication processes, such as injection moulding and extrusion coating. Amongst others, the crater shape with sloped sidewalls facilitates easy releasing of the shaped items from the tool surface at the end of the moulding process (de-moulding).

Further according to one embodiment of the replication tool, the tool surface is made of a metal, such as aluminium or steel. The tool surface has to be suited for the fast replication processes for which the method is intended. The tool surface comprising the microscale master structure can be directly produced on a mould surface for contacting the replication material and/or on an inlay attached to the inside of a mould. It is understood that the tool surface may be broken up in sub-surfaces that form part of the mould as is customary in tool design for fast replication processes, such as injection moulding or extrusion coating. Examples of commonly used metals that are also suitable for the present invention include, but are not limited to, aluminium alloys of the types 2017, 1050 or 5754, or tool steel, such as ”Sandvik Corona C60”, Orvar2343 or similar.

Further according to one embodiment of the replication tool, the microscale structured master surface is a lateral arrangement of polydisperse microscale master features. The term polydisperse refers to microscale features having varying transverse dimensions as seen in a vertical projection. Typically, the polydisperse dimensions are characterized by a statistical distribution having a centre value and a spread. The transverse dimensions may be specified as transverse linear dimensions characteristic of the lumen defined by the crater-shaped depression. Given the irregular nature of a polydisperse arrangement, transverse dimensions can also be defined in combination by specifying an area covered by the crater-shaped depression. An equivalent linear dimension characterizing a given crater-shaped depression may then be defined as the diameter of a circle with the same area. The microscale master features on the master surface are preferably densely packed, with neighbouring crater shaped depressions only being separated from each other by a ridge having a width that is comparable to or preferably less than the transverse linear dimension characterizing the crater-shaped depression.

Further according to some embodiments of the replication tool the microscale master features are crater-shaped depressions. Typically the crater-shaped depressions appear more or less circular as seen in a vertical projection. Furthermore, the crater-shape implies an outwardly sloped sidewall providing a positive release angle facilitates de-moulding of the shaped item.

Further according to one embodiment of the replication tool, the vertical profile of the microscale structured master surface has a peak-to-peak amplitude of at least 0.5 μm or at least 1 μm and below 30 μm, below 20 μm, or preferably below 10 μm.

Further according to one embodiment of the replication tool, the lateral pattern of the microscale structured master surface has an area density of microscale master features of at

least 5000/mm^2, at least 8000/mm^2, or at least 10000/mm^2. Thereby, the replication tool is particularly useful for producing parts comprising a microscale textured surface with a reasonably densely packed lateral distribution of microscale features. When using a part with such a densely packed microscale texture in flange portions for forming ultrasonic joints, high precision, fluid tight ultrasonic joints with improved bond strength are achieved.

It should be noted, however, that the process according to the present invention will not exceed an inherent upper limit for the area density of the microscale lateral structuring. Such an inherent limit is due to the fact that the microscale features produced by the microscale phase explosions according to the present invention require a minimum footprint in order to be resolved. While the present invention produces polydisperse features with a distribution that may include submicron elements, their average (most prominent) lateral dimensions are in the microscale. Increasing the area density of the microscale features results in an increasing probability for the occurrence of overlap between adjacent microscale features. Above a critical overlap, the microscale features are overlapping to such an extent that they appear merged and effectively have a much larger lateral extension than a targeted feature size of individual, unmerged microscale features. As a consequence, above a critical area density such merged features increasingly dominate the actual feature size produced on the replication tool.

In a characterization of the microscale surface structure of the master surface, e.g. by commonly known image analysis techniques applied to micrographs thereof, the merged features are then counted as a single feature with a larger lateral dimension or foot print. This effect is best seen in a graph showing the area density of microscale features, e.g. counted in a given surface portion by means of image analysis, as a function of the laser energy exposure applied to that surface portion. By way of example, such a graph is shown in Fig.19. The data shown has been obtained by an analysis of the microscale structuring applied to more than 70 replication tool blanks (tool grade aluminium as specified elsewhere in this application) using the method according to the invention. The ordinate shows the exposure dose expressed in terms of the number of repetitions divided by the scan speed; the co-ordinate shows the area density of holes detected by an image analysis performed on micrographs of the processed surface; and the marker size indicates the size of the detected feature determined by the same image analysis algorithm. In an initial regime at low exposure, the individual microscale features are resolved and all have essentially the same size. The initial regime covers a low density regime up to about 5000/mm^2 where the distribution of the microscale features may be considered as sparse. In an intermediate exposure regime above about 5000/mm^2, the microscale features may be considered as more and more densely packed, reaching a critical density of about 12000/mm^2, where overlap of adjacent microscale features begins to become significant. The critical density is the maximum achievable density for a given system, which in the example of Fig.19 is about 12000/mm^2. Other material systems and laser processing set-ups may have a different maximum achievable area density, such as about 100000/mm^2, or about 50000/mm^2, or 20000/mm^2, or about 15000/mm^2. An inherent limit to the maximum achievable area density is given by the requirement of microscale dimensions of the lateral structuring as achieved by the present invention. Increasing the exposure beyond the critical value then only results in merging of the microscale features and in a deterioration of the desired patterning. In the example of Fig.19, a significant decrease of the area density of microscale features to below 5000/mm^2, accompanied by a corresponding increase of the average feature size is observed. When the microscale structure of the replication tool master surface is transferred onto a replicated item to form a microscale surface texture for the

enhancement of a wetting behaviour, a sparse distribution of microscale features may prove insufficient to provide a significant wetting behaviour enhancement – if any at all. In a preferred exposure regime around the maximum achievable area density of about 100000/mm^2, or about 50000/mm^2, or 20000/mm^2, or about 15000/mm^2, or about 12000/mm^2, the microscale features are adequately dimensioned in their lateral extend, yet are packed sufficiently dense so as to achieve a significant wetting behaviour enhancement. An adequate range may be determined by an exposure experiment as outlined in Fig.19, wherein preferably the area density is at least 60%, at least 70%, at least 80%, or at least 90% of the maximum achievable area density of microscale features. Above a critical exposure, in the regime where merging becomes more and more dominant, the wetting behaviour enhancement of the replicated item also deteriorates more and more.

Further according to one embodiment of the replication tool, the microscale master features have an aspect ratio of a vertical dimension to a lateral dimension of at least 1:2, or about 1:1, wherein the vertical dimension is the peak-to-peak amplitude and the lateral dimension is the square root of the average footprint area per microscale master feature, which for a given microscale structured surface area is calculated as the inverse of the area density of microscale master features per area, i.e. the area of the given surface in lateral projection divided by the count of microscale features in that area.

Advantageously according to a further aspect of the invention, the above-mentioned replication tool and methods are adapted such that the lateral arrangement of microscale protrusions in addition to the flange portions includes further portions on the surface of the first part. Thereby the further portions on the surface of the first part may be functionalised by applying a microscale textured replica surface to these further portions in the replication process. The replication tool is adapted by applying the above-mentioned laser treatment to generate microscale phase explosions also to further portions on the tool surface, in addition to flange portions. The parameters of the laser treatment may be kept the same or set differently for different portions of the tool surface to generate different microscale structured master surface portions depending on the purpose of the respective portions of the microscale textured replica surface to be produced therefrom. The purpose for the microscale texturing of the replicated flange portions is to act as energy directors, whereas the purpose of the microscale texturing of the replicated further portions may be another functionalization. In particular, a microscale textured replica surface produced according to any of the herein disclosed methods also exhibits enhanced wetting properties. For example, the microscale textured replica surface may exhibit enhanced hydrophobicity or even superhydrophobicity, provided that the surface material is hydrophobic. Alternatively, a microscale textured replica surface produced according to any of the herein disclosed methods may also exhibit enhanced hydrophilicity, provided that the surface material is hydrophilic.

The term "wetting properties" refers to the interfacial interactions in a system comprised of three states of matter, a solid, a liquid, and a gas, and can be quantified by a contact angle. The line connecting all three interfaces, e.g. solid-liquid, solid-gas, liquid-solid, is denoted the three phase-contact line. The contact angle is defined as the angle between the tangents of the liquid-gas and the liquid-solid interphases perpendicular to the three-phase line at any intersection of the two tangents on the three phase line. The wetting properties between a solid and a liquid in a three phase system are considered enhanced with respect to the wetting properties of a flat surface if the apparent macroscopic contact angle is altered by the structure on the surface, wherein the wetting properties of a system with a solid-liquid contact angle smaller than 90° (philic behaviour) is considered enhanced if this contact angle

is reduced by the modification (philic enhancement). Likewise, the wetting properties of a system with a solid-liquid contact angle greater than 90° (phobic behaviour) is considered enhanced if this contact angle is increased by the modification (phobic enhancement).

In some embodiments, the laser treatment of the tool surface may be the same for all portions, since the microscale texturing may simultaneously act as microscale energy directors and provide enhanced wetting properties as compared to a flat unstructured surface of the surface material. Alternatively in some embodiments, the laser treatment of the tool surface may be varied for different portions thereof. For example, the laser treatment of flange portions may be optimised for the purpose of forming energy directors for use in the formation of an ultrasonic joint, whereas the laser treatment of further portions of the tool surface may be optimised for producing enhanced wettability on the further portions of the replicated part.

Advantageously according to some embodiments, the further portions of the microscale textured replica surface on a formed item are adapted to exhibit enhanced hydrophobicity, or even super-hydrophobicity. Further advantageously the replica material is hydrophobic or the microscale textured replica surface is covered with a hydrophobic layer.

Alternatively according to some embodiments, the further portions of the microscale textured replica surface on a formed item are adapted to exhibit enhanced hydrophilicity, or even super-hydrophilicity. Further advantageously the replica material is hydrophilic or the microscale textured replica surface is covered with a hydrophilic layer.

The microscale texturing of the replicated first part produced by replication from a microscale structured master surface on a replication tool may thus serve multiple purposes. This may e.g. be useful in providing a packaging having a functionalised surface, such as a superhydrophobic surface, and at the same time allowing for a formation of a precise and reliable ultrasonic joint with a high degree of design freedom. In a further example, such a dual use of the microscale texturing applied to flange portions and further portions may be useful in microfluidics, when forming sealed channels and/or reservoirs that may thus be provided with inner surfaces with an enhanced wettability, such as enhanced hydrophobicity or enhanced hydrophilicity as explained above.

In the context of this application, a material is referred to as hydrophobic, if a flat surface thereof is characterized by a water contact angle of above 90 degrees, such as above 95 degrees, such as about or above 100 degrees. Accordingly, a material is referred to as hydrophilic, if a flat surface thereof is characterized by a water contact angle of below 90 degrees, such as below 85 degrees, such as about or below 80 degrees. For example, a flat surface of the hydrophilic plastics material acrylonitrile butadiene styrene (ABS) may have a water contact angle of about 81 degrees.

C.2 Brief description of the drawings

Preferred embodiments of the invention will be described in more detail in connection with the appended drawings, which show in

FIG. 1a-c SEM micrographs of a microscale structured master surface at different

magnifications,
FIG. 2a-c SEM micrographs of a microscale textured replica surface at different magnifications,
FIG. 3 a SEM micrograph of another microscale structured master surface,
FIG. 4 a SEM micrograph of the microscale textured surface of an injection moulded item (polypropylene) using an isotherm process,
FIG. 5 a SEM micrograph of the microscale textured surface of an injection moulded item (polypropylene) using a variotherm process,
FIG. 6 schematically, the surface modification of a tool surface by pulsed laser treatment to generate microscale phase explosions,
FIG. 7 schematically, an injection moulding process according to one embodiment of the invention,
FIG. 8 schematically, an extrusion coating process according to a further embodiment of the invention,
FIG. 9 schematically an ultrasonic welding process according to one embodiment of the invention,
FIG. 10 schematically an assembly formed using an ultrasonic welding process as shown in Fig.9,
FIGS.11–14 four graphs plotting hole size and hole density on a microscale structured master surface for different parameter settings of the pulsed laser treatment of the tool surface, and in
FIGS.15–18 four graphs plotting hole density on a number of microscale structured master surfaces against the scan speed used during the pulsed laser treatment of the respective tool surfaces;
Fig. 19 a graph plotting hole density on a number of microscale structured master surfaces against the exposure in terms of repetitions divided by scan speed used during the pulsed laser treatment of the respective tool surfaces;
Figs. 20a-d SEM micrographs of

(a) cone like protrusions in an Al2017 mould at a 30° view angle,
(b) cone like protrusions in an Al2017 mould at a 0° view angle,
(c) replication of the Al2017 mould in cyclic olefin copolymer, and
(d) an Orvar2343 steel surface modified using the presented technology as seen at an 0° view angle;

Fig. 21 Schematic drawing of a high aspect ratio chip;
Fig. 22 Actual dimensional data obtained by confocal microscopy on the chip of Fig.22, overlaid with the nominal dimensional data as obtained from the corresponding CAD-design;
Figs. 23a-d - (a-d) SEM micrographs of

(a, c) a laser modified mould on indicated length scales,
(b, d) the corresponding injection moulded piece seen at 30° tilt,
(e-f) optical micrographs of
(e) unbonded microscale structured energy directors, and
(f) an ultrasonic welding seam using the energy directors,
(g-h) cross-sectional SEM micrographs of
(g) a chip prior to ultrasonic bonding, and
(h) an ultrasonic weld formed using the present technique.

C.3 Detailed description of preferred embodiments

C.3.1 Replication Tool

Examples of suitable materials are materials commonly used as inlays or mould materials in e.g. injection moulding or extrusion coating processes. These materials of the tool surface suited to be modified by pulsed laser treatment to generate microscale phase explosions include Aluminium alloys, such as so-called 1050 aluminium, 5754 aluminium, or 2017 aluminium, as well as tool steel, such as Sandvik corona C60 and Orvar2343.

Figs.1a-c show micrographs taken by scanning electron microscopy (SEM) of an aluminium tool surface, more particular a tool surface made of 2017 aluminium, which has been modified by pulsed laser treatment using a picosecond laser with a maximum power output of 50 W operating at a pulse frequency of 200 kHz and at a wavelength of 1064 nm. The surface was scanned repetitively at a given power setting in per cent of the maximum power output and with a given speed. The laser beam was incident on the tool surface in a vertical direction, wherein the laser was slightly defocused by shifting the focal point by 1.3 mm in a vertical direction with respect to the tool surface to be modified. While the apparent spot size was about 50 µm on the surface, a line scan of the laser produced a modified trace width of about 10 µm ± 5 µm. A broader trace as the one shown in Fig.1a and 1b was obtained by a meander line scan with adjacent legs of the meander shifted in a direction perpendicular to the scanning direction. Thereby an arbitrary area can be covered by a microscale surface structure. As best seen in Fig. 1a, the laser treatment results in an ablation of some of the tool surface material. The parameters of the pulsed laser treatment are, however, adjusted such that the bottom of the trace exhibits a lateral arrangement of polydisperse microscale master features, see e.g. Fig.1b. The microscale master features obtained by this pulsed laser treatment are crater-shaped depressions. The crater-shaped depressions at the bottom of the trace are a consequence of the localized pulsed laser treatment generating microscale phase explosions.

Fig. 3 shows a SEM micrograph of tool surface made of tool steel, more particular Sandvik corona C60 tool steel, which has been modified by pulsed laser treatment using the same picosecond laser with a maximum power output of 50 W operating at a pulse frequency of 200 kHz and at a wavelength of 1064 nm. Again, the surface was scanned repetitively at a given power setting in per cent of the maximum power output and with a given speed. The laser beam was incident on the tool surface in a vertical direction, wherein the laser was slightly defocused. Also here, the localized pulsed laser treatment generates microscale phase explosions resulting in a lateral arrangement of polydisperse microscale master features, wherein the microscale master features are crater-shaped depressions.

C.3.2 Replicated Item

Figs. 2a-c show an example of a microscale textured replica surface on a mould insert for injection moulding, as observed in a scanning electron microscope at different magnifications, wherein the width of the image corresponds to 1.2 mm in Fig.2a, 0.23 mm in Fig.2b, and 0.03 mm in Fig.2c. The mould insert for injection moulding was designed and fabri-

cated in 2017 aluminium alloy (MetalCentret, Denmark) by micro milling using conventional techniques to provide a tool surface defining the general shape of the part to be fabricated. To create the microscale structured master surface on the tool surface, a 1064 nm, 200 kHz, 50 W (max power) picosecond laser (FUEGO, Time Bandwidth) mounted in a microSTRUCT vario (3D-Micromac AG) was used to generate microscale phase explosions on the tool surface, thereby producing a densely packed lateral arrangement of microscale crater-shaped depressions. The area intended for structuring was irradiated by the laser in parallel lines separated by 20 µm. In the example shown in Figs.2a-c, this pattern was repeated 20 times, and the laser power was set to 25% of the max power. Focus was offset by +1.3 mm above the surface. The microscale structured master surface produced in this example consisted of 10 lines (200 µm wide) and was 305.5 mm long. The part with the microscale textured replica surface thereon was replicated from this replication tool with the microscale structured master surface on its tool surface using a Victory 80/45 Tech injection moulder (Engel, Schwertberg, Austria). The polymer substrate used for injection moulding was cyclic olefin copolymer (COC) TOPAS grade 5013L-10 (TOPAS Advanced Polymers, Düsseldorf, Germany) with a glass transition temperature (Tg) of 135 °C. Injection temperature of the polymer was 270 C and the mould temperature was kept stable at 120 C. The injection moulding was performed in isothermal mode. The resulting microscale surface texturing is depicted in Figs.2a-c. The microscale textured replica surface on this first part is adapted to act as microscale energy directors for forming an ultrasonic welding joint with a cooperating second part.

Further examples for the microscale textured replica surface on replicated parts are given in Figs.4 and 5. To produce these replica surfaces, the laser structured aluminium insert was installed in a Victory 80/45 Tech injection moulder (Engel). The polymer substrate used for injection moulding polypropylene HD120MO (Borealis) with a Heat Deflection Temperature (0.45 N/mm^2) of 88 °C. Injection temperature of the polymer was 255 °C with an injection pressure of 1200 bar. Both variotherm and isotherm injection moulding processes were tested.

Parameters specific for isotherm injection moulding:

- Temperature of microscale structured aluminium insert face = 80 °C. (constant)
- Temperature of "backside" mould = 60 °C. (constant)

Parameters specific for variotherm injection moulding:

- Temperature of structured aluminium insert face = 120 °C. (injection)
- Temperature of "backside" mould = 100 °C. (injection)
- Active cooling was applied immediately after polymer injection for the duration of the holding time (60 seconds) followed by and additional cooling time (60 seconds). This resulted in a final mould temperature of 40-50 degrees.

The respective surfaces have been characterised with respect to the shape of the microscale features on the microscale textured surface of the replicated item, see Fig.4 and Fig.5. The isothermal process results in a surface texture with rounded tops, see Fig.4, and the variothermal process results in a surface texture with a hairy appearance ("pulled polypropylene"), see Fig.5. Both surfaces faithfully replicate the lateral pattern of the master, but only provide a low fidelity replication of the vertical profile of the master. Nevertheless, both processes result in a fast replication of parts with microscale energy directors on flange portions thereof.

The isothermal process is preferable for high throughput or high volume production, because the isothermal moulding process is not time limited by any process step(s) involving temperature adjustments of mould and/or mould inserts, whereas the variotherm moulding process is partially time limited by one or more process step(s) involving temperature adjustments of mould and/or mould inserts.

C.3.3 Replication Process

Fig.7 shows schematically an injection moulding process for producing a replicated part 4. The process uses a mould having mould parts 1a and 6, wherein mould part 6 has an insert 1b. Tool surfaces 2a, 2b, 7 define a general shape of the replicated item 4. Tool surfaces 2a, 2b are provided with microscale structured master surfaces 3a, 3b, 3c, 3d, which are replicated on the item 4 as microscale textures 5a, 5b, 5c, 5d respectively.

Fig. 8 shows schematically an extrusion coating process for coating a substrate web S, with a coating 14. The process uses a roll 11, 11a with a tool surface 12, 12a defining a general shape of the coating. The tool surface comprises microscale structured master surfaces 13, 13a, which are replicated as microscale surface texture 15 on the coating 14. A microscale structured master surface 13 may be applied directly to the tool surface 12 of the roll 11 and/or a microscale structured master surface 13a may be applied to the tool surface 12a of a replication tool insert 11a for attachment to the roll 11.

C.3.4 Localized Pulsed Laser Treatment Generating Microscale Phase Explosions

Fig.6 shows schematically the configuration of the set-up for localized pulsed laser treatment of a tool surface 2 on a replication tool 1 to generate a microscale structured master surface 3 by scanning a pulsed laser beam 99 over the tool surface.

C.3.4.1 EXAMPLE

The example illustrates different ways of identifying suitable laser processing parameters for modifying a given tool surface to obtain a microscale structured master surface.

Aluminium 2017 (available from "Metalcenteret" Glostrup, Denmark) was surface structured using a 1064 nm, 200 kHz, 50 W picosecond laser (FUEGO, Time Bandwidth) mounted in a microSTRUCT vario (3D-Micromac AG). To perform the surface structuring, the area intended for structuring was irradiated by the laser in parallel lines separated by 20 μm. Every second layer was perpendicular to the previous, and so one set of perpendicular planes of lines is referred to as one "cross repetition". The laser power was set to 25% and 10 repetitions was conducted with focus offset +1.3 mm above the surface.

As illustrated in 11-18, the average dimension and standard deviation of the hole sizes may be adjusted by varying parameters such as laser power in percent of maximum power output,

scanning speed, number of cross repetitions and z offset of the focus plane. To identify the optimal parameter settings for achieving a desired hole size population and hole density in the alloy in question, one may map the parameter space of the laser settings. When replicated in polymer, the hole size population and hole density will determine the surface structure and roughness and hence the final wetting properties of the polymer piece. In the example below, the parameter space was for the

- Laser power in percent of the maximum power of 50 W: from 10 to 100 (both included), in increments of 5;
- Scan Speed in mm/s: from 150 to 1950 (both included), in increments of 100; and from 600 to 4200 (both included), in increments of 200;
- Number of cross repetitions: from 3 to 39 (both included), in increments of 2;

It may be noted that similar surface characteristics may be achieved using different parameter combinations. However, to minimise time consumption for the laser process, the parameter coordinate with the highest (scan speed / cross repetition) value, and hence lowest process time, is preferred.

A recommended method to reduce the number of parameters and experiments is by locking parameter pairs in a fixed ratio, such as keeping (laser power / scan speed) constant, see Fig.11 and Fig.12, where the numerical value of the ratio of (laser power (in percent of the max power of 50 W) divided by the scan speed (in mm/s) is kept constant at 25E-5 (= 0,00025) or 50E-5 (= 0,0005) and allows for identification of the desired modification characteristics: both figures show peaks in hole density X. Likewise, the numerical value of the ratio of the number of repetitions divided by the scan speed (in mm/s) can be kept constant, see Fig.13 and Fig.14, where this ratio is kept constant at 1E-2 (= 0.01) or 2E-2 (= 0.02) and allows for identifying desired modification characteristics. As can be seen in Fig. 14, the high intensity (slow speed) results in few but large holes, whereas Fig. 13 shows that for the numerical value of the ratio of repetitions over scan speed (in mm/s) equal to 0.01 a more densely packed and uniform hole formation is achieved.

Figs.15-18 show four graphs plotting hole density against the scan speed used during the pulsed laser treatment of the respective tool surfaces. At speeds $\leq$ 1250 mm/s, the hole density is consistent regardless of other parameters than speed, and it is concluded that writing speed is the main determining factor in this regime. At speeds $\geq$ 1250 mm/s, the hole density varies with the number of cross repetitions. This is true, even when the product (power X repetitions) is kept constant, (see Fig. 16). Marker size represents cross repetitions in Fig.15 and (cross repetitions X power) in Fig.16. Regardless of the parameter settings used to achieve a desired hole density, the coefficient of variance (CV) of hole size is observed to be stable in the regime where (speed $\geq$ 1250 mm/s), see Fig.17, and accordingly for the standard deviation (STD), see Fig.18. Marker size represents hole size CV in Fig.17 and hole size STD in Fig.18. Similarly, the laser focus parameter space may be mapped to identify applicable laser settings.

C.3.5 Ultrasonic Welding

Fig. 9 shows schematically a process for forming an ultrasonic welding joint between a first part 40 and a cooperating second part 50. The first part 40 is a replicated part produced using a microscale structured replication tool in a method as described before. The first part 40 has a general shape as defined by the tool surface of the replication tool. The general shape includes flange portions 41, 42 carrying microscale textured replica surfaces 43, 44 with a lateral arrangement of microscale protrusions, and a recessed portion 45. The second part 50 has cooperating flange portions 51, 52 facing towards the flange portions 41, 42 of the first part and are aligned with these flange portions 41, 42 of the first part. For welding, the first and second parts 40, 50 are brought in contact with each other such that the tops of the microscale protrusions on the first flange portions 41, 42 form point contacts with the corresponding second flange portions 51, 52. The parts are clamped in an ultrasonic tool 60, here schematically represented by an ultrasonic horn. The ultrasonic tool 60 is adapted for applying ultrasonic energy while applying a uniaxial pressure in the direction of arrow 61 across the contact interface. The ultrasonic energy is dissipated in the contact region, thereby melting the material with an axial pressure applied across the interface to form a welding joint. Fig. 10 shows schematically the assembly 90 formed by welding the first part 40 and the second part 50 together, thereby forming a cavity 95 defined by the recess portion 45 of the first part 40 and the second part 50. The second part 50 forms a lid, which is sealed fluid tight to the first part 40 by the ultrasonic welding joints 92, 94. The following is an example of a welding joint formed between a polymer part and a sheet of cyclic olefin copolymer (COC).

C.3.5.1 EXAMPLE

Ultrasonic welding of the polymer part to a 152 μm thick COC sheet (TOPAS grade 5013S-04, TOPAS Advanced Polymers) was done using a Telsonic-USP4700 ultrasonic welder (Telsonic, Herstad+Piper, Denmark). The chip welding was conducted by depositing 45 J at 90% amplitude, 20 kHz and with a normal force on the piece of 600 N. The normal force could generally be estimated from area (x y cross section) as 10 MN/m^2: area=(305.51e-3*200e-6)m^2 =(6.1102e-05)m^2 6.1102e-05 m^2 * 10 MN/m^2 = 611 N. In a similar fashion, the amount of energy required can be estimated from the volume of the energy directors.

C.3.5.2 EXAMPLE

Referring to Figs.20-23 in the following, a detailed example is given, which shows the high precision and improved strength of fluid tight ultrasonic bonds as achieved by the invention.

The example concerns the use of microscale structured energy directors (ED) for ultrasonic welding of microfluidic systems with a lateral arrangement of microscale features, which in this example are referred to as micropillars. The micropillar EDs are produced by replicating microscale crater-shaped depressions in a mould to obtain cone like protrusion (CLP) structures on the surface of the replicated part. The microscale crater-shaped depressions are introduced on an injection mould surface using a pico-second laser and may therefore be added to any mould surface accessible to a pico-second laser beam. The technology is

demonstrated on an injection moulded microfluidic device featuring high-aspect ratio (w × h = 2000 μm × 550 μm), free standing channel walls, where bonding is achieved with no detectable channel deformation. Bonding strength is similar to conventional EDs and the fabricated system can withstand pressures of over 9.5 bar.

For device fabrication based on replication techniques (e.g. hot embossing and injection moulding), the replication tool has the inverse structure and the ED structures thus have to be realized as depressions in the bottom of the cavity structure used to define the channel wall. ED structures can be realized, e.g., by micro milling, which is a rapid mould tool fabrication process, though the size of the milling tool limits the ED dimensions that can be realized. Milling tools are made as small as 10-50 μm, yet it is often not feasible to make EDs on high-aspect ratio wall structures by milling, since the drill aspect ratio is often limited to 1:3, and the micro mills are short and mounted on large shanks.

In this example, micropillar EDs are used for ultrasonic welding (UW) of microfluidic systems. The EDs are formed by introducing cone-like protrusion structures as a back-end processing of replication moulds using a picosecond laser. The micropillar EDs have the substantial advantage over traditional EDs that they can be defined on any surface accessible to a high energy pico-second laser beam. Moreover, the micropillar EDs can be introduced in designated areas on the tool, and the width of these areas can be chosen independently from the heights of the EDs contrary to traditional EDs, where larger widths are accompanied by higher structures. The CLPs are formed stochastically within the designated area exposed to the laser treatment, so only laser treatment of the general ED layout/shape is required, not an individual laser shaping of each of the individual CLPs. In the example, the technology is demonstrated for an aluminium mould. In addition thereto the CLP formation is verified for tool steel as used for high-throughput industrial moulds. To characterise the performance of the micropillar EDs, CLP-EDs are compared to micromilled EDs with respect to (1) welding strength, (2) structural deformation of a free-standing high-aspect structure, and (3) formation of particles during welding. No significant particle formation was induced by the process in the example.

C.3.6 Chip fabrication

Injection moulding was carried out using a custom-made moulding tool comprising a 50 mm diameter disk cavity with 12 luer inlets. The tool could be combined with mould inserts with structures machined in aluminium 2017 (Al2017). Prior to injection moulding, two types of ED structures were introduced: (1) Traditional EDs introduced by micro milling using a 60° helical engraving tool (#7025, DIXI Polytool, Le Locle, Switzerland). An apex depth of 100 μm was used (width=115 μm). (2) Microstructured CLP-EDs written using a FUEGO 1064 nm, 50 W picosecond laser (Time Bandwidth, 3D-Micromac AG, Chemnitz, Germany) mounted in a microSTRUCT vario (3D-Micromac AG). CLPs were introduced by scanning the designated areas with parallel lines (10 μm spacing), repeated 20 times at 50% power and 1000 mm/s with the focus plane 1.3 mm above the surface. The writing time was 200 seconds/cm^2.

To verify that CLPs can be produced in an equivalent manner also in other industrially relevant mould materials, writing of CLPs in high performance tool steel Orvar2343 (Metal-Centret, Glostrup, Denmark) was also demonstrated. Al2017 was preferred for mould making

in this example, due to its ease of machining. The injection moulding was carried out on a Victory 80/45 Tech hydraulic injection moulding machine (Engel, Schwertberg, Austria) using COC grade 5013L-10 (TOPAS Advanced Polymers GmbH, Frankfurt-Höchst, Germany) with injection and mould temperatures of 270 °C and 120 °C, respectively. Injection pressure was 1766 bar.

Fabricated chips were bonded to a 500 µm thick foil of COC grade 5013S-04 (TOPAS Advanced Polymers GmbH) by ultrasonic welding. UW was performed at ambient temperature using a Telsonic-USP4700 ultrasonic welder (Telsonic, Erlangen, Germany), depositing 25 J with 75% vibrational amplitude, a trigger force of 400 N and 0.5 bar welding pressure. With the fitted 2× booster and sonotrode, the vibrational amplitudes at the sample surface were approximately 44 µm.

C.3.7 Bonding strength

The bonding strength was assessed using the razor-blade test based on fracture propagation developed by Maszara et al., J. Appl. Phys. 64 (1988) p.4943, and employed by Matteucci et al., Microelectron. Eng. 111 (2013) p.294, to assess the bonding strength of thermal bonding in similar chips. To perform the test, two mould inserts with a milled $5.15\times42.5\times0.25$ mm^3 cavity were fabricated by micro milling. In this cavity, the first insert further featured a 40.5 mm long conventional ED made by conventional milling and the second insert featured a laser micromachined ED with CLPs on an area of 40.5×0.2 mm^2. The injection moulded structures were bonded to a COC foil as described above.

C.3.8 CLP and ED structures

Figures 20a and 20b show scanning electron microscopy (SEM) images of the CLPs written in the Al2017 mould. It is noteworthy that although the laser scanning is conducted in bundles of parallel lines, the formed CLPs are stochastically formed within the laser ablated area. This may be ascribed to the fact that the microphase explosions causing the CLPs are caused by a combination of metal impurities (alloy) picking up the energy, the pulsing nature of the laser beam and non-uniformity of the laser fluence distribution. The CLPs have a typical height and spacing of 10 µm and 10 µm, respectively. On average, the CLP area protrudes 47 µm from the plane of the tool (Fig. 23g). Note that the CLPs are locally convex depressions in the mould that hence facilitate easy demoulding during replication. Fig. 20c shows a SEM image of a COC replica of the mould. The replicated structures are observed to have rounded tops due to imperfect filling during replication. We found that operating at conditions yielding higher fidelity replication resulted in more difficult demoulding due to stronger adhesion between the mould and its replica. This rounding did not affect the performance of the EDs. Fig. 20d shows tool steel Orvar2343 ablated to produce CLPs similar to those demonstrated in Al2017.

Figures 23a and 23b show SEM images of the CLP-EDs in the Al2017 mould for fabrication of the high-aspect ratio microfluidic system. The images clearly show the feasibility of writing CLP-ED structures at the bottom of the trenches in the mould. Note that the separation and joining of bundles of laser lines do not alter the pattern and formation of CLPs. Thus,

CLP-EDs can be formed in any pattern or geometry. Corresponding SEM images of the injection moulded COC replica (Figs. 23c,d) clearly show that micropillar structures are well reproduced on the top of the high-aspect ratio wall.

Figures 23e and 23f show optical micrographs of the same structures pre and post UW. Due to the structure of the CLPs, the final micropillar CLP-EDs of the polymer chip are opaque (Fig. 23e). However, like conventional butt joint EDs, the joints are transparent post welding (Fig. 23f). It is noteworthy that no signs of trapped or compressed air are observed in structures surrounded by CLP-EDs, such as the pocket in the corner of the structure (Fig. 23e) where little or no gap is observed post UW in Fig. 23f. This indicates that the micropillar structure facilitates the escape of air during UW. SEM images Figs.23g and 23h highlight the position of CLP-ED polymer pre and post welding. Note the solidified polymer from the welding process in Fig.23h without any significant formation of "bonding flashes". This shows the high precision achieved with the bonding method of the invention.

C.3.9 Bonding strength

Bonding strengths in terms of the surface energy, γ (gamma), calculated from razor-blade tests are listed in Table 1.

Table 1: Bonding strengths.

Bonding method	Material	γ [J/m^2]
UW, conventional EDs	COC Topas 5013L-10	100±30
UW, CLP-EDs	COC Topas 5013L-10	122±23

C.3.10 High-aspect ratio microfluidic system

The performance of CLP-ED structures were tested in the described high-aspect ratio microfluidic system. Fig.21 shows a schematic drawing of the high aspect ratio chip with an outer channel 101, and an inner channel 102 separated by walls 103. Cross sections (I-I, II-II, III-III) for confocal imaging are indicated. A bundle of 20 laser patterning lines 104 were added on the walls 103. Note that the 20 lines 104 are separated into two bundles of 10 lines each (104a, 104b) at the corners, to keep a constant edge distance of 180 μm.

First, it was verified that the microfluidic channels were leak-tight when filled with an aqueous solution containing fruit dye. Further, pressure testing with gas applied to the outer channel while leaving the inner channel at ambient pressure showed that the devices (three tested) could sustain pressure up to at least 9.5 bar (maximum pressure available in the test).

Fig.22 shows confocal imaging data (thick lines) of the free-standing wall structures of the device along the cross sections 1-3 (cf. Fig. 21). The data of the three sections taken along the length of the parallel channel section (I-I, II-II, III-III) are overlaid on each other and fully coincide. The confocal imaging data are further overlaid with the corresponding CAD file used for the mould fabrication. From the confocal images, it is derived that the channel height of the welded structure matches that of the design (2000 μm) with a tolerance of ±4.2 μm. This value is smaller than the confocal image voxel height and we conclude that

any height difference is below our detection limit. This data further supports the particularly high precision of the bonding method according to the present invention.

In conclusion, the present example shows ultrasonic welding of microfluidic systems based on micropillar EDs according to one embodiment of the invention. The micropillar EDs are produced by replication of CLPs in aluminium, formed using a picosecond laser, and can be added to any mould surface accessible to a high power pico-second laser. The example demonstrated the technology by injection moulding microfluidic devices featuring high-aspect ratio structures and shown that ultrasonic welding of the devices is possible with no detectable channel deformation. The performance of the CLP-EDs was characterised showing that bonding strength is similar to conventional EDs, with no particle formation. The bonded devices could withstand 9.5 bar of hydraulic pressure without fracturing. The laser processing method has further been demonstrated to work in high endurance tool steel used for making high performance injection moulding tools. Furthermore, the method of the invention supports a modification rate of 200 seconds/cm^2 and post processing capabilities on full three-dimensional mould surface shapes, as long as these are optically accessible.

C.4 Claims

1. Method of producing a first part having a flange portion for use in the formation of an ultrasonic welding joint with a cooperating second part, the method comprising the steps of
    - providing a forming tool having a tool surface adapted to define a general shape of a part to be formed;
    - modifying at least portions of the tool surface by a pulsed laser treatment to obtain a replication tool with a microscale structured master surface with a lateral master pattern and a vertical master profile; wherein the pulsed laser treatment is adapted to generate microscale phase explosions on the tool surface, thereby forming the microscale structured master surface as a lateral arrangement of microscale crater-shaped depressions; and
    - using the replication tool to form the first part by the replication process, wherein the formed first part has the general shape defined by the tool surface, and wherein the formed first part comprises a microscale textured replica surface with a lateral arrangement of microscale cone-like protrusions produced by the microscale structured master surface on at least the flange portion of the first part, wherein the lateral pattern of the microscale textured replica surface has an area density of microscale cone-like protrusions of at least 5000/mm^2.
2. Method according to claim 1, wherein the replication process is one of injection moulding, hot embossing, compression moulding, and extrusion coating.
3. Method according to claim 1 or claim 2, wherein the microscale textured replica surface has a peak-to-peak amplitude of at least 0.5 µm, or at least 1 µm and up to 5 µm, or up to 10 µm, or even up to 30 µm.
4. Method according to any of the preceding claims, wherein the lateral pattern of the microscale textured replica surface has an area density of microscale cone-like protrusions of at least 8000/mm^2, or at least 10000/mm^2.
5. Method of joining a first part and a second part by ultrasonic welding, the method comprising the steps of

- producing the first part with microscale energy directors on a flange portion thereof by the method according to any one of claims 1-4;
- producing a second part having a cooperating flange portion;
- bringing the microscale cone-like protrusions on the flange portion of the first part in contact with the cooperating flange portion of the second part; and
- applying ultrasonic energy and pressure, thereby flattening out the cone-like protrusions, to form an ultrasonic welding joint between the first and second parts.

6. Method according to claim 5, wherein at least one of the first part and the second part is made of a thermoplastics material.
7. Method according to claim 5 or claim 6, wherein the first part comprises a flexible web carrying the microscale textured replica surface with a lateral arrangement of microscale cone-like protrusions on at least a flange portion thereof.
8. Replication tool for producing a part with a microscale textured replica surface by replication, the replication tool comprising a tool surface defining a general shape of the part, the tool surface comprising a microscale structured master surface having a lateral master pattern and a vertical master profile, wherein said microscale structured master surface has been provided by localized pulsed laser treatment adapted to generate microscale phase explosions, wherein the vertical master profile has a peak-to-peak amplitude of at least 0,5 μm, and wherein the lateral master pattern has an area density of microscale master features of at least 5000/mm^2.
9. Replication tool according to claim 8, wherein the tool surface is made of a metal, such as alloys of aluminium or steel.
10. Replication tool according to claim 8 or claim 9, wherein the microscale structured master surface is a lateral arrangement of polydisperse microscale master features.
11. Replication tool according to any one of claims 8-10, wherein the microscale master features are crater-shaped depressions.
12. Replication tool according to any one of claims 8-11, wherein the vertical master profile has a peak-to-peak amplitude of at least 0.8 μm, preferably at least 1 μm, or at least 2 μm.
13. Replication tool according to any one of claims 8-12, wherein the vertical master profile has a peak-to-peak amplitude below 30 μm, below 20 μm, or preferably below 10 μm.
14. Replication tool according to any one of claims 8-13, wherein the lateral master pattern has an area density of microscale master features of at least 8000/mm^2, or at least 10000/mm^2.
15. Replication tool according to any one of claims 8-14, wherein the microscale master features have an aspect ratio of a vertical dimension to a lateral dimension of at least 1:2, or about 1:1, wherein the vertical dimension is the peak-to-peak amplitude and the lateral dimension is the square root of the average footprint area per microscale master feature.

C.5 Abstract

The invention relates to a replication tool for producing a part with a microscale textured replica surface. The replication tool comprises a tool surface defining a general shape of the item. The tool surface comprises a microscale structured master surface having a lateral master pattern and a vertical master profile. The microscale structured master surface has

been provided by localized pulsed laser treatment to generate microscale phase explosions. A method for producing a part with microscale energy directors on flange portions thereof uses the replication tool to form an item with a general shape as defined by the tool surface. The formed item comprises a microscale textured replica surface with a lateral arrangement of polydisperse microscale protrusions. The microscale protrusions may be provided on a flange portion of a first part and are configured to act as energy directors when forming an ultrasonic joint with a cooperating flange portion of a second part.

Fig. 3

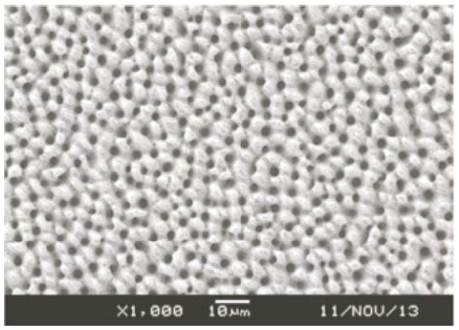

Fig. 4

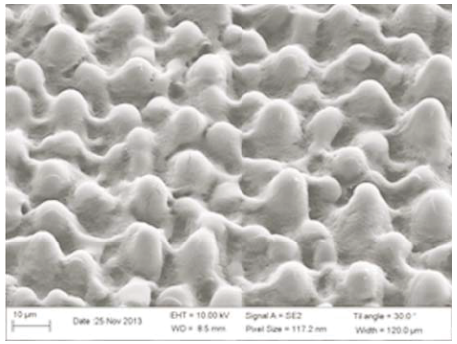

Fig. 5

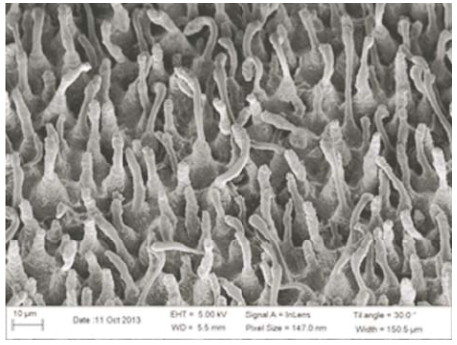

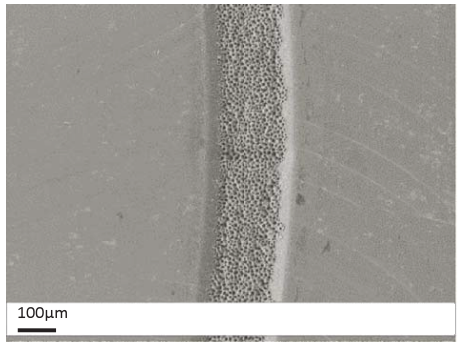

Fig. 1a

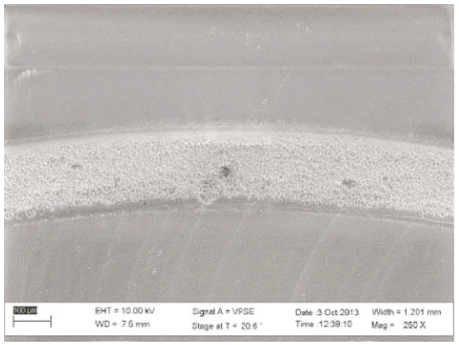

Fig. 2a

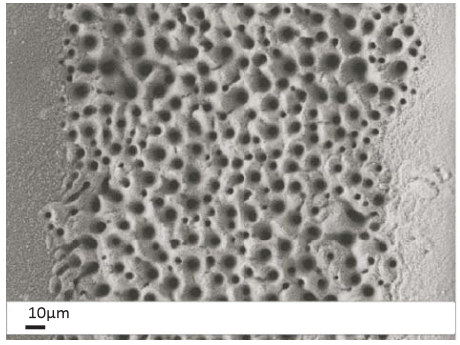

Fig. 1b

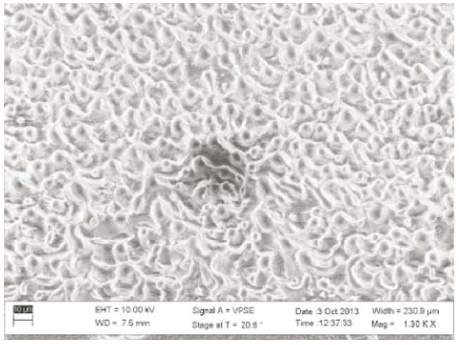

Fig. 2b

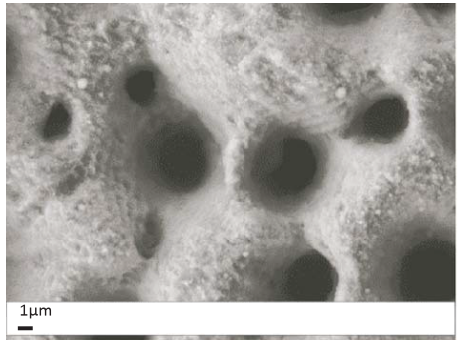

Fig. 1c

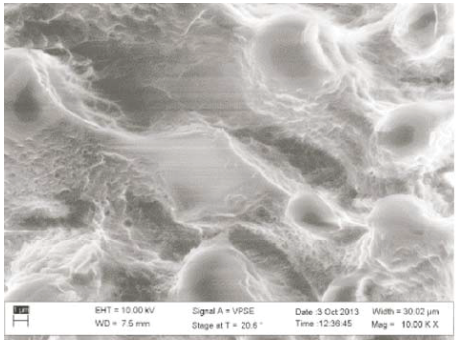

Fig. 2c

3/8

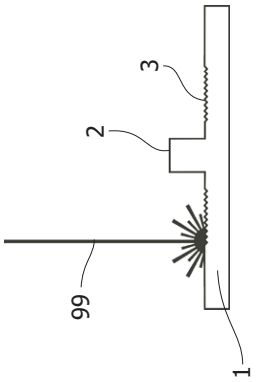

Fig. 6

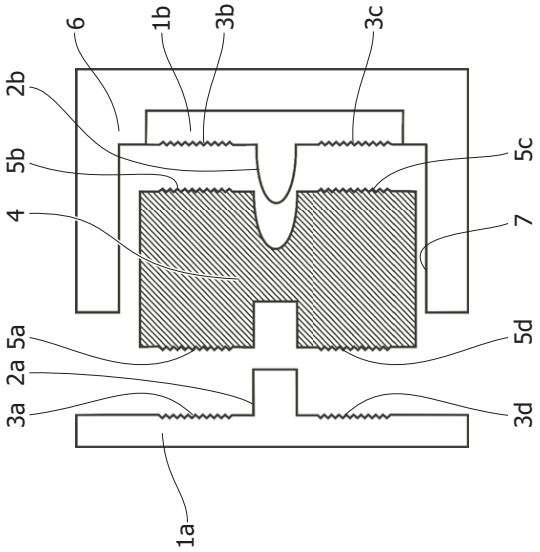

Fig. 7

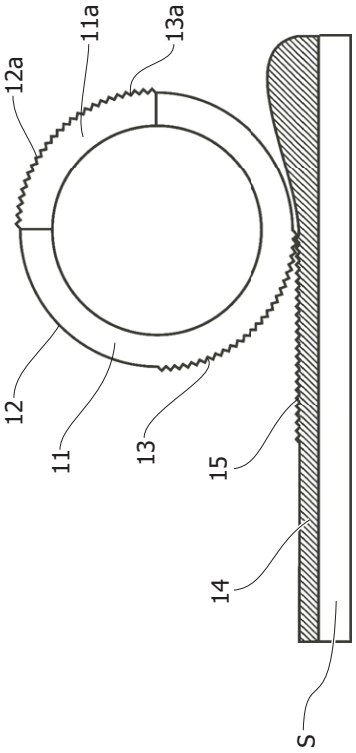

Fig. 8

4/8

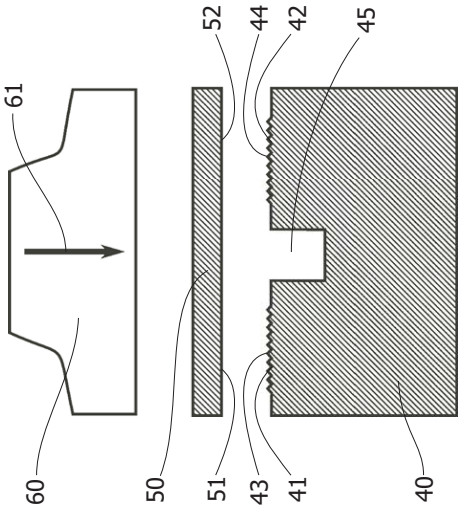

Fig. 9

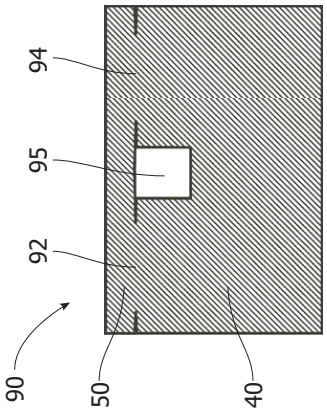

Fig. 10

5/8

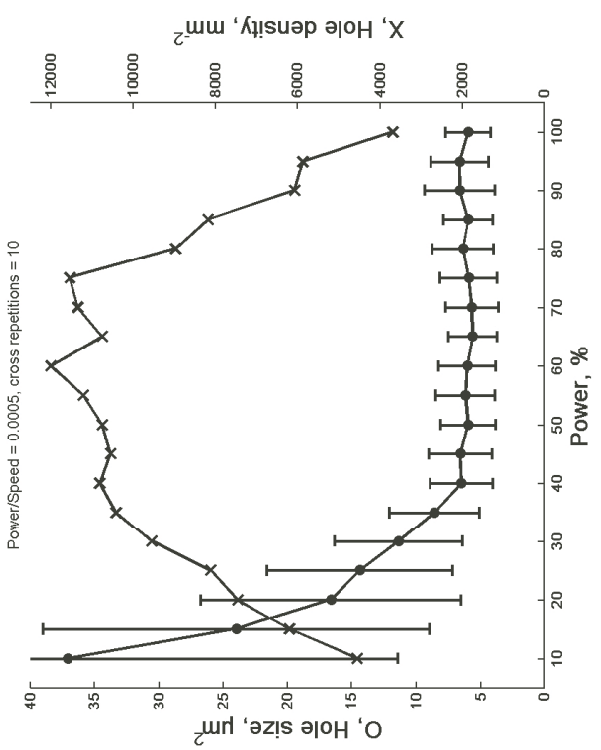

Fig. 11

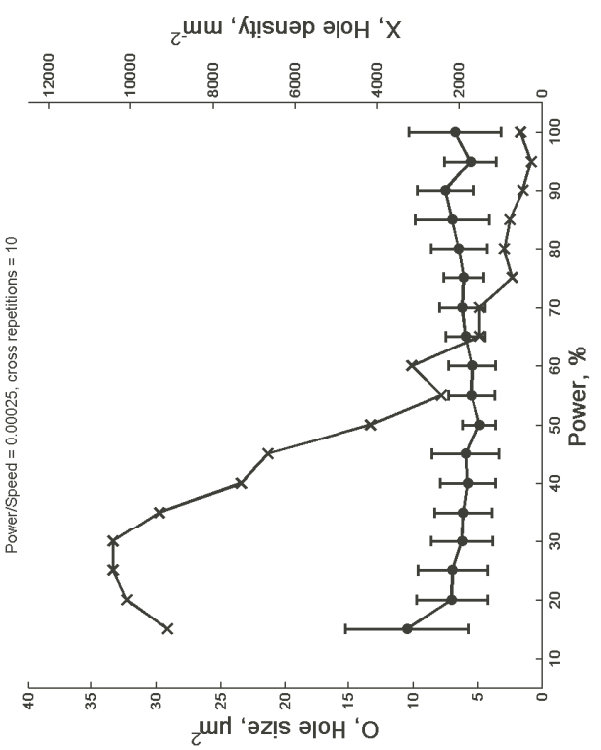

Fig. 12

6/8

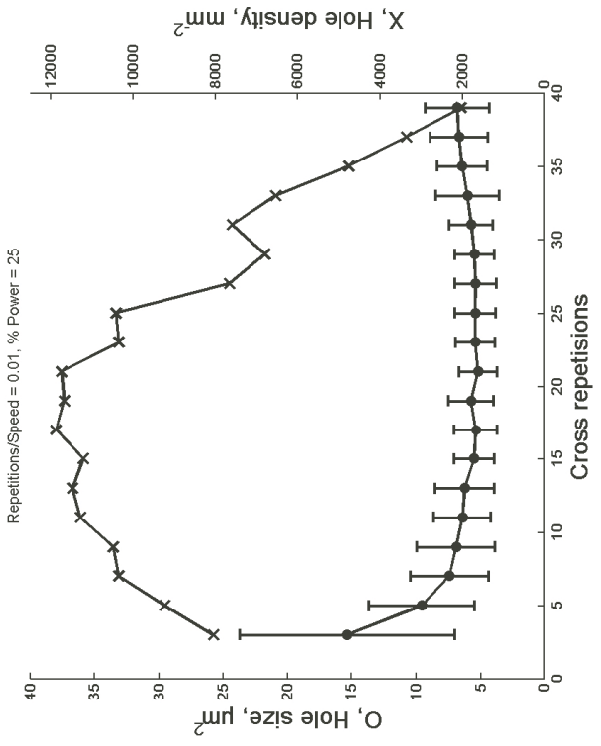

Fig. 13

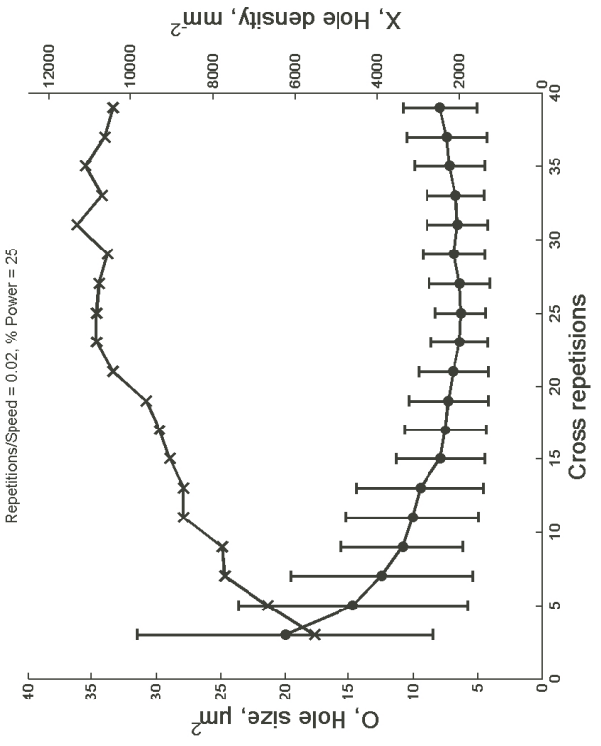

Fig. 14

7/8

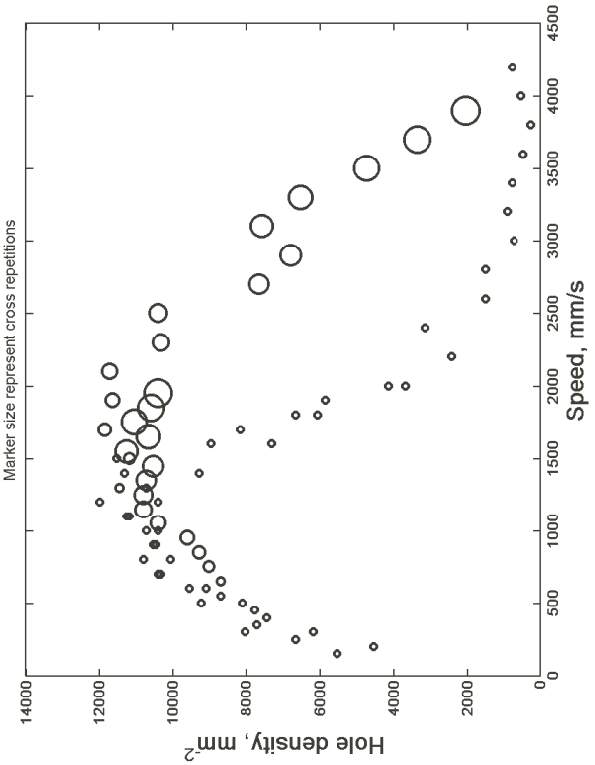

Fig. 15

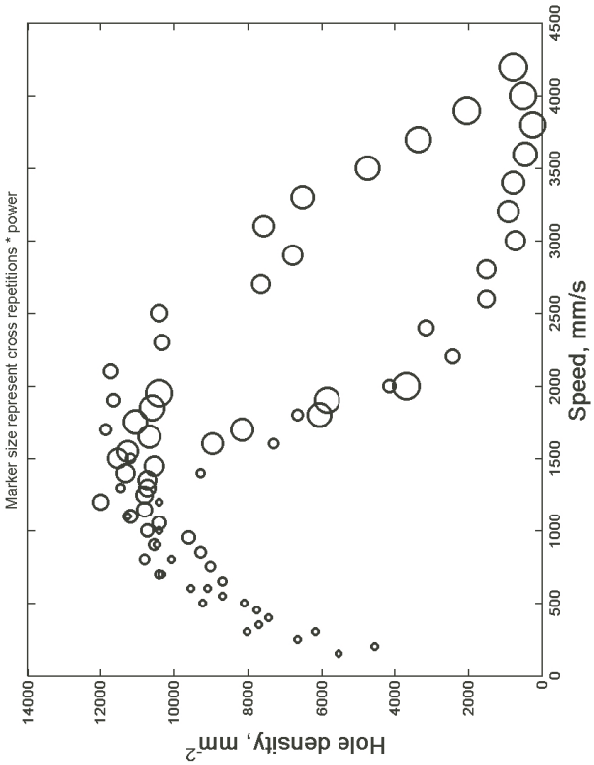

Fig. 16

8/8

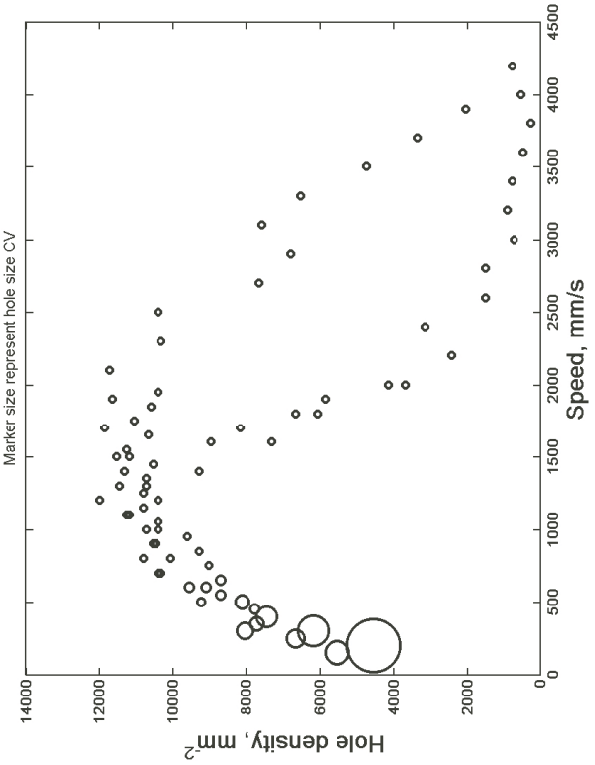

Fig. 17

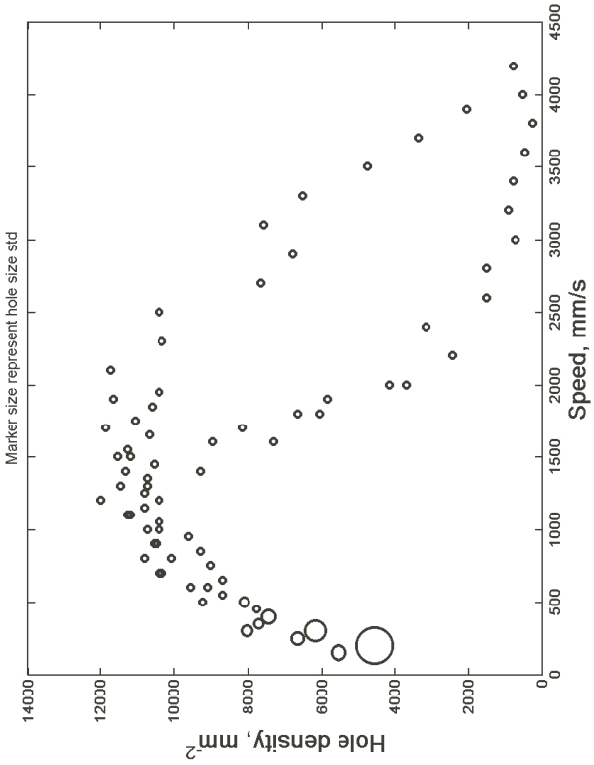

Fig. 18

D

Patent application 3: Micropillar surfaces

Remarks

This patent application describes a device produced by using Patent application 1 where the microstructures are used alter the wetting properties of the polymer surface.

As with the other patent applications, the content, points, argumentation and figures were drafted by me, and the text was written into "patent language" by patent attorney Oliver Kuhn from Guardian IP, Kgs. Lyngby.

D.1 Method of producing an item with enhanced wetting properties by fast replication and replication tool used in the method

The present invention relates in one aspect to a method of producing an item having a surface with an enhanced wetting property by fast replication. In a further aspect, the present invention relates to an item produced by that method. In yet a further aspect the invention relates to a replication tool for use in that method and a method of preparing the replication tool.

D.1.1 Background of the invention

Wetting properties of a surface may be modified by changing the finish of a surface on a microscale and/or on a nanoscale. For example, microscale structuring of hydrophobic surfaces is known to yield an enhanced hydrophobicity with water contact angles well above 120° as compared to a flat surface of the same hydro-phobic material. Micro- and nanoscale structures applied to the surface of a hydro-phobic material may even result in superhydrophobic surfaces, i.e. surfaces with an apparent water contact angle of 150° and above, e.g. when

applying a hierarchical surface structuring with nano-structures on top of a micro-structured surface. In the context of this application, a material is referred to as hydrophobic, if a flat surface thereof is characterized by a water contact angle of above 90°, such as above 95°, such as about or above 100°.

Applications for such superhydrophobic surfaces are numerous. They include, but are not limited to: packaging; medical devices; self-cleaning surfaces on e.g. wind turbine blades, helicopter blades, air plane wings, or solar energy panels; microfluidic devices; and biotechnical devices, such as assays, cell culture vessels, and lab-on-a-chip systems.

Accordingly, the hydrophilicity of a surface may be enhanced by microscale surface modifications. In the context of this application, a material is referred to as hydro-philic, if a flat surface thereof is characterized by a water contact angle of below 90°, such as below 85°, such as about or below 80°. For example, a flat surface of the hydrophilic plastics material acrylonitrile butadiene styrene (ABS) may have a water contact angle of about 81°.

Vast varieties of techniques for micro- and nano-structuring of surfaces exist, and may in principle serve to provide a surface structure enhancing the hydrophobicity of the surface of a hydrophobic material. One technique is based on the use of laser sources for machining a microscale finish into the surface of a work piece. In one approach, laser milling is used for directly micro-structuring the surface of an item that may be made of a metal, such as stainless steel. After applying the microstructure, the micro-structured surface of the stainless steel item may be coated with a hydrophobic substance to thereby generate a superhydrophobic surface. However, an approach based on micro-structuring by sequentially "writing" the micro-structure on the surface of each item is not suited for a large scale/high volume industrial production. In another approach described in US 2013/0189485 A1, femtosecond laser machining is used to generate microstructure cones on a metal or semiconductor surface, and faithfully replicating said microstructure in PDMS using a moulding or hot embossing technique to generate a superhydrophobic surface of the replicated part. The disclosed processes include time consuming heating and setting steps hampering a low-cost production on a large industrial scale. However, considerations of production cost and time are of the essence, if e.g. mass produced low-cost items are to be provided with such superhydrophobic surfaces on a broad basis in a commercially viable way.

Therefore, there is a need for a process for providing items with enhanced wetting properties, such as items with a superhydrophobic surface, wherein the process is suited for low-cost production on an industrial scale.

D.1.2 Summary of the invention

A first aspect of the invention relates to a method of providing a replication tool, the method comprising providing a forming tool having a tool surface adapted to define a general shape of an item to be formed; modifying at least portions of the tool surface by a pulsed laser treatment to obtain a microscale structured master surface with a lateral master pattern and a vertical master profile; wherein the pulsed laser treatment is adapted to generate microscale phase explosions on the tool surface, thereby forming the microscale structured master surface as a lateral arrangement of microscale crater-shaped depressions. The crater-shaped depressions obtained by the microscale phase explosions are irregular in shape and

polydisperse, i.e. varying in size with a spread about a most prominent size. The size may e.g. be characterized by the area covered by the depression as seen in a vertical projection on a lateral plane.

The microscale structuring of the tool surface is provided by the localized application of laser pulses directly to selected portions of the tool surface. This post-treatment of the tool surface by means of localized laser treatment has the advantage that the replication tool with the shape defining tool surface may be designed and produced using existing techniques and equipment for tool making, thereby contributing to a relatively simple and cost effective implementation of the surface functionalization in an existing fabrication process.

At the targeted portion of the tool surface, the localized pulsed laser treatment is adapted to melt and evaporate material at the tool surface to generate microscale phase explosions, thereby producing a randomised surface structure of polydisperse microscale features. The microscale surface features are depressions, which are typically crater shaped with steeply sloped side walls. The process of provoking microscale phase explosions by locally applying laser energy to the tool surface so as to form the crater-shaped depressions is stochastic in nature, wherein upon appropriate exposure the microscale surface features are densely packed and may even partially overlap, thereby forming a microscale lateral pattern with a microscale porous appearance. The localized application of laser power may be scanning a laser spot along a predetermined scanning path at a pre-determined scan speed over the tool surface. The path may follow a single scan along the path over the tool surface, a repetitive scanning along the same linear path, or a combination of both. The path is adapted to cover the selected portions of the tool surface. The path may e.g. be straight, curved, meandering, segmented or a combination thereof and some sections of the path may overlap other sections of the path in order to achieve an even exposure of the selected portions of the tool surface with laser energy.

The pulsed laser radiation has to be of a wave length and pulse characteristics that is absorbed by the tool surface in order to be able to locally melt and evaporate material from the tool surface so as to produce microscale phase explosions creating the crater-shaped depressions. For example, the laser radiation may be from a picosecond laser source with a wavelength in the near infrared, such as 1064 nm, but other wavelength ranges, e.g. in the visible part of the electromagnetic spectrum, and pulse characteristics that are suitable for locally heating the tool surface to generate microscale phase-explosions may be conceived, too. The finish of the targeted portions of the tool surface is controlled by adapting the exposure of these tool surface portions with the pulsed laser radiation. The exposure of the tool surface is controllable e.g. by adjusting the laser power/spot intensity and/or by varying the scan speed, wherein exposure of a given surface portion increases with increasing laser power, but decreases with increasing scan speed. The finish of the targeted portions of the tool in turn determines the finish of the replicated item in the corresponding regions on the item surface via the replication process. Furthermore, multiple exposures of the same surface portions, e.g. by repetitive and/or overlapping scanning of the laser spot over these surface portions, results in an exposure that is increased correspondingly.

Preferably, the lateral pattern of the microscale structured master surface has an area density of microscale master features of at least $5000/\text{mm}^2$. Thereby, a reasonably densely packed lateral distribution of microscale features on the master surface is achieved, thereby allowing for a significant enhancement of wetting properties of items replicated using the replication tool as further detailed below.

Further preferably, the lateral pattern of the microscale structured master surface has an area density of microscale master features of at least 8000/mm^2, or even of at least 10000/mm^2. Thereby, a densely packed lateral distribution of microscale features on the master surface is achieved, thereby allowing for a particularly significant enhancement of wetting properties of items replicated using the replication tool as also detailed further below.

A further aspect of the invention relates to a method of producing an item with enhanced wetting properties by a replication process, the method comprising the steps of

> providing a replication tool with a microscale structured master surface by a method according to the above-mentioned embodiment;
> using the replication tool to form the item by the replication process, wherein the formed item has the general shape as defined by the tool surface, and wherein the formed item comprises a microscale textured replica surface with a lateral arrangement of microscale protrusions produced by the microscale structured master surface.

The method is useful for forming the item from a replication material replicating the microscale structured master surface onto the item to form a surface region with a lateral arrangement of polydisperse microscale protrusions thereon. A lateral replica pattern is defined by the lateral master pattern, and a vertical replica profile has a finite peak-to-peak amplitude to form a three-dimensional texture. Since the lateral replica pattern is defined by the lateral master pattern, it is equally irregular as seen in a projection onto a lateral plane, and the microscale protrusions are polydisperse. The method is for producing the item with enhanced hydrophobicity by a fast replication process using the replication tool, such as required by a commercially viable production of the item in large numbers.

According to some embodiments, the method comprises the steps of

a) providing a replication tool having a tool surface adapted to define a general shape of the item, wherein the tool surface comprises a microscale structured master surface obtained by localized pulsed laser treatment of the tool surface to generate microscale phase explosions, said microscale structured master surface having a lateral master pattern and a vertical master profile.
b) contacting the tool surface with a replication material in the melt phase, wherein the tool surface is maintained at a process temperature below the melt temperature of the replication material, thereby
c) cooling the thermoplastic replication material to a stabilized shape with a microscale textured replica surface, wherein the lateral master pattern defines a corresponding lateral replica pattern of the microscale textured replica surface and wherein the amplitude of a vertical profile of the microscale textured replica surface is in the microscale, and
d) releasing the shaped item from the tool surface.

The method is for the production of items by a fast replication process, thereby al-lowing for a low-cost and/or mass production of the item with a surface that is functionalized for enhanced hydrophobicity by providing the item with a microscale textured surface. A replication process may be considered fast, for example, if the replication period from contacting the tool surface with the molten replication material to releasing the shaped item is short, such as

well below ten minutes, such as less than five minutes, such as less than 3 minutes, such as less than one minute, such as less than 30 seconds, or even less than 10 seconds. In particular, the suggested thermally controlled replication process using a thermoplastic replication material can be performed fast as compared to for example replication processes using thermosetting replication materials, or chemically setting replication materials.

The term microscale refers to dimensions of about 1 μm to 1000 μm that are generally measured in microns (micrometres), typically in the range of about 1 μm to 100 μm. Accordingly, the term nanoscale refers to dimensions of about 1 nm to 1000 nm that are generally measured in nanometres, typically in the range of about 1 nm to 100 nm.

The microscale structure of the master surface and, accordingly, the microscale texture of the replica surface have a three-dimensional topography of microscale elements arranged next to each other and may be decomposed in a lateral pattern and a vertical profile. The term ”lateral pattern” refers to the arrangement in lateral directions of the (3D) microscale elements making up the microscale structure/texture, as seen in vertical projection on to a lateral plane. The term ”vertical profile” refers to the variation of the location of the surface in a direction perpendicular to the lateral directions.

When a surface structuring/texturing is applied to an object having a general shape, such as a tool surface or an item, the surface structuring/texturing can be seen as a vertical variation of the surface, which is added to the general shape of the tool surface/item. Accordingly, on an object with a microscale structured/textured surface, an average surface that flattens out any vertical variations of the surface by averaging on a lateral scale larger than that of the microscale structuring/texturing essentially follows the general shape of the object. The general shape of the object is thus defined independent of any nano- or microscale surface roughness / finish / structuring. At a given point on the surface of the object, lateral directions are parallel / tangential to a surface defining the general shape of the object on a scale larger than the scale of the lateral pattern. Accordingly, the vertical direction at a given point on the surface of the object is the surface normal to the general shape in that point. In each given point, the vertical direction is perpendicular to the corresponding lateral directions.

The general shape of the replicated item is defined by the general shape of the tool surface. The replication process is for accurately replicating the general shape of the item as defined by the tool surface. The surface of the replicated item is functionalised by applying a surface finish with a microscale texture at least on selected regions of the item surface. The particular functionalization is to enhance the hydro-phobic nature of the surface of the item by providing the hydrophobic material with a surface finish having a microscale texture in the selected regions. The micro-textured surface finish in selected regions of the item surface is achieved by providing a microscale structuring in corresponding portions of the tool surface from which the item is replicated.

As mentioned above, the laser treatment of the tool surface results in a porous surface appearance produced by a randomised arrangement of densely packed microscale depressions, which are typically shaped as relatively deep, steep-walled craters with a more or less pointed bottom. The sloped sidewalls facilitate an easy de-moulding of the replicated item in the step of releasing the item from the tool surface.

The term ”wetting properties” refers to the interfacial interactions in a system comprised of

three states of matter, a solid, a liquid, and a gas, and can be quantified by a contact angle. The line connecting all three interfaces, e.g. solid-liquid, solid-gas, liquid-solid, is denoted the three phase-contact line. The contact angle is defined as the angle between the tangents of the liquid-gas and the liquid-solid interphases perpendicular to the three-phase line at any intersection of the two tangents on the three phase line. The wetting properties between a solid and a liquid in a three phase system are considered enhanced with respect to the wetting properties of a flat surface if the apparent macroscopic contact angle is altered by the structure on the surface, wherein the wetting properties of a system with a solid-liquid contact angle smaller than 90° (philic behaviour) is considered enhanced if this contact angle is reduced by the modification (philic enhancement). Likewise, the wetting properties of a system with a solid-liquid contact angle greater than 90° (phobic behaviour) is considered enhanced if this contact angle is increased by the modification (phobic enhancement).

An important insight is that achieving the enhancement in wetting properties for the replicated item does not require controlling the exact 3D-shape of each of the microscale features on the tool surface and their exact arrangement with respect to each other. Also, the exact details of the individual microscale elements and of their arrangement making up the microtexture on the surface of the replicated item are uncritical for achieving an enhanced wetting properties as compared to a flat untextured surface of the replication material.

The fast replication process thus yields proper items as long as the general shape is faithfully obtained reliably, the microscale lateral pattern is reliably reproduced in each reproduction process, and the peak-to-peak amplitude of the vertical profile of the replica surface is sufficient to provide enhanced wetting properties. As mentioned above, the enhanced wetting properties may be an enhancement of the hydrophobicity. Enhanced hydrophobicity is achieved when water droplets on the surface of the replicated item form a so-called Wenzel state or a so-called Cassie Baxter state. Relatively small amplitudes of the vertical profile of the texture of the replica surface may already enhance the hydrophobicity, such as amplitudes of at least 100 nm, alternatively at least 200 nm, alternatively at least 500 nm, and preferably in the microscale, such as 1 μm-100 μm, such as 1 μm-30 μm, preferably in the range 1 μm-10 μm. For ensuring a good production yield it is therefore sufficient to control the lateral scale of the texture which is well controlled by the lateral scale of the pat-tern of the master surface – and ensuring that the amplitude of the profile of the texture on the replica surface is sufficient to enhance hydrophobicity, preferably in the microscale, as detailed above. To achieve super-hydrophobicity, the amplitude of the vertical profile of the texture of the replica surface has to be sufficiently large to support water droplets on the surface of the item in a so-called Cassie Baxter state. A further important insight therefore relates to the nature of the fast replication process. Here, it is exploited that the lateral pattern of the microscale master structure on the tool surface is inherently reproduced with high fidelity on the replicated item. The fidelity of replication of the vertical profile on the other hand tends to be affected by standard parameters of processes for fast replication in thermoplastic materials, such as tool temperature, replication period, and temperature and/or pressure of the thermoplastic replication material in the melt phase. This is owing to the ability of the thermoplastic replication material to fill the depressions of the relatively deep steep-walled master structure before solidifying, which may be controlled by these parameters. Thereby, the fidelity of replication may be controlled. For example, fidelity of microstructure replication may be reduced by reducing the temperature at which the tool surface is maintained. When the replication material contacts the tool surface at the lower the melt is cooled more rapidly, thereby increasing the viscosity of the melt and impeding the filling of the microscale

depressions/crevices/craters/pores of the master structure on the tool surface by the melt before it solidifies. A reduced fidelity is reflected by a reduced amplitude of the replicated profile as compared to the master profile: the replication is more shallow than the master. The fidelity of replication of the vertical profile may thus be characterised e.g. by comparing the peak-to-peak amplitudes of the vertical profiles of the replicated microscale texture and the microscale master structure to each other, wherein for a low fidelity replication the amplitude of the replicated profile as compared to the master profile is lower than for a higher fidelity replication. Typically, the low-fidelity replicated microscale textures exhibit a rounded top. Since the enhancement of the hydrophobicity is uncritical as to the exact shape and arrangement of the individual microstructures, another ad-vantage of the method is that it facilitates a relatively simple and cost effective implementation of the surface functionalization in an existing fabrication process by merely modifying the tool surface of a replication tool in a post-treatment step.

A replication process, where the tool surface is maintained at a more or less constant temperature below the melt transition temperature throughout the production process is sometimes referred to as an ”isothermal” type process. Isothermal processes may be performed at high throughput. As also mentioned above, the surprising insight resides in that the truthfulness of the replication of the vertical profile of the microscale master structure is uncritical for achieving the desired effect of enhanced hydrophobicity, or even superhydrophobicity, as long as the lateral pattern is faithfully transferred and the peak-to-peak amplitude of the vertical profile of the micro-texture on the replica surface is in the microscale.

Note that the item may be made entirely from replication material with a shape de-fined by the tool surface, or the replication material may be applied to/carried by a substrate material, e.g. in an additive moulding step or a coating step.

Further according to one embodiment of the method for producing an item with enhanced wetting properties, the replication process is injection moulding. In a particularly preferred embodiment, the fast replication process is injection moulding. Injection moulding is a cyclic replication process with a fast cycle time, i.e. using this embodiment a large number of separate items with a microscale textured replica surface may be produced at high throughput. The inner surface of the injection mould is the tool surface defining the general shape of the item. At least portions of the tool surface have a finish with a microscale structuring generated by localised treatment with a pulsed laser source. The thermoplastic replication material is in the melt phase injected into the closed mould, which is kept at a temperature below the melt temperature of the replication material. When the molten replication material contacts the cooled tool surface it solidifies, whereby it is shaped and textured, before the item is released from the mould. As mentioned above, a surprising insight is that the replica surface produced in a fast injection moulding process exhibits enhanced wetting properties, such as hydrophobicity or even superhydrophobicity, also if the vertical profile of the microscale texture on the replica surface is a low fidelity replication of the corresponding profile of the microscale structure on the master surface, as long as the lateral pattern is faithfully transferred and the peak-to-peak amplitude of the vertical profile of the micro-texture on the replica surface is in the microscale. Thereby, a robust low-cost mass-production process for items with an enhanced hydrophobic or even superhydrophobic replica surface is achieved.

Further according to one embodiment of the method for producing an item with enhanced wetting properties, the replication process is extrusion coating.

In another particularly advantageous embodiment, the fast replication process is extrusion coating. Extrusion coating is a process for roll-to-roll processing, i.e. using this embodiment the item may be produced in a continuous process as a layered web with a microscale textured replica surface. To that end, a substrate web may be passed between a nib roll and a cooling roll, in a conventional manner, wherein the rotary surface of the cooling roll is the tool surface defining the general shape of the item. The tool surface has a finish with a microscale structuring generated by treatment with a pulsed laser source. The thermoplastic replication material is heated to above the melt transition temperature and in the melt phase supplied between the substrate web and the cooling roll, which is kept at a temperature between the glass transition temperature and the melt transition temperature. When the molten replication material contacts the cooled tool surface it solidifies, whereby it is shaped and textured, before the item is released from the replication tool.

Further according to one embodiment of the method for producing an item with enhanced hydrophobicity, a replication period from contacting the tool surface with the molten replication material to releasing the shaped item is less than 3 minutes, such as less than one minute, such as less than 30 seconds, or even less than 10 seconds. Typically, in an injection moulding process, the replication time may be less than one minute, i.e. a few tens of seconds, such as about 30 seconds. Extrusion coating is a continuous roll-to-roll process. Typically, an extrusion coating process is therefore even faster with replication times of less than 10 seconds, less than 5 seconds, or even less than 1 second.

Further according to one embodiment of the method for producing an item with enhanced wetting properties, the vertical replica profile predominantly has rounded tops with a radius of curvature in the microscale. As described above, the replication process may be controlled to influence the fidelity of replication to provide a vertical replica profile that predominantly has rounded tops with a radius of curvature in the microscale. In fact, a less faithful replication of the crater-like microscale features on the master surface yields a structure with rounded tops, which has a positive effect on reducing the roll-off angle at which water droplets forming on the superhydrophobic replica surface easily roll off as compared to sharp-edged structures. A process goal/constraint of a faithful replication of the vertical profile of the master structure, on the other hand may entail long settling or curing times incompatible with a fast replication process.

Advantageously, the radius of curvature of the rounded tops is of the same order as the lateral distance between adjacent structures/features of the lateral pattern, such as predominantly above 1 μm, above 5 μm, or even above 10 μm, and predominantly less than 300 μm, less than 100 μm or even less than 50 μm. Further advantageously, the vertical amplitude of the replica profile is about equal or less than the lateral distance between adjacent microscale features.

According to some embodiments, the method may further comprise the additional step, after releasing the replicated item from the tool surface, of modifying the replica micro-texture surface by applying a further surface layer capping the surface of the replication material. The additional layer may, for example, be a surface layer modifying the wetting properties of the replication surface, such as a molecular coating. Alternatively or in addition thereto, the additional layer may be brought about by a post treatment of the replica surface.

Wetting properties are determined by the contact angle of a droplet formed on the surface. An enhancement of the wetting properties is reflected by a change in con-tact angle, wherein,

for example, an enhancement of the hydrophobicity of a surface increases the contact angle, and an enhancement of the hydrophilicity decreases the contact angle. Contact angles are understood as static contact angles measured in a commonly known way using an optical tensiometer. Roll-off angle is determined using a base-tilt method by observing the tilt-angle with respect to horizontal at which a droplet rolls off the surface of the base.

The replica material may be hydrophobic, wherein a flat surface of a bulk sample thereof exhibits a contact angle larger than 90°.

Further according to one embodiment of the method for producing an item with enhanced hydrophobicity, the replica material is hydrophobic with a flat surface contact angle larger than 95°, preferably larger than 100°, and less than 120°, preferably less than 110°. The microscale texture on the replica surface enhances the hydrophobicity of the unstructured replica material. Achieving a higher contact angle is therefore easier when starting out with a material that is more hydrophobic, i.e. a material that is characterised by a higher contact angle on the unstructured surface. However, many materials with the highest contact angles may comprise components that are toxic or hazardous to the health or the environ-ment. The recited selection of materials provides a good compromise of hydrophobic response against health and/or environmental impact considerations. A particularly preferred range in that respect is for thermoplastic polymers a flat surface bulk sample water contact angle of 100° – 110°.

Advantageously according to one embodiment of the method for producing an item with enhanced hydrophobicity the thermoplastic replica material is polypropylene.

Further according to some embodiments, the microscale textured replica surface is superhydrophobic.

Further according to one embodiment of the method for producing an item with enhanced hydrophobicity, the replica surface has, upon release from the tool surface, a contact angle of more than 150°, preferably more than 155° or about 160°, and/or a sliding angle less than 10°, preferably less than 8°, about 5°, or even less than 5°.

Further according to some embodiments, the replica material is hydrophilic with a flat surface contact angle below and including 85°, below and including 80°, or preferably below and including 75°, and at least 50°, at least 60°, or at least 70°.

Further according to some embodiments, the microscale textured replica surface is superhydrophilic.

Further according to one embodiment of the method for producing an item with enhanced wetting properties, the replica material is lipophobic with a flat surface water contact angle larger than 95°, preferably larger than 100°, and less than 120°, preferably less than 110°.

Further according to some embodiments, the microscale textured replica surface is superlipophobic.

Further according to some embodiments, the replica material is lipophilic with a flat surface contact angle below and including 85°, below and including 80°, or preferably below and including 75°, and at least 50°, at least 60°, or at least 70°.

Further according to some embodiments, the microscale textured replica surface is super-lipophilic.

A further aspect of the invention relates to a method of preparing a replication tool for producing items with enhanced wetting properties by a fast replication method according to any of the above-mentioned embodiments, wherein the method of pre-paring a replication tool for producing items with enhanced wetting properties comprises the steps of

> providing a forming tool having a tool surface corresponding to a general shape of the items to be formed
> applying a microscale surface structuring to the tool surface using localized laser treatment to generate microscale phase explosions over a predefined portion of the tool surface,

thereby obtaining a replication tool having a tool surface with a microscale structured master surface on at least portions of the tool surface.

The step of providing a forming tool may be producing a tool for the replication process in question, e.g. a mould for injection moulding or a roller for extrusion coating, in a conventional manner and using conventional tooling materials as known in the art, such as tool steel or 2017 aluminium. The step of applying a microscale surface structuring is performed as a post treatment of the tool surface by means of a pulsed laser directly scanned over the tool surface. A suitable pulsed laser may be, but not limited to, an industrial picosecond-laser operating in the near infrared, such as at 1064 nm. The exposure of the surface to the pulsed laser radiation is adapted to generate microscale phase explosions. This includes localised melting of tool mate-rial on the tool surface, evaporating molten tool material, and ejecting molten and evaporated material in microscale eruptions from the melt surface, thereby forming a densely packed arrangement of microscale crater-shaped depressions. The obtained microscale structured master surface has a lateral master pattern and a vertical master profile as described above.

Since the post-treatment applied here does not require the precise micro-milling of a specific pre-determined shape of the master structure, such as a regular array of micro-cones, the post-treatment may be applied using cheaper equipment. Further-more, this post-treatment adapted to generate a microscale porous surface from microscale phase explosions is faster to apply than e.g. micro-milling of microscale features. Furthermore, as also mentioned above, the microscale phase explosions generate microscale crater-shaped depressions with sloped sidewalls that are well suited for fast replication processes, such as injection moulding and extrusion coating. Amongst others, the crater shape with sloped sidewalls facilitates easy releasing of the shaped items from the tool surface at the end of the moulding process (de-moulding).

In a further aspect, a method of producing a plurality of items with enhanced wetting properties comprises preparing a replication tool using the above-mentioned method, and repeatedly performing the method of producing an item with enhanced wetting properties by a fast replication process according to any one of the above-mentioned embodiments. Large numbers of items exhibiting enhanced wetting properties, such as enhanced hydrophobicity or super-hydrophobicity, may thus be produced cheaply.

According to a further aspect, the invention relates to an item with enhanced wetting prop-

erties produced by fast replication according to any of the above-mentioned methods.

A further aspect of the invention relates to a replication tool for producing an item with enhanced wetting properties by fast replication, the tool comprising a tool surface defining a general shape of the item, the tool surface comprising at least on portions thereof a microscale structured master surface having a lateral master pat-tern and a vertical master profile, wherein said microscale structured master surface has been provided by localized pulsed laser treatment of the tool surface, the pulsed laser treatment being adapted to generate microscale phase explosions. Thereby, the localized pulsed laser treatment is adapted to provide a micro-porous structure of the master surface, wherein the micro-porous structure is formed by a densely packed arrangement of crater-shaped microscale depressions with outwardly sloped side walls with the advantages as described above with reference to the method of producing a replicated item as well as with reference to the method of preparing a replication tool for use in a fast replication process, such as isothermal injection moulding, or roll-to-roll processing in e.g. an extrusion coating process.

Further according to one embodiment of the replication tool, the tool surface is made of a metal, such as aluminium or steel. The tool surface has to be suited for the fast replication processes for which the method is intended. The tool surface comprising the microscale master structure can be directly on a mould surface for contacting the replication material and/or on a insert attached to the inside of a mould. It is understood that the tool surface may be broken up in sub-surfaces that form part of the mould as is customary in tool design for fast replication processes, such as injection moulding or extrusion coating. Examples of commonly used metals that are also suitable for the present invention include, but are not limited to, aluminium alloys of the types 2017, 1050 or 5754, or tool steel, such as ”Sandvik Corona C60”, Orvar2343 or similar.

Further according to one embodiment of the replication tool, the microscale structured master surface is a lateral arrangement of polydisperse microscale master features. The term polydisperse refers to microscale features having varying transverse dimensions as seen in a vertical projection. Typically, the polydisperse dimensions are characterized by a statistical distribution having a centre value and a spread. The transverse dimensions may be specified as transverse linear dimensions characteristic of the lumen defined by the crater-shaped depression. Given the irregular nature of a polydisperse arrangement, transverse dimensions can also be defined in combination by specifying an area covered by the crater-shaped depression. An equivalent linear dimension characterizing of a given crater-shaped depression may then be defined as the diameter of a circle with the same area. In order to be able to achieve an enhanced hydrophobicity on the surface of the replicated item, the microscale master features on the master surface are preferably densely packed, with neighbouring crater shaped depressions only being separated from each other by a ridge having a width that is comparable to or preferably less than the transverse linear dimension characterizing the crater-shaped depression.

Further according to one embodiment of the replication tool the microscale master features are crater-shaped depressions. Typically the crater-shaped depressions appear more or less circular as seen in a vertical projection. Furthermore, the crater-shape implies an outwardly sloped sidewall providing a positive release angle facilitates de-moulding of the shaped item.

Further according to one embodiment of the replication tool, the vertical profile of the microscale structured master surface has a peak-to-peak amplitude of at least 0,3 μm, or at

least 0,5 μm or at least 1 μm and below 30 μm, below 20 μm, or preferably below 10 μm.

Further according to one embodiment of the replication tool, the lateral pattern of the microscale structured master surface has an area density of microscale master features of at least 8000/mm^2, or at least 10000/mm^2. Thereby, the replication tool is particularly useful for producing items with enhanced wetting properties, since the formed items comprise a microscale textured replica surface with a densely packed lateral arrangement of microscale protrusions produced replicated from the microscale structured master surface.

It should be noted, however, that the process according to the present invention will not exceed an inherent upper limit for the area density of the microscale lateral structuring. Such an inherent limit is due to the fact that the microscale features produced by the microscale phase explosions according to the present invention require a minimum footprint in order to be resolved. While the present invention produces polydisperse features with a distribution that may include submicron elements, their average (most prominent) lateral dimensions are in the microscale. In-creasing the area density of the microscale features results in an increasing probability for the occurrence of overlap between adjacent microscale features. Above a critical overlap, the microscale features are overlapping to such an extent that they appear merged and effectively have a much larger lateral extension than a targeted feature size of individual, unmerged microscale features. As a consequence, above a critical area density such merged features increasingly dominate the actual feature size produced on the replication tool.

In a characterization of the microscale surface structure of the master surface, e.g. by commonly known image analysis techniques applied to micrographs thereof, the merged features are then counted as a single feature with a larger lateral dimension or foot print. This effect is best seen in a graph showing the area density of microscale features, e.g. counted in a given surface portion by means of image analysis, as a function of the laser energy exposure applied to that surface portion. By way of example, such a graph is shown in Fig.21. The data shown has been obtained by an analysis of the microscale structuring applied to more than 70 replication tool blanks (tool grade aluminium as specified elsewhere in this application) using the method according to the invention. The ordinate shows the exposure dose expressed in terms of the number of repetitions divided by the scan speed; the co-ordinate shows the area density of holes detected by an image analysis performed on micrographs of the processed surface; and the marker size indicates the size of the detected feature determined by the same image analysis algorithm. In an initial regime at low exposure, the individual microscale features are resolved and all have essentially the same size. The initial regime covers a low density regime up to about 5000/mm^2 where the distribution of the microscale features may be considered as sparse. In an intermediate exposure regime above about 5000/mm^2, the microscale features may be considered as more and more densely packed, reaching a critical density of about 12000/mm^2, where overlap of adjacent microscale features begins to become significant. The critical density is the maximum achievable density for a given system, which in the example of Fig.21 is about 12000/mm^2. Other material systems and laser processing set-ups may have a different maximum achievable area density, such as about 100000/mm^2, or about 50000/mm^2, or 20000/mm^2, or about 15000/mm^2. An inherent limit to the maximum achievable area density is given by the requirement of microscale dimensions of the lateral structuring as achieved by the present invention. Increasing the exposure beyond the critical value then only results in merging of the microscale features and in a deterioration of the desired patterning. In the example of Fig.21, a significant decrease of the area density of microscale features to below 5000/mm^2, accompanied by a corresponding increase of the

average feature size is observed. When the microscale structure of the replication tool master surface is transferred onto a replicated item to form a microscale surface texture for the enhancement of a wetting behaviour, a sparse distribution of microscale features may prove insufficient to provide a significant wetting behaviour enhancement – if any at all. In a preferred exposure regime around the maximum achievable area density of about 100000/mm^2, or about 50000/mm^2, or 20000/mm^2, or about 15000/mm^2, or about 12000/mm^2, the microscale features are adequately dimensioned in their lateral extend, yet are packed sufficiently dense so as to achieve a significant wetting behaviour enhancement. An adequate range may be determined by an exposure experiment as outlined in Fig.21, wherein preferably the area density is at least 60%, at least 70%, at least 80%, or at least 90% of the maximum achievable area density of microscale features. Above a critical exposure, in the regime where merging becomes more and more dominant, the wetting behaviour enhancement of the replicated item also deteriorates more and more.

Further according to one embodiment of the replication tool, the microscale master features have an aspect ratio of a vertical dimension to a lateral dimension of at least 1:2, or about 1:1, wherein the vertical dimension is the peak-to-peak amplitude and the lateral dimension is the square root of the average footprint area per microscale master feature, which for a given microscale structured surface area is calculated as the inverse of the area density of microscale master features per area, i.e. the area of the given surface in lateral projection divided by the count of microscale features in that area.

D.2 Brief description of the drawings

Preferred embodiments of the invention will be described in more detail in connection with the appended drawings, which show in

FIGS. 1a–c, SEM micrographs of a microscale structured master surface at different magnifications,
FIG. 2, a SEM micrograph of another microscale structured master surface,
FIG. 3, a microscope image of a droplet of water on an unstructured polypropylene surface,
FIG. 4, a SEM micrograph of the microscale textured surface of an injection moulded item (polypropylene) using an isotherm process,
FIG. 5, a microscope image of a droplet of water on a polypropylene surface of the type as shown in Fig.4,
FIG. 6, a SEM micrograph of the microscale textured surface of an injection moulded item (polypropylene) using a variotherm process,
FIG. 7, a microscope image of a droplet on a polypropylene surface of the type as shown in Fig.6,
FIG. 8, schematically, the surface modification of a tool surface by pulsed laser treatment to generate microscale phase explosions,
FIG. 9, schematically, an injection moulding process according to one embodiment of the invention,
FIG. 10, schematically, an extrusion coating process according to a further embodiment of the invention,

FIGS. 11–14, four graphs plotting hole size and hole density on a microscale structured master surface for different parameter settings of the pulsed laser treatment of the tool surface,
FIGS. 15–18, four graphs plotting hole density on a number of microscale structured master surfaces against the scan speed used during the pulsed laser treatment of the respective tool surfaces,
FIGS. 19, (a) a microscope image and (b) a photographic top view of a droplet of mineral oil on an unstructured polypropylene surface,
FIGS. 20, (a) a microscope image and (b) a photographic top view of a droplet of mineral oil on a microscale textured replica surface as the one shown in Fig.4, and in
FIG. 21, a graph plotting hole density on a number of microscale structured master surfaces against the exposure in terms of repetitions divided by scan speed used during the pulsed laser treatment of the respective tool surfaces.

D.3 Detailed description of preferred embodiments

Super-hydrophobic surfaces are ubiquitous in the plant kingdom. Super-hydrophobic plant leaves possess the so-called lotus-effect, which causes rain drops falling on the leaves to roll off while capturing any dust particles. This way, the surfaces are passively self-cleaning. The super-hydrophobic properties are achieved by a combination of the chemical properties of the surface (molecular level) and its roughness (micro-level). In nature, this is realised as rough leaves covered with a wax layer.

When a water droplet interacts with a hydrophobic surface, several different possible "interaction-state" are possible. However, the one where the droplet is the most mobile is the Cassie-Baxter state. In this state, the droplet is only partially wetting the surface, and air is trapped in the trenches of the surface. Without going into the mathematics of super-hydrophobicity, surface roughness and the hydrophobicity can be understood as a scaling factor. This means that a hydrophobic surface will be more hydrophobic when surface roughness is increased, and a hydrophilic surface will be more hydrophilic when surface roughness is increased. This explains why tissue paper is good for wiping up water, and why lotus leaves are super-hydrophobic. Man-made super-hydrophobic surfaces are typically realised using a Teflon coating, which contains hydrophobic fluor-saturated molecules. This is non-ideal from a mass-production perspective and from a health safety perspective. If the surface roughness is increased, the intrinsic hydrophobicity of the polymer may be exploited to achieve super-hydrophobicity. Alternatively, Teflon coated pieces will also benefit from the increased roughness. Super-hydrophobic injection-moulded plastic parts have many applications in food packaging, pharmaceuticals, medical equipment, consumer plastic products and electronics. How the steps of the invention may be implemented is illustrated by way of example in the following. The examples given are not to be considered as limiting for the scope of the invention.

D.3.1 Replication Tool

Examples of suitable materials are materials commonly used as inlays/ or mould materials in e.g. injection moulding or extrusion coating processes. These materials of the tool

surface suited to be modified by pulsed laser treatment to generate microscale phase explosions include Aluminium alloys, such as so-called 1050 aluminium, 5754 aluminium, or 2017 aluminium, as well as tool steel, such as Sandvik corona C60 and Orvar2343.

Figs.1a-c show micrographs taken by scanning electron microscopy (SEM) of an aluminium tool surface, more particular a tool surface made of 2017 aluminium, which has been modified by pulsed laser treatment using a picosecond laser with a maximum power output of 50 W operating at a pulse frequency of 200 kHz and at a wavelength of 1064 nm. The surface was scanned repetitively at a given power set-ting in per cent of the maximum power output and with a given speed. The laser beam was incident on the tool surface in a vertical direction, wherein the laser was slightly defocused by shifting the focal point by 1.3 mm in a vertical direction with respect to the tool surface to be modified. While the apparent spot size was about 50 µm on the surface, a line scan of the laser produced a modified trace width of about 10 µm ± 5 µm. A broader trace as the one shown in Fig.1a and 1b was obtained by a meander line scan with adjacent legs of the meander shifted in a direction perpendicular to the scanning direction. Thereby an arbitrary area can be covered by a microscale surface structure. As best seen in Fig.1a, the laser treatment results in an ablation of some of the tool surface material. The parameters of the pulsed laser treatment are, however, adjusted such the bottom of the trace exhibits a lateral arrangement of polydisperse microscale master features, see e.g. Fig.1b. The microscale master features obtained by this pulsed laser treatment are crater-shaped depressions. The crater-shaped depressions at the bottom of the trace are a consequence of the localized pulsed laser treatment generating microscale phase explosions.

Figs.2 shows a SEM micrograph of tool surface made of tool steel, more particular Sandvik corona C60 tool steel, which has been modified by pulsed laser treatment using the same picosecond laser with a maximum power output of 50 W operating at a pulse frequency of 200 kHz and at a wavelength of 1064 nm. Again, the surface was scanned repetitively at a given power setting in per cent of the maximum power output and with a given speed. The laser beam was incident on the tool surface in a vertical direction, wherein the laser was slightly defocused. Also here, the localized pulsed laser treatment generates microscale phase explosions resulting in a lateral arrangement of polydisperse microscale master features, wherein the microscale master features are crater-shaped depressions.

D.3.2 Replicated Item

The laser structured aluminium insert was installed in a Victory 80/45 Tech injection moulder (Engel). The polymer substrate used for injection moulding polypropylene HD120MO (Borealis) with a Heat Deflection Temperature (0.45 N/mm^2) of 88 °C. Injection temperature of the polymer was 255 °C with an injection pressure of 1200 bar. Both variotherm and isotherm injection moulding processes were tested.

Parameters specific for isotherm injection moulding:

- Temperature of microscale structured aluminium insert face = 80 °C. (constant)
- Temperature of "backside" mould = 60 °C. (constant)

Parameters specific for variotherm injection moulding:

- Temperature of structured aluminium insert face = 120 °C. (injection)
- Temperature of "backside" mould = 100 °C. (injection)
- Active cooling was applied immediately after polymer injection for the duration of the holding time (60 seconds) followed by and additional cooling time (60 seconds). This resulted in a final mould temperature of 40-50 °C.

The respective surfaces have been characterised with respect to the shape of the microscale features on the microscale textured surface of the replicated item, see Fig.4 and Fig.6. The isothermal process results in a surface texture with rounded tops, see Fig.4, and the variothermal process results in a surface texture with a hairy appearance ("pulled polypropylene"). Both surfaces faithfully replicate the lateral pattern of the master, but only provide a low fidelity replication of the vertical profile of the master. Nevertheless, both processes result in a fast replication of items with a super-hydrophobic surface. The isothermal process is preferable for high throughput or high volume production, because the isothermal moulding process is not time limited by any process step(s) involving temperature adjustments of mould and/or mould inserts, whereas the variotherm moulding process is partially time limited by one or more process step(s) involving temperature adjustments of mould and/or mould inserts.

D.3.3 Enhancement of Wetting Properties

The wetting properties of the obtained surfaces of the replicated items where characterized by performing contact angle measurements. Drop roll-off experiments for determining contact angles were conducted on an Attension Theta optical tensiometer (Biolin Scientific) by applying a 10 μL droplet of water and slowly tilting the stage until roll-off was observed.

Table 1: Results of contact angle measurements.

	Variotherm	Isotherm	Unstructured
Contact angle	160°	160°	104°
Contact angle hysteresis	<5°	<5°	21°
Stage tilt angle (at roll-off)	<5°	<5°	NA*

*Droplet is sticking to the surface.

Fig.3, Fig.5 and Fig.7 show microscope images as obtained during the contact angle measurements performed with water droplets on replicated items, where Fig.3 is for the unstructured material, Fig.5 is for the isotherm process, and Fig.7 is for the variotherm process. A very pronounced hydrophobic enhancement is observed for both types of microscale textured replica surfaces. More particularly, both microscale textured replica surfaces exhibit superhydrophobic behaviour.

Figs.19a/b and 20a/b show in a further example the lipophilic enhancement of a polypropylene surface with a microscale textured replica surface (Fig.20a/b) as compared to a flat, unstructured surface (Fig.19a/b). In these figures, the droplet is a PCR reactant grade mineral oil (Sigma-Aldrich; CAS Number 8042-47-5) with a volume of 5 μL. Figure 19a shows a microscopic side view of the droplet of the mineral oil on flat, unstructured polypropylene, from which a contact angle of 14° can be measured (lipophilic behaviour). The lateral

spreading of this droplet on the unstructured surface is outlined by the circle in the top view in Fig.19b. The polypropylene substrate has a diameter of 5 cm. Fig.20a shows a microscopic side view of the droplet of the mineral oil on a microscale textured surface of the same material as in Fig.19. A contact angle below 1 degree is now observed, which may be characterised as complete wetting of the substrate surface. Accordingly, a large increase in the spreading of the droplet over the surface of the substrate is observed as in Fig.20b, where the circle outlines the droplet border. The substrate has a diameter of 5 cm. Note that the droplets in Fig.19 and Fig.20 both have the same volume of 5 μL. A very pronounced lipophilic enhancement is thus observed for the microscale textured replica surface. More particularly, the microscale textured replica surface exhibits superlipophilic behaviour.

D.3.4 Replication Process

Fig.9 shows schematically an injection moulding process for producing a replicated item 4. The process uses a mould having mould parts 1a and 6, wherein mould part 6 has an insert 1b. Tool surfaces 2a, 2b, 7 define a general shape of the replicated item 4. Tool surfaces 2a, 2b are provided with microscale structured master surfaces 3a, 3b, 3c, which are replicated on the item 4 as microscale textures 5a, 5b, 5c, respectively.

Fig. 10 shows schematically an extrusion coating process for coating a substrate web S, with a coating 14. The process uses a roll 11, 11a with a tool surface 12, 12a defining a general shape of the coating. The tool surface comprises microscale structured master surfaces 13, 13a, which are replicated as microscale surface texture 15 on the coating 14. A microscale structured master surface 13 may be applied directly to the tool surface 12 of the roll 11 and/or a microscale structured master surface 13a may be applied to the tool surface 12a of a replication tool insert 11a for attachment to the roll 11.

D.3.5 Localized Pulsed Laser Treatment Generating Microscale Phase Explosions

Fig.8 shows schematically the configuration of the set-up for localized pulsed laser treatment of a tool surface 2 on a replication tool 1 to generate a microscale structured master surface 3 by scanning a pulsed laser beam 99 over the tool surface.

D.4 Example

The example illustrates different ways of identifying suitable laser processing parameters for modifying a given tool surface to obtain a microscale structured master surface.

Aluminium 2017 (available from "Metalcenteret" Glostrup, Denmark) was surface structured using a 1064 nm, 200 kHz, 50 W picosecond laser (FUEGO, Time Band-width) mounted in a microSTRUCT vario (3D-Micromac AG). To perform the surface structuring, the area intended for structuring was irradiated by the laser in parallel lines separated by 20 μm.

Every second layer was perpendicular to the previous, and so one set of perpendicular planes of lines is referred to as one ”cross repetition”. The laser power was set to 25% and 10 repetitions was conducted with focus offset +1.3 mm above the surface.

As illustrated in 11-18, the average dimension and standard deviation of the hole sizes may be adjusted by varying parameters such as laser power in percent of maximum power output, scanning speed, number of cross repetitions and z offset of the focus plane. To identify the optimal parameter settings for achieving a desired hole size population and hole density in the alloy in question, one may map the parameter space of the laser settings. When replicated in polymer, the hole size population and hole density will determine the surface structure and roughness and hence the final wetting properties of the polymer piece. In the example below, the parameter space was for the

- Laser power in percent of the maximum power of 50 W: from 10 to 100 (both included), in increments of 5;
- Scan Speed in mm/s: from 150 to 1950 (both included), in increments of 100; and from 600 to 4200 (both included), in increments of 200;
- Number of cross repetitions: from 3 to 39 (both included), in increments of 2;

It may be noted that similar surface characteristics may be achieved using different parameter combinations. However, to minimise time consumption for the laser process, the parameter coordinate with the highest (scan speed / cross repetition) value, and hence lowest process time, is preferred.

Additional information:

- Alloy: 2017, aluminium
- Wavelength = 1064 nm
- Pulse frequency = 200 kHz
- Focus plane = z + 1.3 mm
- Max laser power = 50 W

A recommended method to reduce the number of parameters and experiments is by locking parameter pairs in a fixed ratio, such as keeping (laser power / scan speed) constant, see Fig.11 and Fig.12, where the numerical value of the ratio of (laser power (in percent of the max power of 50 W) divided by the scan speed (in mm/s) is kept constant at 25E-5 (= 0,00025) or 50E-5 (= 0,0005) and allows for identification of the desired modification characteristics: both figures show peaks in hole density X. Likewise, the numerical value of the ratio of the number of repetitions divided by the scan speed (in mm/s) can be kept constant, see Fig.13 and Fig.14, where this ratio is kept constant at 1E-2 (= 0.01) or 2E-2 (= 0.02) and allows for identifying desired modification characteristics. As can be seen in Fig. 14, the high intensity (slow speed) results in few but large holes, whereas Fig. 13 shows that for the numerical value of the ratio of repetitions over scan speed (in mm/s) equal to 0.01 a more densely packed and uniform hole formation is achieved.

Figs.15-18 show four graphs plotting hole density against the scan speed used during the pulsed laser treatment of the respective tool surfaces. At speeds $\leq$ 1250 mm/s, the hole density is consistent regardless of other parameters than speed, and it is concluded that

writing speed is the main determining factor in this regime. At speeds $\geq$ 1250 mm/s, the hole density varies with the number of cross repetitions. This is true, even when the product (power X repetitions) is kept constant, (see Fig. 16). Marker size represents cross repetitions in Fig.15 and (cross repetitions X power) in Fig.16. Regardless of the parameter settings used to achieve a desired hole density, the coefficient of variance (CV) of hole size is observed to be stable in the regime where (speed $\geq$ 1250 mm/s), see Fig.17, and accordingly for the standard deviation (STD), see Fig.18. Marker size represents hole size CV in Fig.17 and hole size STD in Fig.18. Similarly, the laser focus parameter space may be mapped to identify applicable laser settings.

D.5 Claims

1. Method of producing an item with enhanced wetting properties by a replication process, the method comprising the steps of
   - providing a forming tool having a tool surface adapted to define a general shape of an item to be formed;
   - modifying at least portions of the tool surface by a pulsed laser treatment to obtain a replication tool with a microscale structured master surface with a lateral master pattern and a vertical master profile, wherein the pulsed laser treatment is adapted to generate microscale phase explosions on the tool surface, thereby forming the microscale structured master surface as a lateral arrangement of microscale crater-shaped depressions, wherein the lateral pattern of the microscale structured master surface has an area density of microscale master features of at least 5000/mm^2;
   - using the replication tool to form the item by the replication process, wherein the formed item has the general shape defined by the tool surface, and wherein the formed item comprises a microscale textured replica surface with a lateral arrangement of microscale protrusions produced by the microscale structured master surface.
2. Method according to claim 1, wherein the replication process is injection moulding or extrusion coating.
3. Method according to claim 1 or claim 2, wherein a replication period from contacting the tool surface with the molten replication material to releasing the shaped item is less than three minutes, such as less than two minutes, such as less than one minute, such as less than 30 seconds, or even less than 10 seconds.
4. Method according to any of the preceding claims, wherein the vertical replica profile predominantly has rounded tops with a radius of curvature in the microscale.
5. Method according to any of the preceding claims, wherein the replica material is hydrophobic with a flat surface contact angle of at least 95°, preferably at least 100°, and up to 120°, preferably up to 110°.
6. Method according to claim 5, wherein the microscale textured replica surface is superhydrophobic.
7. Method according to any one of claims 1-4, wherein the replica material is hydrophilic with a flat surface contact angle below and including 85°, below and including 80°, or preferably below and including 75°, and at least 50°, at least 60°, or at least 70°.
8. Method according to claim 7, wherein the microscale textured replica surface is superhydrophilic.

9. Replication tool for producing an item with enhanced wetting properties by fast replication, the replication tool comprising
    - a tool surface defining a general shape of the item,
    - the tool surface comprising a microscale structured master surface having a lateral master pattern and a vertical master profile wherein said microscale structured master surface has been provided by localized pulsed laser treatment to generate microscale phase explosions, wherein the lateral pattern of the microscale structured master surface has an area density of microscale master features of at least $5000/mm^2$,.
10. Replication tool according to claim 9, wherein the tool surface is made of a met-al, such as alloys of aluminium or steel.
11. Replication tool according to any one of claims 9-10, wherein the microscale structured master surface is a lateral arrangement of polydisperse microscale master features.
12. Replication tool according to claim 11, wherein the microscale master features are crater-shaped depressions.
13. Replication tool according to any one of claims 9-12, wherein the vertical profile of the microscale structured master surface has a peak-to-peak amplitude of at least 0,3 μm, or at least 0,5 μm or at least 1 μm and below 30 μm, below 20 μm, or preferably below 10 μm.
14. Replication tool according to any one of claims 11-13, wherein the lateral pattern of the microscale structured master surface has an area density of microscale master features of at least $8000/mm^2$, or at least $10000/mm^2$.

D.6 Abstract

The invention relates to a replication tool for producing an item with enhanced wetting properties by fast replication, such as injection moulding or extrusion coating. The replication tool comprises a tool surface defining a general shape of the item. The tool surface comprises a microscale structured master surface having a lateral master pattern and a vertical master profile. The microscale structured master surface has been provided by localized pulsed laser treatment to generate microscale phase explosions. A method of producing an item with enhanced wetting properties uses the replication tool to form an item with a general shape as defined by the tool surface. The formed item comprises a microscale textured replica surface with a lateral arrangement of polydisperse microscale protrusions.

1/8

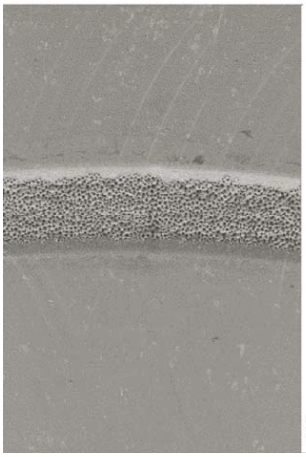

Fig. 1a

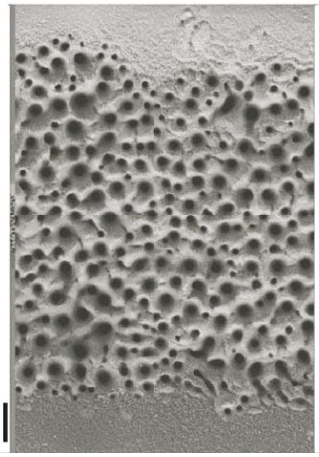

Fig. 1b

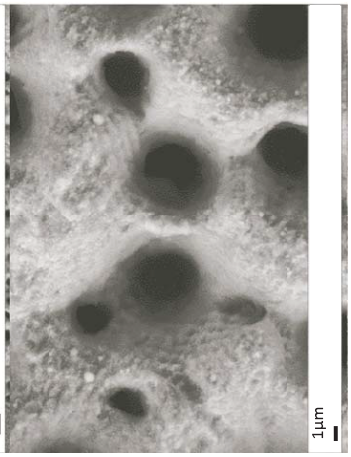

Fig. 1c

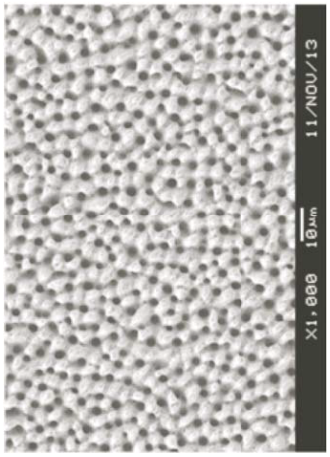

Fig. 2

2/8

Fig. 3

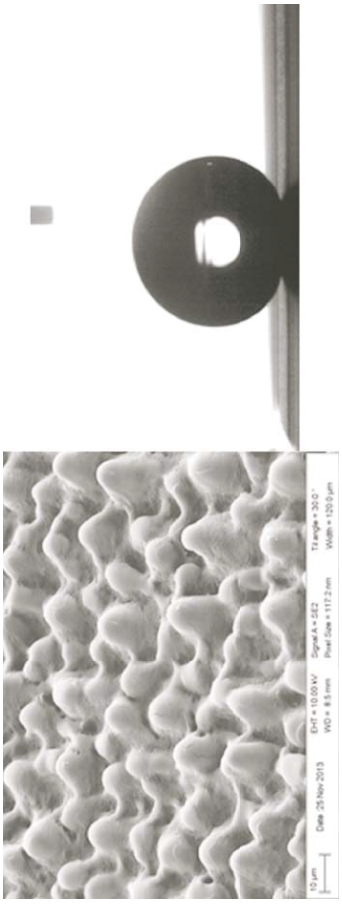

Fig. 4

Fig. 5

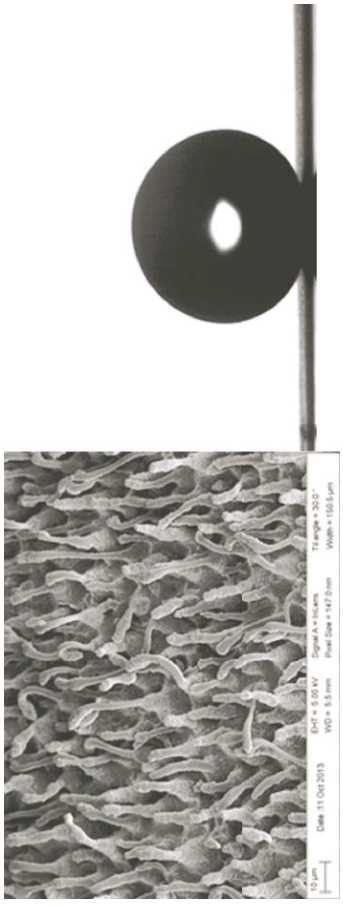

Fig. 6

Fig. 7

3/8

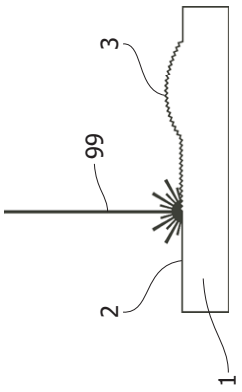

Fig. 8

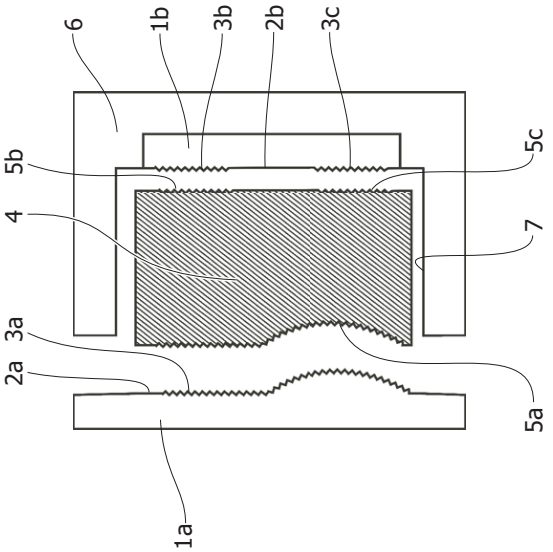

Fig. 9

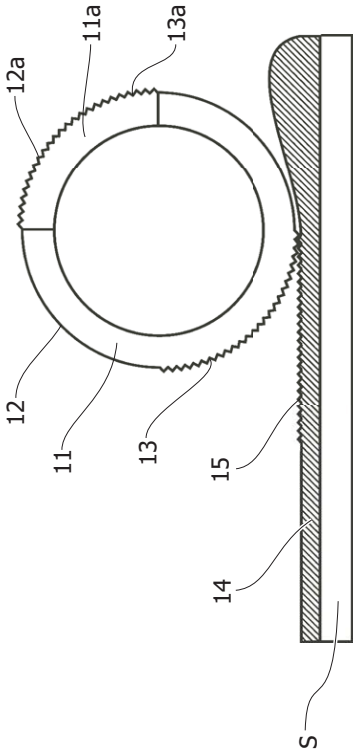

Fig. 10

4/8

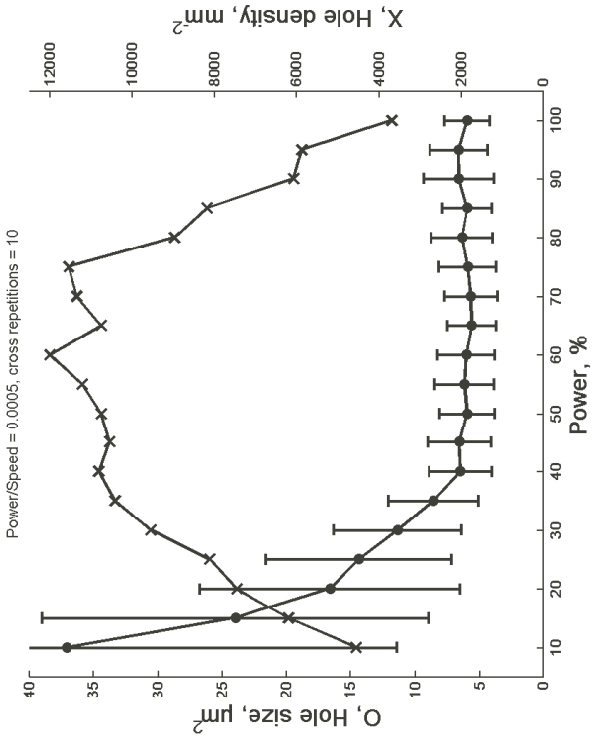

Fig. 11

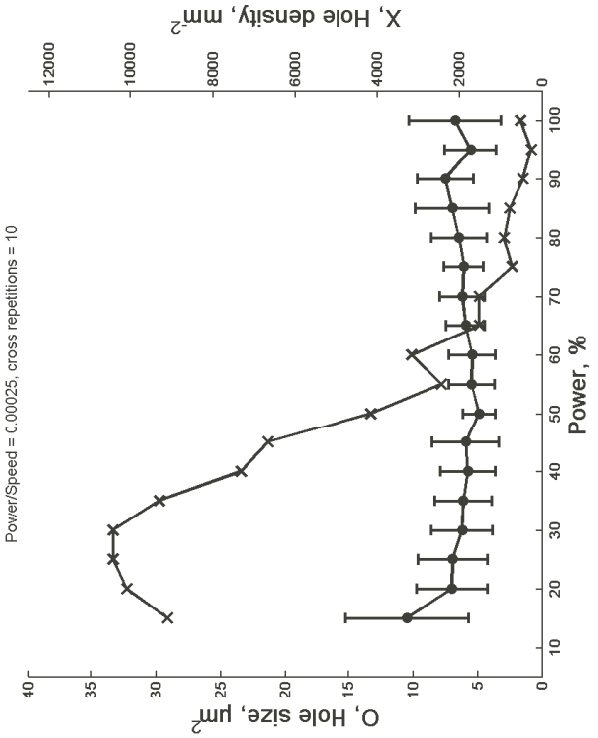

Fig. 12

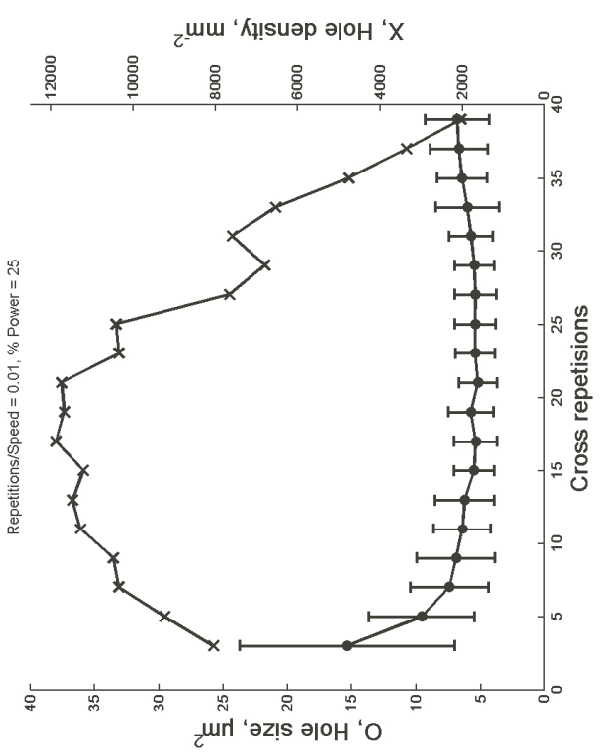

Fig. 13

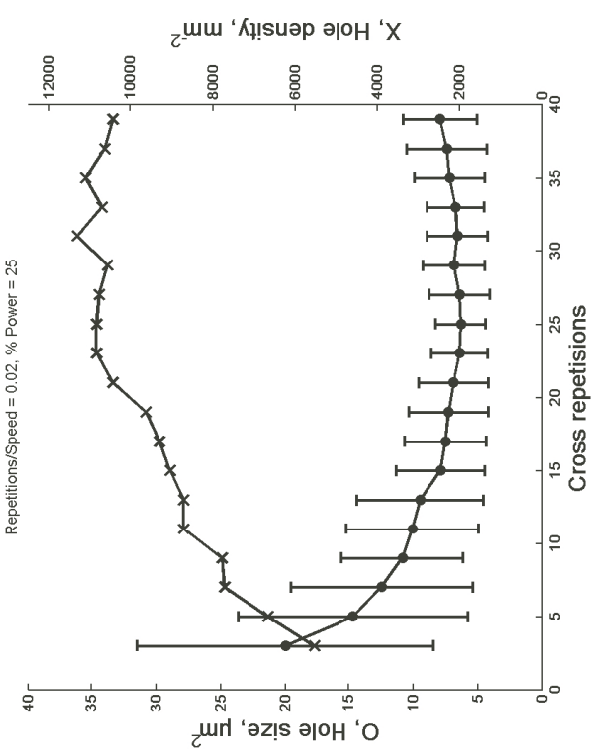

Fig. 14

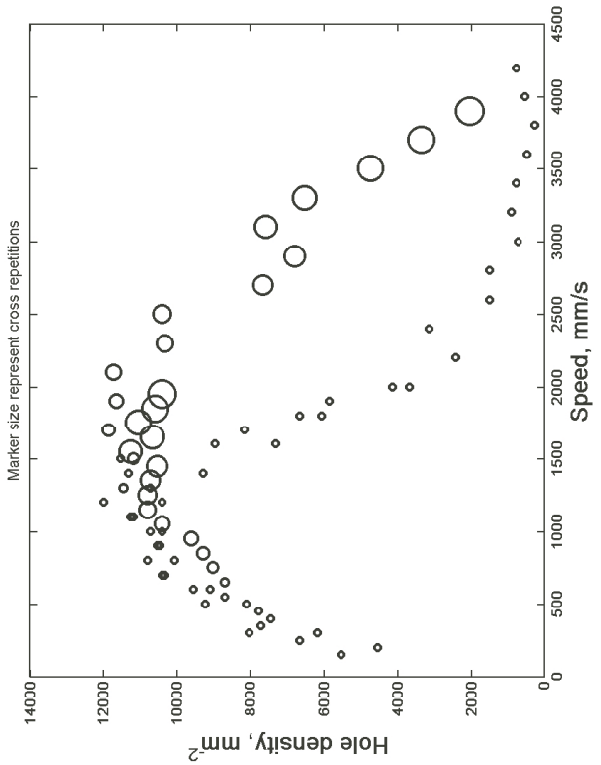

Fig. 15

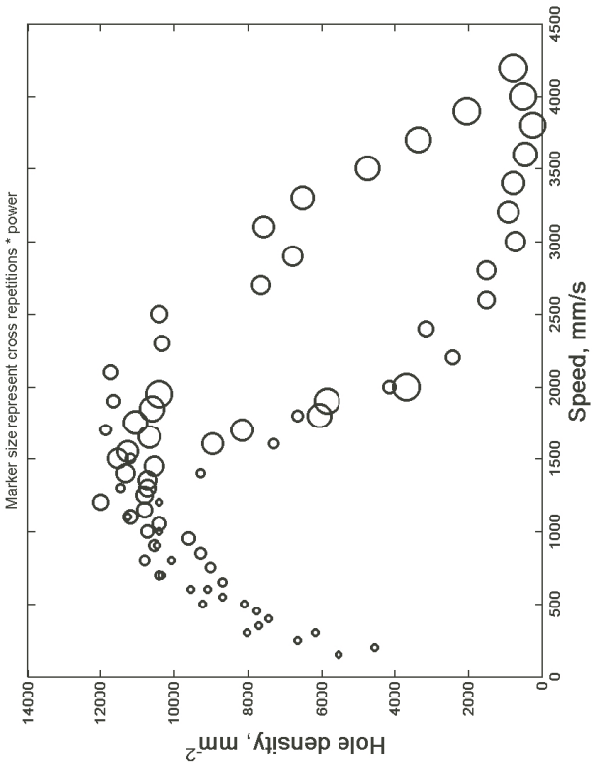

Fig. 16

7/8

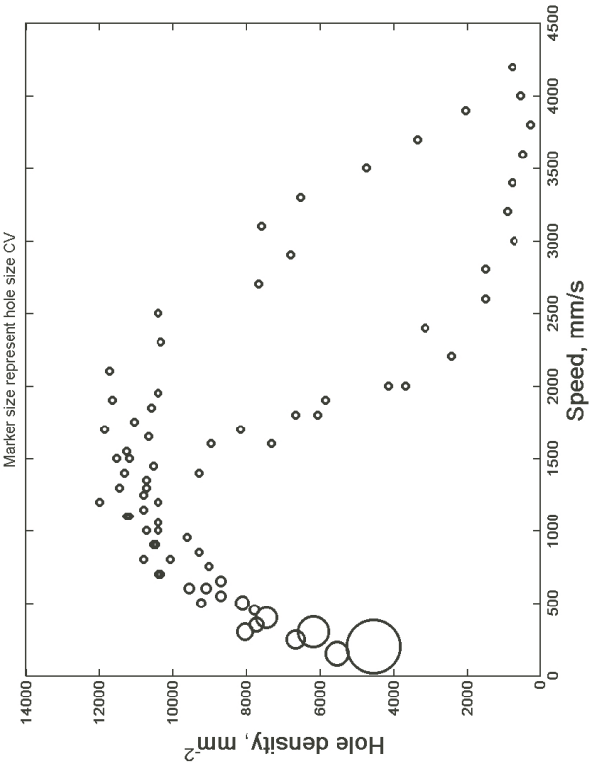

Fig. 17

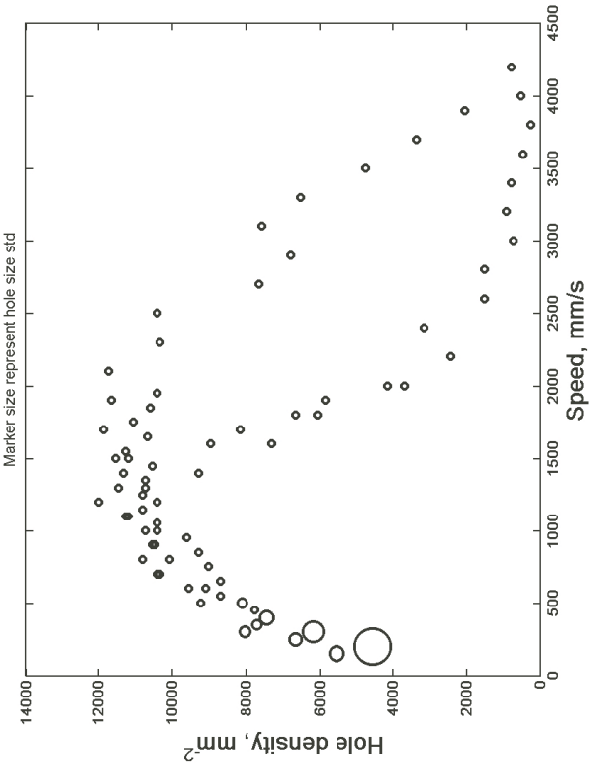

Fig. 18

8/8

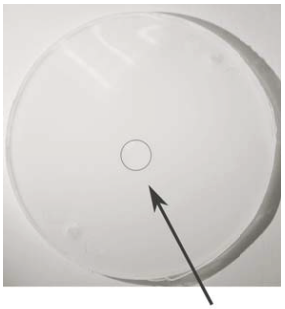

Fig. 19b

Fig. 19a

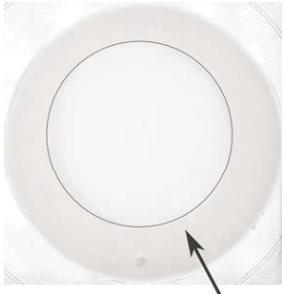

Fig. 20b

Fig. 20a

Published by:
DTU Nanotech
Department of Micro- and Nanotechnology
Technical University of Denmark
Ørsteds Plads, building 345C
DK-2800 Kgs. Lyngby